UNIVERSIDAD COMPLUTENSE DE MADRID

FACULTAD DE CIENCIAS FÍSICAS

TESIS DOCTORAL

Óptica de Neutrones: Caracterización y Uso de Guías de Onda

Neutron Optics: Characterization and Use of Neutron Waveguides

MEMORIA PARA OPTAR AL GRADO DE DOCTOR

PRESENTADA POR

Ignacio Molina de la Peña

DIRECTORES

María Luisa Calvo Padilla

Ramón Fernández Álvarez-Estrada

UNIVERSIDAD COMPLUTENSE DE MADRID
DEPARTAMENTO DE ÓPTICA, FACULTAD DE FÍSICAS

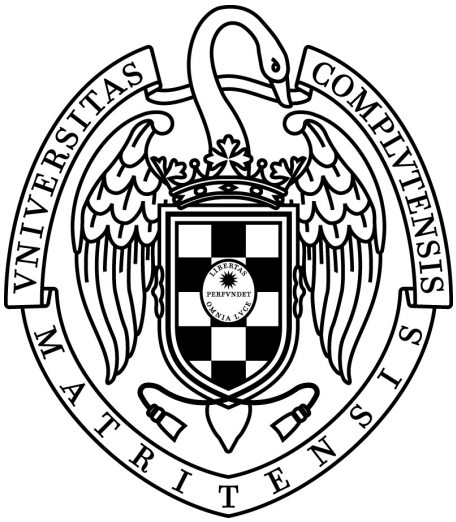

Óptica de Neutrones: Caracterización y Uso de Guías de Onda

Neutron Optics: Characterization and Use of Neutron Waveguides

Memoria presentada por

Ignacio Molina de la Peña

para optar al grado de Doctor en Física

Directores:
María Luisa Calvo Padilla y Ramón Fernández Álvarez-Estrada

Tutor:
Rosa Weigand Talavera

Madrid, 2023

Para mis hijos:
a Guille, por su bondad
a Paula, por su alegría

y para Belén:
por su paciencia y apoyo.

Agradecimientos

Dicen que los agradecimientos es lo que más tienes que trabajar, porque es lo único que todo el mundo se leerá... ¡Qué presión! Y es que este proyecto no hubiera sido posible sin el apoyo y cariño de muchas, muchas, muchas personas que he tenido la suerte de conocer

En primer lugar quiero agradecer el apoyo de María Luisa y Ramón, mis directores de tesis. A María Luisa, por tantos años de amistad y consejos, desde tus primeras clases de óptica hasta el punto final de esta tesis. Nunca podré agradecerte lo suficiente el día que me abriste tu despacho y aceptaste embarcarte en este reto. Ramón, te uniste al poco (igual sin saber lo pesado que puedo ser). A ti te agradezco los cientos de papeles manuscritos con tus fórmulas y pacientes explicaciones que dieron forma a esta tesis. Sólo puedo decir que ha sido un placer y, sobre todo, un lujo haber podido compartir y desarrollar mis ideas con vosotros. Sin vuestro esfuerzo, dedicación y ánimos estas líneas no se habrían escrito.

También quiero agradecer a todos aquellos que han sido soporte de este proyecto. Gracias a Rosa Weigand, porque, aparte de tus fantásticos consejos, te ha tocado lidiar con lo peor de toda la tesis: la burocracia. Quiero agradecer a los dos expertos externos por las molestias de revisar la tesis, sus comentarios y, sobre todo, sus sugerencias. A todos los miembros del Grupo Interdisciplinar de Computación Óptica, GICO-UCM. A Víctor Martín Mayor, por su apoyo económico a través del proyecto PGC2018–094684-B-C21, del Ministerio de Ciencia e Innovación y al proyecto FECI-EU-17–06 de la Universidad Complutense de Madrid, que nos han permitido la participación en varios congresos. A Felipe Llanes por interesarse sobre el tema y darme la oportunidad de contarlo en seminario. A Aitor Villafranca por las estupendas sugerencias que, sin duda, han contribuido a mejorar este trabajo. Y a Ignacio Porras, por acercarnos a la BNCT y su invitación a colaborar. My thanks to Keith A. Gillow, Sam Evans and John McManigle, from whose template I adapted this thesis.

Y luego están todos aquellos que han sido compañeros, amigos y apoyo durante tantos años.

Gracias a mi familia. A Belén, la otra mitad del equipo ¿O quizás el 60%? ¡Si hasta ha maquetado la tesis! No cabe aquí escribirte lo que siento y soy a tu lado. Contigo sólo quiero más. A Guille y Paula, porque desde que llegasteis dais color a

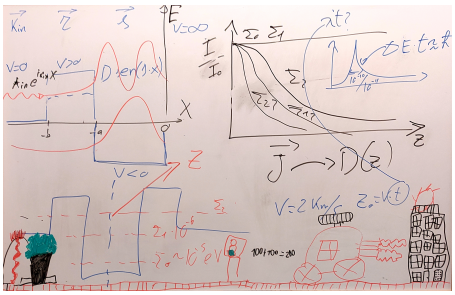

Figura 1: Una reunión de zoom en la que entró la mano de Guille

Figura 2: Resultado final cuando Guille y Paula me robaron la pizarra

cada cosa que hago (véase Figuras 1 y 2 al respecto). He aprendido mucho durante este camino, pero nada comparado con lo que me enseñáis vosotros.

Gracias a mis padres por su amor y cariño incondicional. Soy quién soy gracias a vosotros. Gracias a Marisa, mi madrina, por atreverse a venir al congreso de Barcelona. Y gracias a los Kobryn-Melgarejo: Rocío, Artur, Nico, Carla (mi ahijada), Tomás y Lucas porque siempre estáis ahí (lejos, pero ahí).

Quiero agradecer a Andrés y Flavio, por su amistad, consejos y charlas. Y, sobre todo, por esas comidas y sobremesas sin fin, 'peloti' incluido. A Leyre, María, Esteban, Edurne por compartir las aventuras y desvelos de la paternidad, las casas rurales y la buena conversación.

Gracias a Alfonso (mi hermano), a Jaime (mi wingman), a Malky (de los pocos que quizá se lea el resto) y a Adrián (el alma de la fiesta) por tantas cosas que hemos compartido; comics (que adornan este libro), series, malas pelis, buena música y, sobre todo, risas, muchas risas.

Gracias a Chema, por encender esta llama. Y gracias a tantos otros que me dejo, pero no olvido. Compañeros y amigos durante todo este tiempo, que habéis viajado conmigo hasta hoy.

A todos, gracias.

Table of Contents

List of Figures

List of Tables

Resumen en Español

Introducción

La óptica de neutrones es una rama de la física de neutrones que describe la propagación y dispersión de neutrones lentos a través de medios materiales utilizando ecuaciones mecano-cuánticas similares a las de la óptica clásica para la propagación de la luz.

Solo unos pocos años después del descubrimiento del neutrón en 1932, [1], se demostró experimentalmente, [2], que un haz de neutrones térmicos exhibe fenómenos similares a los de la propagación de la luz como la reflexión, refracción, birrefringencia, difracción, etc. En consecuencia, se comenzaron a utilizar conceptos como el índice de refracción para describir la propagación de neutrones lentos.

Objetivos

Hoy en día, la investigación en óptica de neutrones se interesa cada vez más por la propagación, confinamiento y enfoque de haces de neutrones. En esta tesis se explora la descripción de estos comportamientos a través de una formulación rigurosa.

El objetivo de esta tesis es estudiar el comportamiento de un haz de neutrones térmicos en ciertos medios (por ejemplo, Titanio) y, más específicamente, la posibilidad de excitar modos de propagación en estas guías de onda. Esta tesis es una continuación de las propuestas de Calvo y Álvarez-Estrada [3] y [4] sobre la posibilidad de confinar y guiar un haz de neutrones térmicos, de manera similar a como una fibra óptica o una guía de ondas, confina y propaga la luz. La caracterización matemática adecuada de las guías de onda de neutrones permitirá la optimización del diseño de estos dispositivos.

Proponemos guías de onda con una sección transversal (apertura) de 1000 Å, y longitudes del orden de un metro. Su caracterización no es sencilla debido a la longitud de onda de los neutrones térmicos (1.8 Å). Involucra ecuaciones integrales complejas y un gran volumen de datos que deben manejarse y calcularse, lo que es complejo computacionalmente hablando.

Resultados

El capítulo 1 se dedica a la presentación de esta tesis. Revisamos las bases de la óptica de neutrones: desarrollo histórico y experimentos clave, así como las ecuaciones básicas, relaciones y potenciales para la óptica de neutrones.

En el capítulo 2 exponemos las características básicas y el estado del arte de las guías de onda de neutrones. Aplicamos las técnicas disponibles en la actualidad para caracterizar nuestra propuesta de guías de onda. Intentamos la simulación numérica de la función de onda y el estudio de los niveles de energía del sistema. Además, adaptamos a las guías de onda de neutrones la aproximación propuesta por Snyder y Love para guías de onda débilmente acopladas. Demostramos que todas estas técnicas, a pesar de proporcionar información valiosa, son insuficientes para una caracterización completa las mismas.

En el capítulo 3 proponemos una nueva formulación rigurosa para la función de onda del neutrón mediante el uso de funciones de Green y ciertas funciones auxiliares definidas en las fronteras. Nuestro análisis se restringe a condiciones de contorno de Dirichlet (equivalentes a un medio infinitamente repulsivo). Demostramos que permite la caracterización analítica de: (i) plano infinito, (ii) guía longitudinal infinita, (iii) difracción de una abertura y (iv) guía de onda semi-infinita.

En el capítulo 4 proponemos un nuevo algoritmo iterativo, basado en las ecuaciones anteriores, para calcular recursivamente las funciones auxiliares que definen el sistema. Demostramos que podemos resolver numéricamente diferentes problemas y geometrías con complejidad creciente. Por último, reinterpretamos las condiciones de Dirichlet como objetos en el espacio y mostramos cómo puede aplicarse este algoritmo, con algunas variaciones, para generar hologramas digitales.

La formulación presentada en los capítulos anteriores se limita a las condiciones de contorno de Dirichlet. En el capítulo 5, exploramos el uso de las ecuaciones de Lippmann-Schwinger para situaciones en las que hay penetración de neutrones en el clad. Proponemos un uso recursivo de las ecuaciones de Lippmann-Schwinger para el vacío y los modos de propagación. Mostramos que esta formulación predice correctamente la excitación de los modos de propagación y las amplitudes de propagación y reflexión en guías de onda basadas en Titanio-Silicio.

En el capítulo 6 proponemos el posible uso de dispositivos similares a los acopladores ópticos para mejorar la eficiencia de las actuales guías de onda de neutrones. Nos basamos en una primera guía de Titanio-Silicio para mejorar la formación de modos de propagación y una segunda guía de onda hueca para propagar neutrones con las menores pérdidas posibles. Estos acopladores podrían utilizarse en la Boron Neutron Capture Therapy (BNCT) para tumores de pequeño tamaño. En el capítulo se presenta una breve revisión de esta técnica y su estado actual de desarrollo.

Esta línea de investigación ha generado múltiple producción investigadora. Hemos publicado seis artículos de investigación en diversos campos y un capítulo de libro sobre guía de ondas de neutrones. Destacamos que nuestra investigación dio lugar a la presentación de una patente, [5], en holografía digital.

Conclusiones

La caracterización de las guías de ondas de neutrones sigue siendo un problema abierto e interesante. La descripción de la onda estacionaria, mediante el uso de funciones de Green, y su resolución mediante el algoritmo propuesto en esta tesis suponen una mejora sobre las técnicas actuales y pueden tomarse como una descripción de orden cero de la guía de onda.

Las técnicas aquí propuestas son transversales a diferentes áreas de la física. La nueva formulación establecida en esta tesis abre la posibilidad de estudiar problemas más allá del propio campo de la óptica de neutrones. Hemos demostrado que estas técnicas son interesantes tanto para la investigación en ciencia básica como para su aplicación en el diseño de dispositivos para diversos campos, como el tratamiento de cánceres pequeños o la holografía digital.

Abstract

Introduction

Neutron optics is the branch of neutron physics that describes the slow neutron propagation and scattering through material media by using quantum-mechanical equations similar to those in classical optics for light propagation.

Only a few years after the discovery of the neutron in 1932, [1], it was clearly demonstrated in experiments, [2], that a thermal neutron beam exhibits phenomena similar to those of propagating light, such as reflection, refraction, birefringence, diffraction, etc. Consequently, concepts such as refractive index became used for describing slow neutron phenomena.

Objectives

Today, increasingly active researches in neutron optics focus on confinement, propagation and focusing of slow neutron beams. In this thesis we explore the neutron optics relationships that allow the description of these behaviours through a rigorous formulation.

The aim of this thesis is the study of the confined propagation of a thermal neutron beam in certain media (i.e.: Titanium), specifically, the possibility of exciting propagation modes. It continues the proposals of Calvo and Alvarez-Estrada, [3] and [4], on the possibility of confining and guiding a thermal neutron beam, in a similar way as an optical fibre, or a waveguide, confines and propagates light. The proper mathematical characterization of neutron waveguides will enable an optimal design and improvement of these devices.

We propose waveguides with a transverse section (aperture) of 1000 Å, and lengths up to the order of a meter. This characterisation is not easy, due to the wavelength of a thermal neutron beam (1.8 Å). It involves complex integral equations and a huge volume of data to handle and compute which is normally unaffordable.

Results

Chapter 1 is devoted to introduce this thesis, and review the basis of neutron optics: historical development and key experiments, the basic equations, relationships

and potentials for neutron optics.

In Chapter 2 we state the basic features and state of the art of neutron waveguiding. We apply the currently available techniques for characterizing our waveguide proposal. We attempt the numerical simulation of the wavefunction and the study of the system's energy levels. Moreover, we adapt to neutron waveguides the approximation proposed by Snyder and Love [6] for weakly coupled waveguides. We demonstrate that all these techniques, despite providing valuable information, are insufficient for a complete characterization of these waveguides.

In Chapter 3 we propose a novel rigorous mathematical description for the neutron wavefunction by means of Green's functions and certain auxiliary functions defined at the boundaries. Our analysis is restricted to Dirichlet boundary conditions (which are equivalent to an infinitely repulsive medium surrounding the confining region of the waveguide, namely, the clad). We demonstrate that it allows the analytical characterization of: (i) infinite plane, (ii) infinite longitudinal guide, (iii) diffraction of an aperture and (iv) semi-infinite waveguide.

In Chapter 4 we propose a new iterative algorithm, based on the above equations, to compute numerically and recursively the auxiliary functions defining the system for Dirichlet conditions. We demonstrate that we can solve numerically different problems and geometries with increasing complexity. Finally, we reinterpret Dirichlet conditions as objects in space and show how this algorithm can be applied, with some variations, to generate digital holograms.

The formulation presented in previous chapters is restricted to Dirichlet boundary conditions. In Chapter 5, we explore the use of the Lippmann-Schwinger equations for situations in which there is neutron penetration in the clad. We propose a recursive use of the Lippmann-Schwinger equations for vacuum and modal propagation, recursively. We show that this formulation predicts correctly the excitation of the propagation modes and the propagation and reflection amplitudes in Si-Ti based waveguides.

In Chapter 6 we propose the possible use of devices similar to optical couplers to improve the efficiency of current neutron waveguides. We base them on a first Titanium-Silicon guide for improving the formation of propagation modes and a second empty-core waveguide for propagating neutrons with few losses. These couplers may be possibly used in Boron Neutron Capture Therapy (BNCT)for tumours of small size. In the chapter, we present a brief review of this technique and its current state of development for tumours of large size.

Our research topic has proven to be fruitful, as shown by our research production. We achieved the publication of six research papers in a variety of fields and a book chapter on neutron waveguiding. We emphasize that our research yielded the presentation of a patent, [5], in digital holography.

Conclusions

The characterization of neutron waveguides remains an open and interesting problem. The standing wave description, by using Green's functions, and its resolution by means of the algorithm proposed in this thesis are an improvement on current techniques and can be taken as a zero-th order description of the waveguide.

Moreover, the techniques proposed here are transversal to different areas of physics. The new formulation established in this thesis opens the possibility of studying unexplored problems beyond the field of neutron optics itself. We have demonstrated that these techniques are interesting both for basic science research and for its application in the design of devices for a variety of fields, such as small cancer treatment or digital holography.

Index of Notations and Constants

Along this thesis, we made use of the following constant values (from [7]) in formulas:

Table 1: General Notations and Physical Constants

Constant	**Value**	**Comments**
c	2.998×10^8 m/s	Speed of light in vacuum
$\hbar$	6.58×1022 MeV $\cdot$ s	Planck's constant
m_n or m	939.57 MeV/c^2	Neutron rest mass
	1.674×10^{-27} kg	
m_p	238.27 MeV/c^2	Proton rest mass
	1.672×10^{-27} kg	
$\mid e \mid$	1.602×10^{-19} coulomb	Proton electric charge
K_b	1.38×10^{-23} m^2/(kg^{2}K)	Boltzmann's constant
μ_N	$= \hbar \mid e \mid /2m_pc$	One nuclear magneton
$1eV$		One electron-volt
$1keV$	10^3 eV	One kiloelectron-volt
$1MeV$	10^6 eV	One megaelectron-volt

Table 2: Specific Notations and Physical Constants

Notation	**Value**	**Comments**
Thermal Neutrons	$E = 0.025$ eV	Thermal neutrons energy
	$\lambda_{db} = 1.8$ Å	Thermal neutrons wavelength
	$\mid \boldsymbol{k} \mid = 3.47$ Å^{-1}	Thermal neutrons wavevector
Italics	x, y, z	Independent coordinates
	z	Propagation direction
	x, y	Transverse coordinates
Upper bar case	$\bar{x} = (x, y)$	Two-dimensional (transverse) vector
Bold case	$\boldsymbol{x} = (\bar{x}, z) = (x, y, z)$	Three-dimensional vector

Table 3: List of Acronyms

Acronym	**Explanation**
BNCT	Boron Neutron Capture Therapy
FDM	Finite Difference Methods
FDTD	Finite Difference Time Domain
FFT	Fast Fourier Transform
FZP	Fresnel Zone Plate
GFDM	Generalized Finite Difference Methods
HCC	Hollow Capillary Channel
IFFT	Inverse Fast Fourier Transform
LS	Lippmann-Schwinger (equation)
MCW	Multiple Coupling Waveguides
PDDO	Peridynamic Differential Operator
PGF	Polycapillary Glass Fibres
TCW	Two Coupling Waveguides

- Eh. Sin duda alguna, eso está relacionado con
ese libro que ha amenazado con escribir.
- Bueno, buena suerte Sr. Black...
pero no se ausente mucho tiempo.

Providence

1 Introduction

Contents

Neutron optics is the branch of neutron physics that makes use of the similarities of the mathematical description for the propagation and scattering of neutrons by material media with formally similar equations for the propagation of light used in classical optics. The equations describing both phenomena take the form of a Helmholtz equation under the assumption of long time evolutions ($t \to +\infty$) and the absence of sources in the medium.

Thus, neutron optics is the study of how a beam of slow neutrons scatters and propagates in matter, just as spectroscopy consists of the study of the interaction of electromagnetic radiation with matter. The origin of neutron optics dates back to

only a few years after the discovery of the neutron. While the particle was discovered in 1932 [1], the notion of refractive index for neutrons was set and experimentally characterized for different materials [2]. In those years, neutron optics developed quickly with the advent of the first reactors. Inherently optical phenomena were observed, such as neutron reflection and refraction in different materials, neutron birefringence and neutron diffraction on sharp edges and crystalline materials, neutron guiding, etc. After this initial progress the interest in neutron optics and guiding declined. This was motivated, partly, due to the difficulties of accessing neutron sources for research and, partly, because most of the efforts were focused in the development of nuclear power and reactors (focusing, thus on neutron moderation in media). After those early days, the most challenging experiments focused on the demonstration of the quantum-mechanical behaviour of the neutron. At present, among other investigations, there are increasing interest and research activities in the confined propagation and focusing of slow neutron beams.

1.1 Overview of This Thesis

1.1.1 Challenges on Neutron Waveguiding

Routinely, neutron beams in experiments were directed from their sources by using macroscopic guides: hollow tubes with transverse dimensions of the order of several centimetres to meters and lengths of several meters to tens of meters, [8, 9, 10].

In 1973, [11], the possibility of generating propagation modes for an incoming thermal neutron beam in (essentially two-dimensional) thin films was suggested (i.e.: neutron waveguiding). The proposal was based on quantum-mechanical tunnel effect descriptions on devices whose transverse dimensions are orders of magnitude lower than macroscopic hollow guides (i.e.: the order of μm).

In the 80s, Calvo and Álvarez-Estrada performed theoretical analyses to fully characterize three-dimensional neutron waveguides (fibres) by exploiting analogies with light propagation along optical fibres, [3, 4]. Their proposals included non-hollow guides using natural Titanium in their core. Natural Titanium is a suitably material since it exhibits a refractive index lower than that of vacuum and, thus, it allows for confining and guiding a thermal neutron beam through the rise of propagation modes.

In the 90s, these devices were experimentally achieved, [12, 13]. Two main approaches were used: (i) hollow capillary channels (HCC) based on Silicon and (ii) Titanium thin films, as in 1973 proposal. These devices exhibited interesting "optical" properties such as confined propagation and focusing.

These devices have the potential to be used in a wide variety of subjects, from basic research in matter analysis to clinical applications. It is especially interesting its possible use in Boron Neutron Capture Therapy (BNCT), a cancer treatment used for glioblastomas in brain (a review is performed in Section 6.2).

The characterization of how an impinging thermal neutron beam is confined in the form of propagation modes is, in any case, a necessary first step to identify critical design parameters and geometries and the improvement of current devices. However, the adequate characterization of these waveguides is not a simple task. The thermal neutron beam wavelength is 1.8 Å and our waveguides have transverse dimensions (guide aperture) of 1000 Å (100 nm). The rise of propagation modes is a key effect we are looking for, and diffraction plays a role on it. Thus, its description by means of classical geometric optics is insufficient. Moreover, numerical simulation of the wave equation, Eq.(1.5), fails due to the associated integral equations and the huge volume of computation required.

Nowadays, the full analytical characterization of neutron waveguides continues to pose open and interesting research problems.

1.1.2 Objectives of This Thesis

This thesis may be regarded as a continuation of the research line of our group. Our aim is to provide an extensive and full mathematical description of the propagation of a thermal neutron beam in media. With that knowledge, we focus on the characterization of neutron waveguides of length up to about one meter for which we assume transversal dimensions (guide aperture) of 1000 Å. Since the wavelength of a thermal neutron beam (1.8 Å) is much smaller than the transverse dimensions, the numerical simulation of the wave equation, Eq.(1.5), is a computational challenge, while the waveguide characterization by means of classical geometric optics is insufficient.

We oriented the thesis, in particular, to the study of how the impinging thermal neutron beam is diffracted at the waveguide entrance, propagates and gives rise to propagation modes. For it, we propose a Green's functions formalism under Dirichlet boundary conditions (i.e.: no wave penetration in the waveguide's clad, as if it was infinitely repulsive). It can be taken as a zero-th order description of the waveguide. At a later stage, waveguides with clads which are not infinitely repulsive (thereby removing the strict Dirichlet condition) are also investigated.

Our final goal is the study of the interaction and propagation of a beam of thermal neutrons in certain materials (Titanium) whose associated refractive index is lower than the refractive index in a vacuum. These materials would allow, under certain circumstances, to confine a beam of slow neutrons by themselves or in conjunction with other materials (waveguide's clad). With this, one would be able to design waveguides, couplers and other devices that would improve the use of neutron beams. Multiple science areas such as medicine, matter research, fundamental physics, etc would benefit of these improvements.

While our research is focused on thermal neutron beams, other disciplines making use of scalar wave equations to describe confined propagation are potential users of the formulation developed in this thesis. As an example, an indirect application of our research led us to a patent request in the field of digital holography, [5].

1.1.3 Thesis Organization

This thesis is divided into the following seven chapters. In this chapter, we perform a historical review on the discovery of the neutron and the most important experiments involving neutrons. We characterize the neutron radiation properties, especially in comparison with X-rays. Finally, we list a number of neutron sources, their main features and fluxes achieved, as well as a brief explanation of the main operations to obtain a suitable monochromatic neutron beam.

Chapter 1 is devoted to introducing a brief review of neutron discovery, main properties and its quantum-mechanical description using the Schrödinger equation. In the second part of this chapter we will focus on the basic equations of neutron optics for the study of the propagation of a beam of thermal neutrons in material media using the stationary wave equation. In this description, it is a key feature the interaction potential between the neutron and the media. Therefore, in this chapter we characterize the Fermi pseudopotential. We relate this potential with the coherent and incoherent scattering lengths and how these parameters set the values for the refractive index for neutrons and the effective cross sections.

In Chapter 2, we focus on neutron waveguides, with an introduction to the most relevant characteristics required for a neutron waveguide and a review of the most noteworthy experiments and the current state of the art. We apply currently available techniques for the characterization of these neutron waveguides. Our first attempt is the numerical resolution of the wave equation, Eq.(1.5), by using Finite Difference Time Domain (FDTD). We show that these simulations require an unaffordable amount of computation. The next attempt focuses on the analysis of propagation modes. This method provides information about the structure of the energy levels in the waveguide but it is difficult to obtain direct values from it. At the end of the chapter, we make use of the approximation proposed by Snyder and Love [6] for weakly coupled waveguides adapted to the quantum mechanical description of the neutron. This method shows a good correspondence with the expected values in classical Optics, in particular estimating the critical angle. Even if important and useful information about waveguides may be obtained, these approaches are not the full mathematical characterization we need to deeply study the propagation of thermal neutrons in waveguides.

Given the limitations of the previous methods, in Chapter 3 we propose a new formulation for the description of the stationary wave. The formula is inspired by the studies carried out by Balian and Bloch, [14], for the quantum mechanical description of the atomic nucleus. In our case, as our problem is not constrained to a specific region of space, we have must add an inhomogeneous term that, physically, is interpreted as the incident neutron beam. This method describes the neutron wavefunction by means of Green's functions and certain auxiliary functions defined at the boundaries where the boundary conditions are imposed. Solving for the auxiliary functions (for a particular set of boundary conditions)

results in the general solution of the system. Given our equations, our analysis is restricted to those situations in which the Dirichlet boundary conditions are met (i.e.: an infinitely repulsive medium, that is, the clad, surrounding the region where confined propagation occurs. Throughout the chapter, we use our formulation to solve analytically different simple cases: (i) total reflection by an infinite plane, (ii) propagation modes in an infinite longitudinal waveguide, (iii) diffraction of an aperture and (iv) semi-infinite waveguide. In some occasions, we will have to make certain approximations in order to obtain an analytical solution. Throughout these analyses, we show how our formulation is related to the Fourier and Hilbert transforms of these auxiliary functions, as well as its consistence by proving the conservation of the probability current.

These equations in the preceding chapter usually give rise to integrals that, as they cannot be solved analytically, require an enormous computational load for their numerical resolution. In Chapter 4 we reinterpret certain mathematical equations and structures as Fourier transforms. This opens us up the possibility of solving more complex problems by using Fourier transforms and the Fast Fourier Transform (FFT) algorithm,[15]. In this chapter we propose an iterative algorithm to calculate numerically, in a recursive way, the auxiliary functions that define the system. In a first part, we present and characterize the algorithm. After that, we solve numerically a number of problems and geometries with increasing complexity: total reflection, diffraction from an aperture, double slit and neutron waveguides (all of them in 2D), as well as Fresnel diffraction, the generation of the Arago-Poisson and Fresnel lenses (in 3D simulations). Finally, as a sub product of our research, we show how this algorithm can be applied, with certain variations, for the generation of digital holograms based on a scalar wavefunction. We have requested a patent for its application to digital holography, [5].

The formulation we propose in Chapters 3 and 4 yields interesting results. However, it is restricted to the use of Dirichlet boundary conditions, which are not those expected in neutron waveguides for a thermal neutron beam (such as those used in [13])when there are no infinitely repulsive clads. In Chapter 5, we explore the use of the Lippmann-Schwinger equation for the characterization of waveguides in which there is neutrons penetration into the clad. In the first part, we propose and analyse the recursive use of two coupled Lippmann-Schwinger equations that are the solution of wave propagation in empty space and in the waveguide. Subsequently, we analyse the equations obtained to demonstrate that the probability flows are conserved through the elimination of certain *secular terms* that arise. Finally, we apply these results to simulate numerically the rise of propagation modes in Titanium-Silicon based waveguides for an incident beam of thermal neutrons. Using these equations we can calculate both the propagation and reflection amplitudes at the waveguide's entrance.

In Chapter 6 we address the possible applications of neutron waveguides. In particular, we propose the use of optical couplers to improve the efficiency of

current neutron waveguides. These optical couplers would be based on a first Titanium-Silicon guide that would improve the rise of propagation modes for an incident beam of thermal neutrons, and a second empty-core waveguide that would transmit neutron waves over longer distances (up to about one meter) with relatively few losses. One of the most interesting applications is its possible use in Boron Neutron Capture Therapy (BNCT)for small tumours. BNCT is a cancer treatment technique (especially focused on glioblastomas) that uses slow neutron beams. We make a brief review of the technique and its current state of the art, as well as the possible improvement for the treatment of small tumours that it would experience with the use of optical couplers.

In Chapter 7, we summarize the conclusions obtained from this thesis.

In the appendix, we show the computational load, both in time and memory consumption, of the new algorithm, demonstrating that it represents a huge progress compared to current methods. Additionally, we include an appendix in which we develop in detail the cancellation of certain divergences that formally arise in the probability flux Chapter 5, so as to establish the conservation of probability. Moreover, we include an appendix where we state possible research lines and problems that remain open. For reference, we have included an appendix with the values of the coherent and incoherent scattering lengths, the attenuation coefficient, etc. for a beam of thermal neutrons interacting with most isotopes and elements in their natural abundance. Finally, we also present an appendix in which we summarize the most important activities, congresses, seminars and publications upon which this thesis is based.

Finally, the bibliography used throughout the document is located at the end.

1.2 Neutrons

1.2.1 Historical Background

The discovery of neutrons was the last milestone after extensive research and experiments carried out in the 1930s by researchers such as Bothe, Becker, Curie, Webster, Dee, Curie-Joliot and Joliot, Perrin, Feather, Majorana, Heisenberg, Iwanenko... (see [1, 9, 16]). Those experiments aimed to characterize radiations emitted from certain isotopes. Researchers (in special Bothe) found that beryllium (Be), when bombarded with α particles from a polonium (Po) source, emits a penetrating neutral radiation which initially seemed to be electromagnetic ("γ-ray type"). However, there were inconsistencies in the conservation of energy and momentum associated to this radiation.

Chadwick, in collaboration with Feather, conducted his own experiments, specially those related with Compton recoil. Chadwick indicated that if the radiation was electromagnetic ("quanta"), then the reaction ^{9}Be (two α particle + one proton)

with an α particle would yield ^{13}C and a maximum emitted energy of 14 MeV according to ^{13}C mass defect.

In 1932, he published a letter to the editor of Nature, [1], where he made a brief review of this problem and suggested that:

> *The difficulties disapear, however, if it be assumed that the radiation consists of particles of mass 1 and charge 0, or neutrons.*

In a later paper, [17], he performed a deeper review and estimated the neutron mass to be 1.15 times the proton mass. In both papers, Chadwick stated that, actually, the reaction between ^{9}Be and α particle yields

$$^{9}Be + \alpha \rightarrow ^{12} C + n$$

In 1935, the Nobel Prize in Physics was awarded to James Chadwick "for the discovery of the neutron". Shortly after the neutron discovery, in 1936, experiments conducted by von Halban and Preiswerk, [18] and Mitchell and Powers, [19], showed that crystalline materials could diffract slow neutrons.

From 1934, Fermi conducted systematic investigations on the behaviour of the neutron; effects of bombardment with neutrons, neutron activation, interaction with hydrogenous materials... (see, for example [20]). He also coined the term "slow neutrons" [21] related to those neutrons that have a wavelength (see Eq.(1.1)) of the order of the atomic interspace. In 1938, Enrico Fermi was awarded the Nobel Prize in Physics "for his demonstrations of the existence of new radioactive elements produced by neutron irradiation, and for his related discovery of nuclear reactions brought about by slow neutrons". In 1944, Fermi and Zinn, set the grounds on neutron optics; they used a collimated beam of thermal neutrons from a nuclear reactor at Argonne National Laboratory, allowing the measurement of the refractive index for thermal neutrons (see Eq.(1.9)) [2] and reflection of neutron beams [22, 23].

Since then, a whole variety of experiments have established several optical-like effects with slow neutrons. A number of researchers (Bacon, Brockhouse, Corliss, Hastings, Koehler, Shull, Wilkinson, Wollan, ...) (see [9, 16] and references therein) made important contributions by employing neutron diffraction to analyse the atomic structure of matter (locations of the atoms and their dynamics). In particular, Bertram N. Brockhouse and Clifford G. Shull were awarded the 1994 Nobel Prize in Physics "for the development of neutron spectroscopy" and "for the development of the neutron diffraction technique", respectively.

1.2.2 Neutron Properties

The neutron (denoted by n) constitutes one of the two particles that, along with protons, form the atomic nucleus. The neutron is not strictly an elementary particle since it is composed by other three fundamental entities, named quarks. Specifically, the neutron is a bound system of one quark with electric charge $+2/3 \mid e \mid$ (named quark u) and of two quarks, each with electric charge $-1/3 \mid e \mid$ (named quark d) [9]. For our purposes in this thesis, we assume the neutron an individual particle electrically neutral. The neutron rest mass is $m_n = 939.57$ MeV$/c^2$, its magnetic moment is $\mu_n = -1.913\mu_N$ and its spin is $\hbar/2$, thus being half-integral (since spin values can be $\pm\hbar/2$, it will show birefringence).

The neutron is unstable, its lifetime being $\tau_n = 879.4 \pm 0.6$ s, according to Particle Data Group, [24]. As neutron phenomena treated in this thesis (the propagation of slow neutrons along macroscopic distances) occur during time intervals shorter than its lifetime we will treat it as a stable particle.

Neutrons may have a wide range of energies, from over the order of MeV ($\approx$2 MeV, the maximum peak of ^{252}Cf spectrum) to the order of 10^{-7} eV (ultracold neutrons used for its mean life measurement, [25]). These neutrons are named according to the ranges of their kinetic energy, E, related with their thermodynamic equilibrium, as they propagate in a material medium at absolute temperature, $E = (3/2)K_bT$. Although there does not exist unanimously accepted conventions, we will refer them as in Table 1.1.

Table 1.1: Neutron denomination according to its kinetic energy

Energy Range		**Name**
10 MeV $\lesssim E$		Relativistic
200 keV $\lesssim E \lesssim$ 10 MeV		Fast
10 keV $\lesssim E \lesssim$ 200 keV		Intermediate
0.5 eV $\leqslant E \lesssim$ 10 keV	Epithermal	Slow
0.025 eV $\leqslant E \leqslant$ 0.5 eV	Thermal	
5×10^{-5} eV $\leqslant E <$ 0.025 eV	Cold	
2×10^{-7} eV $\leqslant E \leqslant 5 \times 10^{-5}$ eV	Very Cold	
$E \leqslant 2 \times 10^{-7}$ eV	Ultracold	

In this thesis, we will focus on strictly said "thermal" neutrons. Those neutrons are at thermodynamic equilibrium, as they propagate in a material medium at absolute temperature $T = 293$ K (20°C, say, room temperature). Then, one has, consistently, $E \simeq 0.025$ eV $= (3/2)K_bT$ and a de Broglie wavelength of $\lambda_{db} \simeq 1.8$ Å according to

$$\lambda_{db} = \frac{2\pi\hbar}{\sqrt{2mE}} \tag{1.1}$$

This wavelength has the same order of magnitude as the spacings between two neighbouring atoms in a typical crystal. This allows for a neutron beam of (strictly)

thermal neutrons, propagating through a crystal lattice, to give rise to optical-like phenomena (interference, reflection, refraction and diffraction). In this thesis, we ignore the polarization effects. In a general sense, most of the results stated in this thesis, would also apply to slow neutrons (including epithermal). In the case of neutrons with $E \leqslant 0.025$ eV, one would expect that reflection and neutron confinement effects would gain more relevance in comparison with other effects.

By analysing their diffraction patterns, thermal neutrons allow to explore interatomic spacings and structure in crystals, correlations among atoms and magnetic subdomains ($0.1 \leqslant \lambda_{db} \leqslant 20$ Å), analyse molecular vibrations ($0.5 \leqslant \lambda_{db} \leqslant 5$ Å) and polymers reptation ($5 \times 10^{-5} \leqslant \lambda_{db}$ Å).

Slow neutrons can penetrate into various materials without suffering an appreciable absorption, along a certain distance, and without producing significant modifications in the former. This makes slow neutron beams and X-rays to be complementary of each other for research and imaging. In general, X-rays and thermal neutrons have been and continue to be extremely useful and valuable for the investigation of matter (biological matter being included). In Table 1.2 we summarize the main differences between neutrons and X-rays.

Table 1.2: Comparison between neutrons and X-rays

	Neutrons	**X-Rays**
Forces	Nuclear Strong Interaction	Electromagnetic
Interaction with Media	Scattering in nuclei	Distribution of electric charges
Scattering Amplitude	Change with different isotopes	Change with different chemical species
Scattering Behaviour	Isotropic	Angular dependences
Refractive Index	Irregular Variations	Regular increase with atomic number
Beam Absorption	Relatively low	10^2 to 10^3 cm^{-1}
Magnetic Effects	Interaction with magnetic moments	No magnetic effects

The energies of phonons in crystals are of order 0.04 eV, that is, of the same order as the energies E of thermal neutrons. The energy of one photon in X-rays is, typically, several orders of magnitude larger by a factor 10^5. The relatively non-destructive character of slow neutrons makes them quite convenient for a collection of non-destructive testing methods, exploiting the penetration and attenuation properties of neutrons to investigate the internal structure of the imaged objects, for example: properties and behaviour of biological matter, neutron activation analysis and neutron imaging. Anyway, slow neutron fluxes are usually much smaller than photon fluxes, upon comparing with X-rays.

1.2.3 Neutron Sources

Neutron fluxes may be obtained from different methods. In this section we will make a brief review of the most used neutron sources.

Photoneutronic sources: In certain isotopes, in which the neutron binding energy is sufficiently small (such as ^2H and ^9Be), the incidence energy of a γ-ray may be sufficient enough to release a neutron. In these cases, the neutron is emitted with a kinetic energy, E, smaller than 1 MeV, for example

$$^9Be + \gamma \rightarrow^8 Be + n$$

As an example, the Sb-Be photoneutronic source (used as a neutron source in pressurized water reactors) yields, approximately, $3 \times 10^5\ n/(s \cdot Ci_{Sb})$.

α **sources:** Some light isotopes, such as ^{9}Be, may release neutrons when they are bombarded with α particles. These sources are made up by mixing an α emitter (a heavy isotope, such as ^{226}Ra, ^{210}Po or ^{239}Pu) with a target (usually light) isotope, such as B, Be, Li... Taking the Pu-Be source as an example, the ^{239}Pu acts as a source of α particles for the nuclear reaction $^9Be+\alpha \rightarrow^{12} C+n$. Neutrons are released with an energy of 5 MeV. This reaction yields fluxes of $1.6 \times 10^6\ n/(s \cdot Ci_{Pu})$[9].

Spontaneous fission: Certain heavy elements may experience spontaneous fissions releasing fast neutrons. An example is ^{252}Cf, that decays with 96.91% probability by α emission and 3.09% by spontaneous fission with an overall half-life of 2.6 years. This source yields a neutron flux of $2.3 \times 10^6\ n/(s \cdot \mu g)$ and a specific activity of 0.53 mCi/μg [26].

Nuclear reactors: A nuclear reactor contains in its inner part (the "core") fissile material ("fuel") where nuclear fission is produced. Typical fuels are natural or enriched uranium (higher percentage of ^{235}U) or other fissile isotopes, such as ^{233}U, ^{239}Pu, ^{241} Pu or certain isotopes of Th. Neutrons propagating through the fuel are captured by the fissile atomic nuclei, which suffers nuclear fission into two smaller nuclei and emits fast neutrons (in the order of megaelectron-volt). The neutrons produced after fission can give rise to new fission processes (chain reaction). These neutrons have an energy spectra with an average kinetic energy of $\bar{E}$ =2 MeV and a peak energy E_{peak}=0.7 MeV ([27] and references therein).

In many reactors, the fast neutrons after fission require, first, to be slowed down ("moderated") to the thermal energy range (where the neutron induced fission cross section is appreciable). For our purposes here, the most interesting feature is that beams of slow or thermal neutrons can be extracted from the core of the reactor and employed at a later stage for various purposes, [28].

Small nuclear reactors (with power a few megawatt) provide constant fluxes of slow neutrons about 10^9 epithermal neutrons/$(cm^2 \cdot s)$ [29]. The reactor located at the Institute Laue-Langevin (Grenoble, France), achieves a continuous neutron flux of 1.5×10^{15} epithermal neutrons/$(cm^2 \cdot s)$ with a thermal power of 58.3 MW [30, 31].

Small and medium accelerators: They are based upon accelerating protons (or deuterons), at energies up to tens of MeV. Those protons collide with suitable nuclear targets (Li, Be) and the resulting nuclear reactions yield pulses of fast neutrons, with energies in the MeV range. An example is the reaction induced with protons with energies about 2 MeV in a small accelerator, striking a lithium target [28]

$$H^+ + {}^7 Li \rightarrow {}^7 Be + n$$

Subsequently, the fast neutrons are moderated and employed at a later stage, for example, as an epithermal neutron source in BNCT (see Section 6.2).

Spallation sources: Charged particle beams (usually, protons but also α particles, deuterons...) are accelerated to energies about 100 MeV or higher using synchrotrons, cyclotrons... Such beams strike suitable heavy nuclei. The resulting high energy nuclear collisions (spallation reaction) in the target produce many fast neutrons which, after being moderated, give rise to beams of slow neutrons. For instance, a proton beam with energies of 800 MeV with a target of ^{238}U, may generate about 30 neutrons per proton, on the average.

Spallation sources provide nonstationary (non-constant) neutron fluxes. A spallation source can generate pulsed beams containing up to 10^{17} neutrons/s and even more.

Table 1.3 lists some important spallation sources currently under full operation and under construction.

Table 1.3: Spallation sources in the world

KENS	KEK, Japan
SINQ	PSI, Switzerland
ISIS	Rutherford Lab, UK
CNR-SNS	Oak Ridge, USA
ESS	Lund, Sweden
	(full operation expected in 2027 [32])
SNS	Guandong, China
FRM	Munich, Germany
ILL	Grenoble, France

For obtaining a suitable neutron beam from any of the neutron sources listed above, it is necessary to perform additional operations; thermalisation, collimation, monochromatisation...

Thermalisation: None of the sources listed above produce directly neutrons with suitable energy $E = 0.025$ eV. Neutrons extracted from those sources must be slowed down by a process called *moderation*. Moderation occurs when neutrons propagating in materials loose energy, through successive collisions with the atomic nuclei in the medium, and are slowed down. Since the energy is transferred via particle collisions, the use of low atomic mass isotopes is desirable as well as those that have small probability to capture and absorb slow neutrons. Hydrogen, deuterium (in heavy water) and graphite are some widely used moderators.

After moderation, neutrons reach thermal equilibrium with the scattering medium at absolute temperature, T (*thermalisation*). These neutrons will show a statistical mixture of energies (velocities) which follows a Maxwell-Boltzmann distributions, [8], according to

$$N(E) = \frac{2N_0}{\lambda_{db}} \left(\frac{E}{K_B T}\right)^2 e^{-E/K_B T} \tag{1.2}$$

where $N(E)$ is the number of neutrons with energy between λ_{db} and $\lambda_{db} + d\lambda_{db}$, N_0 is the total number of neutrons extracted from the reactor, λ_{db} is the de Broglie wavelength of the neutron (related to E via Eq.(1.1) and K_B is the Boltzmann's constant. For the case of the spectrum corresponding to thermal equilibrium with a medium at $T = 293$ K (20°C), see Figure 1.1.

Collimation: One must dispose neutron beams with momenta having approximately similar directions through *collimation*. Holes in the shields of nuclear reactors, walls of steel coated with Cd constitute approximate or partial collimators. The collimated beam has a narrow angle of divergence, but still has some spectrum or interval of energies.

Monochromatisation: This step consists in filtering out unwanted energies in order to obtain a monochromatic or, at least, quasi-monochromatic beam. This may be achieved using different devices such as (i) *velocity selectors*, which are devices that enable to transmit only neutrons having velocities belonging to a narrow interval (ii) *choppers*, which consist of a rotating disk or wheel, having one or more apertures. The neutrons, with certain velocities, which reach the chopper when the hole or aperture is open, will pass through it while other neutrons will be absorbed by the chopper. (iii) *crystals* (for instance, calcium fluoride) which can constitute monochromators: incoming partially collimated non-monochromatic neutron beams suffer reflections in crystal planes according to Bragg's law: $2dsin\theta = n\lambda_{db}$ with $n = 1, 2...$, where d is the lattice spacing and θ is the angle between the incident beam and any of the parallel planes.

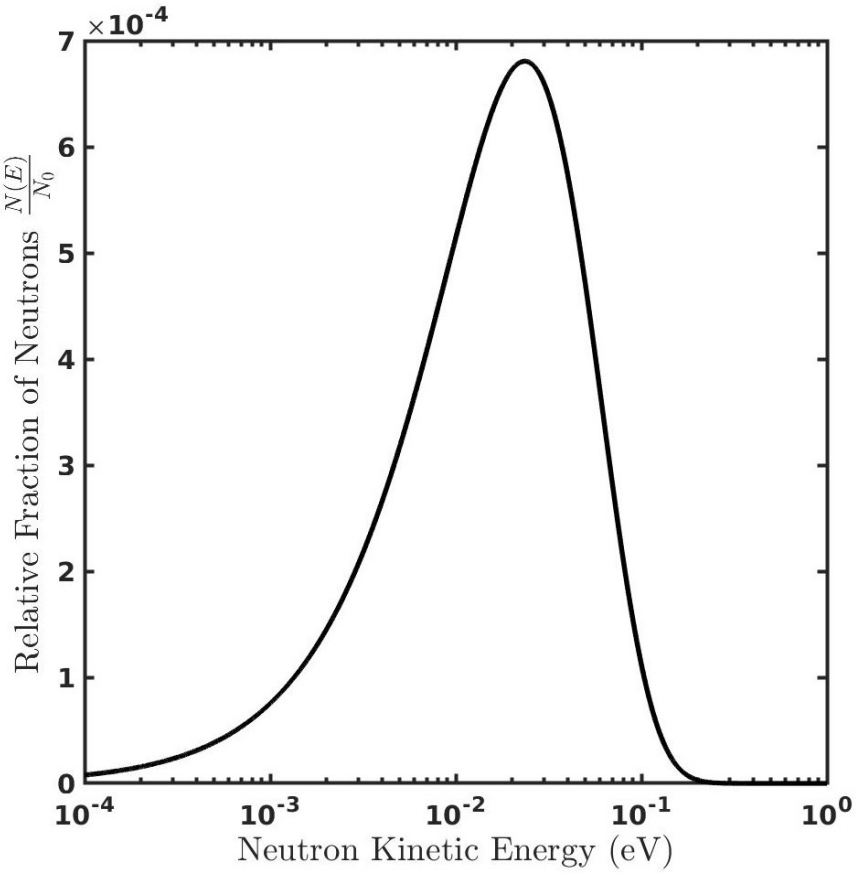

Figure 1.1: Thermalised neutron spectrum for $T = 293$ K (20°C)

1.3 Neutron Optics Fundamentals

Neutron optics is the branch of neutron physics dealing with the theory and applications of the wave behaviour of slow neutrons by studying the interactions of matter with a beam of free slow neutrons.

Being subatomic particles, neutrons propagation is governed by well-known Schrödinger's equation. The wave function $\Psi(\boldsymbol{x}, t)$ for a slow (thermal) neutron at the position $\boldsymbol{x}$ at time t, as the former propagates through a medium, satisfies:

$$\left[\frac{-\hbar^2}{2m}\nabla^2 + V(\boldsymbol{x})\right]\Psi(\boldsymbol{x}, t) = i\hbar\frac{\partial\Psi(\boldsymbol{x}, t)}{\partial t} \tag{1.3}$$

where $\hbar$ is Planck's constant, m is the neutron rest mass, $\nabla^2 = \partial^2/\partial x^2 + \partial^2/\partial y^2 + \partial^2/\partial z^2$ is the Laplacian and $V(\boldsymbol{x})$ is the effective potential due to the nuclei in the medium. In this thesis, this potential will account for the neutron scattering by the material media (see Section 1.4), while $V(\boldsymbol{x}) \equiv 0$ in vacuum. $V(\boldsymbol{x})$ provides an effective description of, at least, neutron optical phenomena arising from strong interactions with atomic nuclei.[1]

[1] In fact, this potential is also known as the "optical potential"

The potential $V(\boldsymbol{x})$ on the neutron during its displacement through media is usually t-independent (i.e.: the nuclei in the media do not change appreciably their location in the lattice). Since atoms are subject to thermal vibration, dislocation movements, phonons... this should be understood as a first approximation in our description. The nucleus, being more massive than the neutron, is regarded to be at rest and its recoil (due to the interaction with the neutron) is, as well, neglected, in this approximation. This is reasonable, since thermal neutrons travel through media at an average velocity of $v = 2200m/s$ [33] and the neutron waveguides, stated in Chapters 2, 3 and 5, have a length of the order of meters in the longest cases, being normally shorter. The consequence is that the neutron does not "see" an appreciable change in the potential during its displacement.

Thus, one can simplify the description of the slow neutron by means of the stationary wave function, $\varphi(\boldsymbol{x})$, with total energy E:

$$\Psi(\boldsymbol{x},t) = \varphi(\boldsymbol{x})\, exp\,(-iEt/\hbar) \tag{1.4}$$

$$\left[\frac{-\hbar^2}{2m}\nabla^2 + V(\boldsymbol{x}) - E\right]\varphi(\boldsymbol{x}) = 0 \tag{1.5}$$

Since $\varphi(\boldsymbol{x})$ is an eigenfunction of the operator $\left[\frac{-\hbar^2}{2m}\nabla^2 + V(\boldsymbol{x})\right]$ with eigenvalue E, Eq.(1.5) becomes an eigenvalue problem for the stationary wave equation.

It is important to state that both $\Psi(\boldsymbol{x},t)$ and $\varphi(\boldsymbol{x})$ may represent a single neutron as well as a neutron beam. In principle, the wave function represents just one individual neutron, since in typical neutron beams the average separations among the centres of the wave packets associated to different thermal neutrons are appreciably larger than their average de Broglie wavelength. In those beams the overlaps among the wave packets associated to any two or more different neutrons are negligible, as a first approximation. Consequently, we will disregard that neutrons are fermions, their wave functions need not to be antisymmetric and they can be treated as independent particles.

Moreover, the different neutrons in the beam can be regarded to constitute, in practice, an ensemble of identical copies of the same quantum system (formed by just one neutron) "prepared" in the same quantum state. In this way, both $\Psi(\boldsymbol{x},t)$ and $\varphi(\boldsymbol{x})$ also give a statistical description of the ensemble of all N_n neutrons that form the beam. Those wavefunctions fulfil Eqs.(1.3) and (1.5), respectively and are, also referred to as a pure state. Both wavefunctions are normalized, $\int d^3\boldsymbol{x} \mid \Psi(\boldsymbol{x},t) \mid^2 = 1$ for any t, or $\int d^3\boldsymbol{x} \mid \varphi(\boldsymbol{x}) \mid^2 = 1$ in the stationary case. With this assumptions, one can imagine that a set of N_n independent identical experiments are carried out on that ensemble of N_n neutrons. The detection of each neutron in the region of interest (i.e.: there is or not a neutron in a differential volume $d^3\boldsymbol{x}$) for a large N_n fulfils the statistical interpretation of quantum mechanics (see for example [34, 35, 36, 37]) and approaches $\mid \Psi(\boldsymbol{x},t) \mid^2$ or $\mid \varphi(\boldsymbol{x},t) \mid^2$ for $N_n \to \infty$. Greenberger provides an extensive discussion of these interpretations in [38].

Equation (1.5) has analogies with scalar wave equations used for classical electromagnetic fields deduced from Maxwell's equations. That can be exploited for characterizing the behaviour of a neutron beam under the action of an approximately constant (say quasi-constant optical) potential

$$\left[\nabla^2 + k^2\right] \varphi(\boldsymbol{x}) = 0 \tag{1.6}$$

$$k^2 = \frac{2m}{\hbar^2} \left[E - V(\boldsymbol{x})\right] \tag{1.7}$$

$$\lambda_{db}^2 = \frac{2\pi^2\hbar^2}{m\left(E - V(\boldsymbol{x})\right)} \tag{1.8}$$

Notice that Eq.(1.1) comes directly from Eq.(1.8) when $V(\boldsymbol{x}) = 0$.

Consequently, the refractive index for slow neutrons with total energy E moving through a medium (and, hence, under the action of the optical potential $V(\boldsymbol{x})$ due to the latter) is defined as [9, 39]

$$n^2(\boldsymbol{x}) = 1 - \frac{V(\boldsymbol{x})}{E} \tag{1.9}$$

The optical potential plays the role of complex refractive index as from classical optics. In paraxial approximation the refractive index can be substituted by the local value.

1.3.1 Evidences of Wave-like Description

Klein and Werner, [40], stated that one of the main motivations of neutron optics experiments consist in testing the fundamental propositions of quantum mechanics and in strengthening the quantum-mechanical description. In this section we will perform a short review of those most interesting experiments performed with neutrons in which the wave-like description is clearly manifested. We omit comments on optical waveguiding since its state of the art is reviewed in Section 2.2.

Arago-Poisson Spot: In the XIX century, the focusing of a light beam by a Fresnel zone plate became the proof that solved the question of whether the light is a wave or a particle. After Fresnel presented his wave theory of light, in which every unobstructed point of a wavefront would act as a secondary spherical emitter, Poisson stated that if one puts a circular obstacle in a ray beam, there would be a on-axis bright point. Later, Arago was able to observe the predicted spot, proving, thus, the validity of Fresnel's theory. In 1980, the same fact was proven with neutrons, [41]. In this experiment, a neutron beam with wavelength, λ_{db} =20 Å was focused by a Fresnel zone plate.

In this thesis, we performed numerical simulations corresponding to a similar experiment in Section 4.2 and Figure 4.9.

Neutron Diffraction: The classical optical experiments on diffraction were extended to neutron beams; (i) diffraction on an edge, [42], in which a monochromatic neutron beam diffraction pattern produced by an Al film is measured obtaining the expected $\frac{sin(x)}{x}$ shaped function (ii) single slit diffraction, [43], in which a monochromatic neutron beam is directed to a Gd slit of different widths, observing that the half-width of the neutron count rate curves matches with theoretical predictions and (iii) diffraction on a grating, [44], in which the researchers studied the reflection of a neutron beam impinging a Ni covered ruled grating for different angles, recovering the predicted interference pattern.

Total Internal Reflection: It is a key fact for the development and implementation of neutron waveguides (for a detailed explanation of its application to neutron waveguides, see Section 2.1). This was first observed for neutrons by Fermi and Zinn in 1944, [22]. Let two media with their associated refractive index, n_1 and n_2, with $n_1 > n_2$. In the case of a light beam impinging from 1 to 2 there would be a certain angle, named *critical angle*, for which $sin\,(\theta_{cr}) = \frac{n_2}{n_1}$. For those incident angles, θ, such that $\theta > \theta_{cr}$ the light beam does not penetrate in medium 2 and suffers total internal reflection. Upon going beyond the geometrical-optics approximation the beam decreases exponentially in medium 2.

Neutron Bottles: This is an extreme case of the previous situation. For ultracold neutrons, typically, E is of order 4×10^{-8} eV and $\lambda_{db} \approx 1400$ Å (an equivalent temperature of 10^{-3} K). In this case, neutron energy is lower than typical values for the optical potential in medium 2, $V\,(\boldsymbol{x}) \approx 10^{-7}$ eV. Consequently there is no refracted wave for any angle of incidence, θ. There is only a reflected wave in medium 1.

These neutron bottles are spatial domains with suitably arranged media 1 (where ultracold neutrons are confined) and 2 (that acts as a barrier). The first neutron bottle was achieved by Shapiro's group, [45, 46] for the measurement of neutron dipole moment. These neutron bottles have been used to perform a wide variety of experiments, including the measure of the neutron lifetime, [25].

Interferometry: It raised as a powerful tool for a wide variety of experiments, [38]. While previous attempts with hollow tubes obtained partial results, [47], the most classical experiment on neutron interferometry consist in the use of a perfect (silica) monocrystal cut (so as to form three parallel plates) to give the appropriate Laue-type interferometer, [48].

In a Lauer-type interferometer, an incoming neutron beam impinging the device is split into partial beams multiple times. Two partial beams leave the interferometer and each of them reaches one of both neutron counters at the

exit of the crystal. By varying the conditions of just one of the partial beams a phase difference is generated between the two exit beams and it will be measured as a change in both detectors neutron counts (i.e.: both detectors are used to measure the phase shift between those two beams). See [28] for a more complete explanation.

Sign Change with Rotation: Any physics student has a classical intuition that, in some moment during his formation, has been defied by the fact that fermions obey a geometry in which the complete 2π rotation imply not only not being the same, but the opposite ($\Psi \underset{2\pi}{\longrightarrow} -\Psi$). The neutron nature as a fermion had been only indirectly verified (i.e.: experiments yield accurate results if one supposes that $s = \pm\frac{1}{2}$).

The proper way to describe a slow neutron is by a spinor, a column matrix describing the two possible states as eigenfunctions of the operator $\boldsymbol{\sigma} \cdot \boldsymbol{l}$, such as $\boldsymbol{\sigma} \cdot \boldsymbol{l}\Psi = \pm\Psi$. Where $\boldsymbol{\sigma}$ are the standard 2X2 Pauli matrices and $\boldsymbol{l}$ is a unit vector. It can be seen, [38] that a rotation of the neutron about an axis $\boldsymbol{n}$, through an angle θ, is accomplished by the operator

$$\Psi' = e^{-i\boldsymbol{\sigma}\cdot\boldsymbol{n}\theta/2}\Psi = \left[cos\left(\theta/2\right) - i\left(\boldsymbol{\sigma}\cdot\boldsymbol{n}\right) sin\left(\theta/2\right)\right]\Psi \tag{1.10}$$

Thus, for a precession of $\theta = 2\pi$, the wave function will become $\Psi' = e^{-i\pi}\Psi$.

Moreover, the neutron will rotate an angle θ in the presence of a magnetic field, $\boldsymbol{B}$, according to

$$\Psi\left(t\right) = e^{ig\mu_n\boldsymbol{\sigma}\cdot\boldsymbol{B}t/\hbar}\Psi\left(0\right) \tag{1.11}$$

where μ_n is the nuclear magneton and g is a dimensionless factor which depends on the nature of the charge distribution (for the case of the neutron dipole, its value is $g = -1.91$).

Since what it is observed in an experiment is the quantum expectation (i.e.: the quadratic value of the wavefunction) this effect would not be seen. The way this aspect manifests consist in the use of a neutron interferometer as described above. In [49], an incident neutron beam is split into two in an interferometer, one of the beams is rotated by applying a magnetic field while the other one is kept unaltered. When the beams are recombined, the setup shows a minimum where before showed a maximum for $\theta = 2\pi$.

According to [38], *This is like being asked whether, while you were out, one of the objects on your desk was rotated by 360°. Classically there is no possible way to distinguish such an effect. But quantum mechanically, if the object were a neutron, it would stand out prominently.*

Slow Neutron Interaction with Gravity: Neutron beams passing through an interferometer may be subject to different small perturbations that will change the relative phase shift between the beams. The influence of the gravitational field is one of such effects. Typical values for the optical potential for slow neutrons (Eq.(1.18)) are of the order of 10^{-7} eV. If one considers a slow neutron subject to the influence of Earth's gravitational field, $V_{grav} = mg\,(z_1 - z_0)$ (where m is the neutron mass, $g = 9.8$ m/s^2 is the acceleration of gravity and $(z_1 - z_0)$ is the difference in heights), then a simple direct calculation indicates that this potential is comparable to the values of the Fermi pseudopotential (Eq.(1.12)) for $(z_1 - z_0) \sim 1$ m.

If one places a neutron interferometer in a way that one of the split neutron beams propagates at a different height than the other, a phase shift difference on their travelling will appear. The COW experiment, [50], (named after the initials of the researchers) is considered a milestone in the history of quantum mechanics [38] since it was the first time that the effect of a gravitational field in a wavefunction was measured.

Quantum states of neutrons in the Earth's gravitational field have been observed experimentally, as another demonstration of the universality of the quantum properties of matter. In [51], researchers showed that neutrons do not move continuously when they fall on a gravitational field but they jump from one height to other discretely.

Both experiments support the (weak) equivalence principle: the equality between the inertial and gravitational masses. In fact we have not distinguished it in our formulations.

Birefringence: The possibility for which a neutron beam would split into two because of the neutron spin was exposed as soon as 1936, [52], stating the possibility that neutrons would be fermions. Consequently, a change in the scattering of a neutron beam might be produced by a change in the orientation of the neutron moments. If a neutron beam passes through a magnetized medium, with an overall magnetic field $\boldsymbol{B}$, the energy of the latter magnetic interaction between the neutron and an atom is $\mu_n \frac{2\boldsymbol{s}}{\hbar}\boldsymbol{B}$, with $\boldsymbol{s}$ the neutron spin (and possible values, $\pm\frac{\hbar}{2}$). Consequently, this medium will show neutron birefringence (i.e.: two refractive indices, $n_{\pm}^2$, see Section 1.5).

In [52], the researchers observed small but significant differences in the neutron count rate between the background, the parallel and the anti-parallel configuration when a neutron beam passes through two sheets of iron magnetized to saturation.

Holography: It is an optical technique in which an interferogram (hologram) is recorded. This interferogram contains in its structure the complete information, in amplitude and phase, of the light wave diffracted by the object whose image we want to reconstruct.

Neutron holography was achieved in 2002, [53]. Researchers obtained a hologram of a spherically shaped single crystal of $Pb_{0:9974}Cd_{0:0026}$ with a diameter of about 7 mm, used as the sample. In the holographic experiment the Cd atoms behaved as highly efficient detectors. The Pb nuclei played the role of the object, while the Cd nuclei served as point-like detectors inside the sample. This experiment determined with atomic resolution, for the first time, the structure of a quasi-crystal by means of the neutron holographic technique.

Interesting reviews of these subjects may be found in [10], in Klein and Werner's article, *Neutron optics*, [40], an illustrative review of neutron interferometry in [38] and a review of neutron holography in [28].

1.4 Fermi Pseudopotential

At this point, we will introduce the optical potential for describing the neutron interaction with the media. We define the so called Fermi pseudopotential [54] corresponding to the j-th scatterer, for a neutron located at position $\boldsymbol{r_j}$, as

$$V(\boldsymbol{r_j}) = \frac{2\pi\hbar^2}{m}\delta(\boldsymbol{r_j})\, a_j \tag{1.12}$$

where a_j is the scattering length and $\delta(\boldsymbol{r_j})$ is Dirac's delta function. The derivation of Eq.(1.12) may be found in [10] from the use of the Lippmann-Schwinger equation and in [55] from scattering theory.

This potential is justified as the cause of the scattering of a (slow) neutron beam by the j-th atomic nucleus. Notice that this potential does not have any angular dependence. In [10] it is explained as the highest contribution comes from the scattered S-wave, neglecting thus, other (angular) contributions. The neutron-nuclei interaction in a lattice may be described as an array of spherical potential wells due to the strong interaction between the neutron and the nuclei. In most cases it is a repulsive one. It is not a real potential [56] but a pseudopotential that accounts for the scattering amplitude.

1.4.1 Considerations about Scattering Length

In a first approximation, a_j (scattering length) may be geometrically interpreted as the j-th atomic nucleus radius in a hard spheres model. Of course, nuclei do not exactly behave as being a hard sphere. In [57] is stated the so called *dispersion formula*, that states that the actual value of the scattering length is determined by the boundary conditions at the nuclear surface. It depends on the presence of resonant compounds neutron-nucleus. The total scattering cross section is

$$\sigma = \frac{4\pi}{k^2}\left| ka + \frac{\frac{1}{2}\Gamma_n^{(r)}}{(E-E_r) + \frac{1}{2}i\left(\Gamma_n^{(r)} + \Gamma_a^{(r)}\right)}\right|^2 \tag{1.13}$$

where a is the hard sphere model radius (as stated before), E is the neutron kinetic energy, E_r is the energy which the neutron must have to produce resonance in the compound nucleus and $\Gamma_n^{(r)}$ and $\Gamma_a^{(r)}$ are the widths for the re-emission of the neutron with its original energy and for absorption, respectively. We will pay latter attention to total cross section. At this moment, it will be sufficient to state that $\sigma = 4\pi \mid a \mid^2$.

In [8, 58], it is stated that the neutron width,$\Gamma_n^{(r)}$, is proportional to the neutron wave number, k. In fact, Eq.(1.13) can be simplified to give the following approximate expression for the scattering length

$$b = a - \frac{\Gamma_n^{(r)}}{2kE_r} \tag{1.14}$$

where b is the scattering length[2]. This equation shows that in the neutron scattering by nuclei, two processes compete; the potential scattering, as if the nuclei would be hard spheres (always a real positive value) and the resonance scattering due to the formation of transient compounds neutron-nuclei. The latter may be a positive or negative value depending on the value of $(E - E_r)$ and may, even, yield a complex value.

One must take b being, in general, a complex number of the form $b = Re(b) + iIm(b)$. Where $Im(b)$ accounts for neutron absorption in the medium. If that absorption can be neglected (as we will do in subsequent chapters), then b is a real number. However, if nuclear absorption is not negligible, then b is complex, with imaginary part $Im(b) < 0$. Inspecting the values in Table D.1 (Appendix D), one sees that the order of magnitude of $Re(b)$ is 10^{-13} cm (or 1 fm).

As an example of these interactions in Eq.(1.14), see Figure 1.2. In this figure we represent the value of the coherent neutron length, b versus the atomic mass number for the isotopes in Table D.1 (Appendix D). We compare it with the theoretical prediction of the hard-sphere model (dotted line, $b = 1.5 \times 10^{-13} A^{\frac{1}{3}}$, A being the isotope mass number). In this figure is clear the irregular variation of the neutron scattering amplitude. Compare this result with the known regular increase for X-rays [8, 59].

[2] As in most common notations, we will refer, from now on, b as the neutron scattering length, instead of a.

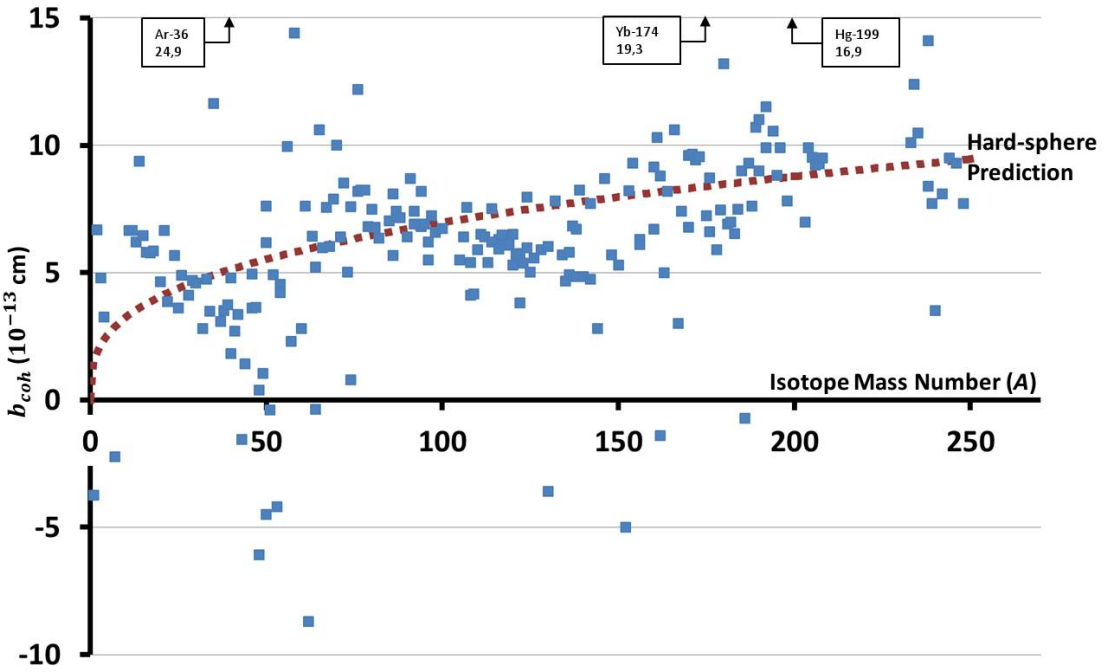

Figure 1.2: Variation of neutron scattering amplitude VS isotope mass number

1.4.2 Coherent and Incoherent Scattering

An additional comment must be done. Since the neutron has spin $\frac{1}{2}$, it may interact with the nuclei spin, $\boldsymbol{I}$. To this point, we have supposed, for simplicity, that nuclei where spinless, $\boldsymbol{I} = 0$, but this effect must be taken into account. The most general rotationally invariant expression for b is

$$b^{'} \equiv b_{coh} + 2\left[I\left(I+1\right)\right]^{-\frac{1}{2}} b_{inc}\boldsymbol{s}\cdot\boldsymbol{I} \tag{1.15}$$

where b_{coh} and b_{inc} are the so called coherent and incoherent scattering lengths, respectively [33], $\boldsymbol{s}$ is the neutron spin and $\boldsymbol{I}$ is the nucleus spin.

If the scattering nucleus has a spin $\boldsymbol{I} \neq 0$, then it may combine with a neutron of spin $\frac{1}{2}$ to form one of two alternative compound nuclei, having a total spin of $I + \frac{1}{2}$ or $I - \frac{1}{2}$. It gives rise to two different scattering lengths, b_+ and b_-. In this case, neutron cross section will have two parts; coherent and incoherent (see Section 1.5.2).

1.5 Macroscopic Scattering

Equation 1.12 accounts for one scatterer but we are interested in describing the behaviour of neutrons in material media (i.e.: taking into account multiple scatterers). Let us consider the total field, $\varphi\left(\boldsymbol{r}\right)_{mi}$, corresponding to the coherent superposition of the incident field, $\varphi\left(\boldsymbol{r}\right)_{in}$, plus the superposition of N spherical waves scattered from N nuclei in the medium using a multiple scattering theory [55] according to

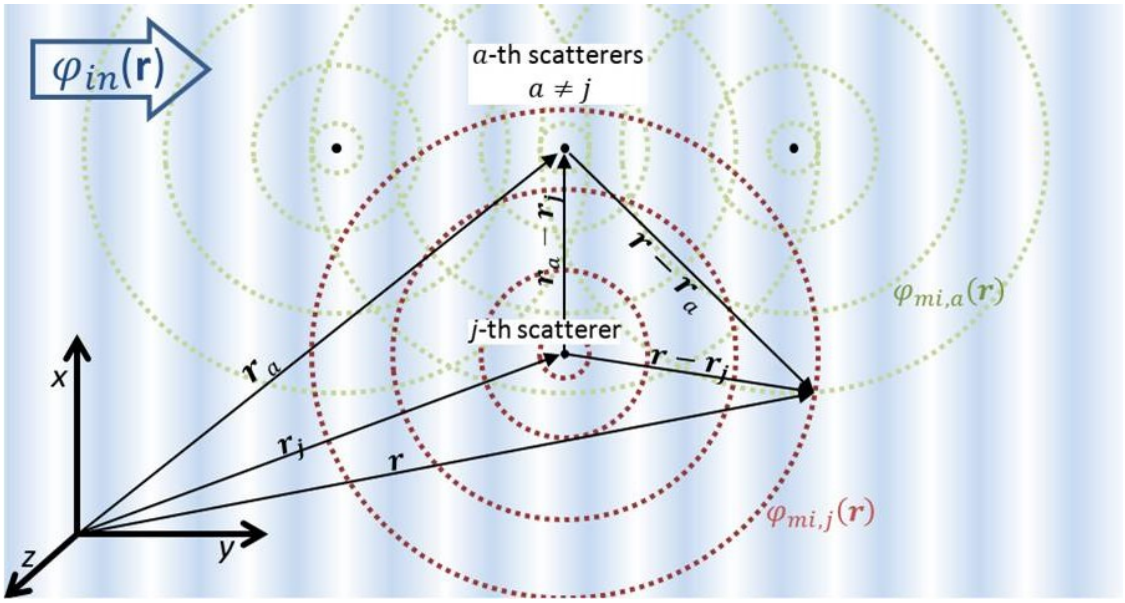

Figure 1.3: Multiple scatterer geometry

$$\varphi(\boldsymbol{r})_{mi} = \varphi(\boldsymbol{r})_{in} + \sum_{j=1}^{N} G(\boldsymbol{r} - \boldsymbol{r_j}) V_j(\boldsymbol{r_j}) \varphi(\boldsymbol{r_j})_{mi,j} \tag{1.16}$$

where $G(\boldsymbol{r} - \boldsymbol{r_j})$ is the standard t-independent three dimensional Green's function in vacuum.

Notice that $\varphi(\boldsymbol{r_j})_{mi,j}$ represents the overall wave function at the j-th scatterer, describing the wave due to all multiple scattering processes (see Figure 1.3). This wavefunction is, in turn, the addition of the incident wave and the summation of the l-th (with $l \neq j$) waves scattered by all the other nuclei. The direct method of solving the scattering problem would consist in solving the linear algebraic equations, recursively. It would yield a series of N^N scattered waves in the form $\varphi_{in}(1 + GV + GVGV + GVGVGV + ...)$ that is unaffordable. In this case, one possibility consist in neglecting higher order terms and working only with the first contribution [55]. This the Born approximation, as if the j-th scatterer only "sees" the incident wave and not those scattered by its neighbours (i.e.: $\varphi(\boldsymbol{r_j})_{mi,j} \approx \varphi(\boldsymbol{r_j})_{in}$)

We recall here the formula, according to Eq.(1.12), to introduce the scattering potential of a scatterer in Eq.(1.16). For convenience, we will recast, equivalently, Eq.(1.16) in an integral form as

$$\varphi(\boldsymbol{r})_{mi} = \varphi(\boldsymbol{r})_{in} + \int d\boldsymbol{r'} \sum_{j=1}^{N} G(\boldsymbol{r} - \boldsymbol{r'}) \frac{2\pi\hbar^2 b_j}{m} \delta(\boldsymbol{r'} - \boldsymbol{r_j}) \varphi(\boldsymbol{r_j})_{in} \tag{1.17}$$

Notice that the integration is extended to the whole space. If we want to obtain the total macroscopic wavefunction we have to perform a spatial averaging, in three dimensions, over all configurations of microscopic scatterers; $\varphi(\boldsymbol{r}) \equiv \overline{\varphi(\boldsymbol{r})_{mi}}$, where the overline indicates the spatial averaging. Accordingly, as $\varphi(\boldsymbol{r})$ is the

macroscopic wavefunction that one would measure outside the media (i.e.: in the experiment, the detector would be located outside the medium), it appears adequate not to append to it the subscript *mi*.

Trivially, $\varphi(\boldsymbol{r})_{in}$ is unaffected by the averaging. For an homogeneous isotropic random distribution of scatterers, one can write for any $\boldsymbol{r}$ in the medium

$$\overline{\sum_{j=1}^{N} \frac{2\pi\hbar^2 b_j}{m} \delta(\boldsymbol{r'} - \boldsymbol{r_j})} \simeq \frac{2\pi\hbar^2 b}{m}\rho \tag{1.18}$$

where ρ is the average number of nuclei per unit volume, (cm^{-3}) in the homogeneous material medium. b should be interpreted as an average (over nuclear spins and over isotopes) coherent amplitude for the low-energy purely neutron-nucleus scattering length for a particular medium. Equation 1.18 also holds for solid materials, upon a suitable averaging allowing regarding them, approximately, as homogeneous and isotropic.

Consequently, if one wants to calculate the equivalent value of b for a certain material, one has to take the average values of b for each isotope in the medium. Table D.1, in Appendix D, has that average performed in the corresponding values for the natural occurring elements (averaged over their natural abundance). As an example, see Table 1.4 in which the *natural occurring* titanium is calculated by averaging over its isotopes

Table 1.4: The value of b_{coh} for natural occurring Ti.

Isotope	Natural abundance w_r	Coherent scattering amplitude $b_{coh} \times 10^{-13}$ cm	$w_r \cdot b_{coh}$
^{46}Ti	8.2	4.93	0.40426
^{47}Ti	7.4	3.63	0.26862
^{48}Ti	73.8	-6.08	-4.48704
^{49}Ti	5.4	1.04	0.05616
^{50}Ti	5.2	6.18	0.32136
Total	—	—	**-3.438**

1.5.1 Refractive Index

In addition to the above, we can introduce in the refractive index expression, Eq.(1.9), the result obtained in Eq.(1.18). The following expression accounts for the neutron refractive index in material media

$$n^2 = 1 - \frac{2\pi b\rho\hbar^2}{mE} \tag{1.19}$$

$b > 0$ (which holds for most materials) implies $n < 1$. In addition, if we neglect nuclear absorption, b is a real value and so n is for any value of the neutron kinetic

energy E (notice that this formulation holds only for slow neutrons). Comparing with refractive optics, this means that most materials behave as being less dense than vacuum, from the standpoint of neutron optics. Only certain naturally occurring materials, such as hydrogen and titanium, behave as more dense than vacuum, so the neutron would exhibit total internal reflection.

Moreover, since the refractive index depends on neutron kinetic energy, E, there are other situations in which the neutron would exhibit total internal reflection; let a neutron beam in the vacuum with total energy E impinges certain medium. In the case that E is such that $1 < (2\pi b\rho\hbar^2)/(mE)$, n is pure imaginary and the neutron suffers total internal reflection and it does not penetrate. Since $\frac{2\pi b\rho\hbar^2}{m}$ is normally of the order 10^{-6} to 10^{-7} eV (see Appendix D), this is the expected behaviour for ultracold neutrons.

Another very important case occurs for thermal neutrons travelling through a crystal, in which the discretized (approximately, periodic) atomic structure has to be taken into account. Then, Eq.(1.18) does not hold as an approximation and the pseudopotential will have the same periodicity as the crystal and neutron diffraction by the latter will occur. In this thesis we will neglect periodicity effects in our calculations unless they would be taken into account with small modifications of formulae.

For last, we have not yet taken into account external fields that may interact with the neutron. In this thesis, we will not not take into account its dipole moment or its interaction with gravity field (see Section 1.3.1). Thus, one has to take into account and include the effective interaction of the magnetic moment of the neutron with, $\boldsymbol{B}$, or with magnetic moments of the atoms in the medium

$$V(\boldsymbol{x}) = \frac{2\pi\hbar^2 b\rho}{m} \cdot I_2 - \mu_n \frac{2\boldsymbol{s}}{\hbar}\boldsymbol{B} \tag{1.20}$$

where the first term in the right side, $\frac{2\pi\hbar^2 b\rho}{m}$, is the usual pseudopotential as in Eq.(1.18) multiplied by the unit 2×2 matrix, $I_2 = \begin{pmatrix} 1 & 0 \\ 0 & 1 \end{pmatrix}$, μ_n is the nuclear magneton and $\boldsymbol{s} = (\hbar/2)(\sigma_1, \sigma_2, \sigma_3)$ is the neutron spin operator. σ_j, $j = 1, 2, 3$ are the Pauli matrices $\sigma_1 = \begin{pmatrix} 0 & 1 \\ 1 & 0 \end{pmatrix}$, $\sigma_2 = \begin{pmatrix} 0 & -i \\ i & 0 \end{pmatrix}$, $\sigma_3 = \begin{pmatrix} 1 & 0 \\ 0 & -1 \end{pmatrix}$ (see, for example [34, 36]).

Under this description, one has to take into account that the neutron wavefunction has two components with eigenvalue (or spin projection) $\pm\hbar/2$, say, $\Psi_+(\boldsymbol{x}, t)$ and $\Psi_-(\boldsymbol{x}, t)$. Let us suppose a magnetic field oriented in z-direction; $\boldsymbol{B} = (0, 0, B)$. In this case, the two components of the wavefunction are subject to different interactions

$$V_\pm(\boldsymbol{x}) = \frac{2\pi\hbar^2 b\rho}{m} \mp \mu_n B \tag{1.21}$$

Thus, the medium behaves as a birefringent one, with two different refractive indices, [60]. These effects constitute the basis of neutron spin optics [61]. This is an entire field that lies outside the scope of this thesis.

1.5.2 Neutron Cross Sections

We define the neutron scattering cross section, σ_{scat}, as the average number of incident neutrons that are scattered per unit time per unit of incident flux (i.e.: in a macroscopic experiment). In [10], it is stated that for a single scatterer (j-th scatterer), the scattering cross section is

$$\sigma_{j,scat} = 4\pi \mid a_j \mid^2 \tag{1.22}$$

A more general expression is obtained by taking into account the neutron-nuclei spin interaction, according to Eq.(1.15).

$$\sigma_{j,scat} = 4\pi \mid b_{coh} + 2\left[I\left(I+1\right)\right]^{-\frac{1}{2}} b_{inc}\boldsymbol{s}\cdot\boldsymbol{I} \mid^2 \tag{1.23}$$

Since we are interested in the macroscopic cross section that yields the experiment, we must perform the average over L nuclear isotopes, each with its own spin I_l and parameters $b_{l,coh}$ and $b_{l,inc}$, averaged over their fractions f_l ($f_l > 0$, $\sum_l f_l = 1$) [28]. Thus, the most general form is

$$\sigma_{scat} = 4\pi \sum_{l=1}^{L} f_l \left[\frac{I_l+1}{2I_l+1} \left| b_{l,coh} + \frac{1}{2} b_{l,incoh} I_l \right|^2 + \frac{I_l}{2I_l+1} \left| b_{l,coh} + \frac{1}{2} b_{l,incoh}(I_l+1) \right|^2 \right] \tag{1.24}$$

In the case that there is only one isotope (only one value for b_{coh} and b_{inc}), there would be two contributions to the neutron scattering cross section, $\sigma_{scat} = \sigma_{coh} + \sigma_{inc}$; a coherent contribution, that can produce interference effects, and an incoherent contribution (see, for example, [58]). Both terms are easy to calculate from Table D.1, in Appendix D

$$\sigma_{coh} = 4\pi \mid b_{coh} \mid^2 \tag{1.25}$$

$$\sigma_{inc} = 4\pi \mid b_{inc} \mid^2 \tag{1.26}$$

In the case that there is a mixture of isotopes previous expressions apply but, one has to take into account a new effect; *isotope incoherence*. Consequently, incoherent scattering cross section must be changed to $\sigma_{inc} = \sigma_{inc}(spin) + \sigma_{inc}(isotope)$, [33] in which the contribution of each term is given by

$$\sigma_{inc}(spin) = \sum_l f_l \sigma_{l,inc} = 4\pi \sum_l f_l \mid b_{l,inc} \mid^2 \tag{1.27}$$

$$\sigma_{inc}(isotope) = 4\pi \sum_{l<m} f_l f_m \mid b_{l,coh} - b_{m,coh} \mid^2 \tag{1.28}$$

In Section 1.4.1, we stated that, in the case that the scattering nucleus has a spin $\boldsymbol{I} \neq 0$, two scattering lengths could be defined; b_+ and b_-. We have focused our

discussion about neutron cross sections, σ_{coh} and σ_{inc}, according to the definition of b_{coh} and b_{inc} used in [33], since it is the most common notation used nowadays. A brief, equivalent but nevertheless illustrating, discussion about coherence and incoherence based in b_+ and b_- can be found in [8].

In the case that absorption would not be negligible, b would be a complex number. Consequently, it is straight to define a neutron absorption cross section as

$$\sigma_{abs} = \frac{4\pi}{\mid \boldsymbol{k} \mid} Im(b) \tag{1.29}$$

where $\mid \boldsymbol{k} \mid$ is the modulus of the neutron wavevector (with $E = \hbar^2 \mid \boldsymbol{k} \mid^2 /2m$).

For last, the total cross section is $\sigma_{tot} = \sigma_{scat} + \sigma_{abs}$.

The parameter that accounts for the attenuation of a neutron beam propagating in a certain medium is the linear coefficient, ν. The linear coefficient for slow neutrons in a certain medium is defined as $\nu \equiv \rho\sigma_{tot}$, [8]. If we consider a slab made up of certain homogeneous material with linear coefficient ν, and some neutron beam which has approached that slab from outside, entering at $z = 0$, the flux, $F(z)$, corresponding to that neutron beam inside the slab, at a distance z from the entrance surface is $F(z) = F(z = 0)\, e^{-z\nu}$ (Lambert law). Typical values for ν are of the order or 0.1 cm^{-1} for regular materials but it may be as high as 121 cm^{-1} for neutron absorbing materials, such as Cd.

For the sake of simplicity, in this thesis we will pay attention to the coherent scattering from macroscopic media (i.e.: averaging over isotopes in the medium) and, unless stated otherwise, neglecting neutron absorption. All these approximations are made in an effort to enlighten the rise of propagation modes in the waveguides and effects such as diffraction due to the waveguide aperture.

Multivac resucitó de golpe. Imprimió cinco palabras:
"Datos insuficientes para respuesta significativa"

Isaac Asimov, *La última pregunta*

2 Foundations on Neutron Waveguides

Contents

In this chapter, we perform a brief discussion about the main characteristics expected for a suitable neutron waveguide: suitable materials, refractive index, proper layer arrangements design and the state of the art on neutron waveguides. For last, we summarize and discuss our initial attempts to characterize waveguides by using refractive optics and appropriate numerical methods. We will show the limitations of these techniques leading us to introduce our formulation in Chapter 3.

This chapter is based on the results and conclusions published in *Phosphorus, Sulfur and Silicon and the Related Elements* [62, 63] and Chapter 3 of *Advances in Neutron Optics* [30].

2.1 Neutron Waveguides

As in classical case of refractive optics, where an optical waveguide is a device (with small transverse dimensions) for guiding the light by total internal reflection, a neutron waveguide is, as well, a device, made from suitable materials, allowing

the confinement of a neutron beam in, for convenience, transverse directions as it propagates along a defined path (propagation direction).

As stated in Section 1.3.1, neutron confinement occurs by means of total internal reflection phenomena. In the case of geometrical optics description, this happens as a light beam propagates from a denser medium (higher refractive index) to a lighter one (lower refractive index). This interpretation is similar for a neutron beam; total internal reflection may occur when the neutron beam approaches the interface from a medium 1 whose associated Fermi pseudopotential is lower than that for medium 2. The neutron beam does not penetrate in medium 2 and suffers total internal reflection.

Following the classical structure of optical waveguides, neutron waveguides are, usually, formed by an inner cylinder-like (the core, along the axis of the guide), surrounded by a cylinder-like one (clad or cladding) composed by a different material (the clad) with a smaller refractive index (or by several ones, disposed concentrically). The core may be empty or made up by a suitable material. Another class is based upon layer arrangements (planar waveguides or thin films) allowing to discard one of transverse directions.

In the context of geometrical optics, confined propagation of slow neutrons occurs only in the waveguide's core. It occurs if the refractive index of the clad is smaller than that of the core:

$$n_{core} > n_{clad} \tag{2.1}$$

Or, by applying Eq.(1.19):

$$(b\rho)_{core} < (b\rho)_{clad} \tag{2.2}$$

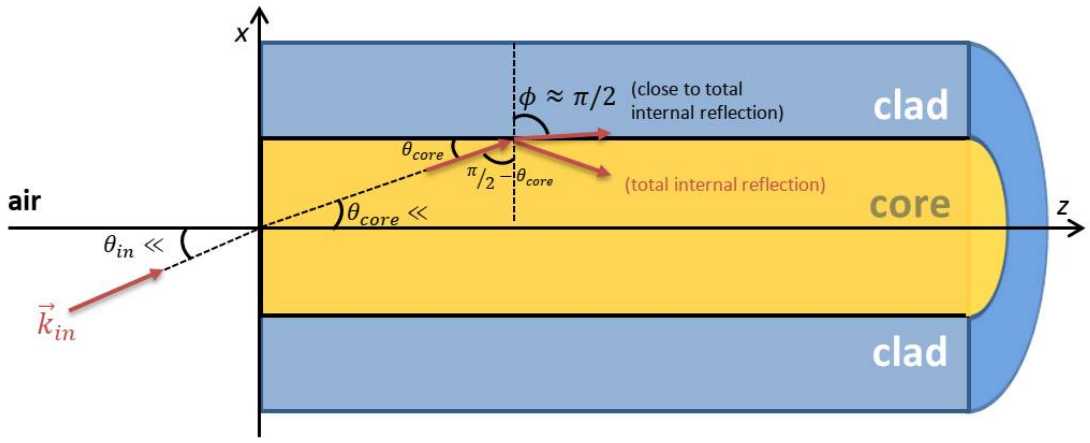

Figure 2.1: Geometrical optics-like description of total internal reflection in a waveguide

Notice that the potential, V, by recalling from Eq.(1.18) and Table D.1 (Appendix D) is of the order $\pm 10^{-8}$ to $\pm 10^{-7}$ eV. Consequently, if we compare with the

thermal neutron beam energy (i.e.: $E = 25 \times 10^{-3}$ eV), total internal reflection and neutron confinement would be a slight effect. For illustrating so, considered within the geometrical optics approximation, let a slow neutron beam approaches, from vacuum, the core of one end of a waveguide, (see Figure 2.1) with an angle θ_{in}. Let $\boldsymbol{k_{in}}$ be the incoming neutron momentum forming an angle, θ, with the propagation axis, $\boldsymbol{z}$, of the waveguide. When the neutron impinges from air the waveguide's core, it is refracted according to $sin\,(\theta_{in}) = n_{core} sin\,(\theta_{core})$, n_{core} and θ_{core} being the refractive index and refracted angle in the core, respectively. It is clear, from Figure 2.1, that the neutron beam will be, again, refracted in the clad according to $n_{core} sin\,(\pi/2 - \theta_{core}) = n_{clad} sin\,(\phi)$, where ϕ is the angle between the refracted neutron beam and the normal to the limiting surface separating the core from the clad and n_{clad} is the refractive index of the clad. The acceptance, or critical glancing angle θ_{cr} [30] is the one for which, if $\theta \leqslant \theta_{cr}$, neutron suffers total reflection in the inner surface (clad-core) and, thus, confinement occurs. According to geometrical optics-like arguments, since n_{core} and n_{clad} are a bit smaller than +1, θ_{in}, and θ_{core} are extremely small angles and $\phi \simeq \pi/2$. Then, applying Eq.(1.19) the following approximation holds

$$\theta_{cr} \simeq n_{core}^{1/2} \left(\frac{2\pi\hbar^2 \Delta b\rho}{mE} \right)^{1/2} = n_{core}^{1/2} \lambda_{db} \frac{(\Delta b\rho)^{1/2}}{\pi^{1/2}} \tag{2.3}$$

where $\Delta\,(b\rho) = (b\rho)_{clad} - (b\rho)_{core}$. According to Eqs. (2.1) and (2.2), the condition for confined propagation to occur is $\Delta\,(b\rho) > 0$.

For typical materials θ_{cr} is of the order of 10^{-2} to 10^{-3} radians. Thus, the geometrical optics description of total reflection has provided the basis for the neutron guides (with suitably large transverse dimension), enabling the channelling of a slow neutron beam along relatively long distances. The neutrons propagate along the core of the waveguide and, if $\theta_{in} < \theta_{cr}$ holds, they suffer multiple total reflections on the inner walls. See Figure 2.2.

Geometrical optics description provides, as well, a (geometrical) upper limit for the waveguide efficiency. Let F_{in} be the flux of an incoming beam of slow neutrons approaching the end face of a guide. The flux F_{out} of neutron beam which have entered into and propagated confined along the core of the guide is of the order of $F_{in}\theta_{cr}^2$, within the geometrical optics approximation. Typically, the influence of the acceptance angle reduces the propagating flux F_{out} by a factor of order 10^{-4}, compared to F_{in}. This kind of reduction in the propagating flux, due to θ_{cr} value, is independent on (and has a different physical origin from) that arising from the beam attenuation represented by the linear coefficient ν (see Figure 2.2).

However this limited characterization of neutron waveguides comes only from applying a refractive optics description. Upon going beyond the geometrical optics approximation, the confined propagation of slow neutrons occurs mainly along the core of the waveguide. It is possible to find neutrons in the clad, since the

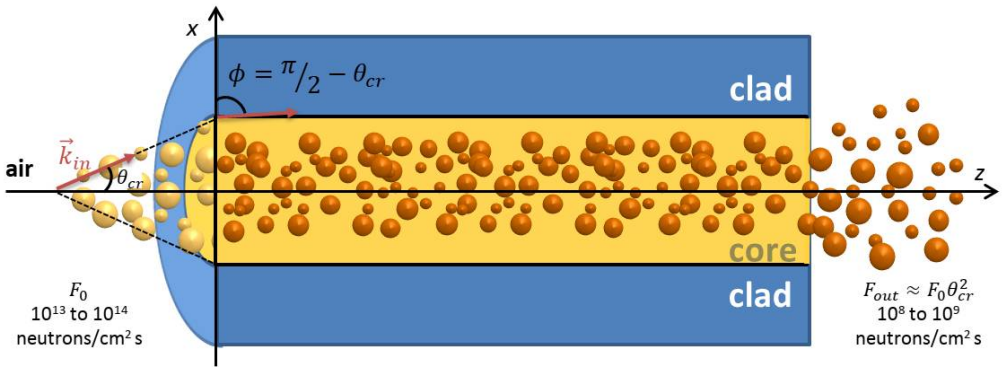

Figure 2.2: Critical angle θ_{cr} for a cylinder-like waveguide

neutron beam penetrates and decreases exponentially as it propagates inside the medium. This case is described by means of certain specific solutions of the stationary Schrödinger equation, Eq.(1.5), named propagation modes. Specifically, a propagation mode $\Psi(\boldsymbol{x}, t) = \varphi(\boldsymbol{x})\, exp(-iEt/\hbar)$ is a solution of Eq.(1.3) with time dependence $e^{\frac{-iEt}{\hbar}}$, E being the neutron energy, which oscillates and, so, describes a wave along the core (say, in the z direction). In the clad, it decays rapidly (say, exponentially) along transverse directions for confined propagation, far from the core. Those transverse directions reduce to one (say, the x direction) for planar waveguides (two spatial dimensions, defined in XZ plane in the present model).

As confinement occurs, there is always, at least, one propagation mode (the so-called fundamental one). An important issue is whether other propagation modes exist, in addition to the fundamental one. Let A be the total area of the core, in the XY plane. In general, the total number of propagation modes increases if $A \cdot \Delta(b\rho)$ increases. Notice that:

$$A \cdot \Delta(b\rho) = \pi \left(\frac{A}{\lambda_{db}^2}\right)\left(\frac{V_{clad} - V_{core}}{E}\right) \tag{2.4}$$

An important ratio for thermal neutrons is $\left(\frac{V_{clad}-V_{core}}{E}\right)$ the order of about 10^{-6} . $A^{1/2}$, which is of order of the transverse dimension of the core, (in the XY plane). It has to be larger than λ_{db} by about a factor 10^3 for allowing additional propagation modes.

As stated in this section, it is clear that two interesting configurations for clad and core materials are:

1. A core with $b < 0$ (Titanium, for example), the clad being air (i.e.: having negligible $b\rho$) or a material with $b > 0$.

2. A hollow waveguide, with a (hollow) core formed just by air, the clad being one concentric cylinder or some films with $b > 0$ (and, possibly, more concentric surrounding cylinders or layers).

2.2 State of the Art

In Section 1.2.2 we stated that neutrons and X-rays are complementary techniques for probing the structure and dynamics of condensed matter. One of the main difficulties in the development of neutron optics comes from the fact that the thermalised neutrons produced in a fission reactor may be compared to an ideal gas at pressures the order of 10^{-10} atm, [47]. In Section 1.2.3 , we stated that the beam extracted from a reactor ranges from 10^9 to 10^5 neutrons/$(cm^2 \cdot s)$. This implies that the 'brightnesses' of fission reactors as neutron sources are many orders of magnitude smaller than its X-rays counterpart. This, in conjunction with the inverse square law, made necessary to work in the close proximity of the reactor core.

One significant improvement comes from the use of hollow guides (tubes) allowing cold neutrons transportation along lengths the order of tens of meters. They can be connected directly to nuclear reactors to extract slow neutron beams and channel and transport such beams along relatively long distances, allowing more experiments to be carried out simultaneously (an example is found on [64]). Hollow guides have usually rectangular transverse dimensions the order of 10 cm and their lengths may be about 80 m. They are not straight, but have some radius of curvature R_{cu}. Those designed to transport thermal neutron beams [9, 10] have R_{cu} about one to several hundred meters. Since typical transverse dimensions of these guides are much larger (by several orders of magnitude) than the de Broglie wavelengths for thermal neutrons, the latter have been described through geometrical optics approximation.

At later stages, suitable (and, technologically, more sophisticated) guides enable to focalize slow neutron beams onto smaller transverse scale, say, down to mm for various purposes (in the case of polycapillary glass fibres (PGFs), down to tens of microns). For certain applications, like BNCT (see Section 6.2), the beam size and the aimed spot size (scale of focalization) were about 100 mm and 1 mm respectively [65]. One can expect that work on improved techniques for neutron focusing would constitute a promising development. Microguides for thermal neutrons have been experimentally performed (using a suitable evaporation technique) [66]. In that work, one microguide consisted on a sandwich of alternate Ni and Al layers. They were also employed to study the deflection of neutrons [66]. There are further and interesting developments on neutron guides using certain devices named super-mirrors (see [67, 68, 69]).

Among the first theoretical proposals about the possibility of achieving propagation modes for neutron waveguides (with small transverse dimensions), we mention the work of De Wames and Sinha, in 1973, [11]. They propose a thin film sandwich structure made of layers of certain material (not specified) with an arrangement similar to the one we simulate in Figure 5.10. The proposed arrangement acts as an optical coupler with lateral illumination. An incoming (slow) neutron beam impinges laterally on the neutron waveguide (clad) and penetrates via tunnel effect. In the next layer (core), if the component of the incoming wavevector perpendicular

to the film (k_x in our notation, x being the transverse direction) matches one of the resonant guided modes, a propagation mode would arise.

Different theoretical analyses were made with the aim to fully characterize these neutron waveguides by exploiting analogies with light propagation along optical fibres. Among the first, two papers from our research group stand out exploring the possible application of neutron optics to the design of neutron fibres, [3] and [4]. In these papers, the authors perform an analytical study of the confined propagation of thermal neutrons in solid (non-hollow) thin fibres. In [3] they focus their research on natural Titanium (of which 73.8% is ^{48}Ti, which is a spinless nucleus having $Re(b_{coh}) = -6.08 \times 10^{-13}$ cm). Table 1.4 shows that Titanium, in its natural mixture of isotopes, has $Re(b_{coh}) = -3.44 \times 10^{-13}$ cm and, thus, maximizes the effect of neutron confinement and waveguiding. In that paper, the following subjects were discussed: (i) an analysis of the rise of propagation modes in uncladded fibres, (ii) an analysis of the flux attenuation in these waveguides due to σ_{abs} and σ_{scat} and its relation with the spectral density of the neutron flux, (iii) a study of the propagation modes assuming the fibre as a infinite periodic potential (rigid lattice) and (iv) a study of the neutron flux behaviour due to neutron-phonon interaction (vibrating lattice) and how this interaction may be replaced by a temperature dependent potential. Some speculations about possible applications (to neutron radiotherapy) were stated and shall be reviewed in Section 6.2. In [4], they extend the previous analysis to suitable cladded fibres and circular cross section as an improved alternative to a single Ti uncladded fibre. An analysis for the rise of propagation modes in this case is performed. The paper shows that the expected tunnel effect in the cladding (neutron losses) is negligible due to the neutron high travelling speed along the waveguide. For last, an analysis of losses in the waveguide due to bending is performed, concluding that bending losses are negligible for most propagation modes except for those whose energies are close to the value of the potential barrier formed by clad and core.

After those first theoretical proposals in [11], slow neutron guided waves in thin planar waveguides were established experimentally, by Feng, in 1994, [13]. Neutrons propagated along z and there was lateral confinement only along one transverse direction (x). The thin film was a TiO_2/Ti/Si layer. The guiding layer (core) was a thin Titanium (Ti) planar waveguide with thickness 120 nm along the x direction. The device had three well differentiated sections along z; a coupling section of 40 mm, where the beam impinges, a guiding section of 20 mm, and an exit section of 40 mm where the beam emerges. The upper film in the clad was formed by three successive layers (TiO_2, SiO_2, and Gd_2O_3) in the guiding section above the core. See Figure 2.3. Sizes along the y direction were about a few tens of millimetres. In this experiment, the ratio of the thermal neutron flux detected after the waveguiding effect in the Ti layer over the measured incoming flux (namely, I_d/I_0, as displayed in Figure 2.3) was about 3.5×10^{-4}, within the order of magnitude expected. The confined neutron flux along z was strongly attenuated beyond 20 mm.

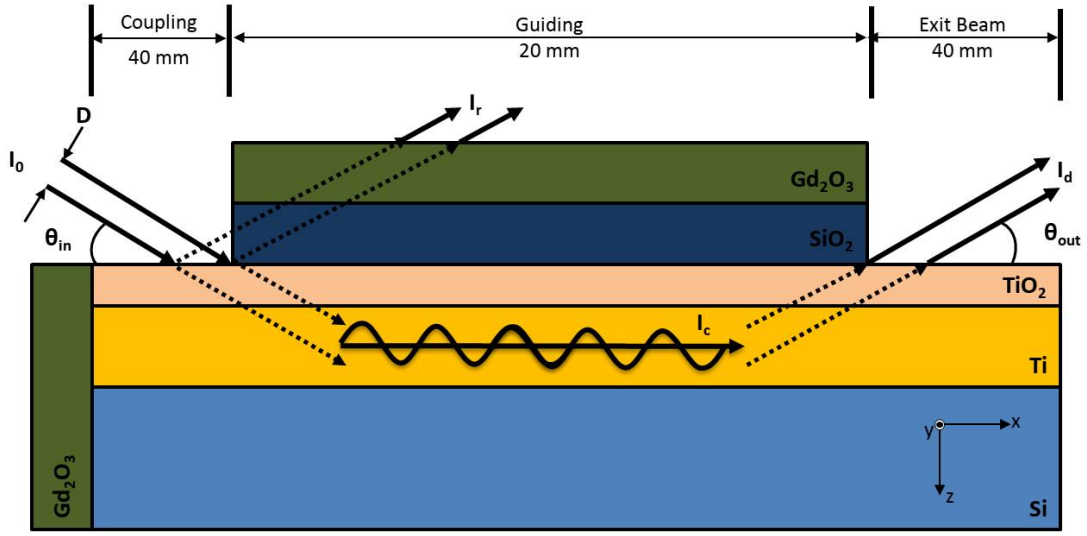

Figure 2.3: Experiment arrangement in TiO_2/Ti/Si thin planar waveguides (as in [13])

Polycapillary glass fibres (PGFs, see Figure 2.4) have been an important proposal and development for cold neutrons confined propagation. It has been experimentally established in PGFs made of lead-silica glass in 1992 [12, 70]. These polycapillary glass fibres were developed and employed in the context of X-rays optics as a focusing device ([71], where it appears that Kumakhov developed a patent for experimental capillary optics in 1984 and, later applied it in the context of neutron waveguiding). In general, PGFs could be obtained by stretching glass tubes adequately, at suitably high temperatures. A typical polycapillary fibre may have a diameter in the millimetre range (a bit smaller, eventually) and a length about a few tens of centimetres. Each PGF is composed of about 10^3 individual capillary channels with an internal diameter about a few microns. Each of them behaves as a hollow waveguide for the confined propagation of radiation with wavelengths smaller than the internal diameter.

In the experiments [12, 70] the used PGFs have a diameter $d_{pf} = 0.4$ mm and a length between, 150 mm and 200 mm and were made of lead-silica glass (which, according to Table D.1, in Appendix D, yields $Re(b) > 1$, or equivalently $Re(n) < 1$). As in the case of X-ray radiation, each single hollow capillary channel (HCC) in a PGF had an internal diameter $d_{HCC} = 6$ μm and a width of about $d_{clad} = 5$ μm. That is, two neighbouring (essentially parallel) capillary channels were separated, on average, by a lead-silica clad of width about 5 μm. It is clear that each of them could be regarded, quite reasonably, as a hollow waveguide of very small cross section, along which the confined neutrons propagate. The fibres may be straight or bent: in the latter case, they have curvature radius $R_{cu} \geqslant 0.1$ m [12, 70]. See Figure 2.4.

Those devices enabled to increase the flux of confined neutrons emerging from the exit end of a parallel assembly of PGFs and concentrate onto a small region (focal spot), located at the focal distance. In [12] the lens was constructed from 721 fibres

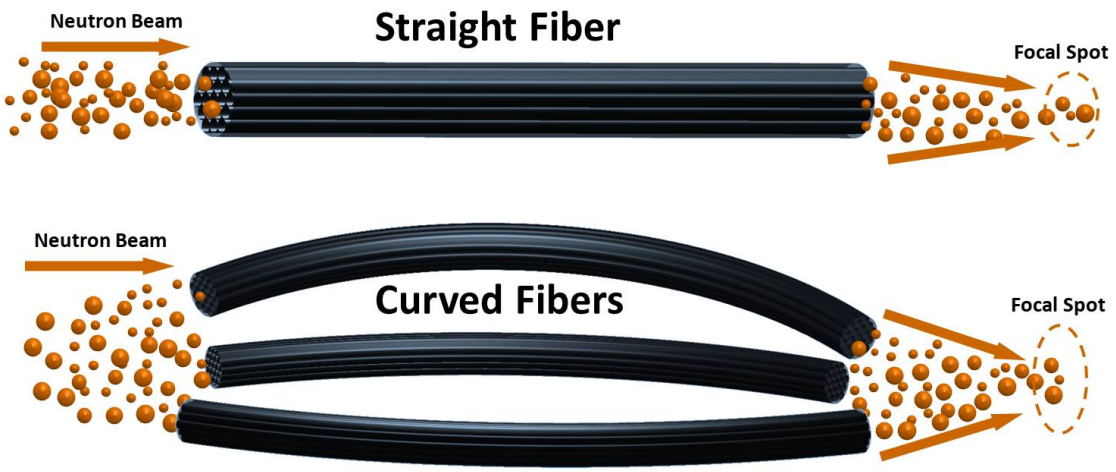

Figure 2.4: Various examples of polycapillary glass fibres as focusing devices

(each of them containing more than 10^3 parallel channels) with an overall diameter of 15 mm at the exit end. It yielded an amplification of the neutron flux by a factor 7, at a focal distance equal to 104 mm and a diameter of the focal spot of 1 mm. In [70] similar devices are bent to measure the losses for different curvatures. Their results indicate that these fibres may be well characterized assuming an internal reflectivity of about 0.98-0.99, yielding a transmission of 10 % of neutrons for bending angles as high as 59.3°, thus, demonstrating the ability to deflect neutron beams by a large angle over a small distance. From those first experiments, neutron polycapillary optics has evolved quite considerably, achieving more efficiency (less focal distance, smaller lenses, smaller focal spot size...) by reducing the hollow channel size and increasing their number in each fibre (see, for example [72]).

Interesting experiments were carried out to show the waveguiding effects for polarized slow neutrons in magnetic thin films [73, 74, 75, 76]. These experiments made use of a magnetic $Co_{0.95}Zr_{0.05}/Al/Co_{0.95}Zr_{0.05}$ three layer deposited over a suitable substrate ($Gd_3Ga_5O_{12}$, GGG or a float glass substrate depending on the case) with an arrangement similar to that of Feng experiment, as in Figure 2.3. B_4C is used in the waveguiding section. Polarized slow neutrons propagated confined in the magnetized Al layer (core). Authors rose propagation modes for only one of the two components of the polarized neutron beam. In any case, the experiment resolution does not allow distinguishing each propagation mode.

Nowadays, slow neutron 2D waveguiding stands as an active field of research: see, for instance, [76], in which the authors demonstrate the possibility of waveguiding in enriched Uranium thin films to be applied in energy production, or [77], that investigates the use of polarized neutron to measure weak magnetization in thin films (being, thus, the inverse to that presented in previous paragraph). All these theoretical proposals, as well as the experimental results obtained show the convenience and interest in fully characterizing these waveguides and predicting the behaviour of an impinging neutron beam.

2.3 Numerical Analysis Technique: FDTD Method

Let us set a semi-infinite film[1] waveguide as our region of interest, Ω (see Figure 2.5), to perform a characterization of the rise of propagation modes after an incoming neutron beam impinges and enter the waveguide at a certain angle. This region has an aperture x_0 along the x-axis and is centred at the origin of coordinates. The waveguide is composed by two parallel (and usually concentric) media along the z-axis (clad and core) that fulfil the condition in Eq.(2.2) with no distinction whether $(b\rho)$ for clad and core are positive or negative each of them. The core of the waveguide extends along the z-axis, parallel to it, from $z = 0$ to $z \to +\infty$ and $-x_0/2 \leqslant x \leqslant x_0/2$. There are two clads parallel to this core in the regions from $z = 0$ to $z \to +\infty$ and $x \leqslant -x_0/2$ or $x \geqslant x_0/2$ made of the same material for simplicity. We assume a zone of incidence for $z \leqslant 0$ with an incoming plane wave striking the aperture from $z = -\infty$ in the form of $\varphi_{in}(x, z) = e^{ik_x x} e^{ik_z z}$. Notice that $| \bar{k_{in}} |^2 = k_x^2 + k_z^2 = \frac{2mE}{\hbar^2}$. Consequently k_x and k_z are bounded for real modes since one of these components being $> \frac{2mE}{\hbar^2}$ would imply a decreasing exponential function. The potential in the zone of incidence is assumed to be $V = 0$ ($b\rho = 0$, i.e.: no material). See Figure 2.5.

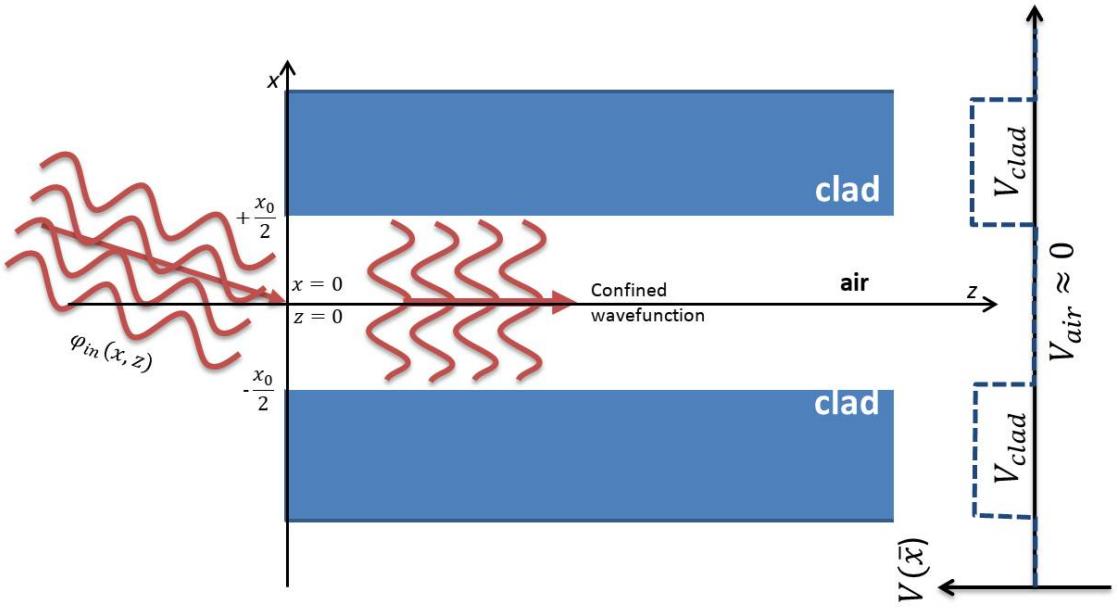

Figure 2.5: Geometry description of an straight thin film waveguide with x_0 aperture.

The first and most obvious attempt to characterize a waveguide is by solving analytically the waveguiding conditions. Thus, the typical procedure consists in

[1]For simplicity, we will focus on the XZ plane by using a two-dimensional formulation, neglecting the y coordinate. The extension to a 3D formulation is trivial.

setting the form of the solution of Eq.(1.5) for each one of the three defined media (zone of incidence, core and clad). These solutions will have the form of a wave or a decreasing exponential depending on the value of the wavevector in Eq.(1.5) (i.e.: according to Eq.(1.7), $\mid \bar{k} \mid^2 = \mid \bar{k_{in}} \mid^2 - \frac{2mV(\bar{x})}{\hbar^2} > 0$ or < 0)and are multiplied by certain amplitudes to be determined by imposing boundary conditions across the interfaces (see, for example, [78]).

This geometry has an intrinsic problem, since the wavefunction value is overdetermined at the points $\left(\pm\frac{x_0}{2}, 0\right)$. These points are shared between the zone of incidence (vacuum), the clad and the core (see Figure 2.5). We omit here mathematical details for brevity. Nevertheless, these two points cannot be discarded in the formulation, since they define the waveguide aperture and, thus, relate with the diffraction of the incoming wave.

The subsequent next approach results in modelling the waveguide and exploring numerically the possibility of slow neutron confinement in 2D waveguides. This approach has the clear advantage of its flexibility; once correctly modelled the waveguide it is easy to try different media, multilayers, bendings, etc... Nowadays, the most common methods to solve numerically a differential equation are Finite Difference Methods (FDM). They constitute a set of methods that approximate the differential operator by its Taylor expansion (commonly truncating the series in the linear term, unless other approximations are used as well).

We simulated the waveguide by applying Finite Difference Time Domain (FDTD) algorithm directly to the Schrödinger equation, according to

$$\begin{aligned}\Psi^{n+1}(x,z) = {} & 2\Psi^{n}(x,z) - \Psi^{n-1}(x,z) \\ & + A^2(x,z)\left[\Psi^{n}(x+\Delta x,z) + \Psi^{n}(x-\Delta x,z) + \right. \\ & \left. + \Psi^{n}(x,z+\Delta z) + \Psi^{n}(x,z-\Delta z) - 4\Psi^{n}(x,z)\right] \end{aligned} \tag{2.5}$$

where $\Psi^{n}(x,z)$, $\Psi^{n+1}(x,z)$ and $\Psi^{n-1}(x,z)$ are the wavefunction values at the point (x,z) at t, $t+\Delta x$ and $t-\Delta x$ respectively. Δt, Δx and Δz are the time step and interval lengths of the spatial coordinates, respectively. $A^2(x,z) = k(x,z)^2 \Delta t^2 \left[\frac{1}{\Delta x^2} + \frac{1}{\Delta z^2}\right]$ is known as the Courant–Friedrichs–Lewy (CFL) condition and is a restriction for the stability of the solution. This parameter allows modelling the refractive index of the media and imposes certain values for the time step and the mesh grid. At certain point or region, one imposes the value of the wavefunction in time (known as signal injection, it is a *probability injection* in this case), for example, $\Psi^{n}(0,0)) = e^{i\omega t}$ for a radiating point at the origin of coordinates with frequency ω, and let the system update and propagate the radiation until a steady state is achieved.

Equation 2.5 is quite similar to that of electromagnetic waves according to Yee's algorithm (see [79] and references therein) but some differences exist. First, in Eq.(2.5), a scalar complex wavefunction is involved while in the case of electromagnetic waves, one deals with electric and magnetic fields, $\boldsymbol{E}(x,z)$ and $\boldsymbol{H}(x,z)$

instead of $Re\left(\Psi\left(x,z\right)\right)$ and $Im\left(\Psi\left(x,z\right)\right)$. As a consequence, $\boldsymbol{H}\left(x,z\right)$ is displaced by $\left(x+\frac{\Delta x}{2},z+\frac{\Delta z}{2}\right)$ with respect to $\boldsymbol{E}\left(x,z\right)$ in Yee's algorithm. In the case of the Schrödinger equation, if one pursues implementing absorbing boundary conditions to encircle the computing grid (i.e.: Ω), both real and imaginary parts must be dumped, while in the case of electromagnetic waves, only one of the fields needs to be dumped. Second, contrary to an electromagnetic simulation, where light propagates at the same speed no matter what the wavelength is, the wave propagation speed changes with the wavelength and, thus, there is a nonlinear dispersion in the wavepackets when one implements absorbing boundary conditions. Thus acumulated numerical errors rise and destabilize the simulation. A deeper analysis of the use of FDTD applied to Schrödinger equation and its singularities may be found in [80].

We simulated the behaviour of a thermal neutron plane wave striking an aperture of 25 Å and its diffraction pattern propagated on air (neglecting the potential associated to it). We compared them with the ones for the propagation mode for a Hg-Ti-Hg thin layer. These layers arrangement were chosen for maximizing the confinement effect using naturally occurring materials, since $b_{Ti_{nat}}=-3.44\times10^{-13}$ cm and $b_{Hg_{nat}}=12.69\times10^{-13}$ cm (see Table D.1, in Appendix D). In fact, we performed the FDTD simulation twice; one for obtaining the corresponding wavefunction for a certain wave propagation in air, $\varphi_{air}\left(x,z\right)$, and another one for the wavefunction with the presence of the Hg-Ti-Hg waveguide $\varphi_{Hg-Ti}\left(x,z\right)$.

Figure 2.6 displays the results of numerical simulations. The figure represents, for each point (x,z), the gain percentage (according to the colourbar) in the Hg-Ti-Hg arrangement in comparison with air propagation, according to

$$gain\left(x,z\right)=\frac{\left(\varphi_{Hg-Ti}\left(x,z\right)-\varphi_{air}\left(x,z\right)\right)^{2}}{\varphi_{Hg-Ti}^{2}\left(x,z\right)}\% \tag{2.6}$$

By inspecting Figure 2.6, one observes that there are no significant differences in the wave propagation along the first 1000 Å , since in this domain diffraction effects are dominant in both cases, because of the finite dimensions of the aperture. After some propagation, the intensity of the simulated field is reinforced inside the Ti guide and attenuated in the outer clad medium (Hg), in comparison with what would be the case for neutron propagation in air. Propagating further, at 2000 Å approximately, one sees that the propagation mode is formed inside the waveguide. Numerical simulations reveal that this is a slight effect, with a gain (achievement of confinement) for approximately 2 % of the neutrons, which is physically intuitive since matter exhibits low interaction effects with neutrons (it is mostly transparent regarding their propagation). Notice that the wave attenuation effects due to incoherent scattering and nuclear absorption have not been introduced in the simulations. Thus, even if 2 % can be regarded as an acceptable (or high) gain, it is expected to decrease with a more accurate simulation (losses). The

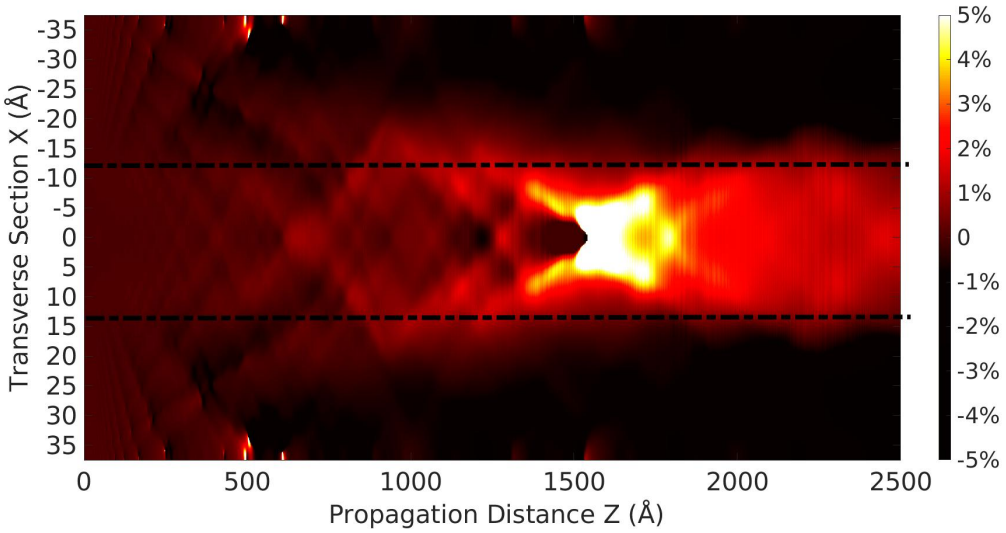

Figure 2.6: FDTD simulation comparing a free neutron wave in a 25 Å aperture VS 25 Å aperture Hg-Ti-Hg waveguide according to Eq.(2.6). Ti core is represented between dotted lines. Adapted from [62].

counterpart of the 2 % rise seen inside the core is a 1–2 % lowering observed in the clad, representing the loss of neutrons that have been confined in the waveguide.

These simulations confirm our expectation for neutron confinement and waveguiding in Titanium. Moreover, they demonstrate the computational challenges and limitations that one may face (taking into account the relationships between the system's aperture, propagation... versus the beam wavelength).

The key problem is that for a proper numerical characterization of the wavefunction, one complete wave (along one wavelength) must be represented with sufficient resolution. It is a standard in FDTD simulations to use from 10 to 20 points per wavelength (see, for example [81]). Less points would lead to numerical errors while more points would lead to an ineffective increase of the computational cost.

We recall here that, for a thermal neutron beam, $\lambda_{db} = 1.8$ Å compared with the size of our simulation in Figure 2.6, 75×2500 Å^2. It is natural to assume a precision of $\Delta x = \Delta z = 0.1$ Å. This led us to deal with arrays of 750×25000 complex-valued numbers of 1 GB average memory.

In order to obtain those results, the cost was about 80 hours of computation in a personal computer laptop MSI Intel Core i5 (7th gen) with 8GB-DDR4 RAM memory, under software MATLAB-2020a running on Linux Ubuntu18.04. This computer has 4 CPU as well as a Nvidia GeForce 1050 GTX graphics card. Nevertheless, we have not implemented code parallelization or CUDA computing, so all running times come from one single CPU.

The choice of a FDTD method for our simulations is not an arbitrary one. In fact, these simulations were completely solving the t-dependent Schrödinger equation and reaching a steady state for a long enough computation time. On one

hand, this may not look as an appropriate method, since we are not interested in the t-dependent part of the wavefunction. On the other hand the use of any other method (for example, finite differences applied directly to the Schrödinger equation) implies wider arrays to be diagonalized. In that case, we should use a set of arrays that, instead of having a size of $N \times M$ (N being the number of points in the x direction and M the number of points in the z direction), their size would be $(N \times M)^2$. In our simulations, these arrays would have sizes of 2.62×10^6 GB in comparison with the 1GB arrays we use in the FDTD method. This is unaffordable for any personal computer. Consequently, with the use of FDTD, we swapped the cost in memory in favour of a cost in computation time, since we had to update arrays until a steady state is achieved.

In this thesis, we have set our interest in waveguides of aperture size 100 nm (1000 Å) and propagation distances of $5000 - 10000$ Å rather similar to those waveguides used in [12] and [70]. If one would try to apply FDTD method to larger scales (i.e., a wider transverse section of the guide or longer propagation distances, as needed) the computing cost would be extremely high. Obviously, we did not apply this method.

2.4 Propagation Modes

FMD methods, even being precise methods, yield a bulk set of complex values (i.e.: the wavefunction values) for each point $\boldsymbol{x}$ without providing any information of the distribution of energy levels (propagation modes) unless a deeper analysis be made.

To overcome the difficulties found in Section 2.3, we will perform a quantum-mechanical analysis of the propagation modes for different cases of neutron fibres previously stated in Section 2.2 by analysing solutions to Eq.(1.5) with Eq.(1.18) as its potential. Consequently, we omit the neutron spin (i.e.: we will not treat magnetized fibres). Moreover, the possible absorptions of slow neutrons by both the core and the clad are taken as negligible, so that the potentials involved are assumed to be real.

2.4.1 Straight Single Fibre

Let us consider, in three-dimensional space, a straight neutron fibre with zero curvature and finite transverse cross section T in the plane XY and oriented along the propagation direction z (see Figure 2.7a). The confined propagation of slow neutrons along the fibre can be modelled through Eq.(1.5) where the potential fulfils $V(\boldsymbol{x}) = V_{core} = \frac{2\pi\hbar^2(b\rho)_{core}}{m}$ for $\boldsymbol{x}$ inside the inner part of T, while $V(\boldsymbol{x}) = V_{clad} = \frac{2\pi\hbar^2(b\rho)_{clad}}{m}$ for $\boldsymbol{x}$ outside T.

The thermal neutron propagation modes, with total energy E and propagation constant β_α are solutions to the Schrödinger equation, Eq.(1.3) bearing the following structure

$$\Psi(\boldsymbol{x}, t) = \varphi(\bar{x})_\alpha \, exp(i\beta_\alpha z) \, exp(-iEt/\hbar) \tag{2.7}$$

with $\int d^2\bar{x}\,|\varphi(\bar{x})_\alpha|^2 = 1$ (normalization). α denotes a set of additional quantum numbers, also required in order to specify uniquely the solution, together with E or β_α.

Since the potential, $V(\boldsymbol{x})$ is real, so it is β_α and we take $\beta_\alpha > 0$. If $E > V_{clad}$ (there are propagation modes), then Eq.(1.5) becomes

$$\left[\frac{-\hbar^2}{2m}\nabla^2_{\bar{x}} + V(\bar{x}) - V_{clad}\right]\varphi(\bar{x})_\alpha = \frac{-\hbar^2}{2m}\chi^2_\alpha\varphi(\bar{x})_\alpha \tag{2.8}$$

$$E = V_{clad} + \frac{\hbar^2}{2m}\beta^2_\alpha - \frac{\hbar^2}{2m}\chi^2_\alpha \tag{2.9}$$

with $\nabla^2_{\bar{x}} = \partial^2/\partial x^2 + \partial^2/\partial y^2$. Moreover, since the potential, $V(\boldsymbol{x})$ is real, so it is χ_α and fulfils $\chi_\alpha > 0$. In particular, these properties hold for a hollow fibre with a clad in which absorption of neutrons be negligible.

Equation (2.8) can be solved with the standard boundary conditions (i.e.: both φ and its normal derivative have to be continuous across all walls, and $\varphi(\bar{x})$ has to vanish exponentially as the modulus of $\bar{x} \to +\infty$) and it fully determines, a finite set of real negative eigenvalues $-\chi^2_\alpha$. Then, for a given E and for the finite set of values of $-\chi^2_\alpha$, β^2_α is uniquely determined by Eq.(2.9). Since Eq.(2.8) refers to two spatial dimensions and involves an attractive potential [3, 4], the fundamental mode (or ground state) always exists, but there may be or not higher propagation modes. The following bound holds [82].

$$\chi_\alpha \leqslant [4\pi\Delta(b\rho)]^{1/2} \equiv \chi_{max} \tag{2.10}$$

where $\Delta(b\rho) = (b\rho)_{clad} - (b\rho)_{core}$ as in Eq.(2.3).

The largest value of χ_α (>0) allowed by Eq.(2.8) and compatible with the bound in Eq.(2.10) corresponds, precisely, to the fundamental mode. The values of χ_α associated to higher modes decrease in magnitude.

For an unbent fiber, the number of allowed propagation modes, $N_{pm}(\chi^2_0)$ in the range $0 \leqslant \chi^2_0 \leqslant \chi^2_\alpha \leqslant \chi^2_{max}$ is the number of independent solutions $\varphi(\bar{x})_\alpha$ of Eq.(2.8) as α varies. In the case that $N_{pm}(\chi^2_0)$ be a high number (the neutron fiber being multimode, then), the former can be estimated easily in quasi-classical approximation. In turn, the previous condition will be fulfilled provided that transverse dimension of the fiber (say, the square root of the area $A(T)$ of T) be adequately (or much) larger than β^{-1}_α. General studies about quasi-classical approximations in quantum mechanics [82] provide the foundations for the approximate formula

$$N_{pm}\left(\chi^2_0\right) = \frac{A(T)}{4\pi}\left[4\pi\Delta(b\rho) - \chi^2_0\right] \tag{2.11}$$

A similar and complementary analysis is in Section 5.5.1

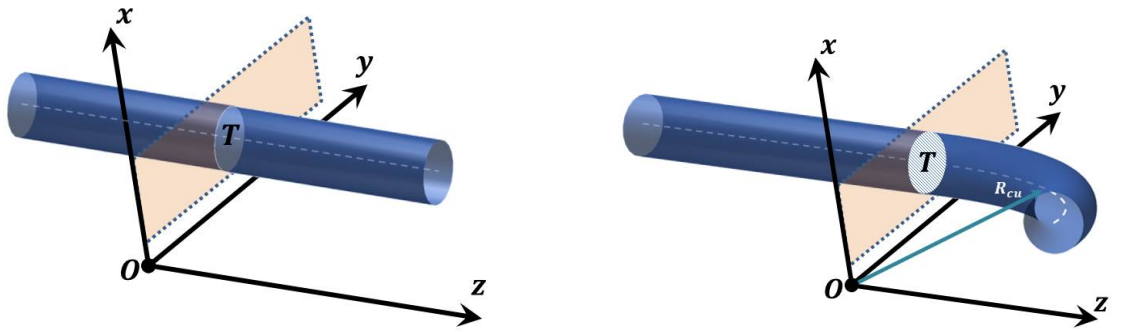

(a) (b)

Figure 2.7: Geometry for neutron fibres, including section T and curvature R_{cu}. (a) Straight fibre and (b) bent fibre.

2.4.2 Curved Single Fibre

Let us now consider a very lengthy three-dimensional fibre and assume: (i) the fibre is perfectly straight for $z \leqslant 0$ up to some $z = 0$, (ii) the fibre has a large curvature radius R_{cu}, for $0 \leqslant z \leqslant z_1$ (z_1 being finite). We define l as the length of the curved part of the fibre. R_{cu} is much larger than any neutron wavelength. Then, the transverse dimensions of the fibre, z_1, can be regarded as the length, l, of the curved part of the fibre. See Figure 2.7b.

We suppose a confined beam of slow neutrons, propagating initially along the straight part of the fibre with F_{in} its associated flux across the transverse section of the waveguide. As those neutrons propagate along the curved part of the fibre at $z = 0$, there is a non-vanishing probability for them to have no longer confined propagation but to escape outside the fibre, known as bending loss. One can calculate the quantum-mechanical probability flux for neutrons to propagate still confined across the transverse cross section of the fibre at z_1 (the end of the curved part of the fibre)

$$F(z_1) \simeq F_{in} \cdot \Upsilon \tag{2.12}$$

where Υ is the transmission coefficient and describes the decrease of the probability flux of the confined neutron propagating along the curved fiber, due to curvature losses. Υ depends on R_{cu} by means of the following approximate formula that has been justified in [82]

$$\Upsilon \simeq exp\left[-a_{cu} l \; exp\left(-b_{cu} R_{cu}\right) / R_{cu}^{1/2}\right] \tag{2.13}$$

where the constants a_{cu} and b_{cu} depend on whether the waveguide be multimode or monomode. Notice that if $R_{cu} \to +\infty$ then $\Upsilon \to 1$ which is physically consistent (no bending losses in straight waveguides). In [82], it is justified that $b_{cu} = \frac{2}{3}\beta_0 \left(\frac{\chi_0}{\beta_0}\right)^3$ (>0). Since χ_0 is the smallest in the set of all χ_α which are excited effectively

in the unbent part of the fiber (the highest achievable propagation mode), the corresponding $\beta_\alpha \equiv \beta_0$ is maximum. Thus, all modes such that $\chi_0 \leqslant \chi_\alpha \leqslant \chi_{max}$ do get excited effectively. It is not so easy to provide a precise compact formula for a_{cu} and it must be fit from experimental data, [82]. For a theoretical study of bending losses for a curved neutron fiber in the simpler case of two spatial dimensions, see [4].

2.4.3 Polycapillary Fibres

In this case, each single individual hollow channel in a PGF may be regarded as a single neutron fibre. In Section 2.2 we stated that each single hollow capillary channel has an average internal diameter of about 5 μm.

A priori, one could entertain the possibility that one slow neutron, propagating initially confined along a certain hollow channel, could escape, by transmission through the surrounding clad due to quantum-mechanical tunnel effect, to one of the neighbouring parallel channel and, eventually, escape finally toward the externally surrounding medium (air). Let d be the radial distance from the internal surface limiting the hollow channel to some point in its surrounding clad, so that $0 \leqslant d \leqslant 5$ μm. The probability for such a tunnel effect is exponentially small and, hence, negligible, for almost all thermal neutrons, for the lead-silica clad, provided that the clad thickness be about or larger than $d \geqslant 0.5$ μm $= d_{tunnel}$ [4]. Consequently, one may regard neutrons propagating along individual hollow channels as if they were surrounded by an infinite clad.

We can use arguments similar to those of Sections 2.4.1 and 2.4.2 to characterize the PGFs (and their individual hollow channels) propagation modes. In this case, $b_{core}\rho_{core} = 0$ and, by applying Eq.(2.10) for typical values of $b_{core}\rho_{core} = 0$ (>0), one obtains values for χ_{max} in the range of 10^{-3} Å to 10^{-2} Å. Then, for typical values of β_α ranging from, say, 0.7 Å^{-1} to 3 Å^{-1}, the dimensionless parameter χ_α/β_α varies from 10^{-12} to 10^{-4} for, say, the fundamental mode and the first few ones above it. Each hollow channel behaves as a multimode waveguide. Moreover, an analysis of bending losses equivalent to that of Section 2.4.2, makes consistent with experiment, [70], the values of Υ in Eq.(2.13) for $a_{cu}l \simeq 0.95$ m$^{1/2}$ and $b_{cu} \simeq 0.51$ m^{-1}. For last, the case with N (more or less) parallel hollow channels, which occurs in reality with polycapillary fibres, can be treated similarly, and leads, approximately, to the same Υ [4].

2.5 Refractive Optics Approximation

Once the propagation modes of a waveguide are characterized, one can make some simple assumptions to describe approximately the penetration of a neutron wave through one endface of a waveguide. In [6], Snyder and Love exposed a classical electromagnetic wave based approximation. This algorithm has proved to be effective in the case of weakly coupled optical waveguides. This is our case,

taking into account that the thermal neutron energy is of the order of 10^{-3} eV, the potential of material media is of the order of 10^{-7} to 10^{-8} eV.

In [6], authors argue that, for weakly guiding fibres, *The total transverse fields of the fibre at its endface [...] can be represented by the transverse portion of the eigenfunction expansion of [...] the bound-mode fields.*[2]. Although they state that it is in general not possible to find an analytical expression for the fields at the endface, they propose that for a weakly guiding fibre, one can ignore the spread in angles of the incident field and, thus, it can be adequately represented by a plane wave refracted according to Snell's law.

That proposal, translated to neutron optics, is made by two steps:

Step 1: Consider the incoming wave from the incident zone (vacuum or air) for $z < 0$ impinging the endface of the waveguide, assumed to be made of the material of the core. In this case, the classical refraction law is used to describe the wave inside the core using Fresnel coefficients (both in the optical case and the actual neutron case).

Step 2: Once computed the refracted wave into the core, one takes into account the clad to calculate the normalized propagation modes (for an infinite waveguide) and computes the projection of the refracted wave on those propagation modes using, in the actual neutron case, quantum mechanical probability amplitudes.

As an example, we calculate the results for a semi-infinite waveguide of aperture $x_0 = 1000$ Å with a core of Titanium surrounded by an infinite clad of Silicon. A thermal neutron beam impinges the waveguide. It is represented by a plane wave with an arbitrary incidence angle, $\varphi_{in}(x,z) = e^{ik_x x}e^{ik_z z}$ with $E = \frac{\hbar^2\left(k_x^2+k_z^2\right)}{2m} = 0.025$ eV.

For calculating the normalized propagation modes for the waveguide, we simulate it as a potential well of energy ($V_{core} - V_{clad} = V_{Ti_{nat}} - V_{Si_{nat}} = -1.05 \times 10^{-7}$ eV)[3]. By solving the well-known potential well problem (see, for example [78, 83]), there are three negative (discrete) propagation modes with energies 9.68×10^{-8} eV (fundamental mode), 4.78×10^{-8} eV (first excited state) and 1.23×10^{-8} eV (second excited state). See Figure 2.8.

The projection of the wavefunction, refracted inside the waveguide, on the previously calculated propagation modes, has the following analytical expression

$$\int_{-\infty}^{\infty} dx \varphi_{ref}(x, z=0)\, \varphi_n^*(x, z=0) = \tag{2.14}$$

$$= \begin{cases} A\left[\frac{sin\left((k'_x+\chi_n)\frac{x_0}{2}\right)}{k'_x+\chi_n} + \frac{sin\left((k'_x-\chi_n)\frac{x_0}{2}\right)}{k'_x-\chi_n}\right] & (even\ modes) \\ \frac{A}{i}\left[\frac{sin\left((k'_x+\chi_n)\frac{x_0}{2}\right)}{k'_x+\chi_n} - \frac{sin\left((k'_x-\chi_n)\frac{x_0}{2}\right)}{k'_x-\chi_n}\right] & (odd\ modes) \end{cases} \tag{2.15}$$

[2]Certain parts of the text refer to electromagnetic fields and have been omitted for the sake of clarity.

[3]Subscript "nat" indicates the naturally occurring elements (say, mixtures of the corresponding isotopes).

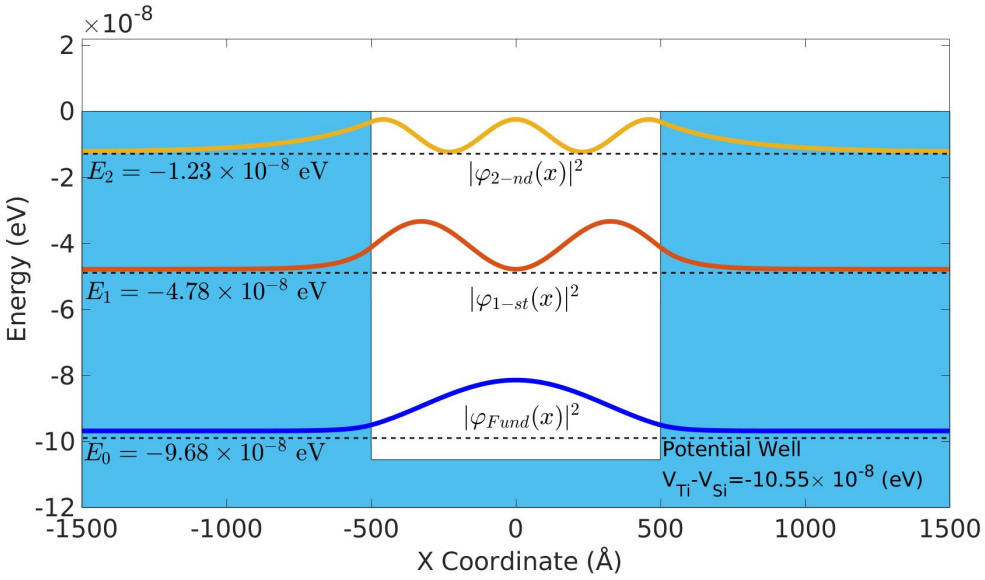

Figure 2.8: Discrete energy levels corresponding to a Si-Ti waveguide with aperture 1000 Å and infinite Si clad. Adapted from [63].

where $\varphi_{ref}(x, z = 0)$ is the refracted wave at $z = 0$, and $\varphi_n(x, z = 0)$ is the corresponding n-th propagation mode ($n = 0, 1, 2$ in this case), and * is the complex conjugate. A is the normalization factor for a normalized mode corresponding to the finite potential well problem. χ_n $(n = 0, 1, 2)$ is the transverse wavenumber of the propagation mode, x_0 is the waveguide aperture and k'_x is the x-component of the wavevector of the refracted wavefunction.

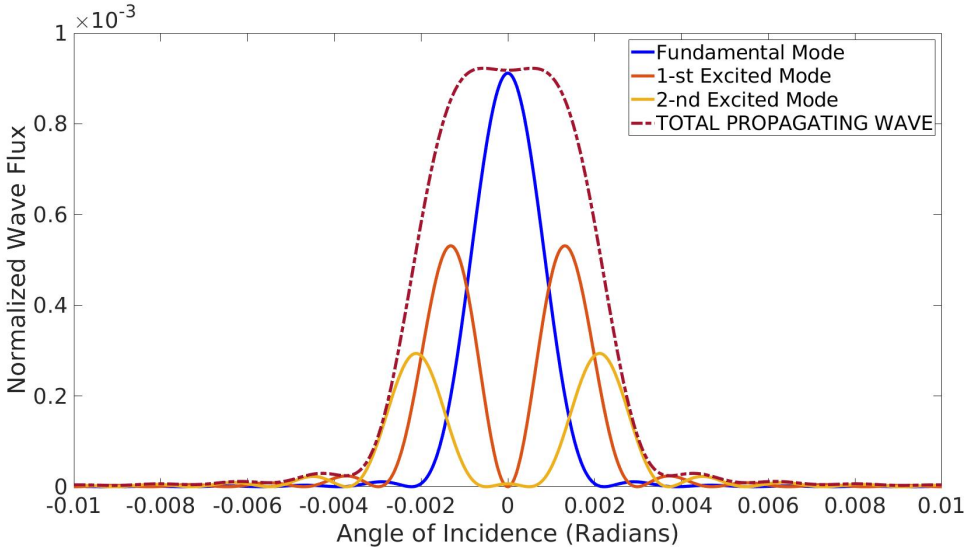

Figure 2.9: Excited propagation modes VS angle of incidence of the neutron beam for a Si-Ti-Si waveguide with 1000 Å aperture and infinite Si clad. Adapted from [63].

The results of our computations, are represented in Figure 2.9, where we represent the excitations of the different modes for different angles of the impinging neutron

beam and their contributions to the total value of the flux. By inspecting the figure one can appreciate the good correspondence with the expected classical behaviour of an optical waveguide. In the present neutron waveguide case, the critical angle is estimated to be $\theta_{cr} = 3 \times 10^{-3}$ radians implying a reduction of the flux by orders of magnitude for the actual planar neutron waveguide.

Empujados a este estrecho desfiladero,
su número no cuenta para nada.

300

3

Green's Functions Formalism for Neutron Waveguides

Contents

In previous Chapter 2 we exposed the limits of different approaches for a description of the behaviour of neutron waveguides. As a first attempt, geometrical optics approximation presents limitations for waveguide characterization. Indeed, it fails to describe the rise of modes of propagation and its distribution. Moreover, the complete numerical simulation of Eq.(1.5) is computationally unaffordable and only yields a set of complex numbers that must be treated to interpret physical results. The analysis of modes of propagation and the use of refractive optics approximation (Section 2.5) yields only approximate results and neglects important physical effects at the entrance such as diffraction and rise of evanescent waves.

In this Chapter, we will use a new and different approach to analyse the behaviour and confinement of an incoming neutron beam, $\varphi_{in}(\boldsymbol{x})$, at the waveguide. We will simplify the problem as much as possible, supposing that the confined propagating beam does not penetrate into the clad (i.e.: Dirichlet boundary conditions).

This simplification, although extreme, provides us with information about the mathematical behaviour of the neutron beam due to the geometry of the problem and may serve as a zero order approximation for the waveguiding description.

This chapter is based on the results and conclusions published in *Journal of Modern Optics* [84].

3.1 Analytical Formalism

Let there be a region of interest, Ω (that may be or not limited by certain frontiers $\partial\Omega_i$, $i = 1...n$), where the neutron beam propagates. In this region, assuming that there is no source term inside, the stationary scalar wave equation from Eq.(1.5) takes the form a homogenous Helmholtz Equation

$$\left[\nabla^2 + k^2\right] \varphi(\boldsymbol{x}) = 0 \tag{3.1}$$

For simplicity, we will assume that, in this region, $V(\boldsymbol{x}) = 0$ (i.e.: no media) an thus, $k^2 = \frac{2mE}{\hbar^2}$. It is trivial to extent this statement to any arbitrary potential, with the correspondent modification of k^2. In any case, notice that different media would imply the definition of disjoint regions Ω, and analysing the interaction of one with the others. It is beyond this formulation.

We will assume that the region of interest, Ω, extends to infinity in certain arbitrary directions or it is limited by certain boundaries, $\partial\Omega_i$, enclosing the region. For simplicity, we will assume, as a first approximation that neutrons do not penetrate in the boundaries. This is known as Dirichlet boundary conditions for the differential equation, Eq(3.1), and it is mathematically equivalent to impose that $\varphi(\partial\Omega_i) = 0$. Notice that we will not impose this condition in those directions for which the region tends to infinity (in fact, we will add an inhomogeneous term corresponding to the incoming neutron beam).

We propose here to use a non-trivial extension of the mathematical formulation, in [14], in order to solve Eq.(3.1). In that article, Balian and Bloch obtained integral equations involving Green's functions both for Dirichlet and Neumann boundary conditions, and developed iterative algorithms for their computation in a different physical context, namely, the analysis of the density of states for a large atomic nucleus. Indeed, they discuss a systematic procedure for calculating the Green's function for different boundary conditions (Dirichlet, Neumann,...) on an arbitrary surface, $\partial\Omega$. In the case of Dirichlet boundary conditions, they search for a function $G_D(\boldsymbol{x})$ that is said to be a Green's function with Dirichlet boundary conditions of the form

$$G_D(\boldsymbol{x}) \equiv G_0(\boldsymbol{x}) + G_1(\boldsymbol{x}) \tag{3.2}$$

where $G_0(\boldsymbol{x})$ is the Green's function for the infinite space and $G_1(\boldsymbol{x})$ is a correction for this Green's function (that will be understood as a *double layer potential*). In order that the third term in Eq.(3.2) obeys Dirichlet conditions, $G_1(\boldsymbol{x})$ must satisfy

$$\begin{cases} [\nabla^2 + k^2] G_1(\boldsymbol{x}) = 0 \quad for\ \boldsymbol{x} \in \Omega \\ G_1(\boldsymbol{x}) = -G_0(\boldsymbol{x}) \quad for\ \boldsymbol{x} \in \partial\Omega \end{cases} \tag{3.3}$$

Balian and Bloch proposed for $G_1(\boldsymbol{x})$

$$G_1(\boldsymbol{x}) = \int_{\partial\Omega} d\boldsymbol{x'} \left. \frac{\partial G_0(\boldsymbol{x} - \boldsymbol{x'})}{\partial \boldsymbol{n}} \right|_{\boldsymbol{x'} \in \partial\Omega} \mu(\boldsymbol{x'}) \tag{3.4}$$

where the differential with respect to $\boldsymbol{n}$ represents the inner normal derivative at a generic point, $\boldsymbol{x'}$, of the boundary surface $\partial\Omega$ (for example, see Figures 3.1, 3.2 and 3.4), $d\boldsymbol{x'}$ is the differential element and $\mu(\boldsymbol{x'})$ is understood as a certain density function to be found (in fact, in the potential theory, it is understood as a density of dipole charges). Simple arguments (close to those that we will state in Section 3.1.2) show that $\mu(\boldsymbol{x'})$ can be fully characterized uniquely as a linear inhomogeneous integral equation, not displayed here for brevity (one may refer to [14] and [59] for expanded arguments). This solution leads to an infinite expansion of $G_D(\boldsymbol{x})$ in terms of $G_1(\boldsymbol{x})$ in the context of perturbation theory.

Our approach differs from that of Balian and Bloch, [14]. Our domain is not constrained to a large bounded spatial region (the atomic nucleus) but it may be unbounded in some directions (for example, $z \to -\infty$ in the case of semi-infinite waveguides), so that an inhomogeneous term is included. Thus, we look for solutions of the stationary scalar wave equation, Eq.(3.1), $\forall \boldsymbol{x} \in \Omega$, in the form of

$$\varphi(\boldsymbol{x}) = \varphi_{in}(\boldsymbol{x}) + \sum_{i=1}^{n} \int_{\partial\Omega_i} d\boldsymbol{x_i'} \left. \frac{\partial G\left(\boldsymbol{x} - \boldsymbol{x_i'}\right)}{\partial \boldsymbol{n_i}} \right|_{\boldsymbol{x_i'} \in \partial\Omega} \mu_i\left(\boldsymbol{x_i'}\right) \tag{3.5}$$

where we have added an inhomogeneous term $\varphi_{in}(\boldsymbol{x})$ accounting for the incoming neutron beam. That makes Eq.(3.4) complete for those regions whith $\partial\Omega \to \infty$. Green's theorem [85, 86, 87] ensures that this term, $\varphi_{in}(\boldsymbol{x})$, corresponds to the incident wave. In this case, we will treat the frontier of Ω as a set of boundaries, $\partial\Omega_i$, $i = 1...n$, instead of being a continuous one. Notice that, for simplicity, we omit the subindex 0 in the Green's function notation. Rather, we use the expansion in plane waves of the scalar spherical Green's function in three-dimensional, 3D, representation

$$\begin{aligned} G(\boldsymbol{x}, \boldsymbol{x'}) =& \frac{exp(ik \mid \boldsymbol{x} - \boldsymbol{x'} \mid)}{\mid \boldsymbol{x} - \boldsymbol{x'} \mid} = \\ =& -\int\int\int_{-\infty}^{\infty} \frac{d^3\boldsymbol{K'}}{(2\pi)^3} \frac{exp\left[i\boldsymbol{K'}(\boldsymbol{x} - \boldsymbol{x'})\right]}{E + i\varepsilon - \frac{\hbar^2}{2m}\boldsymbol{K'}^2} \end{aligned} \tag{3.6}$$

Frequently, we will make use of the two-dimensional, 2D, representation

$$G\left(\bar{x},\bar{x}'\right)=-\int\int_{-\infty}^{\infty}\frac{d^{2}\bar{K}'}{\left(2\pi\right)^{2}}\frac{exp\left[i\bar{K}'\left(\bar{x}-\bar{x}'\right)\right]}{E+i\varepsilon-\frac{\hbar^{2}}{2m}\bar{K}'^{2}} \tag{3.7}$$

Notice that, both in Eq.(3.6) and (3.7), $\varepsilon>0$ is an infinitesimal term and that the limit $\varepsilon\to 0$ is taken at the end of the calculations. A detailed and rigorous derivation of the general solution of Laplace's equation inside a finite volume with Dirichlet (and Neumann) boundary conditions is given in [88].

Notice, as well, integrals containing the Green's function in Eq.(3.5). Those Green's functions are locally singular, but the integrals containing them in Eq.(3.5) are finite, that is, the local singularities are smoothed out by the integration.

3.1.1 General Formalism for Neutron Waveguides

In this section, we demonstrate that Eq.(3.5) is, in fact, a solution for the stationary Schrödinger equation, Eq.(1.5). For the sake of clearness, we will perform our demonstration for a particular case, with $V\left(\boldsymbol{x}\right)=0$ (i.e.: in vacuum), in which there is only a boundary condition at $z=0$ and $-\infty\leqslant x,y\leqslant\infty$ (reflecting wall). Thus, the proposed solution, for $z<0$, must be of the form

$$\varphi\left(\boldsymbol{x}\right)=\varphi_{in}\left(\boldsymbol{x}\right)-\iint_{-\infty}^{\infty}dx'dy'\left.\frac{\partial G\left(\boldsymbol{x}-\boldsymbol{x'}\right)}{\partial z'}\right|_{z'=0}\mu\left(x',y'\right) \tag{3.8}$$

The proposed equation would be the desired solution of the problem, for $z<0$, if it fulfils at the same time both Eq.(1.5) and the set of boundary conditions. If we substitute Eq.(3.8) into Eq.(1.5) we obtain

$$\left[\frac{-\hbar^{2}}{2m}\nabla^{2}-E\right]\left[\varphi_{in}\left(\boldsymbol{x}\right)-\iint_{-\infty}^{\infty}dx'dy'\left.\frac{\partial G\left(\boldsymbol{x}-\boldsymbol{x'}\right)}{\partial z'}\right|_{z'=0}\mu\left(x',y'\right)\right]=0 \tag{3.9}$$

where $\nabla^{2}=\left(\frac{\partial^{2}}{\partial x^{2}}+\frac{\partial^{2}}{\partial y^{2}}+\frac{\partial^{2}}{\partial z^{2}}\right)$ is the laplacian operator. We will not pay attention to the inhomogeneous term, since it is clear that it must fulfil the equation by its definition. If we apply this operator, $\left[\frac{-\hbar^{2}}{2m}\nabla^{2}-E\right]$ to the Green's function in Eq.(3.6) we have

$$\begin{aligned}\left[\frac{-\hbar^{2}}{2m}\nabla^{2}-E\right]G\left(\boldsymbol{x},\boldsymbol{x'}\right)=&\\ =-\iiint_{-\infty}^{\infty}\frac{dK'_{x}dK'_{y}dK'_{z}}{\left(2\pi\right)^{3}}\left[\frac{-\hbar^{2}}{2m}\left(K_{x}'^{2}+K_{y}'^{2}+K_{z}'^{2}\right)-E\right]\times&\\ \times\frac{e^{i\left[K'_{x}\left(x-x'\right)+K'_{y}\left(y-y'\right)+K'_{z}\left(z-z'\right)\right]}}{E+i\varepsilon-\frac{\hbar^{2}}{2m}\left(K_{x}'^{2}++K_{y}'^{2}+K_{z}'^{2}\right)}=&\\ =+\iiint_{-\infty}^{\infty}\frac{dK'_{x}dK'_{y}dK'_{z}}{\left(2\pi\right)^{3}}e^{i\left[K'_{x}\left(x-x'\right)+K'_{y}\left(y-y'\right)+K'_{z}\left(z-z'\right)\right]}=&\\ =+\delta\left(x-x'\right)\delta\left(y-y'\right)\delta\left(z-z'\right)&\end{aligned} \tag{3.10}$$

Thus, Eq.(3.7) is, as stated, a Green's function for the stationary Schrödinger equation.

Returning to Eq.(3.9), we have

$$\left[\frac{-\hbar^2}{2m}\nabla^2 - E\right] \iint_{-\infty}^{\infty} dx'dy' \left.\frac{\partial G\left(\boldsymbol{x}-\boldsymbol{x'}\right)}{\partial z'}\right|_{z'=0} \mu\left(x',y'\right) = \\ = \iint_{-\infty}^{\infty} dx'dy' \left.\frac{\partial}{\partial z'}\delta\left(x-x'\right)\delta\left(y-y'\right)\delta\left(z-z'\right)\right|_{z'=0} \mu\left(x',y'\right) = 0 \tag{3.11}$$

since $z > 0$. Consequently, Eq.(3.5) is a solution of the scalar Schrödinger equation, for any function $\mu\left(\boldsymbol{x}\right)$ and it solves the problem for a particular set of boundary conditions as the complete solution of the problem. We understand these functions (and will refer to them) as auxiliary functions.

3.1.2 Dirichlet Boundary Conditions

In the physical situations treated in this chapter, the penetration of the slow neutron beam into the materials is not considered to be an important effect. Then, as a zeroth-order approximation, we consider the confinement phenomenon as a strong one as if the material would give rise to an infinite repulsive potential on the neutron. By imposing Dirichlet boundary conditions at the corresponding boundaries, the conditions determining all functions $\mu_i\left(\boldsymbol{x'}\right)$ are obtained. They represent the exact solution with further conditions for computational analysis. Thus, the wavefunction limits in the boundaries have to be calculated.

Imposing Dirichlet boundary conditions is not as simple as imposing $\varphi\left(\boldsymbol{x}\right) = 0$ at the boundaries. The integral always yields 0 following by symmetric integration. To illustrate, consider, as in the previous Section 3.1.1, a simple case where there is only a boundary condition at $z = 0$ and $-\infty \leqslant x, y \leqslant \infty$ (Section 3.2.1). The value of Eq.(3.5) at $z = 0$ (where there is the only boundary, $z' = 0$) always yields

$$\left.\frac{\partial G\left(x-x',y-y',0-z'\right)}{\partial z'}\right|_{z'=0} = 0 \tag{3.12}$$

The result implies that, in the case of multiple boundary conditions $i = 1...n$, the function $\mu_i\left(\boldsymbol{x'}\right)$ associated to that wall does not contribute to the final solution. This is a natural conclusion of Green's theorem since we have already chosen the formulation corresponding to Dirichlet boundary conditions.

Balian and Bloch, [14], derived such conditions stating that $G_D\left(\boldsymbol{x}\right)$ in Eq.(3.2): (i) must be continuous inside the volume bounded by the surface $\partial\Omega$ and vanish as the vector $\boldsymbol{x}$ approaches the boundary from inside $\partial\Omega$, (ii) does not vanish at the boundaries (that is, if $\boldsymbol{x}$ is taken to lie exactly at the boundaries, without the process of approaching them from inside) .

In our formulation, let assume a general geometry in which there are both inhomogeneous term (incoming wave) and a set of n Dirichlet boundary conditions. Notice that we have not stated yet the geometry of the problem, since we want to keep the formulation as general as possible. The wavefunction in Eq.(3.5) is a generic solution for the stationary Schrödinger equation. Let us impose at certain boundary i to fulfil

$$\varphi\left(\boldsymbol{x}-\boldsymbol{n}_{\boldsymbol{\epsilon}}\right) \xrightarrow[\epsilon\to 0^{+}]{} 0 \tag{3.13}$$

where $\boldsymbol{n}_{\boldsymbol{\epsilon}}$ is a vector normal to the boundary surface that tends to 0. We calculate the result

$$\begin{aligned}
&\lim_{\epsilon\to 0^{+}} \varphi\left(\boldsymbol{x_i}-\boldsymbol{n}_{\boldsymbol{\epsilon}}\right)-\varphi\left(\boldsymbol{x_i}\right)= \\
&\quad=\lim_{\epsilon\to 0^{+}} \varphi_{in}\left(\boldsymbol{x}-\boldsymbol{n}_{\boldsymbol{\epsilon}}\right)+\sum_{j=1}^{n}\int_{\partial\Omega_j} d\boldsymbol{x_j'}\left.\frac{\partial G\left(\boldsymbol{x_i}-\boldsymbol{n}_{\boldsymbol{\epsilon}}-\boldsymbol{x_j'}\right)}{\partial \boldsymbol{n_j}}\right|_{\boldsymbol{x_j'}\in\partial\Omega_j}\mu_j\left(\boldsymbol{x_j'}\right)- \\
&\qquad\qquad-\varphi_{in}\left(\boldsymbol{x}\right)-\sum_{j=1}^{n}\int_{\partial\Omega_j} d\boldsymbol{x_j'}\left.\frac{\partial G\left(\boldsymbol{x_i}-\boldsymbol{x_j'}\right)}{\partial \boldsymbol{n_j}}\right|_{\boldsymbol{x_j'}\in\partial\Omega_j}\mu_j\left(\boldsymbol{x_j'}\right)
\end{aligned} \tag{3.14}$$

In equation 3.14, all terms are not singular at the boundary $\partial\Omega_i$ (i.e.:$\boldsymbol{x}=\boldsymbol{x_i}$) and cancel one to one except that of the boundary itself (i.e.: $\forall \boldsymbol{x_j}\ i\neq j$). Moreover, according to Eq.(3.12), the latter term yields the following result to Eq.(3.14)

$$\begin{aligned}
&\lim_{\epsilon\to 0^{+}}\int_{\partial\Omega_i} d\boldsymbol{x_i'}\left.\frac{\partial G\left(\boldsymbol{x_i}-\boldsymbol{n}_{\boldsymbol{\epsilon}}-\boldsymbol{x_i'}\right)}{\partial \boldsymbol{n_i}}\right|_{\boldsymbol{x_i'}\in\partial\Omega_j}\mu_i\left(\boldsymbol{x_i'}\right)= \\
&\qquad\lim_{\epsilon\to 0^{+}}\int_{\partial\Omega_i} d\boldsymbol{x_i'}\left.\frac{\partial G\left(-n_{\epsilon}\right)}{\partial \boldsymbol{n_i}}\right|_{\boldsymbol{x_i'}\in\partial\Omega_j}\mu_i\left(\boldsymbol{x_i'}\right)=\frac{2m}{\hbar^2}\frac{1}{2}\mu_i(\boldsymbol{x_i})
\end{aligned} \tag{3.15}$$

The calculation is straightforward by making use of the definition of the Green's function stated above and the residue theorem. We omit details here for brevity, but notice that the derivative of the Green's function yields a delta function. An example applied to a concrete geometry may be found in [84]. Notice that this result, yielding $\mu_i\left(\boldsymbol{x_i}\right)$ is obtained before imposing Dirichlet boundary conditions.

If one imposes Dirichlet boundary conditions to $\lim_{\epsilon\to 0^{+}}\varphi\left(\boldsymbol{x_i}-\boldsymbol{n}_{\boldsymbol{\epsilon}}\right)-\varphi\left(\boldsymbol{x_i}\right)$, it is clear that the first term must equal 0 since this is, precisely, the definition of Dirichlet conditions. Moreover, in the second term we will have all contributions in Eq.(3.5) except the one of the boundary itself since it vanishes by virtue of Eq.(3.12). Thus, a system of inhomogeneous linear integral equations for the auxiliary functions $\mu_i\left(\boldsymbol{x}\right)=f\left(\varphi_{in},\mu_j\right)\ \ i\neq j$ is obtained

$$\frac{2m}{\hbar^2}\frac{1}{2}\mu_i(\boldsymbol{x})=\varphi_{in}\left(\boldsymbol{x}\right)+\sum_{j=1,i\neq j}^{n}\int_{\partial\Omega_j} d\boldsymbol{x_j'}\left.\frac{\partial G\left(\boldsymbol{x}-\boldsymbol{x_j'}\right)}{\partial \boldsymbol{n_j}}\right|_{\boldsymbol{x_j'}\in\partial\Omega}\mu_j\left(\boldsymbol{x_j'}\right) \tag{3.16}$$

Equation 3.16 determines μ_i $i = 1...n$ functions in terms of the incoming wave $\varphi_{in}(\boldsymbol{x})$ (the inhomogeneous term). Some useful approximations to the exact solution (series expansion, functional analysis, numerical methods, iterative methods, etc.) are applicable. Notice, in Balian and Bloch [14] use of analogous equations with other inhomogeneous terms (not representing any sort of incoming plane wave) led to the development of an iterative algorithm simulating certain properties of an atomic nucleus. In any case, obtaining an exact solution for the system of equations leading to the characterization of the field, $\varphi(\boldsymbol{x})$ is not feasible.

In general, no analytical representation for the functions μ_i $i = 1...n$ is able to be computed. Moreover, a rigorous control of the convergence of the successive iterations of the system or application of Fredholm's theory is not easy to achieve.

3.2 Analytical Characterization of Waveguides

In this Section, we propose simple analytical forms for the functions $\mu_i(\boldsymbol{x})$ and related approximations. This is aimed to demonstrate the existence, for suitably large E, of trapped energy levels inside the waveguide (propagation modes). The computation of the energy levels achieved in the guide relies on finding some convenient relationships between the characterization of the system and some mathematical transforms related to optics, in particular Fourier and Hilbert transforms. For simplicity, we will focus on the XZ-plane, neglecting the y-coordinate by using a two dimensional formulation (i.e.: a thin film).

Firstly, we anticipate that terms and integrals of the form $\frac{\partial}{\partial x'}G\left(\bar{x}-\bar{x'}\right)$ and $\frac{\partial}{\partial z'}G\left(\bar{x}-\bar{x'}\right)$ will arise throughout the following Sections. By introducing the definition for the Green's function in Eq.(3.7) and assuming a boundary at $x' = a$ (a being a fixed value), one can solve, for example

$$\left.\frac{\partial G\left(\bar{x}-\bar{x'}\right)}{\partial x'}\right|_{x'=a} = -\int_{-\infty}^{+\infty}\frac{dK'_z}{2\pi}e^{iK'_z(z-z')}\int_{-\infty}^{+\infty}\frac{dK'_x}{2\pi}\frac{(-iK'_x)e^{iK'_x(x-a)}}{E+i\varepsilon-\frac{\hbar^2}{2m}\left(K'^2_x+K'^2_z\right)} \tag{3.17}$$

We use : $\frac{1}{A-K'^2_x} = \frac{1}{2\sqrt{A}}\left(\frac{1}{\sqrt{A}-K'_x}+\frac{1}{\sqrt{A}+K'_x}\right)$ with $A = \frac{2mE}{\hbar^2}-K'^2_z$

$$= +\int_{-\infty}^{+\infty}\frac{dK'_z}{2\pi}e^{iK'_z(z-z')}\int\frac{2m}{\hbar^2}\frac{dK'_x}{2\pi}e^{iK'_x(x-a)}\frac{i}{2\sqrt{\frac{2mE}{\hbar^2}-K'^2_z}}\times$$
$$\left(\frac{K'_x}{\sqrt{\frac{2mE}{\hbar^2}-K'^2_z}+i\varepsilon-K'_x}+\frac{K'_x}{\sqrt{\frac{2mE}{\hbar^2}-K'^2_z}+i\varepsilon+K'_x}\right) \tag{3.18}$$

One can see that there are two poles at $K'_x = \pm\sqrt{\frac{2mE}{\hbar^2} - K_z'^2} \pm i\varepsilon$. By applying the residue theorem, Eq.(3.18) reads

$$\begin{aligned} &-\frac{2m}{\hbar^2}\frac{1}{2}\int_{-\infty}^{+\infty}\frac{dK'_z}{2\pi}e^{iK'_z(z-z')}e^{-i(x-a)\sqrt{\frac{2mE}{\hbar^2}-K_z'^2}} \quad \text{for } (x-a)<0 \\ &+\frac{2m}{\hbar^2}\frac{1}{2}\int_{-\infty}^{+\infty}\frac{dK'_z}{2\pi}e^{iK'_z(z-z')}e^{+i(x-a)\sqrt{\frac{2mE}{\hbar^2}-K_z'^2}} \quad \text{for } (x-a)>0 \end{aligned} \tag{3.19}$$

An equivalent result is obtained for $\frac{\partial}{\partial z'}G\left(\bar{x}-\bar{x'}\right)$ at an arbitrary point $z'=b$

$$\begin{aligned} &\left.\frac{\partial G\left(\bar{x}-\bar{x'}\right)}{\partial z'}\right|_{z'=b} = \\ &\quad -\frac{2m}{\hbar^2}\frac{1}{2}\int_{-\infty}^{+\infty}\frac{dK'_x}{2\pi}e^{iK'_x(x-x')}e^{-i(z-b)\sqrt{\frac{2mE}{\hbar^2}-K_x'^2}} \quad \text{for } (z-b)<0 \\ &\quad +\frac{2m}{\hbar^2}\frac{1}{2}\int_{-\infty}^{+\infty}\frac{dK'_x}{2\pi}e^{iK'_x(x-x')}e^{+i(z-b)\sqrt{\frac{2mE}{\hbar^2}-K_x'^2}} \quad \text{for } (z-b)>0 \end{aligned} \tag{3.20}$$

3.2.1 Total Reflection in the Semi-Infinite Plane $Z < 0$

To test our formulation, according to Eq.(3.5), we propose the simplest possible case; total reflection by an infinite wall with zero absorption. For the sake of simplicity we will focus on a 2D formulation, (x, z). Let be Ω the total semi-infinite negative region $z \leqslant 0, \forall x$. In that region, an incoming plane wave of thermal neutrons, $\varphi_{in}(\bar{x}) = e^{i\bar{k}_{in}\bar{x}}$ with incoming wavevector $\bar{k}_{in}^2 = \frac{2mE}{\hbar^2} = k_{in,x}^2 + k_{in,z}^2$ and energy E, impinges an infinite barrier located at $z = 0, \forall x$ (see Figure 3.1). In the region $z \leqslant 0, \forall x$ we set the potential to be $V(\bar{x}) = 0$ (i.e.: vacuum), while in the region $z \geqslant 0, \forall x$ we set the potential to be $V(\bar{x}) = +\infty$. Consequently, one may describe the total wave to obey Dirichlet conditions at $z = 0, \forall x$. It is clear that the expected behaviour is the reflection and change of phase (to $-\pi$) of the reflected wave. Figure 3.1.

Only one surface, obeying Dirichlet conditions is defined. Consequently, according to Eq.(3.5), and, by using Eq.(3.19) for $z < 0$ the system may be described as

$$\begin{aligned} \varphi(\bar{x}) =& \varphi_{in}(\bar{x}) - \int_{-\infty}^{\infty} dx' \left.\frac{\partial G(x-x', z-z')}{\partial z'}\right|_{z'=0} \mu(x') = \\ =& \varphi_{in}(\bar{x}) + \int_{-\infty}^{\infty} dx' \mu(x') \frac{2m}{\hbar^2}\frac{1}{2}\int_{-\infty}^{+\infty}\frac{dK'_x}{2\pi}e^{iK'_x(x-x')}e^{-iz\sqrt{\frac{2mE}{\hbar^2}-K_x'^2}} \end{aligned} \tag{3.21}$$

notice that, in this case, the vector is normal to the surface and points towards $z < 0$ (see Figure 3.1). We propose an analytical representation of the auxiliary function in the form of $\mu(x) = -\mu e^{ik_{in,x}x}$ where μ is a constant to be set for a correct normalization. Equation 3.21 reads now

$$\varphi(\bar{x}) = \varphi_{in}(x, z) - \frac{2m}{\hbar^2}\frac{1}{2}\mu e^{ixk_{in,x}}e^{-izk_{in,z}} \tag{3.22}$$

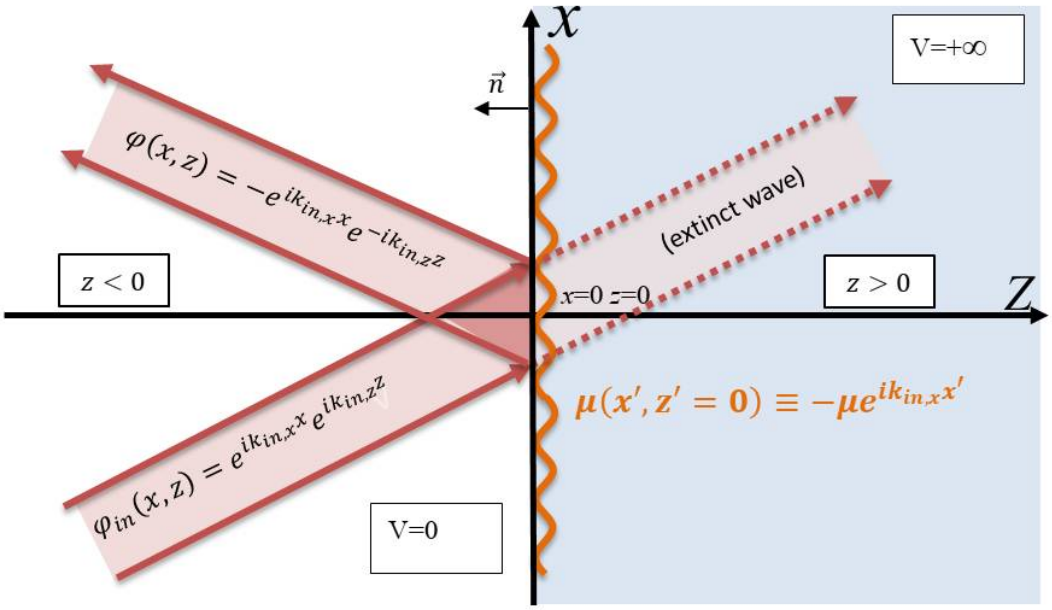

Figure 3.1: Geometry for the case of external reflection in the semi-infinite plane $Z < 0$

The second term in the right side is the reflected wave, as expected, by imposing that $\frac{2m}{\hbar^2}\frac{1}{2}\mu = 1$.

We will stress this formulation by calculating its result for the region $z \geqslant 0$. Again, according to Eq.(3.5) and Eq.(3.19), the system may be described as

$$\begin{aligned}\varphi(\bar{x}) =& \varphi_{in}(\bar{x}) + \int_{-\infty}^{\infty} dx' \left.\frac{\partial G(x-x', z-z')}{\partial z'}\right|_{z'=0} \mu(x') = \\ =& \varphi_{in}(\bar{x}) + \int_{-\infty}^{\infty} dx' \mu(x') \frac{2m}{\hbar^2}\frac{1}{2}\int_{-\infty}^{+\infty} \frac{dK'_x}{2\pi} e^{iK'_x(x-x')} e^{iz\sqrt{\frac{2mE}{\hbar^2} - K'^2_x}}\end{aligned} \tag{3.23}$$

Notice that, since we deal with the region $z > 0$, the normal vector points opposite direction to the previous case. In addition, we make use of Eq.(3.19) for $z > 0$ (i.e.: again a global change of sign and the z-dependent exponential changes its sign). If we assume the same auxiliary function $\mu(x) = -\mu e^{ik_{in,x}x}$, the result is $\varphi(\bar{x}) = 0\ \forall z > 0$. The auxiliary function propagated by using the Green's function equals the incident wave but with a difference in phase of π.

This result shows the extinction of the incoming neutron beam when it strikes the boundary (i.e.: an infinitely repulsive potential barrier) as it should be expected. It is remarkable that this formulation accounts for the extinction theorem in the case of Dirichlet conditions.

Initially we searched by eye for the auxiliary function, $\mu(x')$ that solved the system satisfactorily but this function becomes clear by applying the results for Dirichlet conditions in Eq.(3.16). The case showed in this section is represented in Figure 3.1.

Neumann Boundary Conditions

If we look at the formulation used in Eq.(3.5), it turns out to be similar to the *second Rayleigh-Sommerfeld diffraction integral* (wherein the normal derivative of the scalar wave is specified), $\psi = \int_{\partial\Omega} \mu \frac{\partial G}{\partial n}$. See, for example, [85], Section 2.5.3. It is, nevertheless, curious that the latter integral form relates in Kirchhoff approximation with what would be Neumann boundary conditions (instead of Dirichlet ones).

One would think that Eq.(3.5) can be directly derived from Green's theorem[1]; $\psi = \int_{\partial\Omega} \mu \frac{\partial G}{\partial n} - G \frac{\partial \mu}{\partial n}$ by applying the Kirchhoff approximation. It should not be confused, since in the case of Kirchhoff approximation a specific Green's function (allowing the boundary conditions to be fulfilled) has been imposed.

In any case, it is interesting to analyse the equations that would fulfil Dirichlet conditions in the Kirchhoff approximation (i.e.: *first Rayleigh-Sommerfeld diffraction integral*). Now, let us suppose we take a simple case such as total reflection by an infinite wall. Focusing on the semi-infinite region $z > 0$ in the previous case (see Figure 3.1) the total wavefunction describes by the *first Rayleigh-Sommerfeld diffraction integral* would be

$$\varphi(\bar{x}) = \varphi_{in}(\bar{x}) - \int_{-\infty}^{\infty} dx' \left. \frac{\partial \mu(x', z')}{\partial z'} \right|_{z=0} G(x - x', z - z') \tag{3.24}$$

We can set an auxiliary function $\mu(x, z) = -\mu e^{ik_{in,x}x} e^{ik_{in,z}z}$ or directly its derivative $\left.\frac{\partial \mu(x')}{\partial z}\right|_{z=0} = -\mu i k_{in,x} e^{ik_{in,x}x}$. The first one has a physical interpretation, since it relates the auxiliary function with the incoming wave's value at the boundary ($z = 0$) with a phase change of $-\pi$. In both cases, it is straightforward to see that we recover the result in Eq.(3.22). We omit details for brevity.

This result is promising and encourages the possibility of making a description of a more complex system (i.e.: obeying Fresnel's laws) through the use of Green's theorem and Kirchhoff approximation. In this case, it would be a matter of finding the auxiliary functions (and their derivatives at the boundaries) that solves the system. As will be seen, some attempt has been made that, however, has not provided generalizable results (see Section C.1).

3.2.2 Longitudinal Infinite Waveguide

Total reflection in Section 3.2.1, shows how to operate with the associate equations. To apply it to the simplest possible waveguiding case, let us suppose the region Ω to be an infinite waveguide, extending parallel to the propagation axis, $-\infty < z < +\infty$, centred, and of size x_0. Inside the waveguide (core) the potential $V(\bar{x}) = 0$ (i.e.: no material) while outside the waveguide the potential $V(\bar{x}) = +\infty$ (i.e.: Dirichlet conditions at the boundaries). Two boundaries are defined in $x = +\frac{x_0}{2}, \forall z$ and $x = -\frac{x_0}{2}, \forall z$ (see Figure 3.2).

[1]Notice that Green's theorem seems to identify what we call the auxiliary function with the total wavefunction, $\phi \equiv \mu$, but it is important to keep μ as a free function to work with

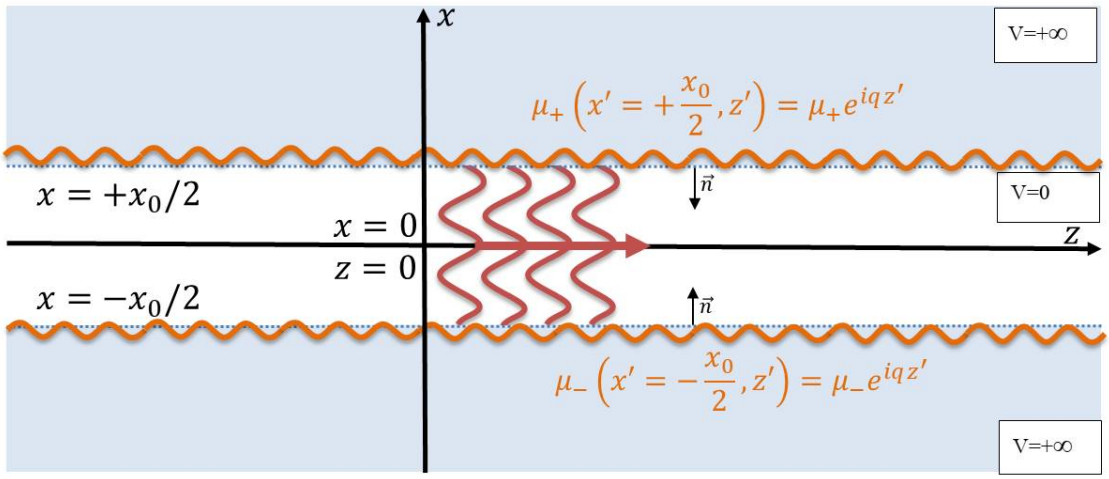

Figure 3.2: Geometry for the case of an infinite waveguide extended $-\infty < z < +\infty$

The total wavefunction will be

$$\begin{aligned}\varphi(\bar{x}) = \varphi_{in}(\bar{x}) \quad & - \int_{-\infty}^{\infty} dz' \left.\frac{\partial G(x-x', z-z')}{\partial x'}\right|_{x'=+\frac{x_0}{2}} \mu_+(z') + \\ & + \int_{-\infty}^{\infty} dz' \left.\frac{\partial G(x-x', z-z')}{\partial x'}\right|_{x'=-\frac{x_0}{2}} \mu_-(z') = \\ = \varphi_{in}(\bar{x}) \quad & + \int_{-\infty}^{\infty} dz' \mu_+(z') \frac{2m}{\hbar^2}\frac{1}{2}\int_{-\infty}^{+\infty}\frac{dK'_z}{2\pi} e^{iK'_z(z-z')} e^{-i\left(x-\frac{x_0}{2}\right)\sqrt{\frac{2mE}{\hbar^2}-K'^2_z}} + \\ & + \int_{-\infty}^{\infty} dz' \mu_-(z') \frac{2m}{\hbar^2}\frac{1}{2}\int_{-\infty}^{+\infty}\frac{dK'_z}{2\pi} e^{iK'_z(z-z')} e^{i\left(x+\frac{x_0}{2}\right)\sqrt{\frac{2mE}{\hbar^2}-K'^2_z}}\end{aligned} \tag{3.25}$$

notice that for the boundary $x = +\frac{x_0}{2}$ $\forall z$, the normal vector to the boundary points towards the negative x-direction while it is the opposite for the boundary $x = -\frac{x_0}{2}$ $\forall z$ (see Figure 3.2). In this geometry, we will assume that there is no incoming neutron beam, $\varphi_{in}(\bar{x}) \equiv 0$, since the waveguide extends to $z \to -\infty$. This is not a physically feasible situation, but it serves to show the conditions to be imposed and the possible mathematical solutions in the waveguide obeying Dirichlet conditions.

We set the two auxiliary functions to be $\mu_\pm(z') = \mu_\pm e^{iqz'}$, q being an arbitrary wavevector to be defined. $\mu_\pm$ are two constants to be computed for the normalization of the wavefunction. Inserting these auxiliary functions, removing $\varphi_{in}(\bar{x})$ and using

Eq.(3.19), we can solve Eq.(3.25)

$$\begin{aligned}
&\frac{2m}{\hbar^2}\frac{1}{2}\mu_+\int_{-\infty}^{+\infty}\frac{dK'_z}{2\pi}e^{izK'_z}e^{-i\left(x-\frac{x_0}{2}\right)\sqrt{\frac{2mE}{\hbar^2}-K'^2_z}}\int_{-\infty}^{\infty}dz'e^{iz'(q-K'_z)}+\\
&\quad+\frac{2m}{\hbar^2}\frac{1}{2}\mu_-\int_{-\infty}^{+\infty}\frac{dK'_z}{2\pi}e^{izK'_z}e^{i\left(x+\frac{x_0}{2}\right)\sqrt{\frac{2mE}{\hbar^2}-K'^2_z}}\int_{-\infty}^{\infty}dz'e^{iz'(q-K'_z)}=\\
&=\frac{2m}{\hbar^2}\frac{1}{2}\mu_+\int_{-\infty}^{+\infty}\frac{dK'_z}{2\pi}e^{izK'_z}e^{-i\left(x-\frac{x_0}{2}\right)\sqrt{\frac{2mE}{\hbar^2}-K'^2_z}}2\pi\delta\left(q-K'_z\right)+\\
&\quad+\frac{2m}{\hbar^2}\frac{1}{2}\mu_-\int_{-\infty}^{+\infty}\frac{dK'_z}{2\pi}e^{izK'_z}e^{i\left(x+\frac{x_0}{2}\right)\sqrt{\frac{2mE}{\hbar^2}-K'^2_z}}2\pi\delta\left(q-K'_z\right)=\\
&=\frac{2m}{\hbar^2}\frac{1}{2}e^{iqz}\left[\mu_+e^{-i\left(x-\frac{x_0}{2}\right)\sqrt{\frac{2mE}{\hbar^2}-q^2}}+\mu_-e^{i\left(x+\frac{x_0}{2}\right)\sqrt{\frac{2mE}{\hbar^2}-q^2}}\right]
\end{aligned}\tag{3.26}$$

Now, to obtain the value for the constants $\mu_\pm$ we proceed to impose Dirichlet conditions to Eq.(3.26); $\varphi\left(x=\pm\frac{x_0}{2},z\right)=0$.

$$\begin{aligned}
&\text{for } x=+\frac{x_0}{2} \qquad \mu_++\mu_-e^{ix_0\sqrt{\frac{2mE}{\hbar^2}-q^2}}=0 \quad \forall z\\
&\text{for } x=-\frac{x_0}{2} \qquad \mu_-+\mu_+e^{ix_0\sqrt{\frac{2mE}{\hbar^2}-q^2}}=0 \quad \forall z
\end{aligned}\tag{3.27}$$

It implies that $e^{ix_0\sqrt{\frac{2mE}{\hbar^2}-q^2}}=\pm1\Rightarrow\sqrt{\frac{2mE}{\hbar^2}-q^2}=\frac{\pi n}{x_0}$, $n\in\mathbb{N}$ and $\mu_+=\mp\mu_-$. Consequently we have two possible solutions for the complex amplitude

$$\varphi(x,z)=\begin{cases}-2i\frac{2m}{\hbar^2}\frac{1}{2}\mu_+e^{iqz}sin\left(\frac{2\pi nx}{x_0}\right) & \text{for odd modes}\\ 2\frac{2m}{\hbar^2}\frac{1}{2}\mu_+e^{iqz}cos\left(\frac{(2n+1)\pi x}{x_0}\right) & \text{for even modes}\end{cases}\tag{3.28}$$

As we commented before, this case cannot represent a real physical situation, since we have removed the inhomogeneous term from Eq.(3.25). In any case, this result will be interesting to be recalled in Section 3.2.4.

3.2.3 Limited Aperture Diffraction

We propose here a modification of Section 3.2.1. In that section, we showed that the formulation in Eq.(3.21) also accounted for the extinction of the incoming wave at $z>0$, behind the barrier of infinite potential. Thus, we formulated the analytical solutions of the proposed equations.

Here, we propose a geometry similar to that of Figure 3.1, with an incoming neutron plane wave impinging from $z\to-\infty$ an infinite potential barrier located at $z=0\ \forall x$, obeying Dirichlet boundary conditions. Suppose that this boundary is of negligible thickness along z and that an opening of size x_0 centred on the origin of coordinates is considered. In this occasion we make use of Eq.(3.21) but

assuming two boundaries at $z=0$, $x \geqslant \frac{x_0}{2}$ (with auxiliary function $\mu_1(x')$) and $z=0$, $x \leqslant -\frac{x_0}{2}$ (with auxiliary function $\mu_2(x')$)

$$\begin{aligned}\varphi(\bar{x}) = \varphi_{in}(\bar{x}) \quad &+ \int_{\frac{x_0}{2}}^{\infty} dx' \left.\frac{\partial G(x-x', z-z')}{\partial z'}\right|_{z'=0} \mu_1(x') + \\ &+ \int_{-\infty}^{-\frac{x_0}{2}} dx' \left.\frac{\partial G(x-x', z-z')}{\partial z'}\right|_{z'=0} \mu_2(x') = \\ = \varphi_{in}(\bar{x}) \quad &+ \int_{\frac{x_0}{2}}^{\infty} dx' \mu_1(x') \frac{2m}{\hbar^2}\frac{1}{2}\int_{-\infty}^{+\infty} \frac{dK'_x}{2\pi} e^{iK'_x(x-x')} e^{iz\sqrt{\frac{2mE}{\hbar^2}-K'^2_x}} + \\ &+ \int_{-\infty}^{-\frac{x_0}{2}} dx' \mu_2(x') \frac{2m}{\hbar^2}\frac{1}{2}\int_{-\infty}^{+\infty} \frac{dK'_x}{2\pi} e^{iK'_x(x-x')} e^{iz\sqrt{\frac{2mE}{\hbar^2}-K'^2_x}} \end{aligned} \tag{3.29}$$

notice that, this time, we are focusing on the region $z>0$ and, thus, the normal vector to the boundary points towards the positive z-direction.

This geometrical configuration cannot be represented by any analytical representation of the auxiliary functions and, so, we are constrained to perform approximations. At this point, we make a physical ansatz for the functions $\mu_1(x')$ and $\mu_2(x')$ for generic incoming neutron energy E with an arbitrary angle. We check whether the final result obeys, approximately, the expected physical behaviour. Notice that Eq.(3.16) provides a good hint

$$\mu_1(x') = \mu_2(x') \simeq -\varphi_{in}(x', z=0) = -\mu e^{ik_{in,x}x'} \tag{3.30}$$

The above approximation is consistent with the conservation of the probability flux along the z-axis, as outlined in Section 3.3. It is also consistent with total reflection in $z<0$, for $x>0$ and large (for $\mu_1(x')$) and $x<0$ and large (for $\mu_2(x')$). Recalling Eqs.(3.29) and (3.30)

$$\begin{aligned}\varphi_{in}(\bar{x}) - \frac{2m}{\hbar^2}\frac{1}{2}\mu \int_{-\infty}^{+\infty} \frac{dK'_x}{2\pi} e^{iK'_x x} e^{iz\sqrt{\frac{2mE}{\hbar^2}-K'^2_x}} \\ \left[\int_{\frac{x_0}{2}}^{\infty} dx' e^{ix'(k_{in,x}-K'_x)} + \int_{-\infty}^{-\frac{x_0}{2}} dx' e^{ix'(k_{in,x}-K'_x)}\right] = \\ = \varphi_{in}(\bar{x}) - \frac{2m}{\hbar^2}\frac{1}{2}\mu \int_{-\infty}^{+\infty} \frac{dK'_x}{2\pi} e^{iK'_x x} e^{iz\sqrt{\frac{2mE}{\hbar^2}-K'^2_x}} \\ \left[\int_{-\infty}^{\infty} dx' e^{ix'(k_{in,x}-K'_x)} - \int_{-\frac{x_0}{2}}^{+\frac{x_0}{2}} dx' e^{ix'(k_{in,x}-K'_x)}\right] \end{aligned} \tag{3.31}$$

notice that the first term between brackets corresponds to the incoming wave extinction by virtue of Eq.(3.23) while the second term must account for the plane wave diffraction of the neutron beam by the limited aperture.

In [84], this second term between brackets arose in our equations and it is compulsory to analyse and interpret it. In this case, since we know that it is the term arising from the limited aperture contribution (diffracted wave), we will

demonstrate that it shows the expected physical behaviour for $z \to \infty$. Since the aperture is a finite one, the number of diffracted neutrons passing through it (intensity) must be finite too. Thus, the contribution of this term approaches to 0 for $z > 0$ large enough.

For the sake of simplicity, we omit all constant factors, as we are interested in the function behaviour. We will demonstrate that

$$\int_{-\infty}^{+\infty} \frac{dK'_x}{2\pi} e^{iK'_x x} e^{iz\sqrt{\frac{2mE}{\hbar^2}-K'^2_x}} \int_{-\frac{x_0}{2}}^{+\frac{x_0}{2}} dx' e^{ix'(k_{in,x}-K'_x)} \xrightarrow[z\to\infty]{} 0 \tag{3.32}$$

Notice that the second integral is a finite one that can be computed numerically. Then, recalling Eq.(3.31), it yields

$$\begin{aligned} &\int_{-\infty}^{+\infty} \frac{dK'_x}{2\pi} e^{iK'_x x} e^{iz\sqrt{\frac{2mE}{\hbar^2}-K'^2_x}} \int_{-\frac{x_0}{2}}^{+\frac{x_0}{2}} dx' e^{ix'(k_{in,x}-K'_x)} = \\ &\qquad = \int_{-\infty}^{+\infty} L\left(K'_x\right) e^{iz\sqrt{\frac{2mE}{\hbar^2}-K'^2_x}} dK'_x \end{aligned} \tag{3.33}$$

where $L\left(K'_x\right) = \frac{sin\left[\frac{x_0}{2}(k_{in,x}-K'_x)\right]}{\pi(k_{in,x}-K'_x)} e^{iK'_x x}$

One can decompose the integral interval Eq.(3.33) into three: $-\infty < K'_x \leqslant -k_{in}$, $-k_{in} \leqslant K'_x \leqslant k_{in}$ and $k_{in} \leqslant K'_x \leqslant +\infty$. Notice that the square root function in the term, $e^{iz\sqrt{\frac{2mE}{\hbar^2}-K'^2_x}}$ is purely real only in the interval $K'^2_x \leqslant \frac{2mE}{\hbar^2} = k^2_{in}$. Thus, in the intervals $-\infty < K'_x \leqslant -k_{in}$ and $k_{in} \leqslant K'_x \leqslant +\infty$, this the exponential yields $e^{-z\sqrt{|k^2_{in}-K'^2_x|}}$, which vanish for large z. These two terms represent the evanescent wave arising from the aperture, due to its finite size.

The remaining term (i.e.: the one corresponding to the interval $-k_{in} \leqslant K'_x \leqslant k_{in}$) can be computed numerically. Moreover, in order to perform a physical interpretation for this term, one may rewrite it as a Fourier transform of the integrand. Just by performing the change of variable $\sqrt{k^2_{in} - K'^2_x} = -\tau$ and imposing infinite integration limits with the use of the *rect* function [7], then, this second term yields

$$\begin{aligned} &\int_{-\infty}^{\infty} d\tau \; rect\left(\frac{\sqrt{k^2_{in}-\tau'^2}}{2k_{in}}\right) \frac{sin\left(\frac{x_0}{2}\tau^2\right)}{\pi\tau^2} e^{ix\sqrt{k^2_{in}-\tau'^2}} e^{iz\tau} = \\ &= \mathcal{F}\left[rect\left(\frac{\sqrt{k^2_{in}-\tau'^2}}{2k_{in}}\right) \frac{sin\left(\frac{x_0}{2}\tau^2\right)}{\pi\tau^2} e^{ix\sqrt{k^2_{in}-\tau'^2}}\right](z) \end{aligned} \tag{3.34}$$

where $\mathcal{F}$ denotes the Fourier Transform of the inner function. By applying Riemann-Lebesgue lemma [89], it can be shown that it tends to 0 for large positive z. As a more complete physical explanation, Eq.(3.33) represents the diffraction produced by the aperture directly related with the Fourier transform of the incoming signal. Some values of the angular spectrum are allowed in the phase space associated to the transform and thus, propagate in $z > 0$. Meanwhile, those values

exceeding the incoming wave wavevector values, k_{in}, give rise to evanescent waves. Figure 3.3 shows a direct numerical simulation of Eq.(3.33) for a thermal neutron beam impinging a Dirichlet boundary with a $x_0 = 100$ Å aperture for different incoming wave impinging angles; in Figure 3.3a it is $\theta = 0°$ while in Figure 3.3b, $\theta = 10°$. Both figures, display the squared modulus of the neutron wavefunction (probability). Right colourbar represents the correspondence between values and colour, assuming $\mid \varphi_{in}(\bar{x}) \mid^2 = 1$.

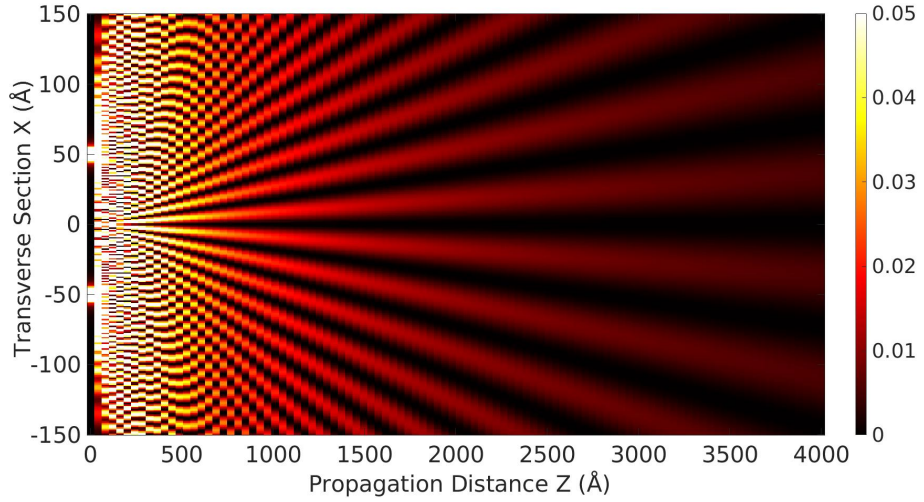

(a)

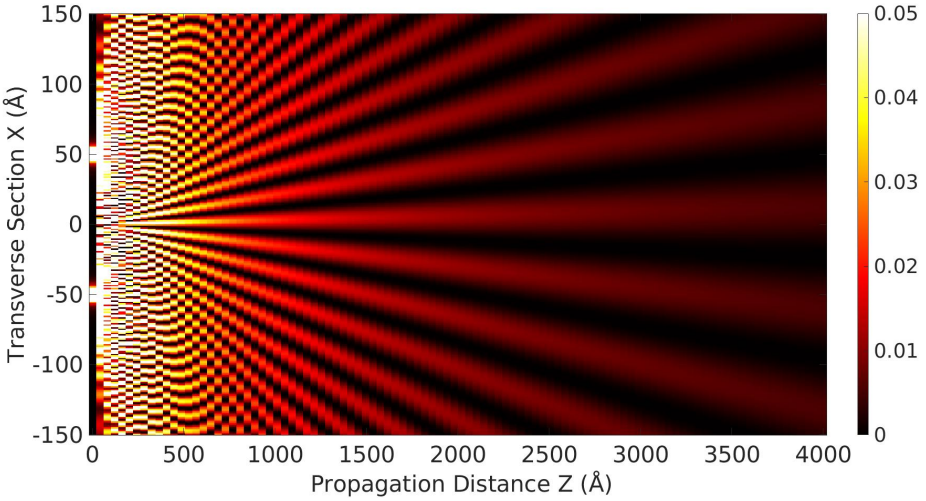

(b)

Figure 3.3: Numerical simulations of a Dirichlet boundary with a diffractive aperture of size $x_0 = 100$ Å for the cases of (a) normal incidence, $\theta = 0°$, and (b) incidence with $\theta = 10°$.

The diffraction pattern obtained is the standard one. However, in both cases these numerical computations become tricky, since they take long computation times; we simulated only 300×100 points, taking about 480 seconds each figure. Besides

that, it is clear that for short propagation distances, numerical errors accumulate and makes computation noisy and not accurate. Furthermore, for sufficiently short distances, the numerical integrals do not converge within Matlab's precision.

3.2.4 Semi-infinite Waveguide

In the previous Sections, we have verified how the method stated in Eq.(3.5) reproduces accurately simple cases. In this section, we will apply the lessons learned to obtain, approximately, the propagation modes associated with a semi-infinite waveguide obeying Dirichlet conditions.

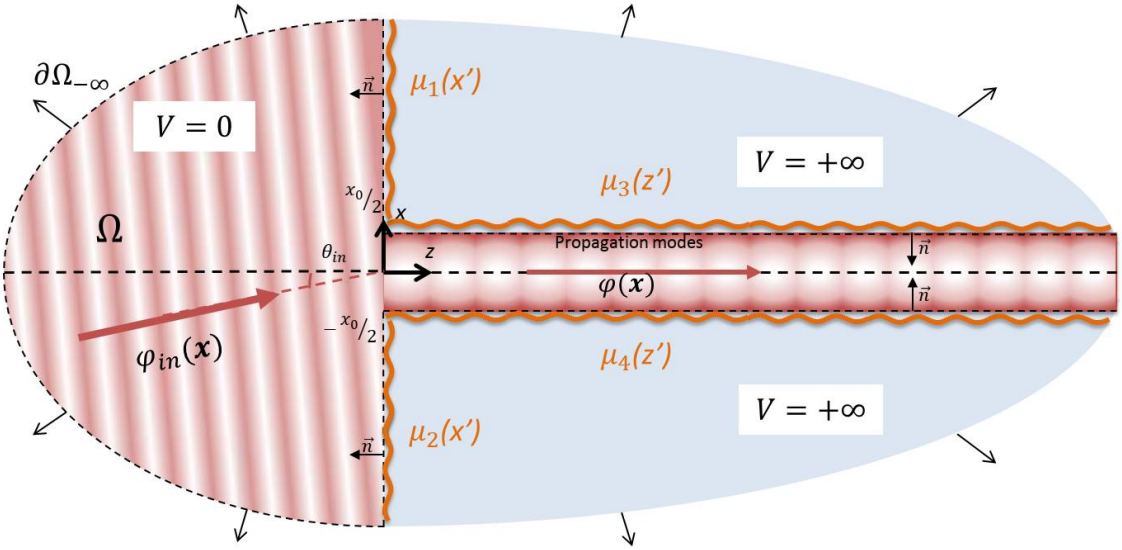

Figure 3.4: Schematic representation of the semi-infinite ideal waveguide with infinitely repulsive potential in the clad

Let us set an ideal semi-infinite film waveguide as our region of interest, Ω (see Figure 3.4). This region has an aperture x_0 along the x-axis and centred at the origin of coordinates. The waveguide extends along the z-axis, parallel to it, from $z = 0$ to $z \to +\infty$. The potential inside and along the guide is assumed to be $V(\bar{x}) = 0$ ($b\rho = 0$, i.e.: no material or air) as well as in the zone of incidence $z < 0$. The clads of the waveguide, say the regions $x \geqslant \frac{x_0}{2}$, $z \geqslant 0$ and $x \leqslant \frac{-x_0}{2}$, $z \geqslant 0$ are assumed to be an infinite ideal repulsive potential $V(\bar{x}) = \infty$. This geometry defines four boundaries, $\partial\Omega_i$, $i = 1 \cdots 4$, on the waveguide; $(x \geqslant \frac{x_0}{2}, z = 0)$, $(x \leqslant -\frac{x_0}{2}, z = 0$, $(x = \frac{x_0}{2}, z \geqslant 0)$ and $((x = -\frac{x_0}{2}, z \geqslant 0)$, respectively (see Figure 3.4). We assume an incoming plane neutron beam, with energy E, striking the aperture from $z \to -\infty$ in the form of $\varphi_{in}(x, z) = e^{ik_{in,x}x} e^{ik_{in,z}z}$ with $k_{in}^2 = k_{in,x}^2 + k_{in,z}^2 = \frac{2mE}{\hbar^2}$. The total wavefunction by

means of Eq.(3.5), for $z > 0$ (and for $z < 0$, as well), $-\frac{x_0}{2} \leqslant x \leqslant \frac{x_0}{2}$ is

$$\begin{aligned}\varphi(\bar{x}) = \varphi_{in}(\bar{x}) \quad & - \int_{\frac{x_0}{2}}^{\infty} dx' \left.\frac{\partial G(x-x', z-z')}{\partial z'}\right|_{z'=0} \mu_1(x') - \\ & - \int_{-\infty}^{-\frac{x_0}{2}} dx' \left.\frac{\partial G(x-x', z-z')}{\partial z'}\right|_{z'=0} \mu_2(x') - \\ & - \int_{0}^{\infty} dz' \left.\frac{\partial G(x-x', z-z')}{\partial x'}\right|_{x'=+\frac{x_0}{2}} \mu_3(z') - \\ & + \int_{0}^{\infty} dz' \left.\frac{\partial G(x-x', z-z')}{\partial x'}\right|_{x'=+\frac{x_0}{2}} \mu_4(z') \end{aligned} \tag{3.35}$$

By introducing the definition for the Green's function in Eq.(3.7) and solving applying the residues theorem (see Eqs.(3.19) and (3.20)), Eq.(3.35) yields

$$\begin{aligned}\varphi(\bar{x}) = \varphi_{in}(\bar{x}) \quad & - \int_{\frac{x_0}{2}}^{\infty} dx' \mu_1(x') \frac{2m}{\hbar^2}\frac{1}{2}\int_{-\infty}^{+\infty} \frac{dK'_x}{2\pi} e^{iK'_x(x-x')} e^{iz\sqrt{\frac{2mE}{\hbar^2}-K'^2_x}} - \\ & - \int_{-\infty}^{-\frac{x_0}{2}} dx' \mu_2(x') \frac{2m}{\hbar^2}\frac{1}{2}\int_{-\infty}^{+\infty} \frac{dK'_x}{2\pi} e^{iK'_x(x-x')} e^{iz\sqrt{\frac{2mE}{\hbar^2}-K'^2_x}} + \\ & + \int_{0}^{\infty} dz' \mu_3(z') \frac{2m}{\hbar^2}\frac{1}{2}\int_{-\infty}^{+\infty} \frac{dK'_z}{2\pi} e^{iK'_z(z-z')} e^{-i\left(x-\frac{x_0}{2}\right)\sqrt{\frac{2mE}{\hbar^2}-K'^2_z}} + \\ & + \int_{0}^{\infty} dz' \mu_4(z') \frac{2m}{\hbar^2}\frac{1}{2}\int_{-\infty}^{+\infty} \frac{dK'_z}{2\pi} e^{iK'_z(z-z')} e^{i\left(x+\frac{x_0}{2}\right)\sqrt{\frac{2mE}{\hbar^2}-K'^2_z}} \end{aligned} \tag{3.36}$$

Notice the sign of the vector normal to each boundary according to Figure 3.4. Notice that since $k^2_{in} = k^2_{in,x} + k^2_{in,z} = \frac{2mE}{\hbar^2}$, there is a constraint in the magnitude of certain exponentials when we perform the integration over the corresponding wavevector (K'_x or K'_z). Consequently, those values such that $K'_x > \sqrt{\frac{2mE}{\hbar^2}}$ and so for K'_z imply evanescent waves.

It is physically acceptable to suppose that the main expected phenomena are: reflection of a part of the incoming wave for $z < 0$, extinction of the incoming wave and penetration of propagation modes of the wave along the aperture for $z > 0$, for adequately large E. Thus, generation of certain diffraction of the incoming wave by the finite aperture (the waveguide entrance) arises. This will be taken into account by means of the appropriate choice of values $\mu_1(x')$, $\mu_2(x')$, $\mu_3(z')$ and $\mu_4(z')$, respectively, for adequately large E.

The terms associated to $\mu_1(x')$ and $\mu_2(x')$, in Eq.(3.36), help to define the opening of the waveguide. These terms will act, mostly, by extinguishing $\varphi_{in}(\bar{z})$ and generating a diffracted wave that will propagate. In Section 3.2.3, we have already dealt with this case by imposing Eq.(3.30) for these auxiliary function. This choice for $\mu_1(x')$ and $\mu_2(x')$ is consistent with the conservation of the probability flux along the z-axis, as outlined in Section 3.3. It is also consistent with total

reflection in $z < 0$, for $x > 0$ and large (for $\mu_1(x')$) and $x < 0$ and large (for $\mu_2(x')$). Notice that, this time, the vector normal to the boundary points towards the opposite direction (i.e.: $z < 0$). In Section 3.2.3 we have shown the extinction of the wave and how at long enough propagation distances, z, these terms vanish. However, on this occasion these terms cannot be neglected in the latter equations since they will not lead to cancellation of the incoming wave.

In search of feasible approximate physical solutions, we shall modify the auxiliary functions $\mu_3(z')$ and $\mu_4(z')$ used in Section 3.2.2 (named as $\mu_\pm(z')$) by introducing a term to cancel out the incoming wave

$$\mu_{3,4}(z') = \frac{\hbar^2}{2m}\left(-e^{ik_{in,z}z'} + \mu_\pm e^{iqz'}\right) \tag{3.37}$$

where, as in Section 3.2.2, $\mu_\pm$ are suitable normalization constants to be evaluated later and q is an arbitrary spatial frequency. The first term will contribute (at least partially) to cancel out the incident wave (extinction) and the second one will represent the propagation modes in the guide, once its wavevector q be determined by imposing Dirichlet boundary conditions. The fourth and fifth terms in Eq.(3.36) will generate both the confinement in the wave as well as the extinction of the incoming wave. In a more general ansatz, in the right-hand side of Eq.(3.37) one should write a sum of terms under the form $\mu_\pm e^{iqz'}$ (different q's with different $\mu_\pm$ depending on q).

Wave confinement for $z > 0$ adequately larger than x_0

Since those terms associated to $\mu_1(x')$ and $\mu_2(x')$ have already been discussed in Section 3.2.3, we will focus on interpreting physically the terms associated with $\mu_3(z')$ and $\mu_4(z')$. Specifically, we will consider the following term arising from inserting Eq.(3.37) in the fourth term in Eq.(3.36) (only the term associated with the propagation modes)

$$\int_{-\infty}^{+\infty} \frac{dK'_z}{2\pi}\left[\int_0^\infty dz' e^{iqz'}e^{-iK'_z z'}\right] e^{iK'_z z} e^{-i\left(x-\frac{x_0}{2}\right)\sqrt{\frac{2mE}{\hbar^2}-K'^2_z}} \tag{3.38}$$

the same arguments apply trivially for the fifth term.

The inner integral is indeed a Fourier transform, denoted by $\mathcal{F}$, of the product of a Heaviside step function, $step(z')$ and $e^{iqz'}$

$$\begin{aligned}\int_0^\infty dz' e^{iqz'}e^{-iK'_z z'} &= \mathcal{F}\left[step(z')\right]_{K'_z - q} \\ &= \pi\left[\frac{1}{i\pi\left(K'_z - q\right)} + \delta\left(K'_z - q\right)\right]\end{aligned} \tag{3.39}$$

where p.v. denotes Cauchy principal value.

Notice that the Dirac delta function would be obtained in the case of performing the integral from $-\infty$ to ∞ (i.e.: if the waveguide would be infinite). Consequently, the term $\frac{1}{i\pi\left(K_z'-q\right)}$ arises from having a semi-infinite (say an initial aperture) waveguide at $z=0$. We will pay attention to it, introducing this term in Eq.(3.38)

$$\text{p.v.}\int_{-\infty}^{+\infty}\frac{dK_z'}{2\pi}\frac{e^{iK_z'z}}{i\left(K_z'-q\right)}e^{-i\left(x-\frac{x_0}{2}\right)\sqrt{\frac{2mE}{\hbar^2}-K_z'^2}} \tag{3.40}$$

We notice that this equation is the Hilbert Transform of the product of two exponential functions, the Hilbert transform being defined by using the Cauchy principal value.

For simplicity, we will denote $f\left(K_z'\right)=e^{iK_z'z}$ and $g\left(K_z'\right)=e^{-i\left(x-\frac{x_0}{2}\right)\sqrt{\frac{2mE}{\hbar^2}-K_z'^2}}$. So, Eq.(3.40) turns out to be

$$\text{p.v.}\int dK_z'\frac{1}{i2\pi}\frac{f\left(K_z^{'}\right)g\left(K_z^{'}\right)}{K_z'-q}=\frac{1}{2i}\mathcal{H}\left[f\left(K_z^{'}\right)g\left(K_z^{'}\right)\right]_q \tag{3.41}$$

here, $\mathcal{H}$ denotes the Hilbert transform operator [90], [91].

We remind here some useful properties of this transform. Let $f\left(K_z^{'}\right)$ and $g\left(K_z^{'}\right)$ be complex functions in the $L^2\left(-\infty,\infty\right)$ space of the real variable K_z' and let both $f\left(K_z^{'}\right)$ and $g\left(K_z^{'}\right)$ be analytic functions of K_z'. Then, by applying Bedrosian's product theorem for Hilbert transforms [92]

$$\mathcal{H}\left[f\left(K_z^{'}\right)g\left(K_z^{'}\right)\right]_q=f\left(q\right)\mathcal{H}\left[g\left(K_z^{'}\right)\right]_q=g\left(q\right)\mathcal{H}\left[f\left(K_z^{'}\right)\right]_q \tag{3.42}$$

$$\mathcal{H}\left[cos\left(K_z^{'}\right)\right]_q=-sin\left(qz\right) \tag{3.43}$$

$$\mathcal{H}\left[sin\left(K_z^{'}\right)\right]_q=cos\left(qz\right) \tag{3.44}$$

Then, combining Eqs.(3.38) to (3.44) one has

$$\begin{aligned}\int_{-\infty}^{+\infty}\frac{dK_z'}{2\pi}\left[\int_0^{\infty}dz'e^{iqz'}e^{-iK_z'z'}\right]e^{iK_z'z}e^{-i\left(x-\frac{x_0}{2}\right)\sqrt{\frac{2mE}{\hbar^2}-K_z'^2}}=\\ =e^{iqz}e^{-i\left(x-\frac{x_0}{2}\right)\sqrt{\frac{2mE}{\hbar^2}-q^2}}\end{aligned} \tag{3.45}$$

An analogous reasoning for the boundary $x=-\frac{x_0}{2}$, $z>0$, yields

$$e^{iqz}e^{i\left(x-\frac{x_0}{2}\right)\sqrt{\frac{2mE}{\hbar^2}-q^2}} \tag{3.46}$$

From this and the following analysis, it should be clear that these terms will be the ones that will give rise to propagation modes.

Extinction conditions

In the approximate formulation exposed, we can combine the obtained results in Eq.(3.45) and Eq.(3.46) following from the ansatz for the auxiliary functions (i.e.: $\mu_1(x') = \mu_2(x') = -\frac{\hbar^2}{m} e^{ik_{in,x}x'}$ and $\mu_{3,4}(z') = \frac{\hbar^2}{2m}\left(-e^{ik_{in,z}z'} + \mu_{\pm} e^{iqz'}\right)$). The approximation for the whole Eq.(3.36) reads

$$\begin{aligned}\varphi(x,z) =& \varphi_{in}(x,z) + e^{ik_{in,x}x} e^{ik_{in,z}z} - \\ &- e^{ik_{in,z}z}\left[e^{-ik_{in,x}\left(x-\frac{x_0}{2}\right)} + e^{ik_{in,x}\left(x+\frac{x_0}{2}\right)}\right] + \\ &+ e^{iqz}\left[\mu_+ e^{-i\left(x-\frac{x_0}{2}\right)\sqrt{\frac{2mE}{\hbar^2}-q^2}} + \mu_- e^{i\left(x+\frac{x_0}{2}\right)\sqrt{\frac{2mE}{\hbar^2}-q^2}}\right]\end{aligned} \tag{3.47}$$

If $k_{in,x} = 0$ or if $k_{in,x}x_0 \ll 1$ (normal or close to normal incidence, respectively) one has an approximate extinction of incoming wave and the second term in the right hand side with the third term, for $-x_0/2 < x < x_0/2$. Equation (3.47) reads then

$$\varphi(x,z) \approx + e^{iqz}\left[\mu_+ e^{-i\left(x-\frac{x_0}{2}\right)\sqrt{\frac{2mE}{\hbar^2}-q^2}} + \mu_- e^{i\left(x+\frac{x_0}{2}\right)\sqrt{\frac{2mE}{\hbar^2}-q^2}}\right] \tag{3.48}$$

which is ready to discuss propagation modes for $z \gg 0$, with a wavevector that must obey the constraint $\bar{q} = (q_x, q_z) = \left(\sqrt{\frac{2mE}{\hbar^2} - q^2}, q\right)$. If $k_{in,x}x_0 \ll 1$ does not hold, then, there is no such extinction in the framework of our approximations. Physically, as propagation modes are excited for adequately large E they are, therefore, the only remaining contributions for deep penetration into the waveguide. The incoming wave has to cancel out there exactly with certain contributions added to the above approximations to the auxiliary functions, $\mu_1(x')$, $\mu_2(x')$, $\mu_3(z')$ and $\mu_4(z')$, and according to Eq.(3.36). Such an exact extinction operates outside our approximations.

As in Section 3.2.2, we can obtain those allowed values of the wavevector $\bar{q}$ by imposing in Eq.(3.48) the fulfilment of Dirichlet conditions at $x = \pm\frac{x_0}{2}$ for a particular wavevector $\bar{q}$. It is trivial to notice that the imposition of these boundary conditions provides odd and even propagation modes in

$$\varphi(x,z) = \begin{cases} -i\ sin\left(\frac{2\pi n x}{x_0}\right) e^{iz\sqrt{\frac{2mE}{\hbar^2} - \left(\frac{2\pi n}{x_0}\right)^2}} & \text{for odd modes} \\ cos\left(\frac{(2n+1)\pi x}{x_0}\right) e^{iz\sqrt{\frac{2mE}{\hbar^2} - \left(\frac{(2n+1)\pi n}{x_0}\right)^2}} & \text{for even modes} \end{cases} \tag{3.49}$$

with $n \in \mathbb{N}$.

As expected, and, assuming large z propagation, they bear the form $cos(\chi_n x)\, e^{iqz}$ for even modes and $sin(\chi_n x)\, e^{iqz}$ for odd modes. For a given neutron incoming wave with $E > 0$, the waveguide allows all propagation modes such that $\chi^2 \leqslant \frac{2mE}{\hbar^2}$.

Thus, for an incoming plane wave with a fixed energy $E = \frac{\hbar^2}{2m}k_{in}^2$ the highest order mode achievable is a function of the guide aperture and the incoming energy.

By taking into account that both even and odd modes are allowed, the total number of modes in the waveguide will be approximately, twice the highest integer n that generates a propagation mode:

$$N_{max} = \frac{x_0}{\pi}\sqrt{\frac{2mE}{\hbar^2}} \tag{3.50}$$

Figure 3.5 shows the result of the maximum number (N_{max}) of modes allowed in these waveguides as a function of the neutron incoming energy, E, and the aperture (x_0)

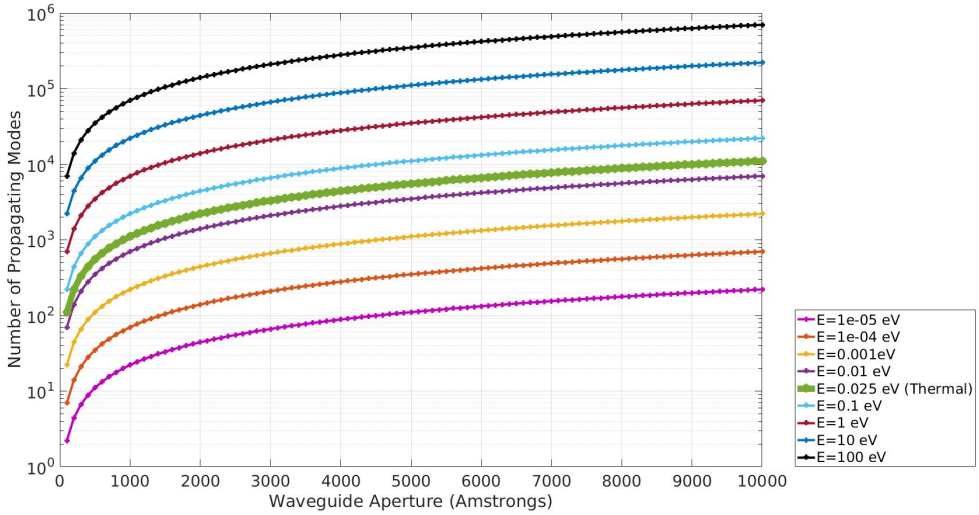

Figure 3.5: Number of allowed propagation modes in waveguides having clad with infinite repulsive potential

Distribution of spatial frequencies

If $k_{in,x}x_0 \ll 1$ does not hold, our approximate treatment is not applicable but we can analyse the relative weight of each propagation mode arising from $k_{in} \neq 0$. We performed numerical computations enabling to calculate those weighting factors (the spectral distribution of the propagation modes) by adapting Eq(3.47) to the quantum-mechanical approximation performed by Snyder and Love [6] (see Section 2.5). For brevity, we shall omit computational details. In Figure 3.6, we show the results as a function of the angle of the transverse wavevector $\chi = \sqrt{k_{in}^2 - q^2}$ for an incident wave of $E = 0.025$ eV.

After Figure 3.6 results, the weighting factors have a maximum peak at an angle coinciding with the incidence angle of the incoming neutron wavevector. Indeed, most of the energy is carried along the waveguide with an angle similar to the one

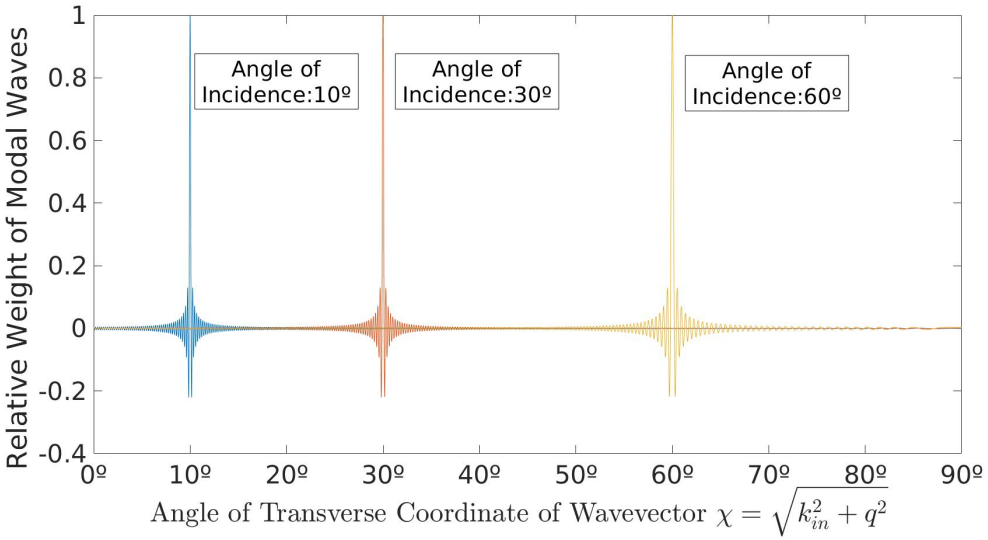

Figure 3.6: Relative weight factor distribution for three values of the angle of incidence

of the incoming wave (in connection with what would be expected in geometrical refractive optics). Moreover, there is some spread in the distribution of the incoming energy for other frequencies: the closest the value to the angle of the incident wave the higher the contribution. In an ideal case (i.e. no waveguide) the consistent result would be a delta function and thus, the incoming wave remaining unaltered. The spreading shape of the wavefunction spatial frequencies is the expected physical behaviour due to the waveguide clad.

Critical angle

In Section 2.1, we stated the critical angle as a critical parameter for correctly describing a waveguide (see Eq.(2.3)). In this case, since we are supposing an ideal waveguide with infinite repulsive potential in the clad (i.e.: Dirichlet boundary conditions) one expects that the critical angle will be almost $\theta_{cr} = \frac{\pi}{2}$, that is, the waveguide allows almost any incident angle for incoming neutrons. In fact, the incident angle can be expressed as

$$sin\phi = \frac{k_{in,x}}{\sqrt{k_{in,x}^2 + k_{in,z}^2}} = \frac{k_{in,x}}{\sqrt{\frac{2mE}{\hbar^2}}} \tag{3.51}$$

In Eq.(3.51) any possible $k_{in,x}$ gives rise to a possible χ_n value (both even and odd modes), with $\chi_n^2 \leqslant \frac{2mE}{\hbar^2}$, $n = 1 \cdots \frac{N_{max}}{2}$, approximately. It would mean that the largest allowed $k_{in,x}$ would correspond to $n = \frac{N_{max}}{2}$ and, so

$$sin\phi_{max} = \frac{max\left(k_{in,x}\right)}{\sqrt{\frac{2mE}{\hbar^2}}} = \frac{\frac{2\pi N_{max}/2}{x_0}}{\sqrt{\frac{2mE}{\hbar^2}}} = \frac{\pi N_{max}}{x_0\sqrt{\frac{2mE}{\hbar^2}}} \tag{3.52}$$

By substituting according to Eq.(3.50)we obtain: $sin\phi_{max} = 1 \Rightarrow \phi_{max} \sim \frac{\pi}{2}$. This is consistent with the above expectation.

3.3 Conservation of Probability Current

In this section, we will check the consistency of our formulation by demonstrating that the quantum-mechanical probability is conserved. The quantum-mechanical probability current along z is, for $z < 0$ and $z > 0$

$$J_z(x,z) = \frac{i\hbar}{2m}\left[\varphi(x,z)\frac{\partial\varphi^*(x,z)}{\partial z} - \varphi^*(x,z)\frac{\partial\varphi(x,z)}{\partial z}\right] \tag{3.53}$$

where $\varphi^*(x,z)$ denotes complex conjugate of $\varphi(x,z)$.

Conservation of the probability current along z, for any x reads $\frac{\partial}{\partial z}J_z(x,z) = 0$. It follows that the total probability flux across the whole x-axis, namely $\int_{-\infty}^{\infty} dx J_z(x,z)$ is constant (independent of z). Then, as $\varphi(x,z)$ vanishes in the clad

$$\int_{-\infty}^{\infty} dx\ J_z(x,z)|_{z\to-\infty} = \int_{-\frac{x_0}{2}}^{\frac{x_0}{2}} dx\ J_z(x,z)|_{z\to+\infty} \tag{3.54}$$

Notice that $\int_{-\frac{x_0}{2}}^{\frac{x_0}{2}} dx\ J_z(x,z)|_{z\to+\infty}$ equals to the contribution of the propagation modes, provided that they be excited, otherwise that integral vanishes. We now turn to $\int_{-\infty}^{\infty} dx\ J_z(x,z)|_{z\to+\infty}$ In order to evaluate the latter, we shall consider Eq.(3.36), trivially for $z < 0$. The contributions of the fourth and fifth terms (associated to $\mu_3(z')$ and $\mu_4(z')$) for $z \to -\infty$ are physically expected to vanish. Moreover, the latter can be easily invoked to vanish, by virtue of the Riemann-Lebesgue lemma, [89]. On the other hand, the second and third term contributions, in Eq.(3.36), for $z \to -\infty$ are given by

$$\int_{-\infty}^{+\infty} \frac{dK_x^{'}}{2\pi} e^{iK_x^{'}x} e^{-iz\sqrt{\frac{2mE}{\hbar^2} - K_x^{'2}}}\, g_1\left(K_x^{'}\right) \tag{3.55}$$

where $g_1\left(K_x^{'}\right) = \frac{2m}{\hbar^2}\frac{1}{2}\left[\int_{x_0/2}^{\infty} dx'\mu_1(x')\, e^{-iK_x^{'}x'} + \int_{-\infty}^{-x_0/2} dx'\mu_2(x')\, e^{-iK_x^{'}x'}\right]$

The direct integration over K_x' is now carried out only over the finite interval in which $0 < \frac{2me}{\hbar^2} - K_x^{'2}$. A direct computation shows that

$$\int_{-\infty}^{\infty} dx\ J_z(x,z)|_{z\to-\infty} =$$
$$= \frac{k_{in,z}\hbar}{m}\int_{-\infty}^{\infty} dx - \frac{\hbar}{m}\int_{-\infty}^{+\infty} \frac{dK_x^{'}}{2\pi}\sqrt{\frac{2mE}{\hbar^2} - K_x^{'2}}\, g_1^*\left(K_x^{'}\right) g_1\left(K_x^{'}\right) \tag{3.56}$$

Again, the integration over K_x' being also carried out only over the finite interval in which $0 < \frac{2me}{\hbar^2} - K_x^{'2}$. Notice that $\int_{-\infty}^{\infty} dx$ in Eq.(3.56) is a divergent integral (which accounts for the infinite probability flux of the incoming plane wave $\varphi_{in}(x,z)$ across the whole x-axis). However, it is exactly cancelled by a completely similar divergent contribution (due to the infinite probability flux of the reflected plane wave), contained in $\frac{\hbar}{m}\int_{-\infty}^{+\infty}\frac{dK_x^{'}}{2\pi}\sqrt{\frac{2mE}{\hbar^2} - K_x^{'2}}\, g_1^*\left(K_x^{'}\right) g_1\left(K_x^{'}\right)$. In fact, approximating

$\mu_1(x) = \mu_2(x) \sim -\varphi_{in}(x,0)$ for $x \gg \frac{x_0}{2}$ and $x \ll -\frac{x_0}{2}$ respectively (i.e.: total reflection) and approximating the sum of $\int_{\frac{x_0}{2}}^{\infty} dx'$ and $\int_{-\infty}^{-\frac{x_0}{2}} dx'$ by $\int_{-\infty}^{\infty} dx'$ as in Eq.(3.31) (neglecting the second term) one has

$$g_1\left(K_x^{'}\right) \simeq \int_{-\infty}^{\infty} dx' e^{ix'\left(k_{in,x}-K_x^{'}\right)} = -2\pi\delta\left(k_{in,x}-K_x^{'}\right)$$

$$\Rightarrow \int_{-\infty}^{+\infty} \frac{dK_x^{'}}{2\pi} e^{iK_x^{'}x} e^{-iz\sqrt{\frac{2mE}{\hbar^2}-K_x^{'2}}} g_1\left(K_x^{'}\right) = -e^{ixk_{in,x}} e^{-izk_{in,z}} \tag{3.57}$$

$$\Rightarrow \frac{\hbar}{m}\int_{-\infty}^{+\infty} \frac{dK_x^{'}}{2\pi}\sqrt{\frac{2mE}{\hbar^2}-K_x^{'2}}\, g_1^*\left(K_x^{'}\right) g_1\left(K_x^{'}\right) \approx \sqrt{\frac{2mE}{\hbar^2}-k_{in,x}^2}\int_{-\infty}^{\infty} dx' \tag{3.58}$$

which leads to the cancellation of the divergent term $\frac{k_{in,x}\hbar}{m}\int_{-\infty}^{\infty} dx$ in Eq.(3.56).

The net outcome is that both sides of Eq.(3.54) are finite. The left-hand side of this equation describes finite corrections to total reflection. The resulting Eq.(3.54), after the cancellation of divergences, turns out to represent the actual counterpart for semi-infinite waveguides with Dirichlet boundary conditions, of the standard optical theorem in scattering theory (see [93]).

Que me zurzan si la entrada no está
oculta tras un holograma.

Planetary

4

Simulation Algorithm For Dirichlet Boundary Conditions

Contents

In previous Chapter 3 we presented a new mathematical approach, based on Green's functions and Dirichlet boundary conditions, that allowed us to draw some physical conclusions about the behaviour of waveguides.

In this Chapter, we will interpret the physical meaning of Eq.(3.16) to propose an iterative algorithm with the aim of calculating numerically the total wavefunction, Eq.(3.5). This approach is a huge improvement in comparison with previous simulation methods. First of all, we will not be constrained because of the neutron beam wavelength and, so, the simulation grid (i.e.: Ω) may have sufficiently spaced points (memory load). Secondly, since we only have to calculate the auxiliary

functions, $\mu_i(\boldsymbol{x_i})$, we reduce one dimension the problem to solve (computation time). Since Fourier transforms are involved, we can calculate them by using Fast Fourier Transform (FFT).

We will show our detailed numerical simulations for several thermal neutron beam diffraction cases, including some related with the experiments stated in Section 1.3.1. Here, we shall focus on the confined propagation of a beam of thermal neutrons (with $E = 0.025$ eV and $\lambda_{db} = 1.8$ Å) in regions, Ω with transversal dimensions of the order of 100 nm and propagation lengths of the order of μm (longer propagation distances could also be considered). In these cases, we set the potential to be: (i) that of vacuum, $V(\boldsymbol{x}) = 0$, inside the waveguide and outside it and (ii) $V(\boldsymbol{x}) = +\infty$ in the clad (i.e.: Dirichlet boundary conditions). The results are half way between geometrical optics, since some of our simulations show a geometrical ray reflecting on a wall, the waveguide's clad, etc, and wave description, since diffraction effects are clearly visible.

This chapter is based on the results and conclusions published in *Applied Mathematical Modelling* [94].

4.1 Iterative Algorithm

In Chapter 3 we stated that, given a particular region of interest, Ω, the propagating wavefunction may be described by Eq.(3.5). If this region of interest is limited by a number, n, of surfaces obeying Dirichlet boundary conditions, Eq.(3.16) sets the conditions for calculating the auxiliary functions $\mu_i(\boldsymbol{x})$.

Notice, as we have already stated, that the Green's functions involved are locally singular in the boundary where they are defined (see, for example Eq.(3.12)). The auxiliary function depends on the incoming wavefunction, $\varphi_{in}(\boldsymbol{x})$, and the other auxiliary functions, $\mu_j(\boldsymbol{x})$, but not on itself (i.e.: $\mu_i(\boldsymbol{x}) = f((\varphi_{in}(\boldsymbol{x}), \mu_j(\boldsymbol{x}))$, $j = 1...n$, $j \neq i$.

Having this condition in mind, it is quite straightforward to interpret Eq.(3.16) in terms of the total wavefunction, by using Eq.(3.5)

$$\begin{aligned}\frac{2m}{\hbar^2}\frac{1}{2}\mu_i(\boldsymbol{x}) =& \varphi_{in}(\boldsymbol{x}) + \sum_{j=1, i\neq j}^{n} \int_{\partial\Omega_j} d\boldsymbol{x_j'} \left.\frac{\partial G\left(\boldsymbol{x}-\boldsymbol{x_j'}\right)}{\partial \boldsymbol{n_j}}\right|_{\boldsymbol{x_j'}\in\partial\Omega} \mu_j\left(\boldsymbol{x_j'}\right) = \\ &= -\varphi(\boldsymbol{x})|_{\boldsymbol{x}\in\partial\Omega_i}\end{aligned} \tag{4.1}$$

In other words, in order to fulfil the Dirichlet conditions, the value for the auxiliary function defined on the boundary, $\partial\Omega_i$, corresponds to the value of the total wavefunction impinging the boundary with a phase change of π. This seems physically acceptable and quite useful upon proceeding to the extinction theorem, since the total value of the wavefunction as the boundary is approached must be 0.

This result implies that one can use a previously computed value for the total wavefunction to set a value for the auxiliary functions in the boundaries and, step by step, come closer to the numerical solution. We shall set our algorithm to update the value of the corresponding auxiliary functions, $\mu_i(\boldsymbol{x})$, in Eq.(3.5). In Section 4.2.4 we will interpret the physical meaning of these updates as multiple reflections (see Figure 4.7).

Once characterized the auxiliary functions, $\mu_i(\boldsymbol{x})$, one has to implement them in the wavefunction equation, Eq.(3.5). We need to achieve a further improvement of the method, since right now it involves computing integrals of oscillating functions along infinite intervals, which is tricky, takes long time to converge, and can lead to numerical errors (we recall here the computational problems that arose by numerically solving Eq.(3.33), see Figure 3.3).

Nevertheless, our method has an additional advantage: If one pays attention to the structure of equations that arise from the use of the Green's function, $\frac{\partial G(\boldsymbol{x}-\boldsymbol{x_j'})}{\partial \boldsymbol{n_j}}$, one realizes that, in fact, each integral associated to each boundary may be interpreted as a Fourier transform (as we already stated in Section 3.2).

It is easier to prove it with an example for a specific geometry. A generic demonstration will lead to the same conclusion, but it is more cumbersome. Let us consider the specific geometry used in Section 3.2.1, in Eq.(3.21). In that case, we made use of the result established in Eq.(3.19) (i.e.: integration by residues of Green's functions) and the integral in Eq.(3.5). The integral involving Green's function, associated to this boundary can be interpreted as

$$
\begin{aligned}
-\int_{-\infty}^{\infty} dx' \left.\frac{\partial G(x-x',z-z')}{\partial z'}\right|_{z'=0} \mu(x') = \\
= \frac{2m}{\hbar^2}\frac{1}{2}\int_{-\infty}^{+\infty}\frac{dK_x'}{2\pi}\left[\int_{-\infty}^{\infty} dx' \mu(x') e^{-iK_x'x'}\right] e^{iK_x'x} e^{-iz\sqrt{\frac{2mE}{\hbar^2}-K_x'^2}} = \\
= \frac{2m}{\hbar^2}\frac{1}{2}\int_{-\infty}^{+\infty}\frac{dK_x'}{2\pi}\mathcal{F}[\mu(x')] e^{iK_x'x} e^{-iz\sqrt{\frac{2mE}{\hbar^2}-K_x'^2}}
\end{aligned}
\tag{4.2}
$$

where $\mathcal{F}[\mu(x')]$ stands for the Fourier transform of the auxiliary function, $\mu(x')$. Notice this transform is a function on the variable $K_x^{'}$. We have omitted that variable to avoid confusion with notation.

Thus, the integrals proposed in Eq.(3.5) can be interpreted as the Fourier transform of the corresponding auxiliary function (its spectral decomposition) and subsequently propagated (for each spatial frequency) through the term $e^{-iz\sqrt{\frac{2mE}{\hbar^2}-K_x'^2}}$ and again reconstructed through the inverse Fourier transform. Note that, in the case that the boundary limits would not be $(-\infty,+\infty)$, as in Eq.(4.2), those limits can be introduced in the definition of the auxiliary function by using appropriate window and step functions, [7]. The definition and use of these Fourier transforms bypasses the problem of computing infinite integrals of oscillating functions since

these transforms can be computed by using FFT [15]. We will pay attention to this advantage in Section 4.1.1.

In this way, we present the following simulation algorithm: Let a mesh be defined in an arbitrary region Ω where a set of n boundaries obeying Dirichlet conditions are imposed, $\partial\Omega_i$. The method consists on the following steps:

Step 1: Compute the values of the incident wave, $\varphi_{in}(\boldsymbol{x})$ both in each point of the defined mesh, Ω, and in each point of the defined boundaries, $\partial\Omega_i$. Notice that the mesh resolution defined for Ω may not be the same of $\partial\Omega_i$.

Step 2: Use the values of $\varphi_{in}(\boldsymbol{x})$ computed over the boundaries in step 1, where Dirichlet conditions are imposed, to calculate the corresponding auxiliary functions, $\mu_i\left(\boldsymbol{x_i'}\right)$. Initially, the complex value for each point of the auxiliary functions, $\mu_i\left(\boldsymbol{x_i'}\right)$, is proportional to the value of the incident wave by applying Eq.(4.1): $\mu_i(\boldsymbol{x_i'}) = -\frac{\hbar^2}{m}\varphi\left(\boldsymbol{x_i'}\right)$, where $\boldsymbol{x_i'} \in \partial\Omega_i$.[1]

Step 3: Perform the Fourier transform of each function $\mu_i\left(\boldsymbol{x_i'}\right)$ calculated in each boundary: $Y_i^{(n)}(\boldsymbol{K'}) = \mathcal{F}\left[\mu_i\left(\boldsymbol{x_i'}\right)\right](\boldsymbol{K'})$ where (n) stands for the number of the iteration. This step calculates the auxiliary functions in the wavevector (spatial frequency) domain. Notice that, since our method comes from the context of neutron optics, the wavevector relates with the neutron energy $\boldsymbol{K'^2} = \frac{2mE}{\hbar^2}$

Step 4: Propagate and integrate the obtained result, from each boundary, $\partial\Omega_i$, to the region of interest Ω according to Eq.(4.2) (or similar ones, depending on the geometry) by performing the inverse Fourier transform. Thus, the function propagated from the boundary, $\partial\Omega_i$, to an arbitrary point in Ω is $\Lambda_i^{(n)}(\boldsymbol{x}) = \mathcal{F}^{-1}\left[Y_i^{(n)}(\boldsymbol{K'})\, e^{i\boldsymbol{K'}\left(\boldsymbol{x}-\boldsymbol{x_i'}\right)}\right](\boldsymbol{x})$. Note that the wavevector $\boldsymbol{K'}$ has one dimension less than the vector $\boldsymbol{x}$ since it arises from the Fourier transform of the auxiliary function, $\mu_i\left(\boldsymbol{x_i'}\right)$, that is constrained to the boundary, $\partial\Omega_i$. This constraint arises from the fact that $\boldsymbol{K'}$ must obey that $\boldsymbol{K'^2} = \frac{2mE}{\hbar^2}$. This condition is set by the chosen boundary. For example, if a boundary is a plane parallel to y and z axis and located at $x = a$, $\boldsymbol{K'}\left(\boldsymbol{x} - \boldsymbol{x_i'}\right)$ would be $(x-a)\sqrt{\frac{2mE}{\hbar^2} - K_y'^2 - K_z'^2} + K_y'y + K_z'z$.

Step 5: Compute a new updated solution for the wavefunction by adding the functions propagated from each boundary, $\partial\Omega_i$ with the incident wave: $\varphi^{(n+1)}(\boldsymbol{x}) = \varphi_{in}(\boldsymbol{x}) + \sum_i \Lambda_i(\boldsymbol{x})$

[1] Notice that, since $\partial\Omega_i$ is a boundary of Ω, $\boldsymbol{x_i'} \in \partial\Omega_i$ has one dimension less than $\boldsymbol{x}$, but we keep $\bar{x}$ as a notation for a vector where the y coordinate is neglected.

Step 6: Update auxiliary functions $\mu_i\left(\boldsymbol{x}_i'\right)$ for each boundary applying Eq.(4.1) by using the new wavefunction computed in previous step.

Step 7: Iterate the above steps 3 to 6, until convergence is achieved. That convergence may be defined at convenience (a total change in each iteration, a value of the total probability...).

We summarize this algorithm in Figure 4.1.

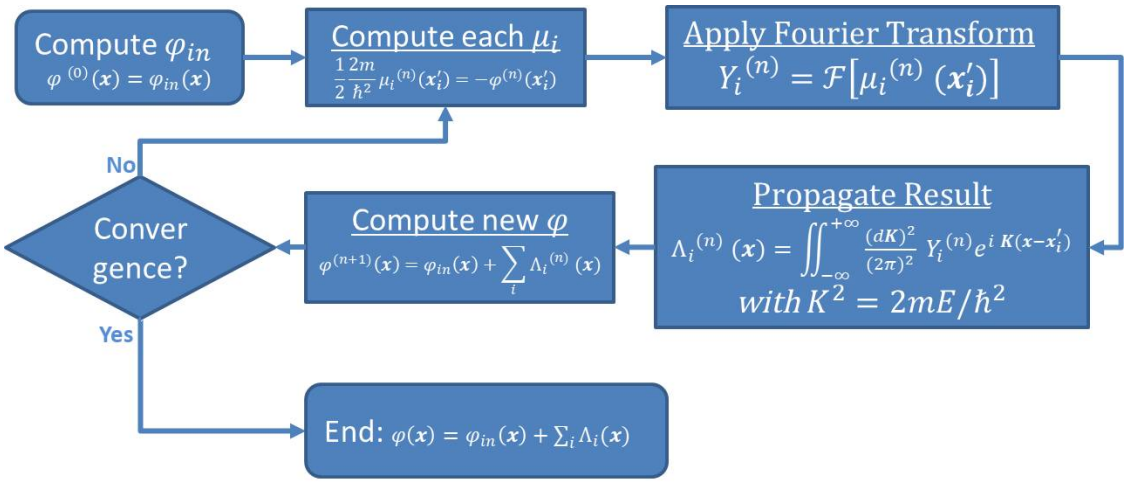

Figure 4.1: Dirichlet boundary conditions algorithm flux diagram

4.1.1 Characterization of the Algorithm

Once the method is set, we will remark some characteristics of this algorithm:

- As exposed in Step 2, this algorithm, before iterations, requires to know explicitly how the incident wave, $\varphi_{in}(\boldsymbol{x})$, impinges the boundaries. In the studied cases, this is trivial, but it could be tricky if one deals with more complex geometries (for instance, one wall shadowing another one). In some way, it implies that the researcher forces how the incoming wave spreads through the region Ω since, as we will show , each iteration is physically interpreted as a reflection of the total wave (see Figure 4.7). The mathematical method which is more accurate would consist in setting initial conditions by using extinction theorem, but we have not explored deeply this possibility, since the studied cases are trivial.

- Our algorithm reduces the amount of running time in comparison to most common numerical methods (i.e.: Finite Differences Methods, FDMs), since the former only deals with the wavefunction values on the boundaries, instead of in the whole region, Ω. Thus, it reduces the problem in one dimension.

- The method focuses on finding the values for the auxiliary functions, $\mu_i(\boldsymbol{x})$. Once these functions are known, the computation at each point is carried out independently for each point by means of Eq.(3.5). Thus, it has the advantage that the code allows trivially direct parallelization.

- In Section 2.3, we stated that one problem associated to FDMs is that the wavelength sets the computation step size to have a resolution 10 to 20 points per wavelength (see, for example [81]). Our method does not have that limitation since the wavelength information is carried by Green's function defined. The meshgrid can have any resolution and it is not required to simulate a high number of points for long propagation distances. Moreover, one can focus on a limited region instead of having to deal with the whole region, Ω (in the case of FDMs, one would have to compute a different grid resolution from scratch).

- Step 3 can be easily computed making use of FFT [15] algorithms available in any commercial mathematical package. Nevertheless, we do not choose any a priori method. FFT has well known advantages: running time (since it scales as $\mathcal{O}(n\log(n))$, [95], simplicity of implementation and accessibility and readiness to be used in many commercial packages.

  Certainly, there are other options for computing both Fourier and inverse Fourier transforms (with features such as a better control of frequencies, signal filtering, etc....). Since we focused in the characterization of the algorithm and not its optimization, we did not choose a particular method in Section 4.1.1. Anyway, in our simulations, we have used FFT algorithm in Step 3, but in Step 4 we have implemented two approaches depending on the case. In one approach, we implement the direct formulation through numerical integration and, in the second one, we implemented Step 4 as the inverse for the FFT algorithm (IFFT). Computation times are clearly in favour of the use of IFFT but, using both FFT and IFFT, wavefunction points are not calculated independently and, so, parallel calculations may not be performed. As a disadvantage, if, once computed with some resolution, one wants to focus on any region, the entire region, Ω, must be computed with a different grid resolution from scratch.

  In Appendix A we summarize the total computing time and memory load when using IFFT and numerical integration. It is clear that the first option has a better performance.

All these features become a great advantage in cases, such as neutron optics, where geometrical parameters are some orders of magnitude larger than wavelengths.

According to [96], this method could be regarded to fall on the category of a meshless, boundary-type method. Nowadays, there is an increasing demand

of this kind of methods to deal with an enormous variety of systems, in many branches of research where FDMs have been dominant. We shall remind here two recent and interesting approaches. Firstly, Generalized Finite Difference Methods (GFDM) stand as relatively new and promising methods: in particular, the Peridynamic Differential Operator (PDDO) method constitutes a new type of GFDM which enjoys certain specific advantages. Specifically, PPDO is capable to reduce differentiation operators to suitable integrations, which facilitates the imposition of boundary conditions and the handling of sharp boundaries. In [96, 97], PDDO has been applied to Helmholtz-type acoustic problems in 2D in bounded and unbounded domains, respectively.

In other methods, FDM, FDTD as well as GFDM and PDDO, if one wants to simulate an unbounded domain it is replaced by a finite one by means of an artificial (absorbing reflectionless) boundary. With the present method, this becomes trivial, since Sommerfeld radiation condition is already carried by the Green's function. One must neither define nor compute an auxiliary function in the unbounded direction.

The scope of this algorithm, even if developed in the context of neutron optics, goes beyond the neutron wave propagation by means of FFT. The relationships emerging here allow solving the problem in the entire space by performing only computations over the boundaries (thus, reducing one dimension the entire problem). In this case, the possibility of performing these computations using FFT is an additional improvement. The potentialities of this algorithm would be useful in any physical field involving wave equations in which geometrical dimensions are several orders of magnitude larger than the wavelength, making hard its computation based upon standard Finite Differences Methods.

4.1.2 Propagation VS Resolution

Our algorithm may be linked to signal theory as follows; for a given input signal, $\varphi_{in}(\boldsymbol{x})$, the algorithm calculates, as the boundary is approached, each of the auxiliary functions, $\mu_i\left(\boldsymbol{x_i'}\right)$, performs the decomposition into spatial frequencies and propagates them iteratively. Once convergence is achieved, the output signal (i.e.: $\varphi(\boldsymbol{x})$) solves the problem for this particular geometry with Dirichlet boundary conditions.

Since the algorithm is based upon performing the spectral analysis of the input signal (through Fourier transform), it is critical to have an adequate control of where are the high cut-off frequencies. It is intuitive that longer simulation time and higher resolution in spatial frequencies will require a higher number of points to compute (i.e. higher memory load and running time).

The spectral decomposition depends on the libraries that have been implemented regarding the program that is used. In our case, since we use MATLAB FFT libraries to perform our computations, an input array of N_p complex numbers, $\{x_n\} \equiv x_0, x_1, \cdots, x_{N_p-1}$ yields a discrete Fourier transform of N_p points with

spatial frequencies defined in the range $K \in \left[-\frac{N_p}{2}, \frac{N_p}{2}-1\right]$, for N_p an even number and $K \in \left[-\frac{N_p-1}{2}, \frac{N_p-1}{2}\right]$ for N_p an odd number.

In our code, our main parameter to be controlled is the highest spatial frequency, K_{max}, that must correspond to the value $\frac{N_p}{2}-1$. Since we simulate a waveguide, this parameter must be chosen to be larger than the incoming neutron wavevector, $K_{max} > k_{in} = \sqrt{\frac{2mE}{\hbar^2}}$. This allows all possible propagation modes to be computed. Nevertheless, this K_{max} must be carefully chosen since the integration over those modes with $K > k_{in}$ will give rise to evanescent modes that, due to the long propagation distances simulated, can be neglected in our set up without loss of precision.

One must correlate the array of complex numbers $\{x_n\}$ with the different spatial points, $\boldsymbol{x}$. In our case, a direct calculation shows that, once K_{max} is fixed, we deal with values of K (integration variable), and z (propagation distance) in the ranges

$$K \in \left[-\frac{N_p}{2}\frac{K_{max}}{\frac{N_p}{2}-1}, K_{max}\right] \tag{4.3}$$

$$z \in \left[-2\pi\frac{\frac{N_p}{2}\left(\frac{N_p}{2}-1\right)}{K_{max}\left(N_p-1\right)}, 2\pi\frac{\left(\frac{N_p}{2}-1\right)^2}{K_{max}\left(N_p-1\right)}\right] \tag{4.4}$$

Notice that the same relationship may be established for the transverse coordinates x and y with a different value of K_{max}. Since coordinates are independent of each other, one may define different ranges in propagation and spatial frequencies for longitudinal and transversal analysis. Notice as well that the range for K we have stated corresponds to an even value of N_p (calculations for the case of an odd value being trivial). We have always performed our simulations with an even value of K, because the FFT algorithm performs better with N_p chosen as a power of 2.

By inspecting Eq.(4.4), it is clear that the maximum propagation distance achievable with this algorithm and the maximum frequency to analyse are related between them and related, as well, to the number of points simulated. Consequently, for propagating a neutron beam with a defined wavevector, one may achieve longer distances only by increasing the number of points simulated for the auxiliary functions, $\mu_i\left(\boldsymbol{x_i'}\right)$ (as expected).

4.2 Numerical Simulations and Results

In this section we will show the power of the algorithm calculation through the resolution of some cases of increasing difficulty. In part, we will follow the case structure used in Chapter 3.

All our simulations were performed in a personal computer laptop MSI Intel Core i5 (7th gen) with 8 GB-DDR4 RAM memory, under software MATLAB-2020a running on Linux Ubuntu 18.04. FFT and IFFT libraries used are those included

in MATLAB software. This computer has 4 CPU as well as a Nvidia GeForce 1050 GTX graphics card. Nevertheless, we have not implemented code parallelization or CUDA computing, so all running times come from one single CPU.

In Table A.1 we have summarized the auxiliary functions, $\mu_i\left(\boldsymbol{x_i'}\right)$, used for each case. The more complex the geometry, the more the auxiliary functions we define.

In certain cases, we have executed Step 4 in two different ways; the first one, through the numerical integration of Eq.(4.2) and the second one by interpreting it as an inverse Fourier transform and applying the IFFT algorithm. The better performance of this second method can be clearly seen in tables in Appendix A. The main disadvantage, as stated before, is that, if one wants to focus on any region, the entire region, Ω, must be computed again from scratch. However, the gain in computation time clearly pays off.

4.2.1 Total Reflection

Total reflection for slow neutron beam free propagation, here simulated, is the simplest case to be considered for this algorithm. In fact, we have already solved it analytically in Section 3.2.1.

Let our region of interest, Ω, be the same as described in Section 3.2.1 (omitted here for brevity). We shall represent the impinging thermal neutron beam as a plane wave of arbitrary angle apodized by a window function, $\varphi_{in}(\bar{x}) = rect\left(\frac{x-\frac{k_{in,x}}{k_{in,z}}}{100}\right)e^{ik_{in,x}x}e^{ik_{in,z}z}$. This wavefunction has a wavevector, $k_{in}^2 = k_{in,x}^2 + k_{in,z}^2 = \frac{2mE}{\hbar^2}$, depending on its total energy $E = 0.025$ eV. *rect* is the window function, [7]. We choose the parameters so as to have a 100 Å centred geometric shadow in the barrier. Note that, for simplicity, we will perform this simulation in 2D.

In this case, only one auxiliary function, $\mu_1(x) = \varphi_{in}(x, z = 0)$, must be considered (see Table A.1). Moreover, only one iteration is needed to compute the final result (i.e.: the auxiliary function need not be updated), since the reflected wave will travel towards $z \to -\infty$ and, consequently, the value of the auxiliary function in the boundary will remain unchanged.

Figures 4.2a and 4.2b display our results for simulating impinging plane waves with angle $\theta = 15°$ and $\theta = 30°$, respectively. These figures, display the squared modulus of the neutron wavefunction (probability). Right colourbar represents the correspondence between values and colour, assuming $\mid \varphi_{in}(\bar{x}) \mid^2 = 1$.

We notice the following features: (i) the incoming wave and its geometrical reflection, with the same incidence angle, (ii) the diffraction pattern produced by the outgoing wave, due to the window function, behaving similarly to a finite aperture, and (iii) the interaction fringes formed in the superposition zone where the incoming and outgoing waves overlap. Notice that there is a spurious Moiré effect due to the resolution of the image generated by MATLAB and the frequencies of the represented waves (the order of 1.8 Å). This effect may be corrected by adding more resolution to the image but then it requires more computing time and memory consumption.

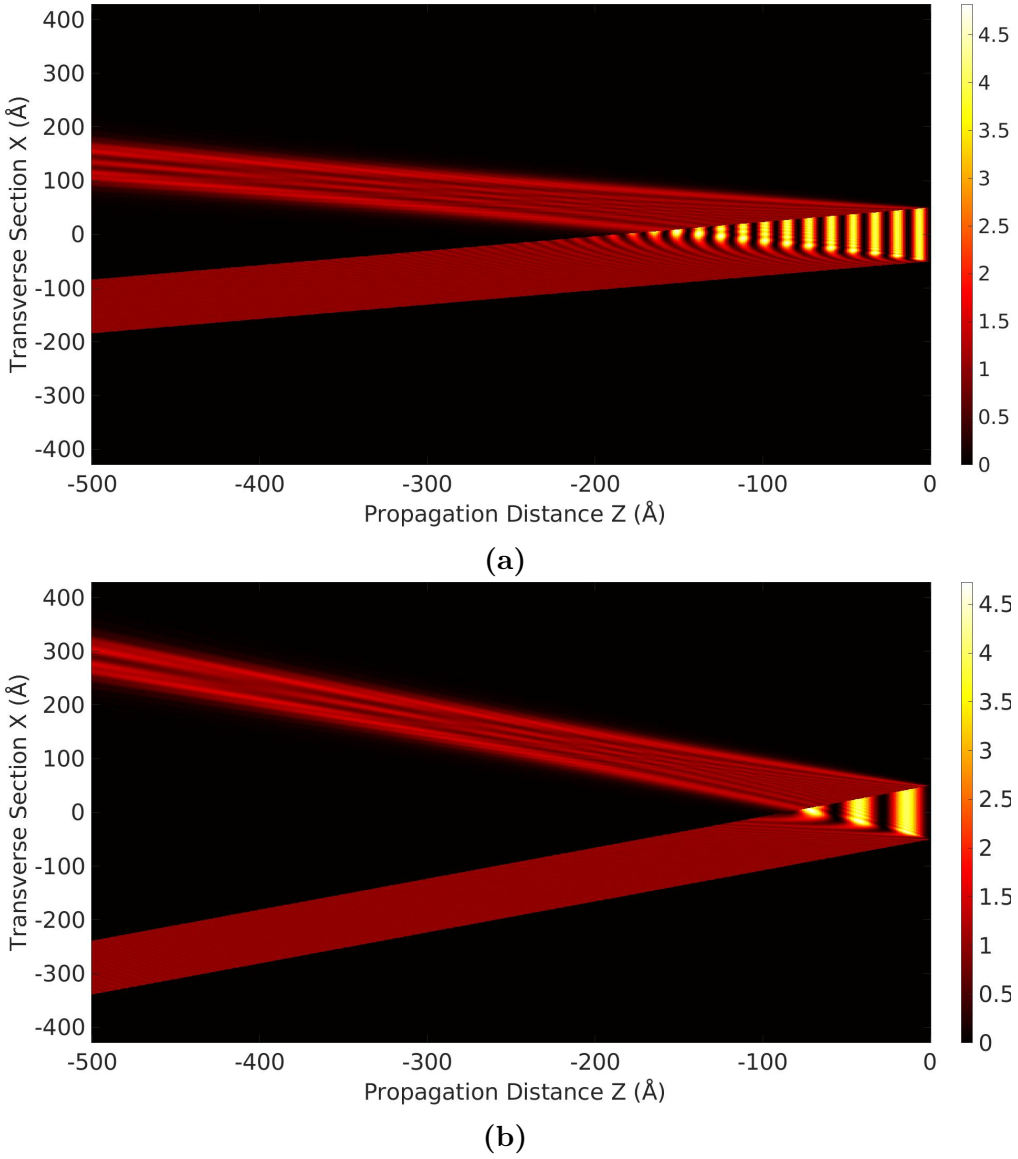

(a)

(b)

Figure 4.2: Simulation of the backward reflection of a thermal neutron plane wave beam for an angleof incidence of (a) $\theta = 15°$ and (b) $\theta = 30°$

4.2.2 Neutron Beam Diffraction

As we said in Section 1.3.1, single-slit diffraction is a key phenomenon resulting from the wave nature for both quantum and electromagnetic physics. Consequently, we will make use of a free-propagating aperture diffraction phenomenon for checking the algorithm well-performance.

This problem and geometry was already treated in Section 3.2.3 with limited results due to complications when numerically simulating the involved equations.

Let us assume a geometry, in which a boundary (screen) is defined at $z = 0$. In this case the potential barrier is a very thin screen located at z = 0 with an aperture of size 100 Å centred at the origin. An incident plane wave, $\varphi_{in}(\bar{x})$ (as

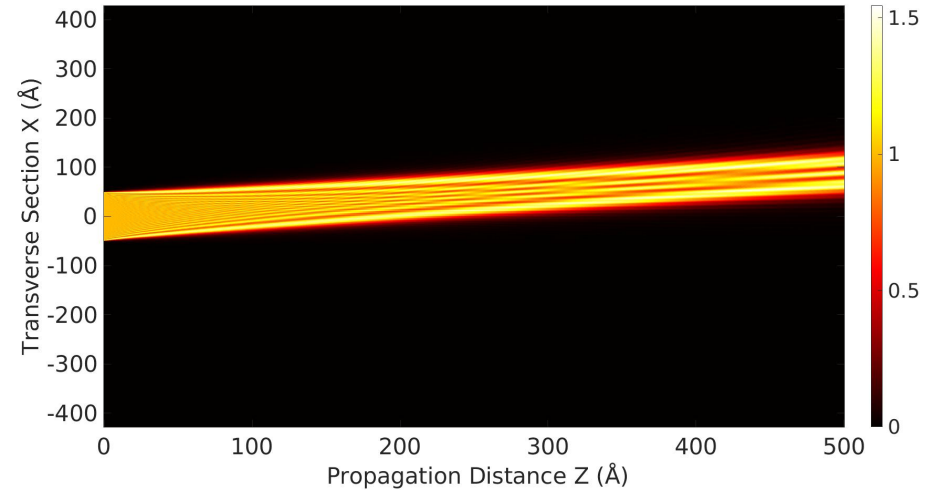

(a)

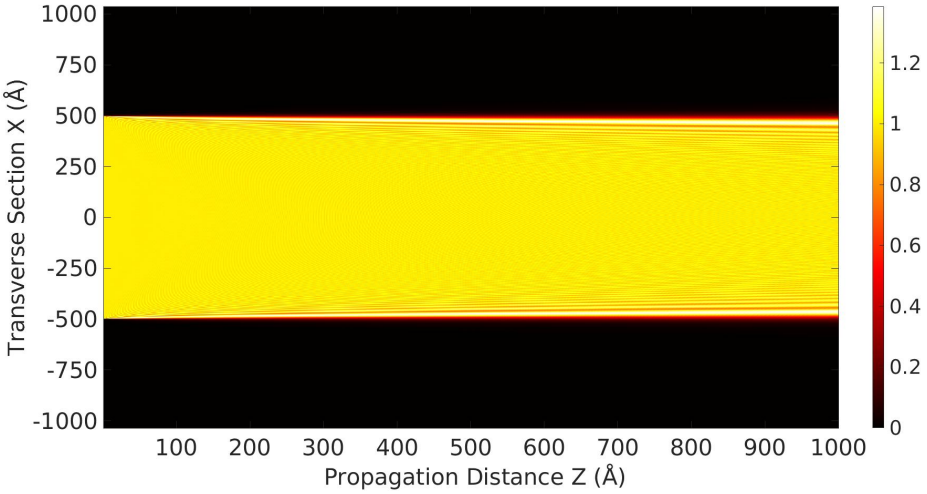

(b)

Figure 4.3: Simulation of a single slit diffraction for a thermal neutron beam for (a) incidence of $\theta = 10°$ and aperture size 100 Å and (b) incidence of $\theta = 0°$ and aperture size 1000 Å. Figure 4.3b is adapted from [94]

in the previous case), impinges from $z \to -\infty$. Let us suppose that the positive z region is now an empty medium (vacuum).

We set Dirichlet boundary conditions at the screen but not on the aperture and perform a free propagation of the resulting wave in the positive z region, $0 \leqslant z \leqslant \infty$, $\forall x$. Consequently, we introduce two auxiliary functions, $\mu_1(x)$, and $\mu_2(x)$, that according to Eq.(4.1), turn out to be proportional to the incoming wavefunction in the boundary (i.e.: $\mu_1(x) = -\frac{\hbar^2}{m}\varphi_{in}(x, z=0)\ \forall x \geqslant \frac{x_0}{2}$ and $\mu_2(x) = -\frac{\hbar^2}{m}\varphi_{in}(x, z=0)\ \forall x \leqslant -\frac{x_0}{2}$, where x_0 is the aperture size). The total result corresponds to the incoming wave minus the propagation of these two terms (as

in step 7, see Figure 4.1). This could be interpreted as performing numerically the extinction theorem at the screen.

Figures 4.3a and 4.3b display our results for simulating a single slit diffraction for different aperture sizes and impinging neutron beam angles. These figures, display the squared modulus of the neutron wavefunction (probability). Right colourbar represents the correspondence between values and colour, assuming $\mid \varphi_{in}(\bar{x}) \mid^2 = 1$.

Figure 4.3a shows the numerical results for the aperture diffraction for an incoming thermal neutron plane wave impinging at 10°. We observe the expected results since: (i) the corresponding diffraction pattern appears as the wave propagates in space, (ii) the main propagation angle is maintained.

In Figure 4.3b, we perform a simulation for a 1000 Å aperture and a thermal neutron wave impinging at 0°. Due to the difference between size aperture and wavelength, diffraction is only a slight effect. Nevertheless, notice the resolution of this algorithm: it is efficient in scales involving a wavelength $\lambda_{db} = 1.8$ Å, apertures of 10^3 Å and propagations of 10^3 Å. These simulations would require a high consumption in memory and/or computation time (see Tables A.2 and A.3), if they would be performed using finite differences methods.

4.2.3 Double Slit Diffraction

Starting from the previous case, and maintaining a similar geometry, it is possible to complicate the simulation. In this Section we will simulate the same situation as the previous one, but now in the potential barrier (defined at $z = 0\ \forall x$) there are two apertures.

Similarly, let us suppose that a plane wave of the form $\varphi_{in}(\bar{x}) = e^{ik_{in,x}x}e^{ik_{in,z}z}$, with a wavevector, $k_{in}^2 = k_{in,x}^2 + k_{in,z}^2 = \frac{2mE}{\hbar^2}$ impinges the potential barrier with arbitrary angle (depending on the value of $k_{in,x}$).

We will focus on the diffraction in the $z \geqslant 0$ region. This time, we will define three auxiliary functions in Eqs.(3.5) and (4.1); $\mu_1(x) = -\frac{\hbar^2}{m}\varphi_{in}(x, z=0)\ \forall x \geqslant \frac{x_1}{2} + x_0$, $\mu_2(x) = -\frac{\hbar^2}{m}\varphi_{in}(x, z=0)$ for $-\frac{x_1}{2} \leqslant x \leqslant +\frac{x_1}{2}$ and $\mu_3(x) = -\frac{\hbar^2}{m}\varphi_{in}(x, z=0)$ $\forall x \leqslant -\frac{x_1}{2} - x_0$, where, again, x_0 is the aperture size (both apertures have the same size) and x_1 is the separation distance between apertures. The simulation procedure is completely analogous to the previous one in Section 4.2.2. Consequently, only one iteration is required.

Figure 4.3a shows the numerical results obtained for an incoming thermal neutron wave impinging at 10° a double slit of size x_0 =100 Å separated a distance x_1 =50 Å. These figures, display the squared modulus of the neutron wavefunction (probability). Right colourbar represents the correspondence between values and colour, assuming $\mid \varphi_{in}(\bar{x}) \mid^2 = 1$. We simulated two cases; (i) a near field (Figure 4.4a) where we observe the two diffracted emerging beams having low interaction and (ii) a far field (Figure 4.4b) where we observe that, for long propagations, both rays approximate a point source and, consequently, the diffraction pattern recalls a $sinc^2(x)$ function.

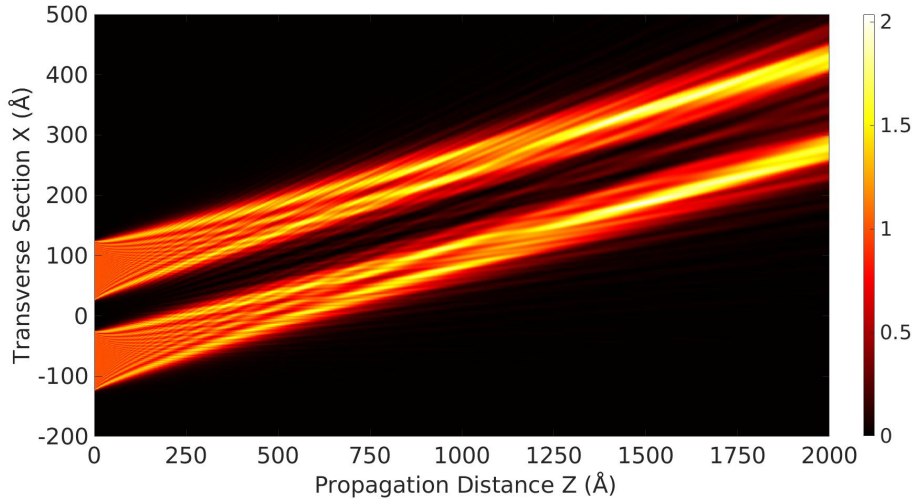

(a)

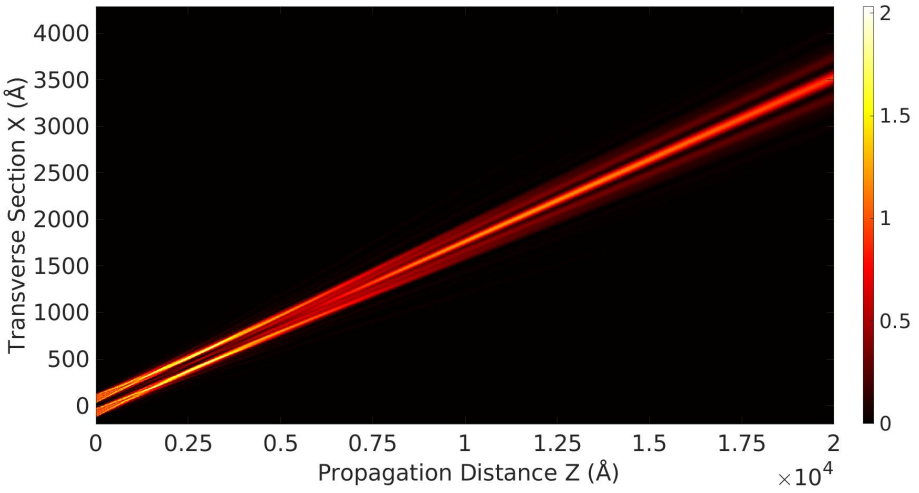

(b)

Figure 4.4: Simulation of (a) near field and (b) far field diffraction of a 100 Å double slit separated 50 Å for a thermal neutron beam impinging at 10°

This is, of course, the expected behaviour and demonstrates that our method is capable of simulating long propagation distances without loss of accuracy (see Tables A.2 and A.3). This computation, involving wavelengths of λ_{db} =1.8 Å, transverse sizes of 250 Å and propagation distances of z =20,000 Å, would be unaffordable to regular Finite Differences Methods.

4.2.4 Neutron Waveguides

In this section, we focus in neutron waveguides as a case other than free propagation. In Chapter 2, we already stated that confinement could be described, as a first

approximation, by means of classical (geometrical) optics since these scales will not produce a strong diffraction pattern.

Nevertheless, the wave behaviour, even if a small (or non-dominant) effect, cannot be neglected, in particular if one wants to characterize the propagation modes generated in waveguides.

In the present case, we set our domain of interest, Ω as a semiinfinite waveguiding thin film, thereby continuing to focus on the XZ plane, centred at the origin of coordinates and parallel to z axis from $z = 0$ to $z \to +\infty$. Thus, the waveguide is limited by four Dirichlet boundaries, located at; $\left(x \geqslant +\frac{x_0}{2}, z = 0\right)$, $\left(x \leqslant -\frac{x_0}{2}, z = 0\right)$, $\left(x = +\frac{x_0}{2}, z \geqslant 0\right)$ and $\left(x = -\frac{x_0}{2}, z \geqslant 0\right)$, where x_0 is the waveguide aperture. Consequently, we will make use of four auxiliary functions $\mu_i(x, z)$, $i = 1, \cdots 4$ (see Figure 3.4 and Table A.1). The iterative updating of these four functions by using recursively Eq.(4.1) will lead to our numerical solution.

We performed the Step 4 in computing Figure 4.5 by using direct numerical integration instead of IFFT. This strategy gives us a better control of the simulations at the cost of a significant increase of computing times (see Tables A.2 and A.3).

In order to lighten up computation, we approximated the diffraction effects of the aperture of the waveguide, for numerical integration, as a new incoming wave, $\varphi^*_{in}(x, z)$. This incoming wave replaces and approximate the former incoming plane wave, $\varphi_{in}(x, z)$, plus the two integrals containing the auxiliary functions, $\mu_1(x)$ and $\mu_2(x)$. This new incoming wave takes the form of Sommerfeld-Rayleigh diffraction integral (see Section A.1). With this approach, $\mu_1(x)$ and $\mu_2(x)$ are not updated and we only update recursively $\mu_3(z)$ and $\mu_4(z)$.

We performed a series of simulations for the propagation of a confined thermal neutron wave under Dirichlet conditions with angle of incidence $\theta = 20°$ and $E = 0.025$ eV ($\lambda_{db} = 1.8$ Å) in a waveguide with an aperture $x_0 = 1000$ Å. The results are in good agreement with those expected enhancing the modal structure of the confined neutron beam. For this angle of incidence, we had to perform 5 iterations (see Table A.3) to converge to the final result. In Figures 4.5a and 4.5b we display the squared modulus of the neutron wavefunction (probability). Right colourbar represents the correspondence between values and colour, assuming $\mid \varphi_{in}(\bar{x}) \mid^2 = 1$.

Figure 4.5a shows a diffraction pattern because of the waveguide's aperture. The longer the propagation in the waveguide the more the spatial frequencies are mixed and then, propagation modes arise.

In Figure 4.5b, we perform another simulation to zoom a concrete region with more resolution. As computation at each point is independent from those for other points, we focus our attention into particular zones in the simulation. This increase of resolution allows seeing the fine structure. The computation of Figure 4.5b took 2195.14 s and is independent of that of 4.5a.

As we stated before, we performed the Step 4 by using two approaches; direct numerical integration and IFFT. The first method implies that each point (x, z)

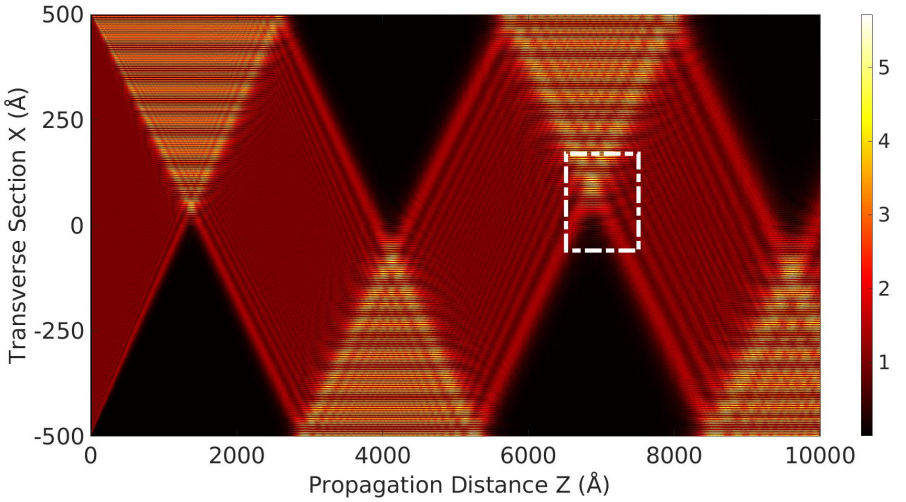

(a)

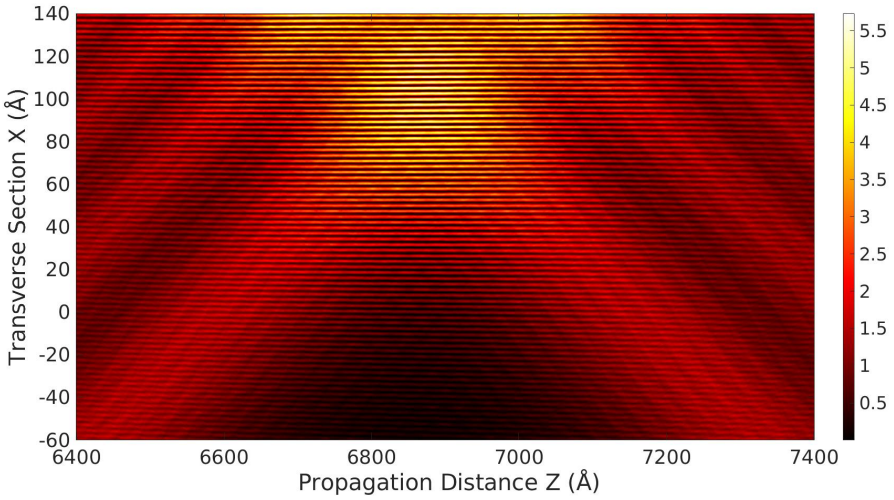

(b)

Figure 4.5: Propagation of a thermal neutron beam impinging at $\theta = 20°$ and $E = 0.025$ eV, under Dirichlet conditions. Simulationsfor (a) the full wavrguide and (b) detailed simulation of hte white rectangle. Adapted from [94]

is computed independently. In the second method, the resolution is tied to the resolution of the defined Fourier transform. Comparing performance of simulation methods for Step 4 (see Tables A.2 and A.3), one realizes that, despite better control of the simulation, lower memory consumption and the trivial possibility of parallelizing the calculations, the difference in computation times may advise the use of inverse FFT. Any potential user could apply one or another method depending on his/her needs.

In any case, notice that these simulations required about one hour computation in comparison to 80 h for that of Figure 2.6 which implies a huge improvement in computation times. Apart from this fact, it is interesting to compare the sizes

of the apertures in both cases (25 Å versus 10^3 Å, 40 times higher) as well as the size of the domain simulated (75×2500 Å versus $10^3 \times 10^4$ Å, about 50 times higher). This clearly demonstrates the power of our method for diffraction and waveguide simulation in situations where the wavelength differs greatly from the sizes of the simulated spatial regions.

4.2.5 Geometrical Interpretation of the Algorithm

From the previous case, we can represent the wavefunction $\varphi(x, z)$ from step 6, after each iteration (i.e.:before convergence to final solution is reached) by using Eq.(4.2). This shows the outcome produced by updating the value of the auxiliary functions $\mu_3(z)$ and $\mu_4(z)$. Results are shown in Figure 4.7. These figures, display the squared modulus of the neutron wavefunction (probability). Right colourbar represents the correspondence between values and colour, assuming $\mid \varphi_{in}(\bar{x}) \mid^2 = 1$.

Here we recall the interpretation of the successive iterations of Green's functions discussed by Balian and Bloch in Eqs. (3.2) and (3.4). In their work they stated: "It may be described as a multiple reflection expansion..." [14]. In our case, each iteration updates the information contained in $\mu_3(z)$ and $\mu_4(z)$ with the internal reflection produced by the beam in the opposite wall. Notice that it is very similar to the behaviour expected in classical optics, but in the present ranges of distances, diffraction effects (that increase with propagation) are visible.

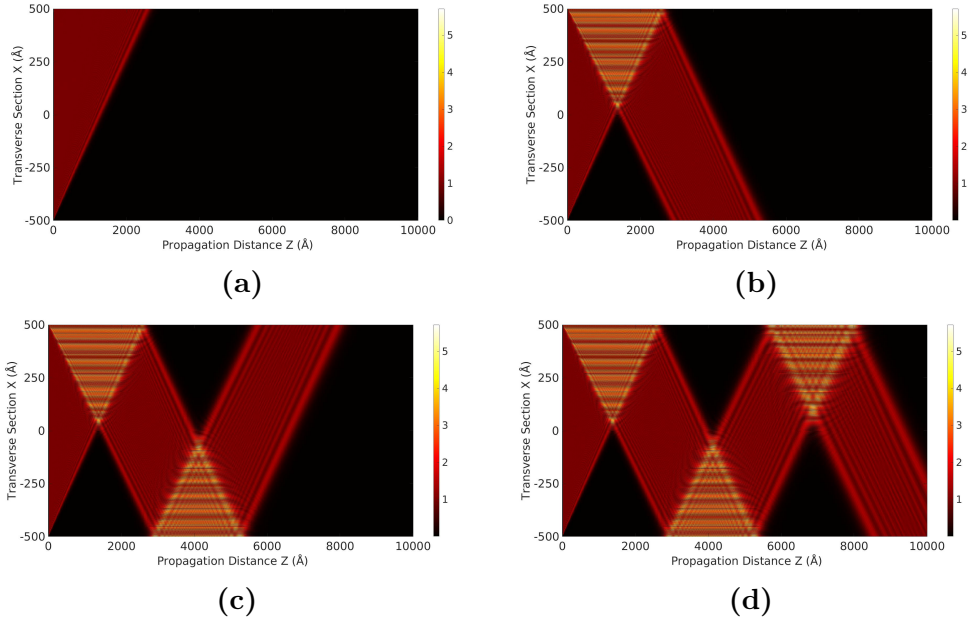

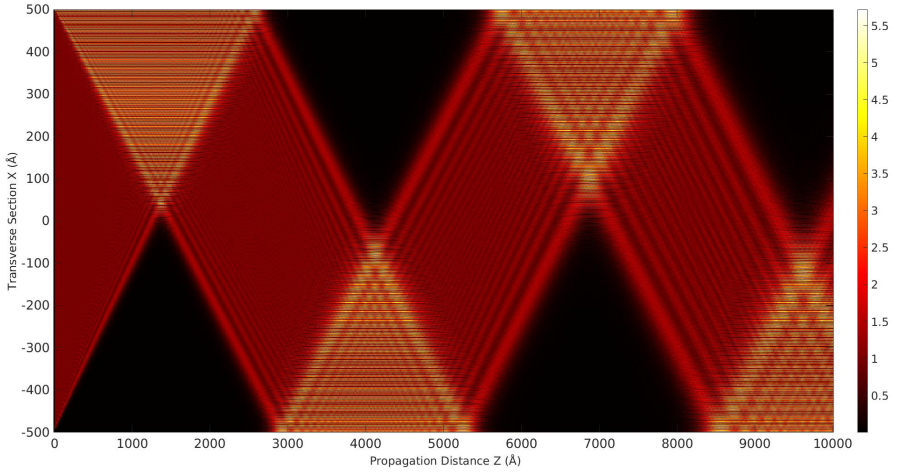

(a)

Figure 4.7: Geometrical interpretation for each of the algorithm's iterations. Simulation for (a) the incoming wave, $\varphi_{in}(x, z)$ and simulation results after (b) one iteration, (c) two iterations, (d) three iterations and (e) four iterations. Adapted from [94]

4.2.6 Fresnel Regime Near Field Free Propagation

In physical optics, different approximations are well established to analyse or solve analytically the diffraction pattern created by an aperture in different regimes and under a scalar treatment. One of those approximations is the well-known Fresnel diffraction regime (i.e., near field diffraction). This regime is applicable, in terms of the so-called Fresnel number: $F = \frac{a^2}{z\lambda_{db}}$. $F < 1$ corresponds to far field approximation, while $F \gtrsim 1$ corresponds to near field approximation. Here a is the dimension of the object (radius, for example), z is the propagation distance and λ_{db} is the wavelength.

In this case, we performed a 3D simulation of a circular aperture of radius, $R = 100$ Å. Notice that this case is an extension to 3D regime of the case proposed in Section 4.2.2. It is indeed a proof of the validity of our algorithm in 3D space (i.e.: adding the, yet unconsidered, y coordinate). It enables to compare the run time required for 3D and 2D simulations (see Table A.3). One can observe that running times in these cases are of the same order as numerical integration in 2D cases.

Since propagation distance in Fresnel regime holds for $z \approx 5500$ Å(assuming $\lambda_{db} = 1.8$ Å), the present case requires a high amount of computation to propagate this long distance in comparison to a 2D case. That is why in this case we have opted for the use of the Inverse FFT method for the execution of Step 4 of the algorithm instead of numerical integration.

In the present case, we set our domain of interest, Ω as the whole 3D empty space for $z \geqslant 0$, where a barrier with an aperture of radius, $R = 100$ Å, centred, is placed at $z = 0$ Å. We simulate an incoming thermal neutron beam as a plane wave with an angle of incidence of $\theta = 0°$, $\varphi_{in}(\boldsymbol{x}) = e^{ik_{in}z}$, with $k_{in}^2 = \frac{2mE}{\hbar^2}$, ($E = 0.025$

eV for thermal neutrons). The incoming wave travels from $z \to -\infty$ and impinges the barrier, where we impose Dirichlet conditions.

Notice that, compared to Section 4.2.2, $\mu(\bar{x})$ is a 2D auxiliary function and, thus, we simulate this aperture in Eqs. (4.1) and (4.2) by making use of 2D FFT instead of the one dimensional case. As in Section 4.2.2, only one iteration is required since the outgoing wave does not interact again with the barrier.

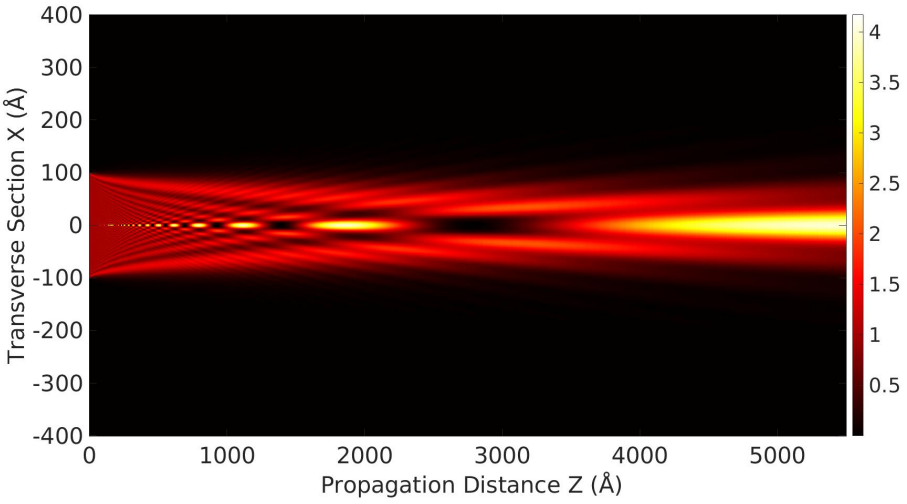

(a)

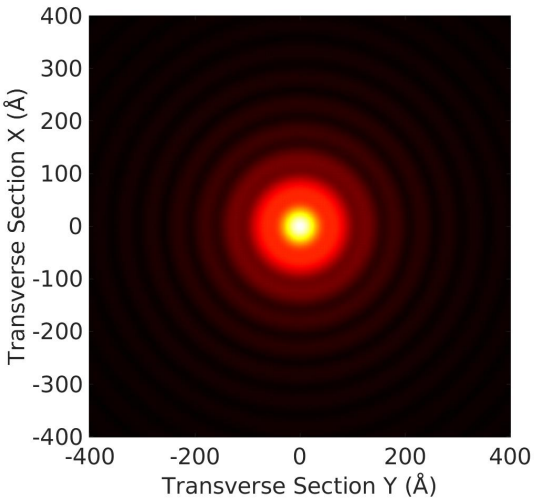

(b)

Figure 4.8: 3D Simulation of aperture diffraction under Fresnel regime for (a) propagation field and (b) diffraction pattern obtained at $F \approx 1$. Adapted from [94]

Our results are displayed in Figure 4.8. It, displays the squared modulus of the neutron wavefunction (probability). Right colourbar represents the correspondence between values and colour, assuming $\mid \varphi_{in}(\bar{x}) \mid^2 = 1$.

Figure 4.8a demonstrates that, for the assumption of a circular geometry (in the aperture), the simulation will exhibit focusing effects as a property of Fresnel free

propagation of diffracted waves, as expected. Moreover, a pattern of minima and maxima in the system axis is shown. These structures, called doughnut-like (for the minima), have already been analysed in the context of Fourier diffraction, see for example [98].

4.2.7 Arago-Poisson Spot

Recalling the previous Section 4.2.6, we carried out the opposite simulation (i.e.: a plate disk instead of an aperture) for determining the appearance of the Arago-Poisson spot. This particular phenomenon serves as a proof of the consistency of our simulation method.

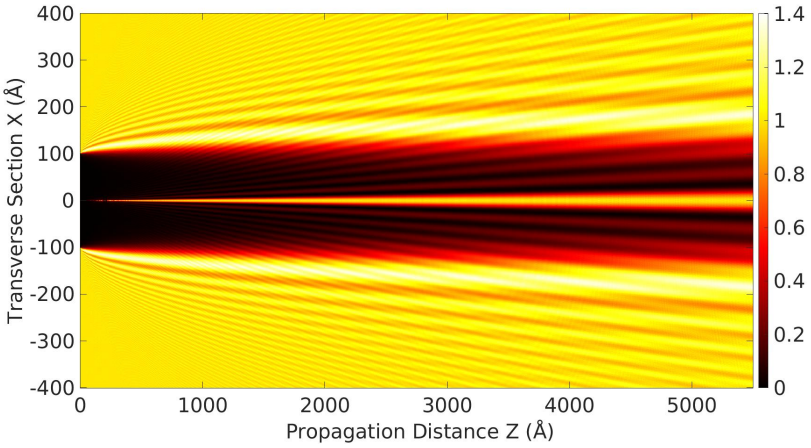

(a)

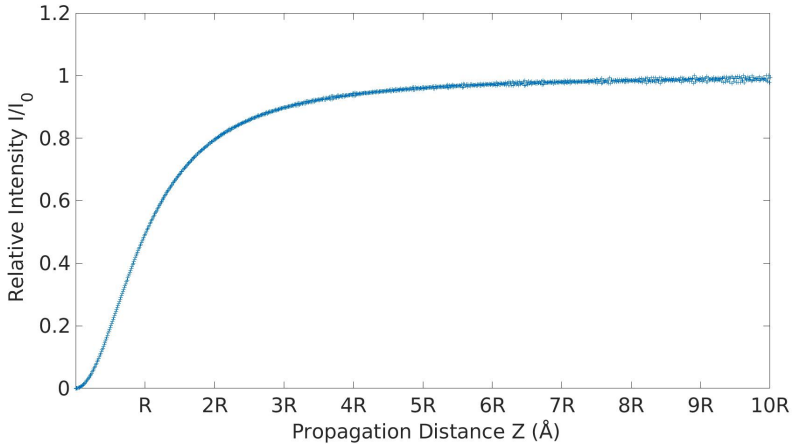

(b)

Figure 4.9: Simulation of circular plate diffraction and formation of Arago-Poisson spot. Figure shows (a) the propagation field obtained in Fresnel regime and (b) the relative intensity in axis versus disc raidus R. Adapted from [94]

In this case, we set conditions identical to those described in Section 4.2.6 but the incoming wave, $\varphi_{in}(\boldsymbol{x}) = e^{ik_{in}z}$ impinges a circular plate (instead of a barrier) of

radius, $R = 100$ Å. We emphasize that, as in the previous Section, all calculations are performed in 3D and, thus, we made use of 2D FFT for Step 4.

Figure 4.9 shows our results. In Figure 4.9a, we display the squared modulus of the neutron wavefunction (probability). Right colourbar represents the correspondence between values and colour, assuming $\mid \varphi_{in}(\bar{x}) \mid^2 = 1$. In this figure, an on-axis intensity point appears in the centre of the shadow of the plate (Arago-Poisson spot). In Figure 4.9b we represent the behaviour of relative intensity (i.e.: the squared modulus of the field divided by the squared modulus of $\varphi_{in}(\boldsymbol{x})$) in the axis of the system, as a function of the propagation distance, z, in units of the disc radius, R. This on-axis relative intensity shows that the Arago-Poisson spot appears just over a few times the plate size and tends to the incoming wave relative intensity, as it would be expected.

4.2.8 Fresnel Lens

Having in mind the focusing properties established in Section 4.2.6, we perform a 3D simulation of a Fresnel Zone Plate (FZP). These plates have the property that, through a set of alternating opaque and transparent concentric fringes, the neutron beam will diffract and interact constructively in a desired focus point. This focusing property may be understood as an extension of the Arago-Poisson spot stated in Section 4.2.7.

In this case, we simulate a FZP, located at $z = 0$ by imposing a 2D auxiliary function, $\mu(x, y) = \varphi_{in}(x, y, z = 0) \cdot T(x, y)$, where $\varphi_{in}(x, y, z = 0) = e^{ik_{in,x}x} e^{ik_{in,y}y}$ is the incoming plane wave. We will assume it impinges at $\theta = 0°$. $T(x, y)$ corresponds to the transmittance of a FZP with the form of, [99]

$$T(x, y) = 1 + 8sin^2 \left[\frac{k_{in} \left(\sqrt{x^2 + y^2 + z_f^2} - z_f \right)}{2} \right] \tag{4.5}$$

where z_f is the focus point distance (that we set, for our simulation, to be at $z_f = 4000$Å), k_{in} is the neutron beam wavevector ($k_{in}^2 = \frac{2mE}{\hbar^2}$).

Figure 4.10 shows our results. It, displays the squared modulus of the neutron wavefunction (probability). It shows how the diffracted neutron beam is focused at $z = 4000$ Å, as expected. Notice that, this time, colour is enhanced by representing its colourmap in logarithmic scale, since otherwise converging rays would not be displayed.

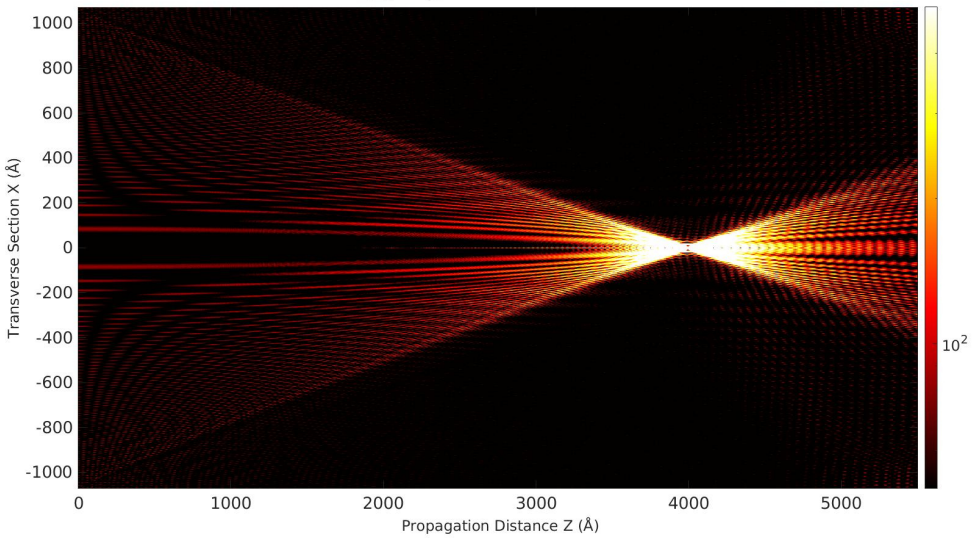

Figure 4.10: Simulation of a Fresnel Zone Plate with focus point at $z = 4000$ Å

4.3 Neutron Holography

As we stated in Section 1.3.1, holography is an optical technique in which an interferogram is recorded. Holography was proposed by Dennis Gabor in 1948, [100]. He stated that when a coherent reference wave interacts with the light diffracted or scattered from an object, they create an interference pattern that can be recorded. If one illuminates this interference pattern with a light source similar to the reference wave, the original object can ultimately be obtained.

This process has two main steps; recording and reading (see Figure 4.11). In the recording process, an object is illuminated by a reference wave. The wave, once scattered by the object, interacts creating an interference pattern in some region of the space. This interference is usually recorded in a photographic plate, detector... Note that for these phenomena to occur, both waves must have at least partial coherence (see Figure 4.11a).

During the reconstruction process (reading), a reference beam impinges the recorded hologram. Part of the wave is transmitted while other part is reflected. In both cases, since this reference wave interacts with the recorded hologram, it will diffract giving, as a result the real and virtual image of the original object (see Figure 4.11b).

For a physical description, let us suppose two scalar complex quasi-monochromatic waves denoted by $\Psi_{ref}(\boldsymbol{x}, t)$ (the incoming reference wave) and $\Psi_{obj}(\boldsymbol{x}, t)$ (the diffracted object wave). If these two waves superimpose under partial mutual coherence condition, the total intensity at $\boldsymbol{x_0}$, where the recorder (photographic plate, detector...) is located, is

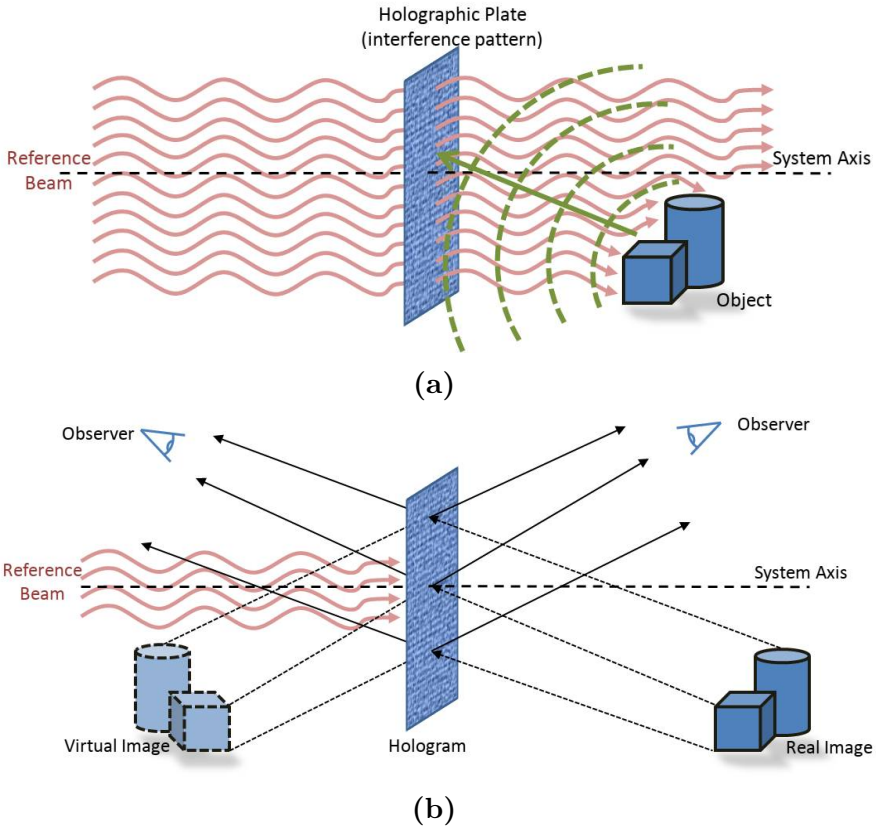

Figure 4.11: Representation of the (a) recording step and (b) reading step of the holographic technique

$$\begin{aligned} I\left(\boldsymbol{x_0}\right) =& \left\langle \left|\Psi_{ref}\left(\boldsymbol{x_0},t\right)+\Psi_{obj}\left(\boldsymbol{x_0},t\right)\right|^2 \right\rangle = \\ =& I_{ref}\left(\boldsymbol{x_0}\right)+I_{obj}\left(\boldsymbol{x_0}\right)+\left\langle \Psi_{ref}\left(\boldsymbol{x_0},t\right)\Psi^*_{obj}\left(\boldsymbol{x_0},t\right)\right\rangle + \\ &+\left\langle \Psi^*_{ref}\left(\boldsymbol{x_0},t\right)\Psi_{obj}\left(\boldsymbol{x_0},t\right)\right\rangle \end{aligned} \tag{4.6}$$

where $\langle\ \rangle$ brackets denote the time average. * denotes complex conjugation and $I_{ref}\left(\boldsymbol{x_0}\right)$ and $I_{obj}\left(\boldsymbol{x_0}\right)$ are the reference and object wave intensities, respectively. Let assume that, once recorded, the transmittance of the hologram is proportional to the intensity, $T \propto I\left(\boldsymbol{x_0}\right)$. If a reference wave Ψ_{ref} (we omit spatial variables and time for simplicity) impinges the hologram, the transmitted wave will be

$$T\Psi_{ref} \propto I_{ref}\Psi_{ref}+I_{obj}\Psi_{ref}+I_{ref}\Psi_{obj}+\Psi^2_{ref}\Psi^*_{obj} \tag{4.7}$$

This equation contains in its structure the complete information, in amplitude and phase, of the scalar wave diffracted by the object whose image we want to reconstruct. During the reconstruction process, two twin images are formed (see Figure 4.11b).

Since it deals with the scalar wave propagation after reflection and diffraction on boundaries obeying Dirichlet conditions, it is straightforward to use our previous formulation to simulate holograms. With the relevant modifications, we can numerically simulate the transmittance function for the three-dimensional reconstruction of the object.

The general idea arises from considering Dirichlet-type boundary conditions (that is, the annulment of the wave function at the boundaries) as if they were solid objects on which an incident wave is reflected. Once the reflected field has been numerically calculated, we propagate it to the space region where we set to be the (digital) recording holographic plate. There, it interacts with the incident wave obtaining the interference pattern associated with the transmittance. These operations involve digitally simulating a process equivalent to recording a reflection master hologram and results in encoding in the form of transmittance of the three-dimensional object (hologram). Consequently, we have to apply the algorithm in two steps; once for simulating the recording process and once for propagating the wave diffracted from the digital plate to obtain the reconstruction:

Recording: According to our formulation, the incident wave, $\varphi_{in}(\boldsymbol{x})$ plays the role of the so called reference beam in holography. We consider a set of (solid 2D) objects that obey Dirichlet boundary conditions and define the corresponding auxiliary functions, $\mu_i(\bar{x})$. When the reference beam impinges the objects, these auxiliary functions are characterized through Eq.(4.1). By using Eq.(4.2), we propagate the reflected (scattered) wavefunction, $\varphi(\boldsymbol{x})$, backwards to the virtual holographic plate, where we record its interaction with the incident wave according to Eq.(4.6). The intensity pattern obtained sets the transmittance of the object as in Eq.(4.7)

$$T(\boldsymbol{x'}) \propto |\varphi_{in}(\boldsymbol{x'}) + \varphi(\boldsymbol{x'})|^2 \tag{4.8}$$

where $\boldsymbol{x'}$ lies in the region where we have set the holographic plate to be. Notice that, since we define the transmittance function to be proportional to the field intensity, $T(\boldsymbol{x'}) \in \mathbb{R}$, as if a reflection master hologram is recorded. Reflectance, $R(\boldsymbol{x'}) \in \mathbb{R}$, can be also obtained from Eq.(4.8) taking into account that the Fresnel equation, $R(\boldsymbol{x'}) + T(\boldsymbol{x'}) = 1$, must be fulfilled.

This is the numerical equivalence of the registration that would be obtained on a photographic plate. This calculated transmittance, implemented in an LCD screen and illuminated with a coherent source (laser) would allow the reconstruction of the three-dimensional image of the object in the laboratory.

These transmittance functions are not feasible to be simulated for macroscopic objects due to the enormous computation required. With the use of our algorithm, the full three-dimensional computation (for example using FDM) would be reduced to a two-dimensional problem. Moreover, since the algorithm

calculates every point independently, there is no need to propagate the entire wave reflected by the object, but only its value in the holographic plate. An additional advantage of this system is that it calculates the point values of the transmittance function independently, so it trivially admits the possibility of parallelization, further improving computation times.

Notice that, the calculation of the transmittance of the simulated object allows the digital storage of said three-dimensional object. That is, one of the outputs of this system is the efficient digital storage of a hologram.

Reading: The encoded information can be retrieved in the form of a wave diffracted by the recorded hologram. The set geometry is close to that used in Sections 4.2.6 to 4.2.8 but, in this case, we use this transmittance, Eq.(4.8), to define a new auxiliary function $\mu(\boldsymbol{x'}) = T(\boldsymbol{x'}) \cdot \varphi_{in}(\boldsymbol{x'})$ (the incident wave may be or not the same used in recording the hologram). Propagation of this transmittance-modulated wave function in space involves performing the three-dimensional reconstruction of the initial object (virtual image). Notice that, if we use reflectance to propagate, $R(\boldsymbol{x'}) \cdot \varphi_{in}(\boldsymbol{x'})$, backwards, according to Eq.(3.5), with a change of sign, we obtain the real image.

This procedure would be the equivalent of numerically performing a Gabor on-axis hologram. We present here two numerical results of this procedure application. We performed these simulations in 2D, neglecting the y coordinate, for simplicity, its 3D extension being trivial. In both cases, simulation times are in the order of those for the cases of reflection and diffraction in Sections 4.2.1 to 4.2.3.

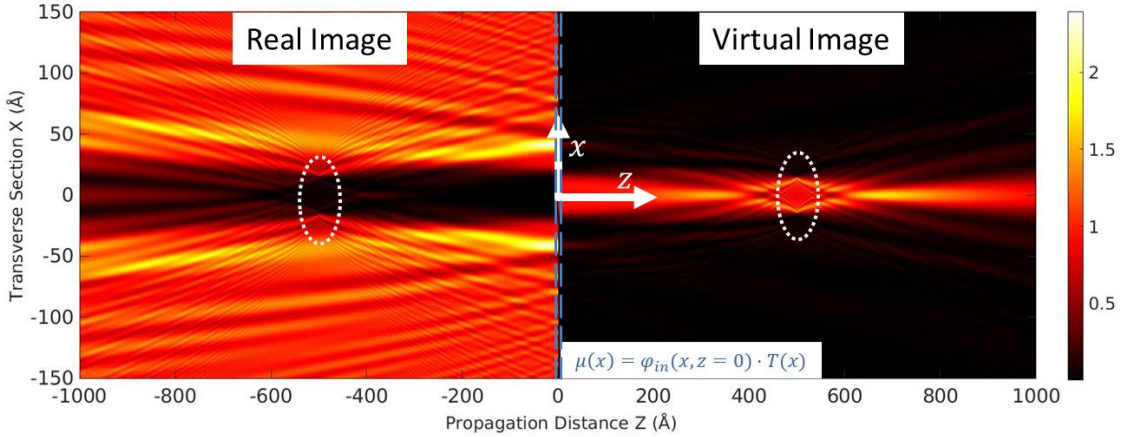

Figure 4.12: On-axis hologram simulation of a 30 Å plate at $z = 500$ Å

In Figure 4.12 we show a 2D digital hologram obtained with this technique, where we recorded the interference pattern from a flat $x_0 = 30$ Å vertical plate located at $z = 500$. After that, we read the hologram by scattering an incident neutron plane wave, $\varphi_{in}(\boldsymbol{x'})$, according to Eqs.(3.5) and (4.8). Both the reflection

and transmission have been simulated. In this case, since we simulated a reflection hologram, the virtual image appears at the right side while the real image appears in the left side, as would be expected.

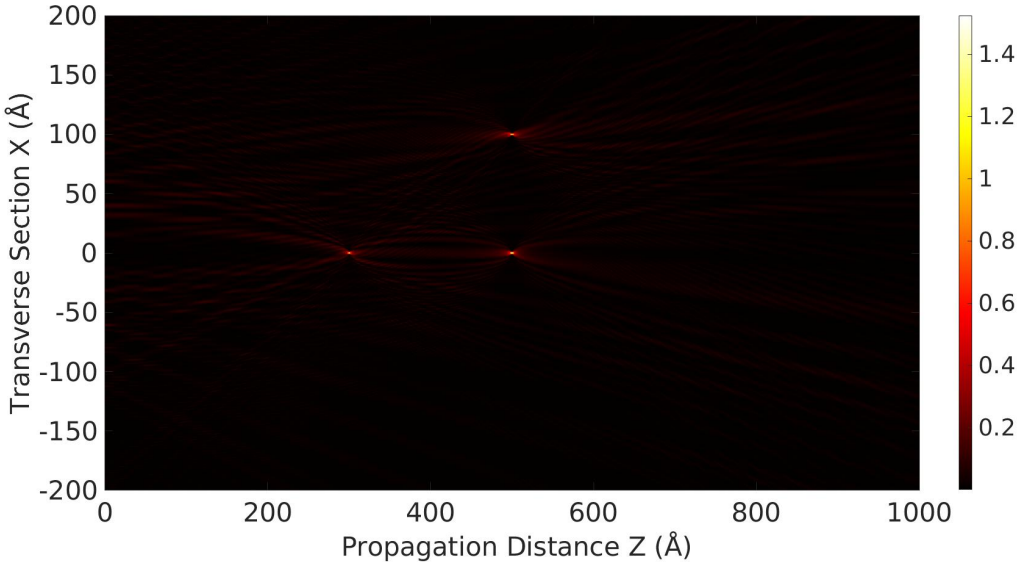

Figure 4.13: 2D Hologram simulation of three points located in space

Moreover, three independent points in space have been simulated; two on-axis points at positions $(300, 0)$ Å and $(500, 0)$ Å and an off-axis point at $(500, 1000)$ Å. Their scattered pattern (according to Eq.(3.5)) were combined into a single transmission function. Once the transmittance function is obtained, we reconstructed the objects by propagating the transmittance-modulated wavefunction as stated above. The recorded hologram is located at $z = 0$. In Figure 4.13, we can see that, indeed, the three points are obtained back in the simulated positions. This shows that our algorithm is capable of simulating an independent set of points in space. In this case, the result can be interpreted as a hologram or a lens with three independent focal points.

All these results led us to claim a patent Ref.P202230979, "Sistema para generación de hologramas digitales vía simulación" (System for generation of digital holograms via simulation), [5], presented by Universidad Complutense and still under review.

Tengo los medios, la habilidad...
Pero me falta el método...
...No. Eso no es cierto.
Tengo cientos de métodos
Pero falta algo...

Batman: Año Uno

5
Finite Potential Waveguides

Contents

In previous Chapters 3 and 4, we achieved a milestone by using a Green's

function formalism analogous to the one for classical optics description and Dirichlet boundary conditions. We were able to carry out simulations, yielding interesting results on the neutron beam diffraction, reflection and confined propagation, with the subsequent extinction of the incoming wave, along the waveguide.

The extension of these results to the more general case including neutron penetration into the clad (i.e.: finite potentials instead of Dirichlet boundary conditions), is a necessary, open and non-trivial problem. Specifically, the involved physical difficulties relate with the fact that the mathematical description of the propagating wave in Eq.(3.5) is constrained to Dirichlet boundary conditions. Indeed a more general formulation must be used.

In this chapter we will perform a direct study of the problem for finite potential waveguides (Si-Ti waveguides) based upon the standard Lippmann-Schwinger equation for quantum-mechanical scattering [101].

This chapter is based on the results and conclusions published in *The European Physical Journal Plus* [102].

5.1 Hamiltonians, Green's Operators and Functions

5.1.1 System Description

We will focus on a straight semi-infinite waveguide with longitudinal and transverse dimmensions similar to those in [13]. Both clad and core have transverse dimmensions the order of 100 μm. The finite domain Ω contains a subdomain with $V(\bar{x})\,(=V_{core})<0$ (the core, strictly speaking) and another one (finite clad) with $V(\bar{x})\,(=V_{clad})>0$. The waveguide is located in and surrounded by a medium with negligible Fermi pseudo-potential on neutrons (i.e.: vacuum or, approximately, air) as if there is an infinitely extended clad, with $V(\bar{x})=0$. The proposed waveguide has its axis parallel to the z-axis, from $z=0$ up to $z=+\infty$. See Figure 5.1.

Let an incoming thermal neutron beam with energy E propagate freely from $z\to-\infty$, in the above medium with negligible Fermi potential in 3D space, and approach the waveguide. The neutron beam is represented by an incoming plane wave with wavevector $\boldsymbol{k}=\left(\bar{k},k_z\right)$ and energy E ($k_z>0$):

$$\psi_{in}(\boldsymbol{x})=e^{i\left(\bar{k}\bar{x}+k_z z\right)} \tag{5.1}$$

$$E=\hbar^2\frac{\bar{k}^2+k_z^2}{2m} \tag{5.2}$$

Physically, the length of the waveguide is assumed to be much larger than the neutron de Broglie wavelength, $\lambda_{db}=2\pi\hbar/\left(2mE\right)^{1/2}$. One approximates such a very lengthy waveguide by a semi-infinite one.

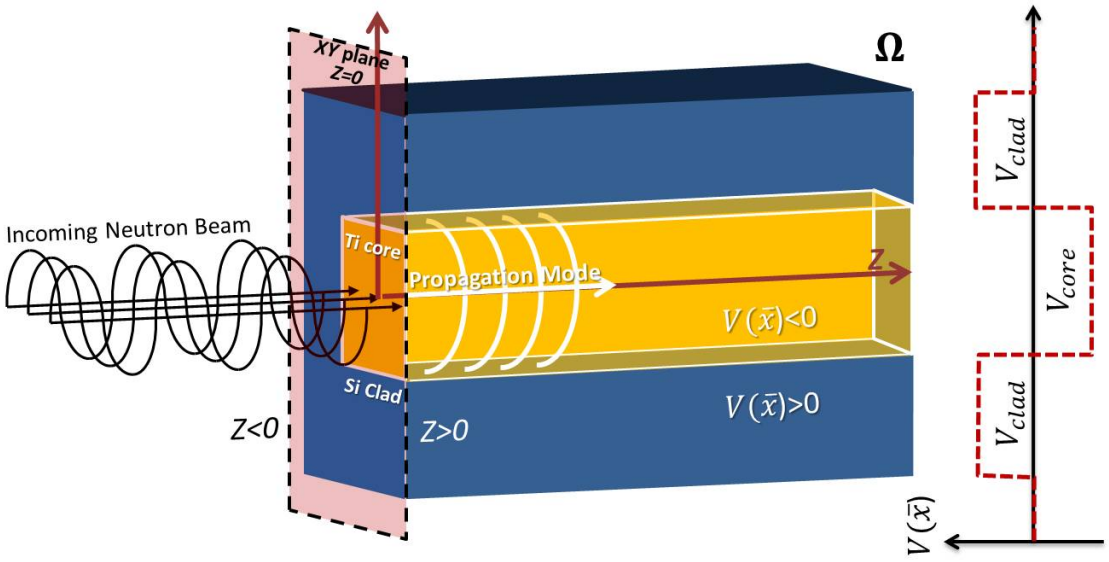

Figure 5.1: Schematic representation of a Si-Ti neutron waveguide. Adapted from [102]

In $z < 0$ and outside the waveguide in $z > 0$ there is no potential acting on the neutron. In $z > 0$, inside the semi-infinite waveguide, the neutron will be subject to interactions with the material medium.

Inside the waveguide, the neutron beam interactions are characterized, by assumption, by the z-independent potential $V(\bar{x}, z) = V(\bar{x})$. See Figure 5.1. We will set the potential, $V(\bar{x})$: (i) real (neglecting absorption in the material) and finite , (ii) vanishes ($V(\bar{x}) = 0$) for $\bar{x}$ outside some finite 2D domain Ω (the projection of the waveguide on the XY-plane), (iii) is strictly attractive in the core with $V(\bar{x}) < 0$. The physical quantum-mechanical wave phenomena to be studied here are: reflection and scattering of the incoming neutron by and its confined propagation along the waveguide (giving rise to propagation modes).

Keeping these assumptions in mind, the present study could be extended readily to the cases in which: (i) takes into account absorption (i.e.: $V(\bar{x}) \in \mathbb{C}$), (ii) $V(\bar{x})$ does not vanish outside any finite domain but, instead, tends to zero quickly as $\mid \bar{x} \mid \rightarrow +\infty$, along any direction and (iii) the core is not strictly attractive while obeying the condition for confined propagation, $\Delta(b\rho) > 0$, as stated in Section 2.1 (there may be propagation modes and resonant states that will be not strictly bound states, see Section 5.5.3).

5.1.2 Total Hamiltonian and Green's Operator

The total Hamiltonian operator of the slow neutron in the whole 3D space ($-\infty < z < +\infty$, and any $\bar{x}$) is

$$H = \frac{-\hbar^2}{2m}\Delta_{\boldsymbol{x}} + V(\boldsymbol{x}) \tag{5.3}$$

$$V(\boldsymbol{x}) = 0, \quad z < 0 \tag{5.4}$$

$$V(\boldsymbol{x}) = V(\bar{x}), \quad z > 0 \tag{5.5}$$

where $\Delta_{\boldsymbol{x}} = \frac{\partial^2}{\partial x^2} + \frac{\partial^2}{\partial y^2} + \frac{\partial^2}{\partial z^2}$ is the 3D Laplacian. For an explanation of notation used in vectors, see Index of Notations and Constants.

The total Green's operator determined by H (see [36, 83]) is:

$$G(E) = \frac{1}{E \pm i\epsilon - H} \tag{5.6}$$

with energy E (i.e.: the incoming neutron energy), $\epsilon > 0$ is small and $\to 0$ at the end of a calculation. The positive sign, $+i\epsilon$ corresponds to the retarded Green's function, while the negative sign, $-i\epsilon$, corresponds to the advanced one. It can be demonstrated (see, for example [10, 103]) that we must choose $+i\epsilon$ for fulfilling the Sommerfeld radiation condition.

Notice that Green's operators and potentials do not commute among themselves in these equations. This noncommutativity poses no problem whatsoever, provided that the orderings of operators, as they stand, be respected.

The above Eqs.(5.3) to (5.6) are general ones and independent from initial conditions (like the one in Section 5.1.1). In order to analyse properly neutron reflection, scattering and confinement, we will define partial Hamiltonians, Green's operators and functions in the following sections. Those definitions, when the initial condition in Section 5.1.1 be included, will lead to the formulations in Section 5.2.

5.1.3 Partial Hamiltonians and Green's Operators

Consider a slow neutron propagating freely in the whole 3D space. In the absence of interaction from $z = -\infty$ to $z = +\infty$, the slow free neutron propagation is described by the partial free Hamiltonian H_1 (see Eq.(5.7)) and its eigenfunctions are plane waves.

The interaction with the waveguide from $z = 0$ to $z \to +\infty$ leads to adding V_1 (Eq.(5.8)) to H_1, yielding Eq.(5.9). Moreover, one may define the partial Green's operator $G_1(E)$ by making use of H_1 and, so, obtain the total Green's operator $G(E)$ (Eq.(5.6)) in terms of $G_1(E)$. Then, the set of Eqs.(5.3)-(5.6), describing the slow neutron propagation from left ($z = -\infty$) to right ($z = +\infty$), is also recast as follows

$$H_1 = -\frac{\hbar^2}{2m}\Delta_{\boldsymbol{x}} \tag{5.7}$$

$$V_1(\boldsymbol{x}) = V(\boldsymbol{x}) \tag{5.8}$$

$$H = H_1 + V_1(\boldsymbol{x}) \tag{5.9}$$

$$G_1(E) = \frac{1}{E + i\epsilon - H_1} \tag{5.10}$$

$$G(E) = G_1(E) + G_1(E)\, V_1 G(E) \tag{5.11}$$

Eq.(5.11) is an exact relationship, following formally by expanding and resumming geometric series: $\frac{1}{A-B} = \frac{1}{A} + \frac{1}{A}B\frac{1}{A} + \frac{1}{A}B\frac{1}{A}B\frac{1}{A} + ... = \frac{1}{A} + \frac{1}{A}B\frac{1}{A-B}$ (with $\frac{1}{A-B} = G(E)$, $\frac{1}{A} = G_1(E)$ and $B = V_1(\boldsymbol{x})$ respectively). For more details, see [83], Chapter XIX.

Apart from that, one may describe the same physical situation by formulating it in an alternative, equivalent, but less familiar, way. In this case, one introduces the partial Hamiltonian H_2 (see Eq.(5.12)). This hamiltonian describes an infinite waveguide (from $z = -\infty$ to $z = +\infty$) by the presence of a potential extended in the whole space, $V_{ext}(\boldsymbol{x})$ accounting for the interaction (matching $V(\bar{x})$). Its eigenfunctions are the propagation modes and scattering states (respectively associated to $\phi_\alpha(\bar{x})$ and $\phi_{\bar{q}}(\bar{x})$ in the forthcoming Section 5.1.4). Then, one may recast the same total Hamiltonian in Eq.(5.3) for $z = -\infty$ to $z = +\infty$ as in Eq.(5.14). This approach leads to a new partial Green's operator $G_2(E)$ and, thus, a new representation for the total Green's operator $G(E)$ in terms of $G_2(E)$. Then, the set of Eqs.(5.3)-(5.6), describing the slow neutron propagation from right ($z = +\infty$) to left ($z = -\infty$), is also given as

$$H_2 = -\frac{\hbar^2}{2m}\Delta_{\boldsymbol{x}} + V_{ext}(\boldsymbol{x}) \tag{5.12}$$

$$V_{ext}(\boldsymbol{x}) = V(\bar{x}), \ -\infty < z < +\infty \tag{5.13}$$

$$H = H_2 + V_2(\boldsymbol{x}) \tag{5.14}$$

$$V_2(\boldsymbol{x}) = 0, 0 < z < +\infty \tag{5.15}$$

$$V_2(\boldsymbol{x}) = -V(\bar{x}), -\infty < z < 0 \tag{5.16}$$

$$G(E) = \frac{1}{E + i\epsilon - H_2} \tag{5.17}$$

$$G(E) = G_2(E) + G_2(E)\,V_2 G(E) \tag{5.18}$$

Also, Eq.(5.18) is another exact relationship, following formally by handling geometric series in similar way: $\frac{1}{A-B} = \frac{1}{A} + \frac{1}{A}B\frac{1}{A} + \frac{1}{A}B\frac{1}{A}B\frac{1}{A} + ... = \frac{1}{A} + \frac{1}{A}B\frac{1}{A-B}$ (now with $\frac{1}{A-B} = G(E)$, $\frac{1}{A} = G_2(E)$ and $B = V_2(\boldsymbol{x})$, respectively). For more details, see [83], Chapter XIX.

Notice that the above Eqs.(5.7) to (5.18) are general ones and independent on initial conditions (as in Section 5.1.1). Eqs.(5.11) and (5.18) play a key role in our development of the Lippmann-Schwinger equations in Section 5.2.1.

5.1.4 Hamiltonian Analysis: 2D Scattering and Bound States

The Hamiltonians stated in Eqs.(5.3) (5.7) and (5.12) are referred to the whole 3D space. Since $\Delta_{\boldsymbol{x}} = \Delta_{\bar{x}} + \frac{\partial^2}{\partial z^2}$ and according to the problem geometry described in Section 5.1.1, these Hamiltonians can be separated in a 1D Hamiltonian (propagation direction z) and a 2D Hamiltonian (transverse direction xy), see Figure 5.1. We will focus in the 2D Hamiltonian $\left[-\frac{\hbar^2}{2m}\Delta_{\bar{x}} + V(\bar{x})\right]$. It describes, in particular, the profile of the propagation modes (its eigenfunctions).

It has the following continuum eigenfunctions $\phi_{\bar{q}}(\bar{x})$ with real eigenvalues $\hbar^2\bar{q}^2/2m\,(\geq 0)$

$$\left[-\frac{\hbar^2}{2m}\Delta_{\bar{x}} + V(\bar{x})\right]\phi_{\bar{q}}(\bar{x}) = \frac{\hbar^2\bar{q}^2}{2m}\phi_{\bar{q}}(\bar{x}) \tag{5.19}$$

$\bar{q}$ being a real 2D wavevector, varying continuously. $\phi_{\bar{q}}(\bar{x})$ describes 2D scattering field of a neutron by the same (short-range) potential $V(\bar{x})$ as in Section 5.1.1. More specifically, $\phi_{\bar{q}}(\bar{x})$ is the total 2D wavefunction determined by the incoming 2D plane wave $e^{i\bar{k}\bar{x}}$. Then, $\phi_{\bar{q}}(\bar{x})$ fulfils the 2D inhomogeneous scattering integral equation [101]

$$\phi_{\bar{q}}(\bar{x}) = e^{i\bar{q}\bar{x}} + \int d^2\bar{x}_1 g(\bar{x}-\bar{x}_1) V(\bar{x}_1)\phi_{\bar{q}}(\bar{x}_1) \tag{5.20}$$

$$g(\bar{x}-\bar{x}_1) = \int \frac{d^2\bar{l}}{(2\pi)^2} \frac{e^{i\bar{l}(\bar{x}-\bar{x}_1)}}{(\hbar^2/2m)\,\bar{q}^2 + i\epsilon - (\hbar^2/2m)\,\bar{l}^2} \tag{5.21}$$

$g(\bar{x}-\bar{x}_1)$ is the standard 2D Green's function as in Eq.(3.7) except for an overall change of sign. The above 2D Lippmann-Schwinger equation is the direct 2D counterpart of the standard 3D one [83], to be used in Section 5.2. The integration in Eq.(5.20) is extended over the whole domain, Ω, for which $V(\bar{x}_1) \neq 0$. On the other hand, since $V(\bar{x})$ is attractive (at least in some subdomain of Ω), the 2D Hamiltonian also has a finite number of bound states $\phi_\alpha(\bar{x})$ with eigenvalues $-\frac{\hbar^2\chi_\alpha^2}{2m} < 0$

$$\left[-\frac{\hbar^2}{2m}\Delta_{\bar{x}} + V(\bar{x})\right]\phi_\alpha(\bar{x}) = -\frac{\hbar^2\chi_\alpha^2}{2m}\phi_\alpha(\bar{x}) \tag{5.22}$$

where χ_α is a real number related with the eigenvalue associated with the bound state, $\phi_\alpha(\bar{x})$. This state, $\phi_\alpha(\bar{x})$, vanishes quickly as $\mid \bar{x} \mid \rightarrow +\infty$ and α is a set of indices, characterizing the finite number of bound states. All those states fulfil the following normalization and orthogonality relationships

$$\int d^2\bar{x}\phi_{\bar{q}}(\bar{x})^*\phi_{\bar{q}_1}(\bar{x}) = \delta^{(2)}(\bar{q}-\bar{q}_1) \tag{5.23}$$

$$\int d^2\bar{x}\phi_\alpha(\bar{x})^*\phi_{\bar{q}}(\bar{x}) = 0 \tag{5.24}$$

$$\int d^2\bar{x}\phi_\alpha(\bar{x})^*\phi_{\alpha_1}(\bar{x}) = \delta_{\alpha,\alpha_1} \tag{5.25}$$

where $*$ denotes complex conjugate. $\delta^{(2)}$ is the 2D Dirac delta function. δ_{α,α_1} is the Kronecker symbol (δ_{α,α_1}=0, 1 for $\alpha \neq \alpha_1$, $\alpha = \alpha_1$, respectively). Completeness of all those 2D wavefunctions reads:

$$\sum_{\alpha} \phi_{\alpha}(\bar{x})\,\phi_{\alpha}(\bar{x}_1)^{*} + \int \frac{d^2\bar{l}}{(2\pi)^2}\phi_{\bar{l}}(\bar{x})\,\phi_{\bar{l}}(\bar{x}_1)^{*} = \delta^{(2)}(\bar{x}-\bar{x}_1) \tag{5.26}$$

According to those posible values for $V(\bar{x})$ (i.e.: negative or zero values in the core and positive or zero values in the clad, being, in any case, $V_{clad} > V_{core}$), let there be several possible values of such $V(\bar{x})$ (recall Section 5.1.1) and let $V_{clad,max}$ be the maximum value among all those V_{clad}. Then, the following class of 2D eigenfunctions will be met: (i) a finite set with $\hbar^2\bar{q}^2/2m = -\frac{\hbar^2\chi_{\alpha}^2}{2m} < 0$, (ii) a continuous set with $0 < \hbar^2\bar{q}^2/2m \leq V_{clad,max}$ and (iii) a continuous set with $0 < V_{clad,max} < \hbar^2\bar{q}^2/2m$. The set (ii) may contain a discrete subset of wavefunctions representing resonant states of positive energy. Section 5.5 will deal with (i) and (ii) in somewhat simpler cases with the actual 2D space replaced straightforwardly by the one-dimensional ($1D$) one: in such a case, compare with Figures 5.3 and 5.4.

Combining these results with the propagation along the z-axis by multiplying those 2D wavefunctions by, $e^{ik_z z}$, a 3D wavefunction, $\psi(\boldsymbol{x})$, is obtained. Notice that, for an arbitrary q^2 and some fixed $E(>0)$ and by imposing $k_z^2 = 2mE/\hbar^2 - q^2$, then the 2D set (i) will be associated to propagation modes for neutrons in the 3D waveguide. The 2D set (ii) has a unique and physically appealing feature: it may contain a discrete subset determined by those resonances and corresponding to 3D quasipropagation modes (travelling trapped along the 3D waveguide along certain finite length and, then, escaping from it by tunnelling effect). The 2D set (iii) will be associated to neutrons experiencing reflection or scattering by the 3D waveguide.

Notice, as well, that the possible combinations of q^2 and $E(>0)$, would yield both propagating modes (i.e.: those such that $2mE/\hbar^2 - q^2 \geq 0$) and evanescent waves (in the case that $2mE/\hbar^2 - q^2 \leq 0$).

Arguments presented here are in some manner an extension of the arguments exposed in Section 2.4 for bound states, being more complete and accurate in the present formulation.

5.1.5 $G_1(E)$ and $G_2(E)$ Equivalent Green's Functions

Eqs.(5.11) and (5.18) will play a key role in our development of the Lippmann-Schwinger equations, named LS_1 and LS_2 in Sections 5.2.2 and 5.2.3, respectively. Previously, we have defined the total Green's operator $G(E)$ in terms of the partial hamiltonians operators $G_1(E)$ and $G_2(E)$. We shall give equivalent representations in spatial coordinates, namely, Green's functions, needed to perform simulations.

$G_1(E)$ is the standard Green's operator for the infinite 3D space. The standard Green's function equivalent to it is [83]:

$$\begin{aligned} G_1(\boldsymbol{x}-\boldsymbol{x}_1) &= G_1(\bar{x}-\bar{x_1}, z-z_1) = \\ &= \int \frac{d^2\bar{l}}{(2\pi)^2} \int \frac{dl_z}{2\pi} \frac{e^{i\left(\bar{l}(\bar{x}-\bar{x_1})+l_z(z-z_1)\right)}}{E+i\epsilon-(\hbar^2/2m)\left(\bar{l}^2+l_z^2\right)} \end{aligned} \tag{5.27}$$

By integrating over l_z by residues:

$$G_1(\boldsymbol{x}-\boldsymbol{x_1}) = \int \frac{d^2\bar{l}}{(2\pi)^2} \frac{(-2mi)}{\left(2mE/\hbar^2-\bar{l}^2\right)^{1/2}} e^{i\bar{l}(\bar{x}-\bar{x}_1)} e^{i\left(2m(E+i\epsilon)/\hbar^2-\bar{l}^2\right)^{1/2}|z-z_1|} \tag{5.28}$$

We proceed in a similar way to characterize $G_2(\bar{x}-\bar{x}_1, z-z_1)$. If one compares the 2D Hamiltonian in Section 5.1.4 with the 3D H_2 in Eq.(5.12), the 3D Green's function $G_2(\bar{x}-\bar{x}_1, z-z_1)$, associated to H_2, yields (through a residue integration, similar to that for $G_1(\bar{x}-\bar{x}_1, z-z_1)$) the equivalent Green's function

$$\begin{aligned} G_2(\boldsymbol{x}) =& G_2(\bar{x}-\bar{x}_1, z-z_1) = \\ & \sum_\alpha \phi_\alpha(\bar{x})\,\phi_\alpha(\bar{x}_1)^* \frac{(-2mi)}{(2mE/\hbar^2+\chi_\alpha^2)^{1/2}} e^{i\left(2m(E+i\epsilon)/\hbar^2+\chi_\alpha^2\right)^{1/2}|z-z_1|} + \\ & + \int \frac{d^2\bar{l}}{(2\pi)^2} \phi_{\bar{l}}(\bar{x})\,\phi_{\bar{l}}(\bar{x}_1)^* \frac{(-2mi)}{\left(2mE/\hbar^2-\bar{l}^2\right)^{1/2}} e^{i\left(2m(E+i\epsilon)/\hbar^2-\bar{l}^2\right)^{1/2}|z-z_1|} \end{aligned} \tag{5.29}$$

displaying the propagation modes along the 3D waveguide associated to the 2D bound states $\phi_\alpha(\bar{x})$. For $2mE/\hbar^2-\bar{l}^2<0$, one has evanescent modes for $|\,z-z_1\,|>0$. In this case, we have made explicit the existence of bound (discrete) states and allowed for resonant (continuum) states (see Section 5.5.3).

Notice in the compact Eq.(5.28) (and, also, in Eq.(5.29)) the presence of the absolute value $|\,z-z_1\,|$. This comes from the l_z integration by residues. In fact, in Eq.(5.27) consider: $e^{il_z(z-z_1)} = e^{iRe(l_z)(z-z_1)}.e^{-Im(l_z)(z-z_1)}$, with $l_z = Re(l_z)+iIm(l_z)$, Re and Im denoting real and imaginary parts of l_z. $e^{-Im(l_z)(z-z_1)}$ is exponentially decreasing in $Im(l_z)>0$ for $(z-z_1)>0$ and, so, forces to integrate in Eq.(5.27) by residues in the half-plane $Im(l_z)>0$. And conversely, $(z-z_1)<0$ forces to integrate in Eq.(5.27) by residues in the half-plane $Im(l_z)<0$.

Physically, that absolute value guarantees that the Green function obeys the Sommerfeld radiation condition for the actual sign choice of $+i\epsilon$ (i.e.: outgoing waves).

Notice that, with this representation of $G_1(E)$, Eq.(5.28) includes both propagating waves and evanescent waves depending on $\left(2m(E+i\epsilon)/\hbar^2-\bar{l}^2\right)$ be ≥ 0 or ≤ 0, respectively, which is the complete set of possible solutions in the waveguide entrance.

5.2 3D Integral Equations

Throughout this section, we will study successively convenient scattering integral equations to describe the physical phenomena associated to Section 5.1.1. The starting point for these scattering integrals is the Lippmann-Schwinger equation, [101]. We will use it in conjunction with $G_1(\boldsymbol{x})$ and $G_2(\boldsymbol{x})$ previously formulated. The integral equations in Sections 5.2.4 and 5.2.5 will provide a complete description of the system. Based upon them we will propose an iterative method and obtain the scatteing amplitude integrals.

5.2.1 Derivation of the LS Equations

In [10], it is demonstrated that, if ϕ is a solution of the equation, $H_0\phi = E\phi$, then $\psi = (1 - G_0V)^{-1}\phi$ (where G_0 is the retarded Green's function operator for H_0) is a solution of $(H_0 + V)\psi = E\psi$. In this case, ψ satisfies the Lippmann-Schwinger equation, [101], $\psi = \phi + G_0V\psi$, ϕ being the incoming wave.

It is more convenient for us to use the integral form under differential equation. See, for example [103]. The integral equation bears the structure (with $\phi = \psi_{in}$)

$$\psi(\bar{x}, z) = \psi_{in}(\bar{x}, z) + \int d^2\bar{x}_1 \int_0^{+\infty} dz_1 G_1(\bar{x} - \bar{x}_1, z - z_1) V(\bar{x}_1) \psi(\bar{x}_1, z_1) \quad (5.30)$$

This Lippmann-Schwinger equation relates the total wavefunction $\psi(\boldsymbol{x})$ with the incoming wave $\psi_{in}(\boldsymbol{x})$ for a particular Hamiltonian.

If one bases on equations Eq.(5.11) and Eq.(5.18), quantum scattering theory [104], [105], [106] provides a useful recipe justifying the 3D Lippmann-Schwinger equation. The recipe is based upon the formula

$$\psi(\boldsymbol{x}) = \lim_{\epsilon^+ \to 0} (+i\epsilon) G(E) \psi_{in}(\boldsymbol{x}) \quad (5.31)$$

where ϵ^+ means $\epsilon > 0$. Notice that, in this case, $G(E)$ is the one corresponding to Eq.(5.6).

5.2.2 LS_1 Equation

The application of the recipe, Eq.(5.31), provides the standard LS_1 equation [101, 83]. In fact, for that purpose, one replaces $G(E)$ by the right-hand-side of Eq.(5.11) (in terms of $G_1(E)$). The limit of $+i\epsilon G_1(E)\psi_{in}(\bar{x}, z)$ yields the wavefunction $\psi_{in}(\bar{x}, z)$. $\psi(\bar{x}, z)$ fulfils the well-known 3D inhomogeneous linear integral equation for $-\infty < z < +\infty$ (the 3D Lippmann-Schwinger equation):

$$\psi(\bar{x}, z) = \psi_{in}(\bar{x}, z) + \int d^2\bar{x}_1 \int_0^{+\infty} dz_1 G_1(\bar{x} - \bar{x}_1, z - z_1) V(\bar{x}_1) \psi(\bar{x}_1, z_1) \quad (5.32)$$

which bears the same structure as the integration in Eq.(5.31) is extended over the whole domain in which $V(\bar{x}_1) \neq 0$. Notice that $V_1(\boldsymbol{x}_1)$ has been replaced by $V(\bar{x}_1)$, by using Eq.(5.8). This equation was used in [3] and [107] to characterize the incoming waves that could give rise to propagation modes in non-absorbing and absorbing optical waveguides, respectively. In any case, neither Eq.(5.32) nor its iterations display explicitly the possibility that the neutron could propagate confined along the waveguide.

Eq.(5.32), to be referred as LS_1 equation, is a useful representation for $\psi(\bar{x}, z)$ in $-\infty < z < 0$ in terms of all values of $\psi(\bar{x}, z)$ in $0 < z < +\infty$ and any $\bar{x}$. For $0 < z < +\infty$, Eq.(5.32), even if a correct one, is not a suitable integral equation for $\psi(\bar{x}, z)$ in $0 < z < +\infty$ as it stands. Difficulties due to the infinite length of the semi-infinite waveguide (and the independence of $V(\bar{x}_1)$ on z_1)) arise upon iterating it. Such difficulties will be named *secular terms*. In fact, for $0 < z < +\infty$ the first iteration of Eq.(5.32) after integrating in $0 \leq z_1 < +\infty$ (leaving aside other factors and contributions) gives rise to: $\int d^2\bar{l}[e^{ik_z z} - e^{i(2m(E+i\epsilon)/\hbar^2 - \bar{l}^2)^{1/2} z}]/[i(k_z - (2mE/\hbar^2 - \bar{l}^2)^{1/2})]$. The latter integral, upon integrating in a domain with $(2m(E+i\epsilon)/\hbar^2 - \bar{l}^2)^{1/2}$ near k_z, yields a contribution proportional to z (a *secular term*), say, an increasing behaviour with length, neatly different from the physically natural ones (oscillatory or evanescent), hindering the interpretation of probabilities. The successive iterations of Eq.(5.32) give rise to increasing powers of z (higher *secular terms*), in direct correspondence with the repeated integrals $\int_0^{+\infty} dz_1 \int_0^{+\infty} dz_2$ and so on, generated by those iterations. Although those difficulties could be dealt with by invoking a systematic order by order procedure [106], one should explore further alternatives aimed to obtain probabilities in a more direct and manageable way.

In spite of the above shortcomings, Eq.(5.32) for $0 < z < +\infty$ will be essential for the improving developments in Sections 5.2.4 and 5.2.5.

A genuine feature of this formulation is that the amplitude and probability for the slow neutron to be scattered by the actual waveguide along a direction parallel to the incoming wavector diverges. The key is the semiinfinite waveguide length, which has to be maintained in the model. To illustrate this statement, one may study the 3D scattering amplitude for incoming wavevector $\left(\bar{k}, k_z\right)$ and outgoing one $\left(\bar{k}_1, k_{z,1}\right)$, which follows from Eq.(5.32) in a standard way [83], [106]. It is easy to check that the (Born) scattering amplitude diverges as $\left(\bar{k}_1, k_{z,1}\right)$ approaches $\left(\bar{k}, k_z\right)$ (forward direction), due to the infinite length of the semi-infinite waveguide ($V(\bar{x}_1)$ being independent on z_1). After the improving developments in Sections 5.2.4 and 5.2.5, the new scattering amplitude will also be seen to diverge as $\left(\bar{k}_1, k_{z,1}\right) \rightarrow \left(\bar{k}, k_z\right)$, as one can see in Section 5.4.

Notice that, contrary to the above 3D LS_1 in Eq.(5.32), the 2D Eq.(5.20) can indeed be solved by successive iterations without those difficulties (as it lacks structures like $\int_0^{+\infty} dz_1$).

5.2.3 LS_2 Equation

As in the previous case, one can derive the corresponding (although less familiar) Lippmann-Schwinger equation associated to $G_2(E)$ (Eq.(5.18)) and also determined by the incoming wave $\psi_{in}(\bar{x})$. We apply again the recipe, Eq.(5.31). In this case, one replaces $G(E)$ by the right-hand-side of Eq.(5.18) (in terms of $G_2(E)$). The limit of $+i\epsilon G_2(E)\psi_{in}(\bar{x},z)$ yields the inhomogeneous term $\phi_{\bar{k}}(\bar{x})e^{ik_z z}$, when use is made of Section 5.1.4. One finds the whole LS_2 equation.

Use will be made of Eqs.(5.15)-(5.16) to avoid further writing of V_2. Then, in $-\infty < z < +\infty$ the total wavefunction $\psi(\bar{x},z)$ (satisfying Eq.(5.32)) also fulfils the inhomogeneous linear integral equation (to be referred to as the LS_2 equation):

$$\psi(\bar{x},z) = \phi_{\bar{k}}(\bar{x})e^{ik_z z} + \\ + \int d^2\bar{x}_1 \int_{-\infty}^{0} dz_1 G_2(\bar{x}-\bar{x}_1, z-z_1)\left[-V(\bar{x}_1)\right]\psi(\bar{x}_1,z_1) \tag{5.33}$$

Comparing (the interaction-free) H_1 and G_1 for the LS_1, Eq.(5.32), with the actual LS_2, Eq.(5.33), it is clear that one deals with H_2 and G_2 (containing interactions in 2D space). Moreover, the role of the inhomogeneous term (incoming free plane wave) $\psi_{in}(\boldsymbol{x})$ for Eq.(5.32) is now played by $\phi_{\bar{k}}(\bar{x})e^{ik_z z}$ (determined in turn by $\psi_{in}(\boldsymbol{x})$) in the LS_2, Eq.(5.33).

Eq.(5.33) has the good feature that it displays, through $G_2(\bar{x}-\bar{x}_1, z-z_1)$, 2D bound-state contributions which give rise to 3D propagation modes. However, the successive iterations of the LS_2, Eq.(5.33), for $-\infty < z < 0$, suffer of similar difficulties also due to the infinite length of the semi-infinite waveguide. In this case, the *secular terms* associated to Eq.(5.33), for $-\infty < z < 0$, give rise to the repeated integrals $\int_{-\infty}^{0} dz_1 \int_{-\infty}^{0} dz_2$ and so on.

5.2.4 The $LS_1 \rightarrow LS_2$ Equation, for $-\infty < z < 0$

To overcome the difficulties associated to the *secular terms*, the pair formed by Eqs.(5.32) and (5.33) suggest the following approximation method: (i) in Eq.(5.32) for $-\infty < z < 0$, one replaces inside the integral over $0 < z_1 < +\infty$ in its right-hand-side $\psi(\bar{x}_1, z_1)$ by $\phi_{\bar{k}}(\bar{x}_1,)e^{ik_z z_1}$ (ii) in Eq.(5.33) for $0 < z < +\infty$, one replaces inside the integral over $-\infty < z < 0$ in its right-hand-side $\psi(\bar{x}_1, z_1)$ by $\psi_{in}(\bar{x}_1, z_1)$. The latter approximation in (ii) is different from the first iteration of Eq.(5.32) alone and constitute an improved approximation that amount to reorderings and resummations of the latter approximations.

The LS_1 and the LS_2 equations will now be combined into a new scattering integral equation (to be referred to as the $LS_1 \rightarrow LS_2$ equation) yielding the total wave function $\psi(\bar{x},z)$ in $-\infty < z < 0$, as follows. Upon considering Eq.(5.32) for

$-\infty < z < 0$ and replacing in its right-hand-side $\psi(\bar{x}_1, z_1)$ by the right-hand-side of Eq.(5.33) for $0 < z < +\infty$, one arrives at the $LS_1 \rightarrow LS_2$ in $-\infty < z < 0$:

$$\psi(\bar{x}, z) = \psi_{in}(\boldsymbol{x}) + \int d^2\bar{x}_1 \int_0^{+\infty} dz_1 G_1(\bar{x} - \bar{x}_1, z - z_1) V(\bar{x}_1) \phi_{\bar{k}}(\bar{x}_1) e^{ik_z z_1} + \\ + \int d^2\bar{x}_1 \int_0^{+\infty} dz_1 G_1(\bar{x} - \bar{x}_1, z - z_1) V(\bar{x}_1) \times \\ \int d^2\bar{x}_2 \int_{-\infty}^{0} dz_2 G_2(\bar{x}_1 - \bar{x}_2, z_1 - z_2) [-V(\bar{x}_2)] \psi(\bar{x}_2, z_2) \tag{5.34}$$

This equation displays explicitly the propagation modes (through G_2). Moreover, its successive iterations contain $\int_0^{+\infty} dz_1$ and $\int_{-\infty}^{0} dz_2$ alternatively since the term $\psi(\bar{x}_i, z_i), i = 1...n$ will be alternatively replaced by its representation in LS_1 (Eq.(5.32)) or LS_2 (Eq.(5.33)) for each iteration. Notice that this implies characterizing alternatively the wavefunction by $G_1(\boldsymbol{x} - \boldsymbol{x_1})$ or $G_2(\boldsymbol{x} - \boldsymbol{x_1})$. This constitutes an improvement (regarding the suppression of *secular terms*) compared to the separate LS_1 and LS_2 equations.

5.2.5 The $LS_2 \rightarrow LS_1$ Equation, for $0 < z < +\infty$

Next, the LS_1 and LS_2 equations will be combined into a new scattering integral equation (to be referred to as the $LS_2 \rightarrow LS_1$ equation) giving the total wave function $\psi(\bar{x}, z)$ in $0 < z < +\infty$, as follows. Upon considering Eq.(5.33) for $0 < z < +\infty$ and replacing in its right-hand-side $\psi(\bar{x}_1, z_1)$ by the right-hand-side of Eq.(5.32) for $-\infty < z < 0$, one gets the $LS_2 \rightarrow LS_1$ equation in $0 < z < +\infty$:

$$\psi(\bar{x}, z) = \phi_{\bar{k}}(\bar{x}) e^{ik_z z} + \int d^2\bar{x}_1 \int_{-\infty}^{0} dz_1 G_2(\bar{x} - \bar{x}_1, z - z_1) [-V(\bar{x}_1)] \psi_{in}(\bar{x}_1, z_1) + \\ + \int d^2\bar{x}_1 \int_{-\infty}^{0} dz_1 G_2(\bar{x} - \bar{x}_1, z - z_1) [-V(\bar{x}_1)] \times \\ \int d^2\bar{x}_2 \int_0^{+\infty} dz_2 G_1(\bar{x}_1 - \bar{x}_2, z_1 - z_2) V(\bar{x}_2) \psi(\bar{x}_2, z_2) \tag{5.35}$$

As in Section 5.2.4, the above equation also displays explicitly the propagation modes (through G_2 and its successive iterations contain $\int_{-\infty}^{0} dz_1$ and $\int_0^{+\infty} dz_2$ alternatively. So, Eq.(5.35) is more suitable for describing the wavefunction behaviour for z positive (i.e.: the waveguide).

5.3 Neutron Wavefunction Behaviour

5.3.1 Region $z < 0$: Reflection Scattering Amplitudes

For $z < 0$, by using Eq.(5.28) for $G_1\left(\bar{x} - \bar{x}_1, z - z_1\right)$, the $LS_1 \rightarrow LS_2$ Eq.(5.34) yields

$$\psi\left(\bar{x}, z\right) = \psi_{in}\left(\bar{x}, z\right) + \\ + \int \frac{d^2\bar{l}}{\left(2\pi\right)^2} e^{i\bar{l}\bar{x}} e^{-iz\left(2m(E+i\epsilon)/\hbar^2 - \bar{l}^2\right)^{1/2}} T_{ref}\left(\vec{l}\right) \tag{5.36}$$

The integral is convergent (due to $\int d^2\bar{l}$), so that $\psi\left(\bar{x}, z\right)$ is indeed finite (see next paragraph). The $+i\epsilon$ in the exponential in Eq.(5.36) warrants the correct (vanishing) behaviour of the evanescent contributions as $z \rightarrow -\infty$ (the corresponding comment will apply for Eq.(5.38) as $z \rightarrow +\infty$).

For $2mE/\hbar^2 - \bar{l}^2 \geq 0$, one has oscillatory behaviour in $z < 0$ and $T_{ref}\left(\vec{l}\right)$ is the reflection amplitude of the slow neutron by the waveguide. For $2mE/\hbar^2 - \bar{l}^2 < 0$, one has an evanescent behaviour in $z < 0$. Eq.(5.32) also yields Eq.(5.36) for $z < 0$. It is far more convenient to express $T_{ref}\left(\vec{l}\right)$ in terms of ψ, by using Eq.(5.34) and Eq.(5.28). As Eq.(5.34) in $-\infty < z < 0$ is iterated successively, one generates an infinite series for ψ into powers of V and the 2D eigenfunctions ϕ_l ´s and ϕ_α ´s (the latter two also depending on V). This series gives rise, as indicated above, to an infinite series for $T_{ref}\left(\vec{l}\right)$. All terms in such a series are finite if $E > 0$, $k_z > 0$, $2mE/\hbar^2 - l^2 \neq 0$.

The lowest approximation reads:

$$T_{ref}(l)_0 = \frac{(-im)}{\hbar^2(2mE/\hbar^2 - l^2)^{1/2}} \frac{i\int d^2x \phi_k(x) V(x) e^{-ilx}}{k_z + (2mE/\hbar^2 - l^2)^{1/2}} \tag{5.37}$$

which is, indeed, finite and will be used in (2D) numerical simulations performed in Section 5.5.5.

5.3.2 Region $z > 0$: Propagation Modes and Scattering Amplitudes

For $z > 0$, by using Eq.(5.29) for $G_2\left(\bar{x} - \bar{x}_1, z - z_1\right)$, the $LS_2 \rightarrow LS_1$ Eq.(5.35) yields:

$$\psi\left(\bar{x}, z\right) = \phi_{\bar{k}}\left(\bar{x}\right) e^{ik_z z} + \sum_\alpha \phi_\alpha\left(\bar{x}\right) e^{i\left(2m(E+i\epsilon)/\hbar^2 + \chi_\alpha^2\right)^{1/2} z} T_{pm,\alpha} \\ + \int \frac{d^2\bar{l}}{\left(2\pi\right)^2} . \phi_{\bar{l}}\left(\bar{x}\right) e^{i\left[\left(2m(E+i\epsilon)/\hbar^2 - \bar{l}^2\right)^{1/2} z\right]} T_{scat}\left(\vec{l}\right) \tag{5.38}$$

where $T_{pm,\alpha}$ is the amplitude for the slow neutron to propagate confined along the waveguide in the α-th propagation mode.

For $2mE/\hbar^2 - \bar{l}^2 \geq 0$, one has oscillatory behaviour in $z > 0$ and $T_{scat}\left(\vec{l}\right)$ is the amplitude for the slow neutron to be scattered by the waveguide. For $2mE/\hbar^2 - \bar{l}^2 < 0$, one has evanescent behaviour in $z > 0$. Eq.(5.33) also yields Eq.(5.38) for $z > 0$. Let $2mE/\hbar^2 - \bar{l}^2 \neq 0$, $E > 0$, $k_z > 0$. It is more adequate to express $T_{pm,\alpha}$ and $T_{scat}\left(\vec{l}\right)$ in terms of ψ, by using Eq.(5.35). When Eq.(5.35) in $0 < z < +\infty$ is iterated successively, one generates an infinite series for ψ into powers of V and the 2D eigenfunctions ϕ_l´s and ϕ_α´s. This series gives rise, as indicated above, to two separate infinite series for $T_{pm,\alpha}$ and $T_{scat}\left(\vec{l}\right)$. All terms in such a series for $T_{pm,\alpha}$ are finite ones.

The lowest order approximation reads

$$T_{pm,\alpha_0} = \frac{(-2im)}{\left(2mE/\hbar^2 + \chi_\alpha^2\right)^{1/2}} \quad \frac{i\int d^2\bar{x}\phi_\alpha\left(\bar{x}\right)^* e^{i\bar{k}\bar{x}}\left[-V\left(\bar{x}\right)\right]}{\left(2mE/\hbar^2 + \chi_\alpha^2\right)^{1/2} - \left(2mE/\hbar^2 - \bar{k}^2\right)^{1/2}} \tag{5.39}$$

In the case of $T_{scat}\left(\vec{l}\right)$, it is adequate to decompose it as

$$T_{scat}\left(\vec{l}\right) = T_{scat,1}\left(\vec{l}\right) + T_{scat,2}\left(\vec{l}\right) \tag{5.40}$$

$$T_{scat,1}\left(\vec{l}\right) = \frac{(-2im)}{\left(2mE/\hbar^2 - \bar{l}^2\right)^{1/2}} \quad \frac{(-i)\int d^2\bar{x}\phi_{\bar{l}}\left(\bar{x}\right)^* e^{i\bar{k}\bar{x}}\left[-V\left(\bar{x}\right)\right]}{k_z - \left(2mE/\hbar^2 - \bar{l}^2\right)^{1/2}} \tag{5.41}$$

In this case, $T_{scat,1}\left(\vec{l}\right)$ is the contribution due to the first term on the right-hand-side of Eq.(5.35), in $0 < z < +\infty$. $T_{scat,2}\left(\vec{l}\right)$ is the infinite series formed by all contributions to $T_{scat}\left(\vec{l}\right)$ except the lowest one, given in $T_{scat,1}\left(\vec{l}\right)$. That is, $T_{scat,2}\left(\vec{l}\right)$ arises from all higher iterations (except the first one) of Eq.(5.35) in $0 < z < +\infty$.

As Eq.(5.41) shows, due to the denominator $\left[k_z - \left(2mE/\hbar^2 - \bar{l}^2\right)^{1/2}\right]^{-1}$, $T_{scat,1}\left(\vec{l}\right)$ diverges as $\bar{l} \to \bar{k}$ (say, in the forward direction). $T_{scat,2}\left(\vec{l}\right)$ is finite for $2mE/\hbar^2 - \bar{l}^2 \neq 0$, $E > 0$, $k_z > 0$, as so are all terms in the infinite series contribution to it. In Eq.(5.38), the integration over $d^2\bar{l}$ overcomes the divergence of $T_{scat,1}\left(\vec{l}\right)$ as $2mE/\hbar^2 - \bar{l}^2 \to 0$ and gives rise to a convergent integral.The contribution of $T_{scat,2}\left(\vec{l}\right)$ to Eq.(5.38) is also finite. Then, $\psi\left(\bar{x}, z\right)$ in $z > 0$ is indeed finite.

Summarizing, the $LS_1 - LS_2$ and $LS_2 \to LS_1$ equations enable to get rid of all difficulties in the successive iterations involved in obtaining T_{ref}, $T_{pm,\alpha}$ and $T_{scat,2}$. The same are always finite for $E \neq 0$ and $k_z \neq 0$. However, there is still just one contribution which is divergent in the special case $\bar{l} \to \bar{k}$ (forward direction), namely, $T_{scat,1}\left(\vec{l}\right)$. Then, it follows that $T_{scat}\left(\vec{l}\right)$ also diverges as $\bar{l} \to \bar{k}$. In order to display explicitly the possible confined propagation, the Green's operator $G_2\left(E\right)$ and the LS_2 equation have been employed. The divergence for the forward direction remains (as it is inherent to the infinite length of the semi-infinite waveguide), but the approach in Sections 5.2.4 and 5.2.5 has enabled to isolate it compactly in $T_{scat,1}\left(\vec{l}\right)$.

5.4 Probability Fluxes

In this section we will demonstrate that the contribution of the divergence of $T_{scat,1}$ in the forward direction to the total probability flux cancels.

The probability flux of the wavefunction, $\psi(\bar{x}, z)$, across an infinite plane orthogonal to the z-axis at the position z is

$$Flux(z) = \int d^2\bar{x} \frac{\hbar}{m} Re\left[-i\psi(\bar{x}, z)^* \frac{\partial}{\partial z}\psi(\bar{x}, z)\right] \tag{5.42}$$

where Re denotes the real part.

Conservation of the total probability flux reads

$$Flux(\bar{x}, z < 0) = Flux(\bar{x}, z > 0) \tag{5.43}$$

We state three main contributions to the total flux in Ω:

Incoming flux: For the incoming plane wave, upon replacing $\psi(\bar{x}, z)$ by $\psi_{in}(\boldsymbol{x})$:

$$Flux_{in}(z) = \int d^2\bar{x} \frac{\hbar k_z}{m} \tag{5.44}$$

which diverges due to the infinite extension of the XY-plane.

Reflected flux: For $z < 0$ with $z \to -\infty$, Eqs.(5.36) and (5.42) yield the total flux for the total wave function $\psi(\bar{x}, z)$:

$$\begin{aligned} &Flux(z, z < 0) = \\ &\quad = \int d^2\bar{x} \frac{\hbar k_z}{m} - \frac{\hbar}{m} \int_{\left(2mE/\hbar^2 - \bar{l}^2\right)^{1/2} \geq 0} \frac{d^2\bar{l}}{(2\pi)^2} \left(2mE/\hbar^2 - \bar{l}^2\right)^{1/2} \mid T_{ref}\left(\bar{l}\right) \mid^2 \end{aligned} \tag{5.45}$$

Confined and scattered flux: For $z > 0$ with $z \to +\infty$, Eqs.(5.38) and (5.42) yield the total flux:

$$\begin{aligned} Flux(z, z > 0) = &\int d^2\bar{x} \frac{\hbar k_z}{m} + \frac{\hbar}{m} \sum_\alpha \left(2mE/\hbar^2 + \chi_\alpha^2\right)^{1/2} \mid T_{pm,\alpha} \mid^2 + \\ &+ \frac{\hbar}{m} \int_{\left(2mE/\hbar^2 - \bar{l}^2\right)^{1/2} \geq 0} \frac{d^2\bar{l}}{(2\pi)^2} \left(2mE/\hbar^2 - \bar{l}^2\right)^{1/2} \mid T_{scat}\left(\bar{l}\right) \mid^2 + \\ &+ \frac{\hbar k_z}{m} Re\left[T_{scat}\left(\bar{k}\right) + T_{scat}\left(\bar{k}\right)^*\right] \end{aligned} \tag{5.46}$$

Notice that evanescent waves do not contribute to either $Flux(z, z < 0)$ or $Flux(z, z > 0)$. Both $Flux(z, z < 0)$ and $Flux(z, z > 0)$ contain divergent contributions.

The probability flux for the neutron to propagate confined as the α-th propagation mode, normalized to the incoming flux per unit area, is

$$\frac{1}{\hbar k_z/m}\frac{\hbar}{m}\left(2mE/\hbar^2+\chi_\alpha^2\right)^{1/2}\mid T_{pm,\alpha}\mid^2 \tag{5.47}$$

By replacing $T_{pm,\alpha}$ by T_{pm,α_0} (Eq.(5.37)), one gets the following approximate normalized probability flux for the neutron to propagate confined as the α-th propagation mode

$$\frac{1}{\hbar k_z/m}\frac{\hbar}{m}\left(2mE/\hbar^2+\chi_\alpha^2\right)^{1/2}\mid T_{pm,\alpha_0}\mid^2 \tag{5.48}$$

Notice that Eq.(5.48) is a counterpart of a related approximation given in Section 2.5 for the probability for an incoming slow neutron to propagate confined along a semi-infinite waveguide. Since both formulations describe the same physical phenomena, it is expected that they yield similar results.

Recalling the divergent contributions mentioned, by using Eqs.(5.45), (5.46) and (5.43) and cancelling out the divergent $\int d^2\bar{x}\frac{\hbar k_z}{m}$ (incoming flux), Eq.(5.43) becomes:

$$\begin{aligned}&\frac{\hbar}{m}\int_{\left(2mE/\hbar^2-\bar{l}^2\right)^{1/2}\geq 0}\frac{d^2\bar{l}}{(2\pi)^2}\left(2mE/\hbar^2-\bar{l}^2\right)^{1/2}\mid T_{ref}\left(\vec{l}\right)\mid^2+\\&+\frac{\hbar}{m}\sum_\alpha\left(2mE/\hbar^2+\chi_\alpha^2\right)^{1/2}\mid T_{pm,\alpha}\mid^2+F_{scat,fin}=0\end{aligned} \tag{5.49}$$

$$\begin{aligned}F_{scat,fin}=&\frac{\hbar k_z}{m}Re\left[T_{scat}\left(\bar{k}\right)+T_{scat}\left(\bar{k}\right)^*\right]+\\&+\frac{\hbar}{m}\int_{\left(2mE/\hbar^2-\bar{l}^2\right)^{1/2}\geq 0}\frac{d^2\bar{l}}{(2\pi)^2}\left(2mE/\hbar^2-\bar{l}^2\right)^{1/2}\mid T_{scat,1}\left(\vec{l}\right)+T_{scat,2}\left(\vec{l}\right)\mid^2\end{aligned} \tag{5.50}$$

In Eq.(5.49), the first two contributions in the left-hand-side are finite. Then, the third contribution in the left-hand-side, namely $F_{scat,fin}$, has to be also finite. The point is that the divergent terms in Eq.(5.50) resemble, term by term, with the contributions in Eq.(B.5) as the latter fulfils the *2D optical theorem*. For more details, see Appendix B.

In fact, Eq.(5.49) is a generalization of the *standard optical theorem*, [83], [106] for the actual 3D interaction of the slow neutron with the semi-infinite waveguide. Eq.(5.49) is the counterpart for the actual 3D semi-infinite waveguide without any infinitely extended clad having an infinitely repulsive potential (no Dirichlet conditions) of another generalized optical theorem for a 2D semi-infinite waveguide with the opposite clad structure (namely, an infinitely extended clad with an infinitely repulsive potential and, so, with Dirichlet conditions), presented in Section 3.3.

The (finite) total probability flux for reflection is given by the first contribution in the left-hand-side of Eq.(5.49). A related computation of the total probability for

reflection proceeds, in short, as follows. Starting from Eq.(5.32), we introduce, in the standard way [83], [106], the 3D amplitude for the slow neutron to be scattered with outgoing wavevector $\left(\bar{k}_1, k_{z,1}\right)$ $\left(E = \left(\bar{k}_1^2 + k_{z,1}^2\right)/2m\right)$

$$f\left(\boldsymbol{k}_1, \boldsymbol{k}\right) = -\left(m/2\pi\hbar^2\right) \int d^2\bar{x}_1 \int_0^{+\infty} dz_1 e^{-i\left(\bar{k}_1\bar{x} + k_{z,1}z\right)} V\left(\bar{x}_1\right) \psi\left(\bar{x}_1, z_1\right) \qquad (5.51)$$

where ψ is given by the right-hand-side of Eq.(5.35).

This scattering amplitude is easily seen to diverge for $\left(\bar{k}_1, k_{z,1}\right) \rightarrow \left(\bar{k}, k_z\right)$ (forward direction), due to the infinite length of the semi-infinite waveguide. In addition, the integral of $\mid f\left(\left(\bar{k}_1, k_{z,1}\right), \left(\bar{k}, k_z\right)\right) \mid^2$ by integrating over all angles corresponding to $k_{z,1} < 0$ yields the total scattering cross section for backward scattering (which, in turn, is finite and corresponds to the total probability for reflection). The total scattering cross section, by integrating over all angles corresponding to $k_{z,1} < 0$ and $k_{z,1} > 0$, diverges.

5.5 Numerical Results

We have performed numerical simulations for the scattering amplitudes including reflection ones ($T_{scat}\left(\vec{l}\right)$ and $T_{ref}\left(\vec{l}\right)$), for different impinging neutron angles. So far to this point, equations in the general 3D case have been developed. However, in order to obtain results, a 2D waveguide (i.e.: a thin film) disregarding the y coordinate will be considered. Correspondingly, typical wavefunctions for 2D are $\psi(\boldsymbol{x}) = \phi\left(x\right) e^{ik_z z}$ and superpositions thereof.

While, in previous equations, we displayed explicitly the dependences of the neutron wavefunctions in the z coordinate, if a simulation is to be performed, we need to obtain first the corresponding behaviours in the transverse 1D coordinate (say, $\phi\left(x\right)$). The actual 1D potential $V\left(x\right)$ to be considered here will be analogous to $V\left(\bar{x}\right)$ in Section 5.1.4, with one additional qualification regarding condition (iii): we will set V to be strictly attractive (constant and < 0) only in the waveguide's core. In the waveguide's clad, V will be finitely repulsive, taking on one or several finite constant values $V_{clad} > 0$ (See Figures 5.2a and 5.2b).

Standard quantum-mechanical continuity conditions for $\phi\left(x\right)$ and $d\phi\left(x\right)/dx$ at the points where V has finite discontinuities (and so on for $\phi\left(x\right)$ at points with infinite discontinuities) will be understood.

5.5.1 Propagation Modes

Let us assume an incoming neutron beam represented by a plane wave of arbitrary angle of incidence; $\psi_{in}(\boldsymbol{x}) = \psi_{in}\left(x, z\right) = e^{ik_x x} e^{ik_z z} = e^{i\boldsymbol{k_{in}}\boldsymbol{x}}$ with associated 2D wavevector $\boldsymbol{k_{in}} = \left(k_x, k_z\right)$. For a thermal neutron: $E = 0.025$ eV, $\mid \boldsymbol{k_{in}} \mid = \sqrt{k_x^2 + k_z^2} = 3.47$ Å^{-1}.

Two cases of layers arrangements (clad and core) will be simulated, displayed in Figure 5.2a (Si-Ti-Si symmetrical waveguide) and Figure 5.2b (Si-Ti waveguide located over a highly repulsive substrate that will be understood as not allowing neutrons to penetrate inside) both of them in a relatively large domain surrounded by vacuum $V = 0$. Notice that in Figure 5.2a the origin of coordinates is located at the core center while in Figure 5.2b is located in the Ti-substrate interlayer.

The first layers arrangement, Si-Ti-Si waveguide (Figure 5.2a), matches with the proposals in forthcoming Chapter 6 and is a natural extension of the analysis in Section 2.5. The second one, Si-Ti-substrate waveguide (Figure 5.2b), is closer to actual experiments on neutron waveguiding (see, for example, [13] and [108]). Anyway, in those cases, the experimental device is designed with lateral coupling to control angle of incidence and improve waveguide efficiency (it has not been considered here). In both of the cases analysed here, the thermal neutron beam impinges on the waveguide entrance, directly to the Ti core. This is kept for internal comparison over those two simulations. Both cases, even if similar (as infinitely extended plane waves will continue to be employed) imply a different arrangement of layers (waveguide clad and core as well as symmetries) and, consequently, the arising propagation modes will be different ones.

The eigenfunctions that solve Eqs.(5.19) or (5.22) relate, in this case, with the angle of incidence of the neutron beam. As stated in Section 5.1.4, when examining the energy eigenvalues for these eigenfunctions, one finds three possibilities:

Negative energies: These eigenfunctions constitute a discrete set and correspond (provided that the z-dependence be included) to confined propagation modes. They have the 2D structure: $\psi(\boldsymbol{x}) = \phi_\alpha(x)\, e^{iz\left(2m(E+i\epsilon)/\hbar^2+\chi_\alpha^2\right)^{1/2}}$. Since these modes cannot give rise to free propagation in vacuum, they propagate along the waveguide without losses (as no absorption is assumed in the material).

Positive energy lower than $V_{clad,max}$: Their structure is: $\psi(\boldsymbol{x}) = \phi_{\boldsymbol{q}}(x)e^{iq_z z}$. These eigenfunctions constitute a continuous set. In this energy region there may be a discrete subset of eigenfunctions that correspond to resonant levels and behave as quasidiscrete propagation modes. These states are different from those mentioned above, as they describe travelling neutrons trapped in the waveguide along some propagation distance, escaping from it (via tunnelling effect) and, finally, propagating in free space. Consequently, these excited modes amount to effective losses in the waveguide (even if there are no absorption in the material, since V is real).

Positive energy higher than $V_{clad,max}$: These eigenfunctions are continuous and not trapped in the waveguide, so that they will be disregarded here.

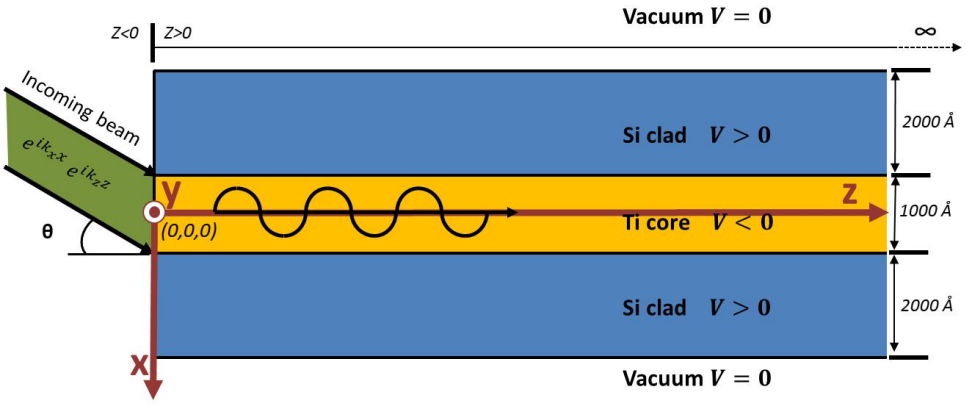

(a)

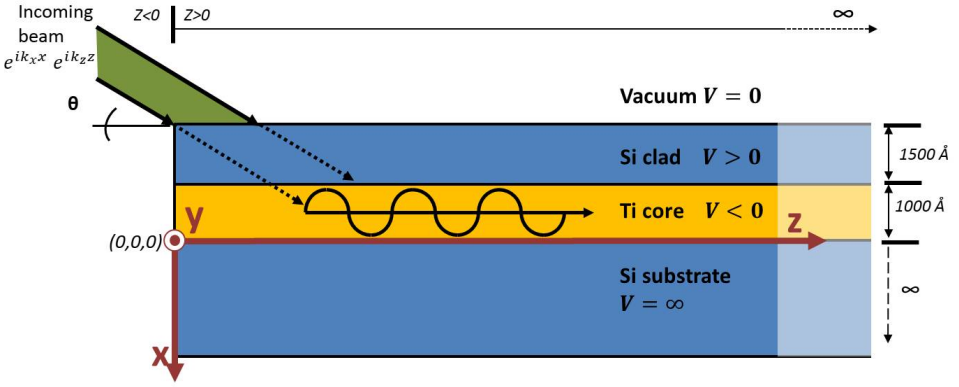

(b)

Figure 5.2: Layer arrangement for (a) Si-Ti-Si waveguide and (b) Si-Ti over a substrate with a highly repulsive potential. Adapted from [102]

5.5.2 Structure of the Energy Levels

We will focus in Si and Ti as suitable materials (clad and core, respectively) for neutron waveguiding. We summarize in Table 5.1 their experimental data to be applied, (see [8, 9])

Table 5.1: Data and potential values for Si and Ti

Material	ρ (kg/m^3)	b (m)	V (eV)	$4\pi b\rho$ (Å^{-2})
Ti	4507	-3.438×10^{-15}	-5.0798×10^{-8}	-2.4497×10^{-5}
Si	2330	4.150×10^{-15}	5.4028×10^{-8}	2.6054×10^{-5}

Using the values in Table 5.1, the 1D transverse section of the 2D waveguide is characterized, as will the possible propagation modes and continuum wavefunctions that will arise. These functions are the eigenfunctions fulfilling Eqs. (5.19) and (5.22) and can be solved asuming the potential $V(x)$ as a combination of potential barriers and wells.

The standard procedure is to represent the various $\phi(x)$ as linear combinations of arbitrary amplitudes times suitable plane waves or real exponentials (linear in x). Then we formulate the continuity equations for $\phi(x)$ and $d\phi(x)/dx$ at the points where V is discontinuous, and solve the resulting system of equations for the amplitudes (see for example [78]).

In the case of a Si-Ti-Si waveguide impinged by a thermal neutron beam with an arbitrary θ angle (directly to the Ti core, see Figure 5.2a), the potential is set to be a potential well 1000 Å wide in the center, corresponding to the Ti core negative potential, surrounded by two 2000 Å potential barriers corresponding to the Si clad. In this case, our simulation yields three energy levels, represented in Figure 5.3. Two of them are discrete bound-state levels, Σ_0, Σ_1, ($E_{\Sigma_0} < 0$, $E_{\Sigma_1} < 0$, so there is no wave propagation in free space). The third one corresponds to an unbound-state level, Σ_2. This level is not, in a strict sense, a discrete level since it has positive energy, but it could be regarded as a quasidiscrete solution of the system of equations. It will be interpreted in Section 5.5.3 as a resonance in the continuum of eigenfunctions and physically it will yield some sort of unstable propagation mode with neutron losses across the clad via tunnel effect. For last, in those cases with energies higher that the clad potential, $V_{Si} = 5.4 \times 10^{-8}$ eV, there is a continuum of wavefunctions for any energy with different wavenumber depending on the region (free space, clad or core).

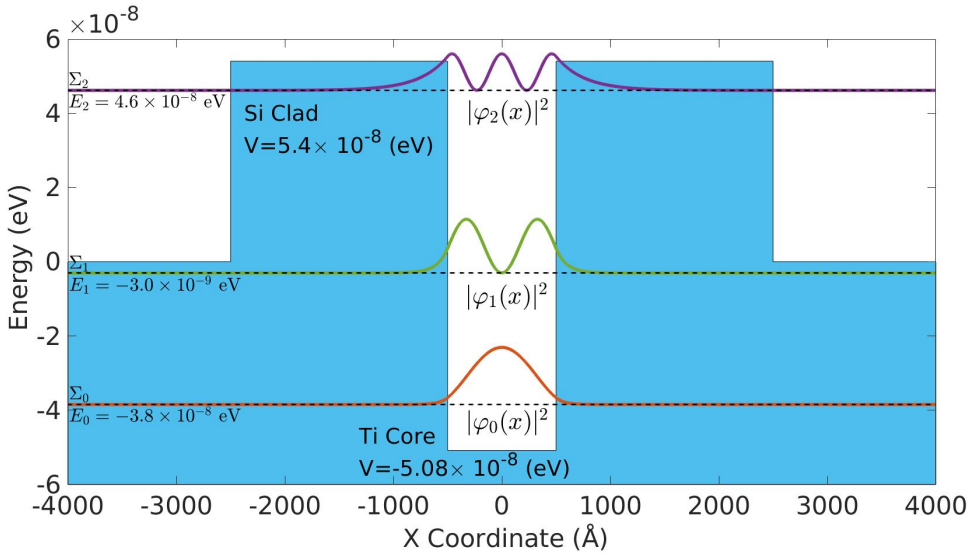

Figure 5.3: Energy levels for a Si-Ti-Si waveguide. Adapted from [102]

In the case of a Si-Ti-substrate waveguide impinged by a thermal neutron beam with an arbitrary θ angle (see Figure 5.2b), the scheme is rather closely related to (but does not coincide with) the proposal in [11] and the setup in [13]: a potential well 1000 Å wide, corresponding to the negative potential of the Ti core, over a substrate of Si (assumed to be an infinite potential barrier, or infinitely repulsive

clad, with vanishing wavefunctions at $x = 0$, for convenience). We performed numerical simulations investigating the possible differences. We assumed a finitely repulsive V_{Si} instead of an infinitely repulsive barrier but the results do not differ significantly. This potential well is covered with a 1500 Å Si layer that acts as a potential barrier. In this case, our simulation shows that there are two discrete energy levels, represented in Figure 5.4. Similarly to the previous case, Υ_0 represents a bound state level (giving rise to a propagation mode) and Υ_1 represents a resonant positive energy level (lossy propagation mode).

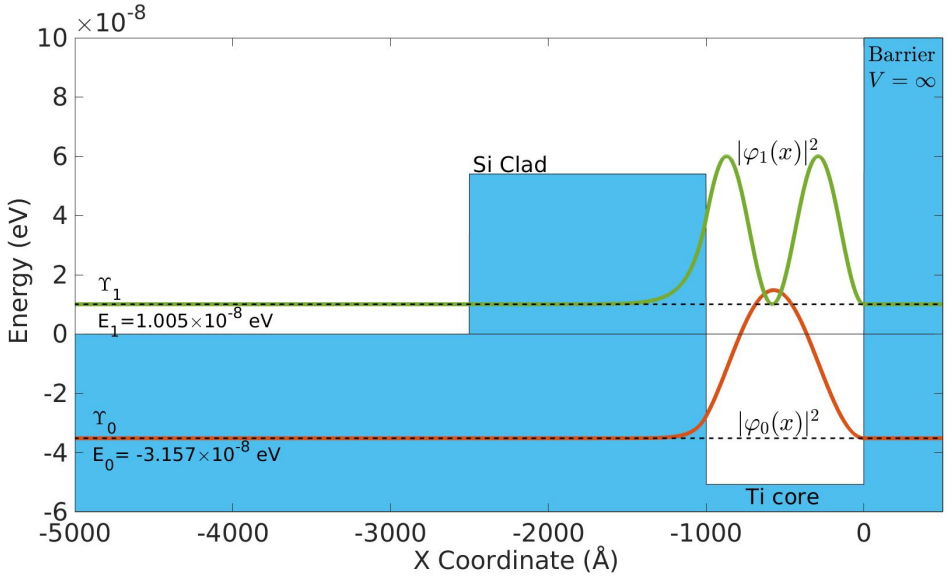

Figure 5.4: Energy levels for a Si-Ti-substrate waveguide. Adapted from [102]

Notice that eigenfunctions corresponding to Σ_2 and Υ_1 in Si-Ti-Si and Si-Ti-substrate waveguides, respectively, cannot be normalized since the associated planewave functions extends to infinity. In any case, in order to compare the rising of propagation modes for different neutron beam impinging angles, one may change conveniently the normalization used to $N = \int_{-b}^{+b} \phi(\bar{x})^* \phi(\bar{x}) \, d\bar{x}$. So, physically, one normalizes the total probability of the wavefunction excited inside the waveguide (including clad and core) to unity.

5.5.3 Resonant States

As previously said, the eigenfunctions corresponding to energy levels Σ_2 and Υ_1 (for Si-Ti-Si waveguide and Si-Ti-substrate waveguide, respectively) have positive values of energy. Consequently, they are not a discrete state, as it happens with the eigenfunctions with negative energies. In fact, there is a continuous set of eigenfunctions (among them, either Σ_2 or Υ_1) for the corresponding Hamiltonian.

These eigenfunctions were described in [36] as resonances in quasidiscrete levels of energy. Since a slow neutron is susceptible to escape via tunnelling effect across

the potential barrier (finitely extended clad), they do not belong to any discrete spectrum of energies. The neutron will eventually escape from the waveguide to vacuum (the infinitely extended clad). The main difference between Σ_2 or Υ_1 and any other positive energy eienfunction is that the former have a small probability of escaping from the waveguide.

For obtaining the continuous spectrum of solutions, instead of finding the Hamiltonian eigenfunctions, one must excite the system from the outside. It implies adding an inhomogeneous term (incoming wave, $A_{in}e^{ik_x x}$) to the continuity equations for for $\phi(x)$ and $d\phi(x)/dx$, so as to obtain an inhomogeneous linear system of equations for the amplitudes, that will always have a solution for any value of k_x (i.e.: angle of incidence).

Considering D as the density of neutrons inside the Ti core, when we represent the ratio $\mid D/A_{in} \mid^2$ *versus* energy, a peak appears, that matches with the resonant quasidiscrete eigenfunction obtained by finding a vanishing value for the determinant of the homogeneous system of equations (Section 5.5.2). It corresponds to those quasidiscrete propagation modes which escape from the waveguide by tunneling effect. Notice that, in the case of negative energies, an inhomogeneous term $A_{in}e^{ik_x x}$ can not be imposed since it would give rise to a divergent exponential.

This way of obtaining resonant states is quite interesting since it matches with the experimental result in papers [13] and [73]. In these experiments, authors obtain the excitation of the waveguide (neutron counts) for different incident beam angles. In these cases there is a resonant peak curve for a certain angle, a Lorentzian-shaped curve, that is interpreted as an excited propagation mode.

There is another interest in these Lorentzian-shaped curves, since their width at half height, $\Delta_{1/2}E$ yields a measure of the particle (or neutron beam) half life in this quasistable state and, thus, an good estimation of the propagation distance of this lossy mode.

For the case of Si-Ti-Si waveguide, the simulations yield the results showed in Figure 5.5 (Ti core = 1000 Å and Si clads = 2000 Å, as in Figure 5.2a). It can be seen that the maximum peak occurs at an energy of $E = 4.6 \times 10^{-8} eV$ (that for an incoming thermal neutron beam of energy 0.025 eV, corresponds to an impinging angle of $\theta = 0.077°$) that totally matches with the values obtained for Σ_2, and a width at half height, $\Delta_{1/2}E = 8.65 \times 10^{-12} eV$. Moreover, it is clear that this curve has a Lorentzian shape, as expected.

For the case of Si-Ti-substrate waveguide, the simulations are shown in Figure 5.6 (Ti core = 1000 Å and Si clad = 1500 Å, as in Figure 5.2b). The maximum peak occurs at an energy of $E = 1.005 \times 10^{-8} eV$ (that corresponds to an impinging angle of $\theta = 0.036°$). It matches with the value obtained for Υ_1. Its width at half height is $\Delta_{1/2}E = 2.83 \times 10^{-14} eV$. In this case, as expected, the curve has a Lorentzian shape as well. If one compares these results with those in [13], they are found in good accordance (the maximum peak occuring at $\theta = 0.098°$ in the experiment). One should take into account that the incoming neutron beam had, in those experiments,

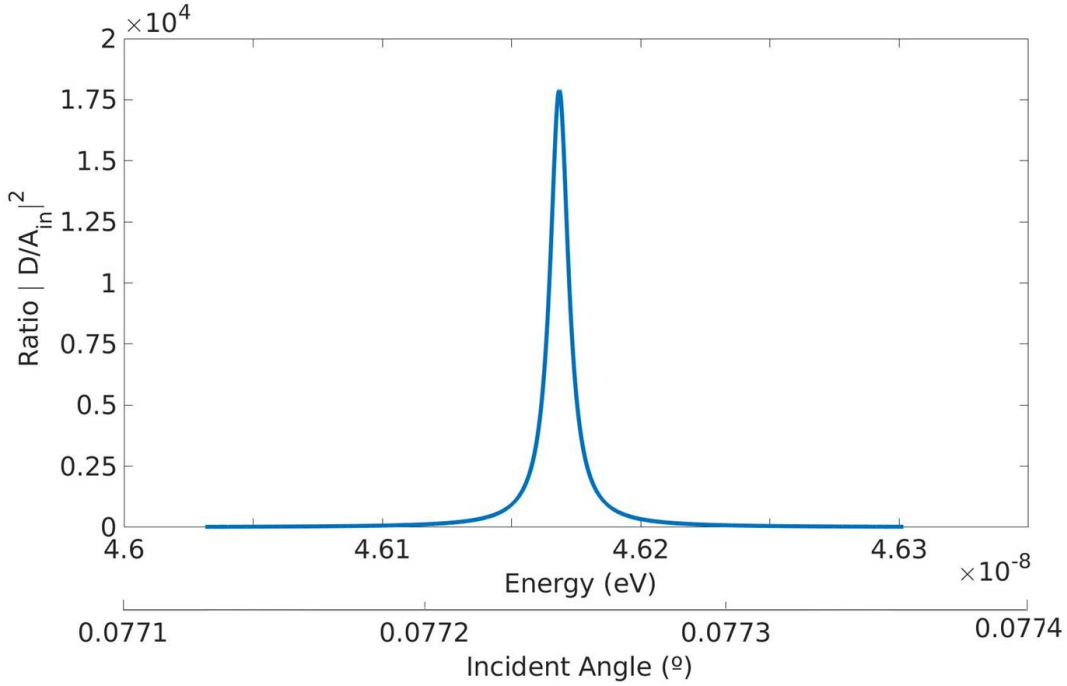

Figure 5.5: Resonant level for Si-Ti-Si waveguide at $\theta = 0.077°$ of incidence. Adapted from [102]

a wavelength of 2.35 Å and that the potential barrier simulated here is not exactly the same as in [13]. The scheme here is kept for internal comparison between the cases of Si-Ti-Si and Si-Ti-substrate waveguides.

Comparing results for the resonant states from Figures 5.5 and 5.6, it is clear that the higher the energy of the state, the wider the associated Lorentzian curve and consequently the higher probability for escaping the waveguide (lower travelling distance) as it is expected. Indeed, there will be neutron losses via tunnelling effect and the results may be used to perform a rough estimation of the neutron travelling distance, $d_{\Sigma,\Upsilon}$ along the waveguide in a quasi-discrete propagation mode (resonant state). In fact, the fundamental time-energy uncertainty relationship $\Delta E \Delta t \approx \hbar$ combined with the width, $\Delta_{1/2}E$ of each resonant peak (calculated for Σ_2, and Υ_1) may quantify the neutron beam propagation length in this mode. A thermal neutron with $\lambda_{db} = 1.8$ Å has a velocity, $v = d_{\Sigma,\Upsilon}/\Delta t \simeq 2.2$ km/s and, thus it yields a propagation distance of $d_{\Sigma_2} \simeq 0.17$ m (for Si-Ti-Si waveguide) and $d_{\Upsilon_1} \simeq 51.15$ m (for Si-Ti-substrate waveguide).

Notice that, unless similar, there is not total correrspondence between the models simulated and those in [70] (i.e.: absorption is not taken into account in our model). In an experiment, the impinging beam angle can not be fixed a priori since it strongly depends on the illumination conditions. The source's shape, in our model with ideal inclinated plane waves, is critical. Moreover, lateral illumination would change the peak structure, that may not be simmetric. Notice as well that the maximum peak would remain and our results are consistent with those experiments.

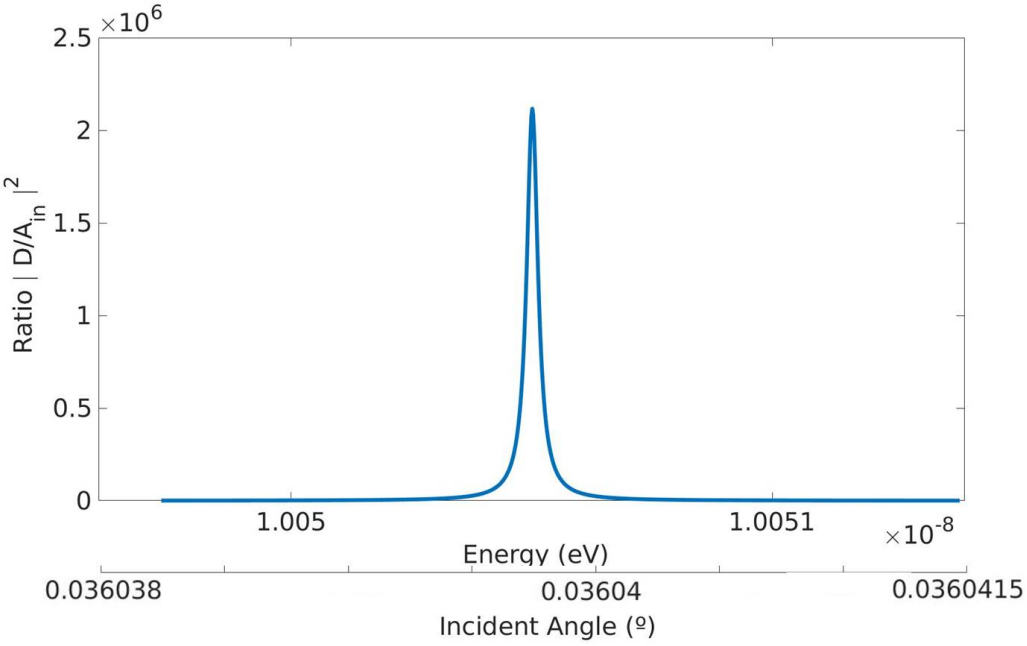

Figure 5.6: Resonant level for Si-Ti-substrate waveguide at $\theta = 0.036°$ of incidence. Adapted from [102]

For last, in the experimental setup in [70], neutron counts are measured for the detector being in a different angle. The opposite setup may be possible (i.e.: measuring counts for different impinging angles). As the peak in Figures 5.5 and 5.6 represents an acceptance window, it implies that angles are close, but not equal to the resonance peak would excite (though less efficiently) the propagation mode. Consequently, the wider the peak the wider the phase range accepted by the waveguide.

5.5.4 Propagation Mode Amplitudes: $T_{pm,\alpha}$ and Scattering Amplitude ($T_{scat,1}$)

In Section 2.5 a first approximation to the study of these systems was conducted by using an approximation recipe given in [6]. This recipe led to represent the solutions for $\int_{-\infty}^{\infty} \left(e^{ik_{in,x}x}\right)^* \phi_{\Sigma_i}(x)\, dx;\ i = 0, 1, 2.$

Recalling the formulation developed in the previous Section 5.3.2, notice that the main difference of Eq.(5.39) with the equations used in Section 2.5 are the denominators; $(2mE/\hbar^2 + \chi_\alpha^2)^{1/2}$ and $(2mE/\hbar^2 + \chi_\alpha^2)^{1/2} - \left(2mE/\hbar^2 - \bar{k}^2\right)^{1/2}$ that will lead to interesting conclusions.

$\mid T_{pm,\alpha_0} \mid^2$ (i.e.: proportional to the probability for the excitation of the α_0 -th propagation mode) versus the angle of incidence, for the case of a Si-Ti-Si waveguide (Ti core = 1000 Å and Si clads = 2000 Å, as in Figure 5.2a) , is represented in Figure 5.7 for Σ_0, Σ_1 and Σ_2. Notice that, since Σ_2 corresponds to a positive energy, the correct representation in this case is $\mid T_{scat,1} \mid^2$, upon comparing Eqs.(5.39)

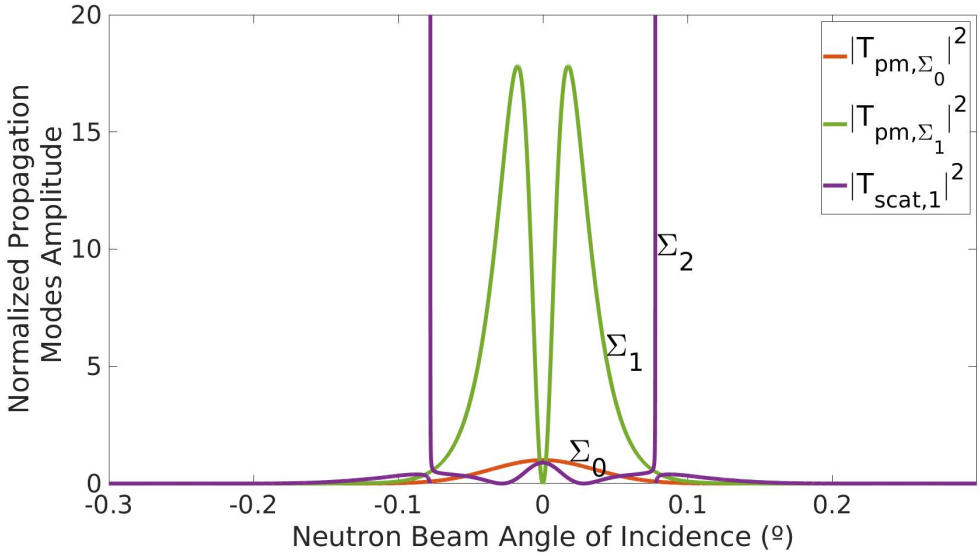

Figure 5.7: T_{pm,α_0} and $T_{scat,1}$ versus angle of incidence for a Si-Ti-Si waveguide. Adapted from [102]

and (5.41). The abscise value is normalized for comparison, with the value for Σ_0, $\mid T_{pm,\Sigma_0} \mid^2 (0°) = 1$. This figure is the counterpart of Figure 2.9 and, since the former comes from a more realistic formulation here, expands its conclusions.

The underlying structure is $sinc\,(k_{in,x} + \chi_\alpha) + sinc\,(k_{in,x} - \chi_\alpha)$ for even modes (i.e.: T_{pm,Σ_0} and $T_{scat,1}$) and $sinc\,(k_{in,x} + \chi_{alpha}) - sinc\,(k_{in,x} - \chi_{alpha})$ for odd modes (i.e.: T_{pm,Σ_1}) and it is close with our results in Section 2.5. One of the most evident characteristics is that $\mid T_{scat,1} \mid^2$ diverges for a certain angle. This has already been discussed in Section 5.3.2: it comes from the infinite length of the semi-infinite waveguide and it is inherent to this formulation used.

The other main characteristic is the high values related to $\mid T_{pm,\Sigma_1} \mid^2$ in comparison with $\mid T_{pm,\Sigma_0} \mid^2$ and is a different result from Section 2.5. This is due to the factor $\left((2mE/\hbar^2 + \chi_\alpha^2)^{1/2} - \left(2mE/\hbar^2 - \bar{k}^2 \right)^{1/2} \right)^{-1}$, since $\chi_0^2 > \chi_1^2$ (because Σ_0 is a level lower than Σ_1). The physical implication of this result is that, since the close to zero is the energy of a bound level, the more easily it may be excited. Then, for a bound (i.e.: with no losses) mode, one can look for negative energy states as close to zero as possible so that they will be efficiently excited. This may be controlled via switching adequate values for clad and core transverse sections and could imply an improvement in the waveguide efficiency.

For the case of Si-Ti-substrate waveguide, similar results are obtained. The simulations for $\mid T_{pm,\alpha_0} \mid^2$ for Si-Ti-substrate waveguide (Ti core = 1000 Å and Si clad= 1500 Å, as in Figure 5.2b) versus angle of incidence are represented in Figure 5.8 for Υ_0. Notice that, in this case, the result is represented in logaritmic scale. The corresponding $\mid T_{scat,1} \mid^2$ (related to Υ_1) is also displayed. The main difference is that the sample substrate (assumed as an infinitely repulsive potential)

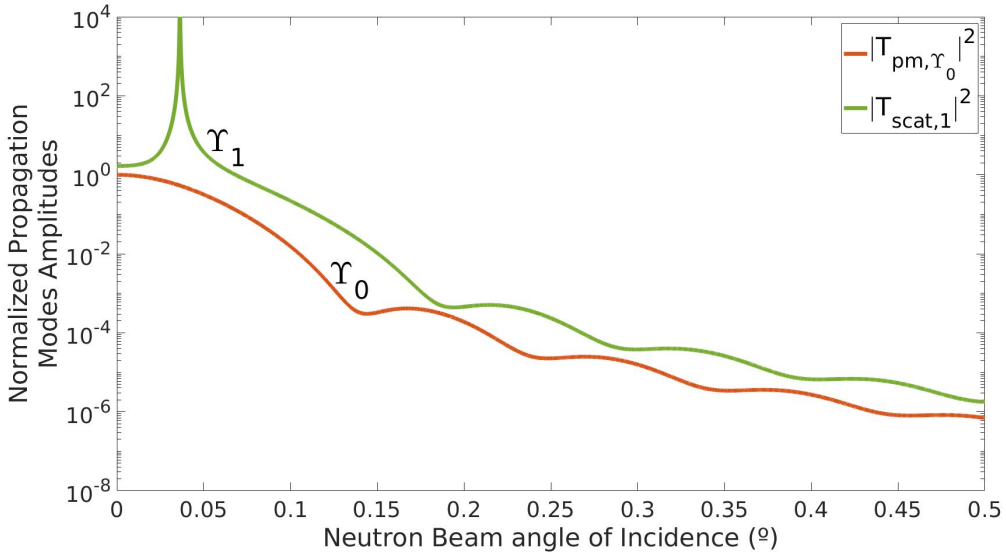

Figure 5.8: T_{pm,α_0} and $T_{scat,1}$ versus angle of incidence for a waveguide made of Si-Ti over a substrate assumed to be infinitely repulsive. Adapted from [102]

breaks the $x \to -x$ symmetry (which holds for Figure 5.7). In [11] and [13] it is stated that only the positive energy propagation mode may rise, since neutrons must penetrate in the clad barrier via tunnelling effect, making the levels with negative energies not accessible. From the results in the present work, it is clear that both Υ_0 and Υ_1 are excited in the waveguide for any impinging angle, but with a low efficiency, in disagreement with [11]. Only in the case of an impinging angle that matches with Υ_1 the difference becomes significant by various magnitude orders. This is in good agreement with the results of the experiment, where only at a certain angle a peak is clearly visible.

Comparing the results for both cases, it is not clear which method would be preferable from the perspective of improving the waveguide efficiency (for wave packets). On one hand, lateral incidence (as in [13]) exposes a wider surface to the neutron beam, allowing more neutrons to be collected. Since impinging angles used here are extremely low, it implies a wider exposed surface: $\frac{W}{tan(\theta_{in})}$ where W is the neutron beam width and θ_{in} is the neutron beam impinging angle. On the other hand, frontal incidence, simulated here, allows to excite more easily highly efficient propagation modes, at the cost of only exposing the waveguide entrance (100 μm in our case) to the thermal neutron beam. Probably a combination of both would yield the best results: lateral incidence at the entrance and frontal escaping at the end of the waveguide as, for example, in [108].

5.5.5 Reflection Amplitudes: $T_{ref}\left(\bar{l}\right)$

It is also interesting to focus attention on the reflection amplitudes, for the sake of completeness of the previous formulation (focused on propagation modes).

Eq.(5.37) in Section 5.3.1 allows to quantify the reflection amplitudes for each spatial frequency ($\bar{l}$) as a function of the impinging neutron beam angle (related to $\bar{k}$, in this case $k_x = k_{in} sin(\theta)$).

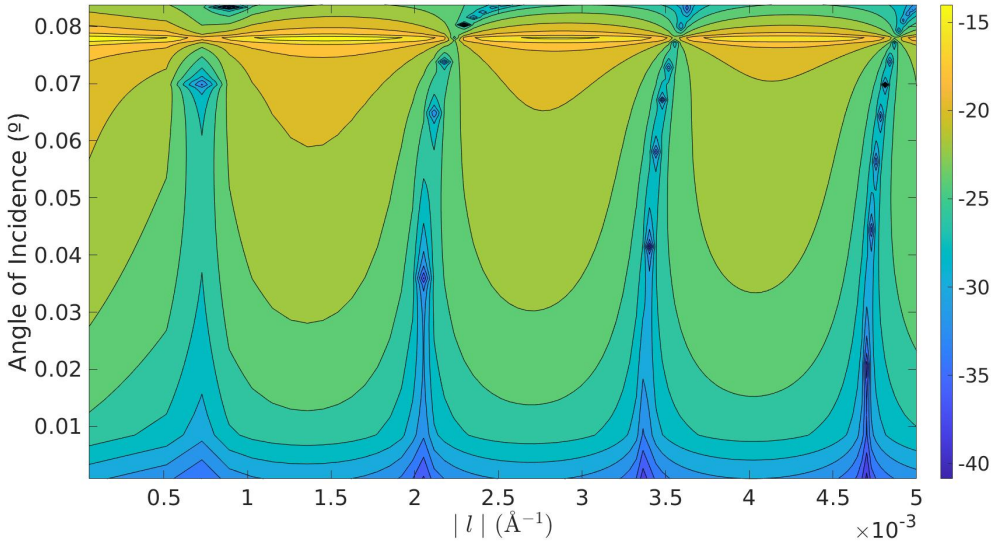

Figure 5.9: Reflection amplitudes for different neutron beam impinging angles, θ, and reflecting angles ($\mid l \mid$) for a Si-Ti-Si waveguide. Adapted from [102]

For the case of Si-Ti-Si waveguide, results are displayed in Figure 5.9, where we display a logarithmic representation of $\mid T_{ref}(l) \mid^2$ in a contour plot. This figure clearly shows a strong peak for an incoming beam angle $\theta = 0.077°$ for any spatial frequency value, $\mid l \mid$ (in yellow colour in Figure 5.9). This peak corresponds to the resonant or quasibounded state, Σ_2 level and results in a decrease on the reflected value of the neutron beam (as expected). Upon examining the figure, a structure of peaks and valleys appears both in l and k_x (impinging angle). This behaviour comes from the term $\int dx \phi_{k_x}(x) e^{-ilx}$ (the scalar product of a wavefunction associated to the incoming beam times a possible plane wave reflected one).

For the case of Si-Ti-substrate waveguide, a similar structure to the previous one is displayed in Figure 5.10. It shows a resonant peak as an horizontal narrow yellow band for an incoming beam angle, $\theta = 0.036°$, for any spatial frequency value, $\mid l \mid$. This peak corresponds to Υ_1.

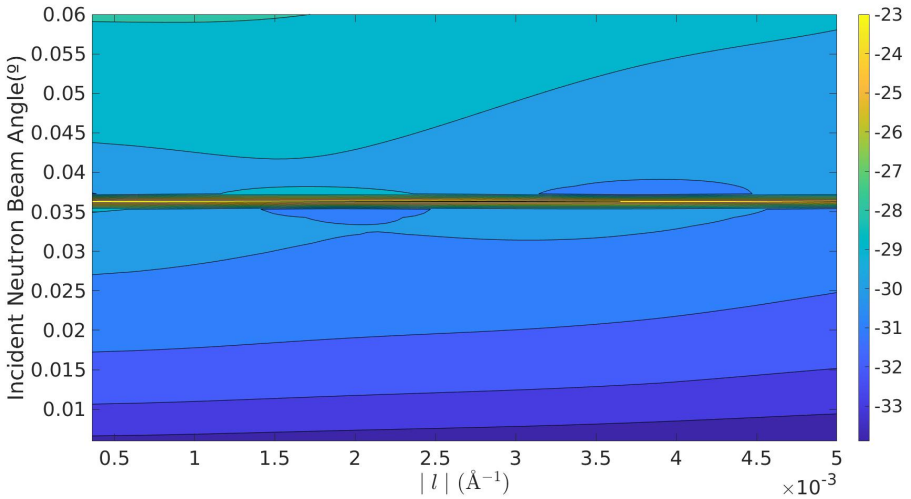

Figure 5.10: Reflection amplitudes for different neutron beam impinging angles, θ, and reflecting angles ($| l |$) for Si-Ti-substrate waveguide. Adapted from [102]

Para cambiar la frecuencia de
la criatura, mis chicos sugieren
un aparato de interferencia estándar
modificado para tal efecto.

La Cosa del Pantano

6 Applications

Contents

Until this point of the thesis, we paid our attention on the characterization of neutron waveguides. We have focused on how geometry and materials (i.e.: the characteristics for each isotope) have an influence on the efficient rise of propagation modes for an incoming thermal neutron beam.

In this chapter, we will apply the lessons learned to propose various configurations of neutron guides and neutron coupling waveguides. The latter can be used to improve the efficiency of neutron beam uses, in particular Boron Neutron Capture Therapy (BNCT) and neutron analysis of matter.

6.1 Neutron Couplers

We cannot lose sight of the ultimate goal that motivates this thesis: the improvements in the characterization of neutron waveguides. These advances will allow the devices design to improve the confinement and transmission of neutron beams. In this way, from an unconfined neutron beam, we will be able to advance in its guidance, collimation, monochromatization and, eventually, its focusing.

As we exposed in Section 2.2, the experiments of Feng et al., [13], showed the confinement from the use of Ti. Moreover, the experiments carried out by Kumakhov et al., [12], and Chen et al., [70], showed the possibility of developing guides of hollow capillary channels by using Si and SiO_2.

Thus, the combined use of Ti and Si-based waveguides can improve the collection and confinement of neutrons in the waveguide. Then, we will call these devices neutron couplers, in analogy with optical couplers of refractive optics based photonic devices. The waveguides will be based on a segment with Ti, where neutron capture and the formation of propagation modes will prevail, and a Si-based hollow waveguide section that allows the reduction of losses in the confined beam. These proposals are the natural continuation of those presented by Álvarez-Estrada and Calvo in the 80's, [3, 4].

Titanium is a good candidate for designing a neutron coupler since (i) its values for coherent scattering length, b_{coh}, and linear coefficient for attenuation, ν, are more favourable than those for other possibilities (see Table 1.4), (ii) its natural abundance, (iii) pure samples of it can be prepared in a laboratory, (iv) its interesting mechanical, chemical and physical properties.

In Section 5.1.4, we already discussed the possible propagation modes in a finite potential waveguide. Strongly bound discrete modes or weakly bound continuous modes (resonant states) may appear in the Ti, while only the latter may appear in the Si-based hollow waveguides. As commented in Section 5.5.4, some negative-energy propagation modes raised in Ti waveguides may be highly efficient.

By inspecting Eq.(5.39), it is clear that the main condition for that is that its value for χ_α be low as possible (i.e.: the level should be as close to zero energy as possible). This propagation mode would rise efficiently for certain impinging angles giving rise to a propagation mode in the hollow section of the waveguide (see Figure 6.1). This may be accomplished by an adequate design of the neutron coupling waveguides transverse section (which is easier than finding an adequate isotope). Then, making the corresponding bound level as close as possible to zero in the Ti section (coupling section) while being close to a resonant mode in the hollow waveguide.

With this in mind, we shall outline some proposals, based upon Two Coupling Waveguides (TCW1 and TCW2), for generating slow neutron beams which, possibly, would propagate along the z-axis for long distances (say, about 1 m) while being confined in transverse directions down to about a fraction of a micron. We will also propose a possible more complex configuration, Multi Coupling Waveguides, (MCW) based on the experiments mentioned above.

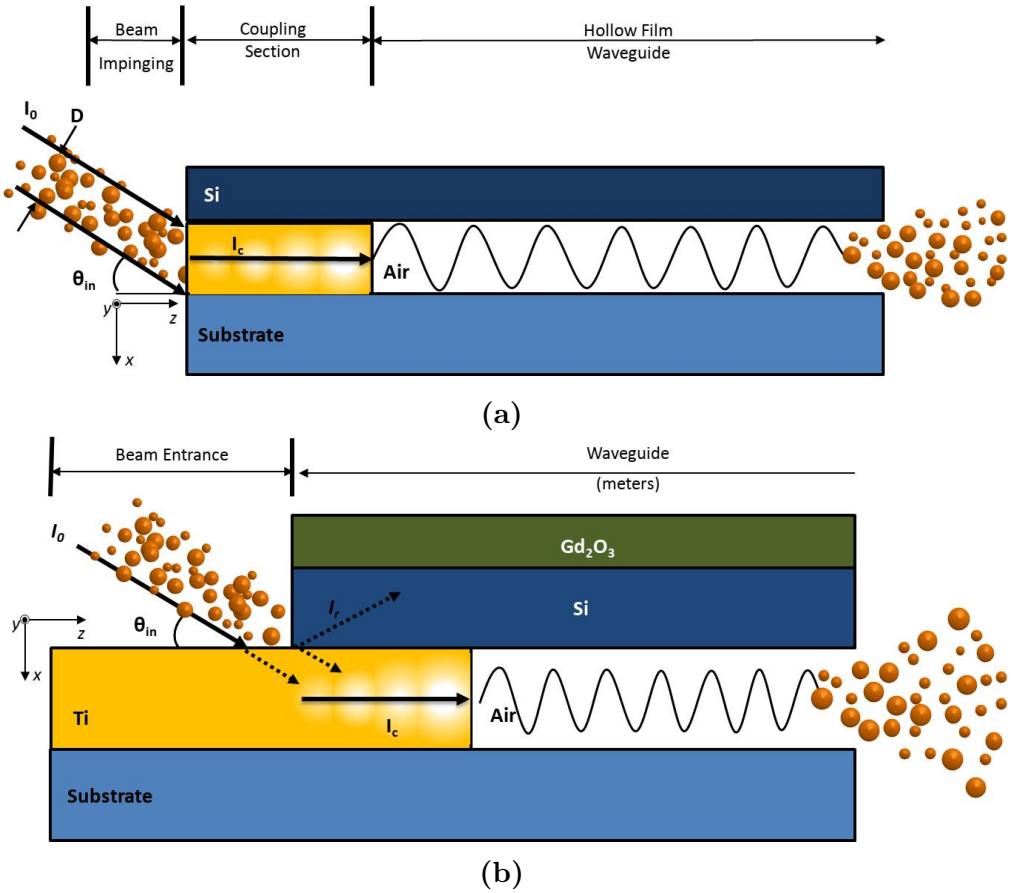

Figure 6.1: Schematic representation of the device in the TCW1 proposal for (a) front illumination and (b) lateral illumination.

6.1.1 Two Coupling Waveguides (TCW1)

The first proposal will be based upon the successful experiment by Feng et al. using a thin Ti film, [13], and includes an additional suitable waveguide (hollow waveguide) in order to reduce neutron absorption (see Figure 6.1a).

Two planar waveguides (thin films) are positioned along the propagation direction (z).The first waveguide has a Ti film (core) over a Si substrate (of infinite thickness) and a clad formed by Si. Confined propagation along z occurs first in the Ti core, like in [13]. Transverse sizes along the x direction could be 1000 Å, for the Ti core, and 1500 Å, for the Si clad, over an infinite substrate. These sizes are similar to those in Section 5.5.2 (see Figure 5.6).

The proposal of using Si, as in Section 5.5.2, instead of SiO_2, as in [13, 62, 63], comes from the fact that both materials have a similar behaviour since Si and O have similar b_{coh} (acting both as a positive potential barrier) while Si is more absorbing than O. Thus, the use of pure Si reduces undesired neutron scape from the waveguide (acting, thus, as a radiation shield).

Notice that here, in comparison with Feng's experiment, [13], we are not interested in detecting neutrons leaving the Ti core but in confining and transporting

the neutron beam with as few losses as possible. There is also another important difference: the length along z of the Ti waveguide is chosen to be definitely shorter than in [13] (say, less than 1 cm), so as to reduce attenuation in the Ti core.

The second waveguide has air as core. Transverse dimensions are similar to those of the first waveguide, although small modifications might be possible to allow the propagation modes of both waveguides to match. The confinement in the core of the second waveguide follows from the very small value of $b_{coh}\rho$ for air (core) and the larger positive value of $b_{coh}\rho$ for the Si cladding (by about three orders of magnitude). However, the latter confinement is not strict, due to the finite widths of Si cladding. In order that losses across the clad (by quantum mechanical tunnelling across it towards air) be negligible, it is required that the Si clad has a width along x sufficiently thick. The overall length of the second waveguide along z could be several tens of cm or even about 1 m.

Confined slow neutrons from the Ti core of the first waveguide would enter, possibly with very small attenuation, into the air core of the second waveguide. Since air has a small linear coefficient ν (compare with Table D.1 two last columns, in Appendix D, and Section 1.5.2), there would be small attenuation in the core of the second waveguide and, hence, there would be an appreciable neutron flux at its exit.

As an alternative, the structure of the first waveguide could be modified by illuminating laterally the Ti guide with the incoming neutron beam so as to become similar to that in [13]. This would facilitate the coupling of an incoming neutron to the propagation mode along the Ti core. An extra layer of an absorbing material (Gd) can also be added to improve radiation shielding. See Figure 6.1b.

6.1.2 Two Coupling Waveguides (TCW2)

We stress that, in TCW1, the neutron beam, as it propagates along z, is confined only along the x direction (thin film). There is practically no confinement in the y direction. A natural improving extension of TCW1: one device aimed to get confinement along y as well, still keeping confinement along x, wherever possible.

In the present proposal TCW2, there would be confinement along both transverse directions x and y, respectively.

It also contains two waveguides (see Figure 6.2). The first waveguide would no longer be a thin film, like in the previous proposal, but a single solid cylinder (with circular cross section), with Ti as inner core and Si as surrounding clad. The diameter of the Ti core would be of the order of one micron and the width of the core of the hollow (second) waveguide would be of the same order. The length of the first waveguide should be smaller than 1 cm to avoid attenuation. The second waveguide would be a hollow cylinder (with circular cross section), having air as inner core and Si as surrounding clad as well. The width of the clad of the second waveguide could be similar to that of the first waveguide. The length of the second waveguide could be some tens of cm and, possibly, about 1 m. Neutrons,

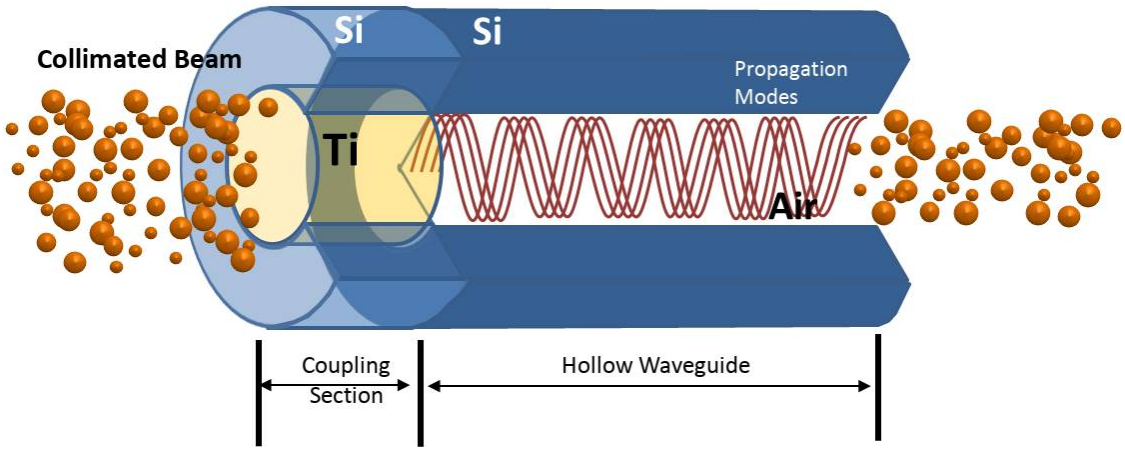

Figure 6.2: Schematic representation of the device in the TCW2 proposal

propagating confined along the Ti core of the first waveguide would enter into the air core of the second waveguide and propagate along the latter without appreciable attenuation along distances similar to those in the proposal TCW1

Like in the TCW1 proposal, the structure of the first waveguide could possibly be modified by some sort of lateral illumination, in order to facilitate and enhance the coupling of an incoming neutron to the propagation mode along the Ti core.

6.1.3 Multiple Coupling Waveguides (MCW)

After the previous proposals it is clear that it is feasible to design and analyse the behaviour of more complex structures. In this way, Multiple Coupling Waveguides (MCW) can be proposed. These structures could be designed to magnify certain effects, such as blackout, confinement, loss reduction, etc. Our third proposal involves three coupling waveguides. It is based upon the experiments carried out previously with PGFs [12, 72] and thin films, [13]. It will constitute a natural extension of them and of the previous proposal in [109] towards the controlled exploration of shorter scales with focalizing slow neutrons in a broad sense.

See Figure 6.3. The first waveguide is a suitable bundle of parallel polycapillary glass fibres (PGFs), with their axes parallel to the z axis, annexed to the second waveguide. The second and third waveguides are very similar to (and similarly oriented as) the ones in the Section 6.1.1: then, they have similar sizes along the directions y and z, while their thickness along x is about a few microns. In each PGF in the first waveguide, any single hollow channel should have an internal diameter (a few microns) matching as much as possible the thickness of the second waveguide along x. The PGFs in the bundle should be disposed forming a layer: only one PGF along x and z, and tens of parallel PGFs along y, as Figure 6.3 shows. In the coupling section, the propagation direction (z) in the Ti and air

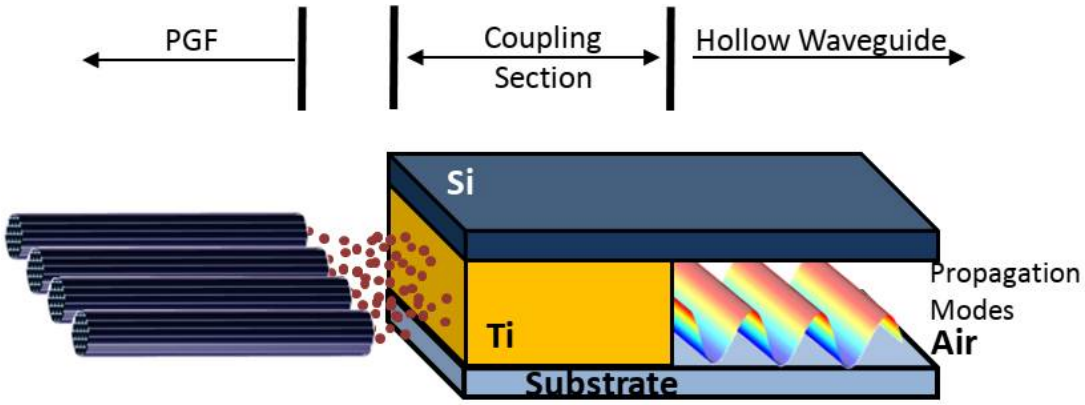

Figure 6.3: Schematic representation of the device in the MCW proposal

cores of the second and third waveguides should be as close as possible to the axes of the parallel PGFs. The neutron beam coupling facilitates the confinement of the neutrons in the air cores of the hollow channels (a few thousands) of each PGF in the bundle forming the first waveguide, entering successively into the Ti and air cores of the second and third waveguides and to propagate confined along them, for distances about 1 m, possibly.

6.2 Boron Neutron Capture Therapy (BNCT)

BNCT is a form of radiotherapy for treating certain malignant tumours, specifically primary brain tumours (glioblastomas) [110], head and neck cancers and some limited application to melanomas, [111], and malignant mesotheliomas (see [112]).

BNCT is based on the following ^{10}B reaction with thermal neutrons

$$^{10}B + n \rightarrow^{7} Li + \alpha \tag{6.1}$$

and

$$^{10}B + n \rightarrow^{7} Li + \alpha + \gamma \text{ (478 keV)} \tag{6.2}$$

The reaction in Eq.(6.2) is produced in 94 % of the captures. Most part of the energy is released in the form of kinetic energies of the final α and ^{7}Li particles (2.8 MeV in Eq.(6.1) and 2.3 MeV in Eq.(6.2)). This reaction is chosen because of the ^{10}B high capture cross section (roughly 3800 barns) for thermal neutrons. The recoil particles due to their mass, have a high linear energy transfer (LET) in comparison with protons or electrons; $\approx 150\ keV/\mu m$ for α and $\approx 175\ keV/\mu m$ for ^{7}Li, [112]. These particles are able to produce strong biological damage to tumours in small domains of sizes 8 and 5 μm, respectively, which are comparable to the cell's diameter. The basic aim of the therapy at the macromolecular level is that one single hit of one slow neutron could produce irreversible damage to both single

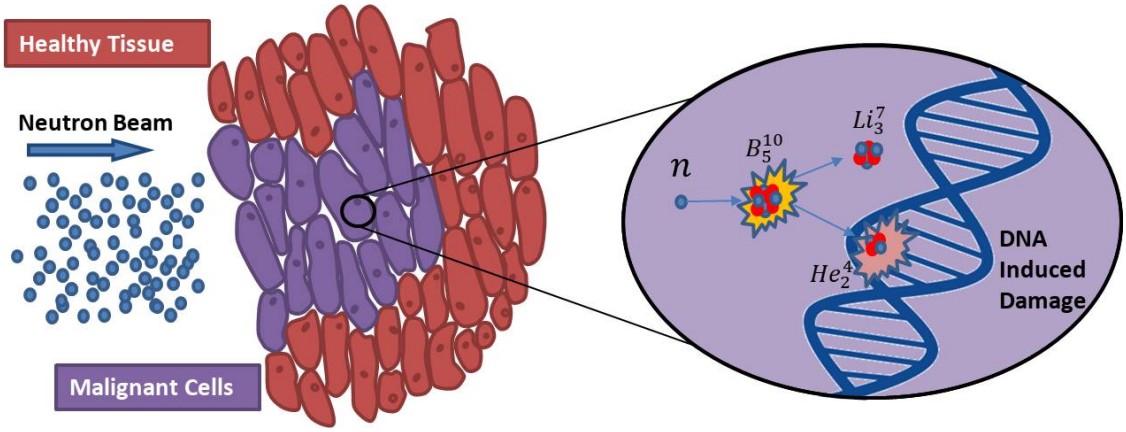

Figure 6.4: The principle of action in BNCT

helices of one double-helix DNA macromolecule of a malignant cell, so that the possibility for its repair be practically forbidden, [113]. See Figure 6.4.

This therapy starts with delivering the patient certain drug containing the (non-radioactive) isotope ^{10}B. These drugs are selectively absorbed and acumulated in malignant cells. Initially, boric acid and its derivatives (first-generation compounds) were employed in the 1950s and 1960s. Nowadays, the most commonly employed drugs (second-generation compounds) are mercaptoundecahydro-closo-dodecaborate (BSH, with chemical formula $Na_2B_{12}H^{11}SH$) and the boron-containing amino acid (L)-4-dihydroxy-borylphenylalanine, or boronophenylalanine (BPA, with chemical formula $C_9H_{12}BNO_4$) and its derivatives. Today, third-generation compounds (boron carriers), including polyhedral anions of borane or carboranes are under investigation to enhance the BNCT requirements of boron delivery to malignant cells (see [112] and references therein).

At a subsequent stage, the patient is irradiated with a slow neutron beam, focused towards the location of the malignant tumour, to which the above drug has been previously delivered. Due to the presence of hydrogenated substances in the human body, the neutron beam is scattered. Thermal neutrons exhibited poor penetrability in tissues. Up to the early 90's, craniotomy was used to reach the tumour and facing it to the thermal neutron beam, especially in deep-seated tumours. Since the early 90s to nowadays, this limitation was overcome by irradiating the patient with epithermal neutrons, that are thermalized in the patient's body. The use of an epithermal neutron flux creates a radiation field with a maximum thermal flux at a depht of 2-3 cm, which drops exponentially thereafter. This procedure has the advantage that no craniotomy is needed when BNCT is applied to malignant brain tumours, [113].

This sets the basis for the IAEA TECDOC-1223, [114], recommendations on the neutron beam characteristics, specially focused on an epithermal neutron flux ($\geqslant 10^9$ n/cm^2/s) with a low fast neutron component and a low thermal neutron

ratio. Efforts have been directed towards modifying available reactors for obtaining the required neutron beams.

While BNCT treatments have been implemented at different research reactors around the world[113], the number of those used for BNCT have decreased to only 4 reactors at 2019: KUR in Japan, RA-6 in Argentina, THOR in Taiwan and BCTC in China. This is in part due to the difficulties in licensing a reactor for clinical use, [115]. Nowadays, researchers moved to the, so called, accelerator based sources for BNCT.

Different neutron generation procedures and reactions are under investigation for BNCT. Actually, proton accelerators have been used for BNCT since electron accelerators produce high intensity γ rays. Different reactions candidates were proposed; p-Li, p-Be, d-Be, d-Li... depending on various factors: (i) the incident particle energy and reaction required (a lower energy produces lower energy neutrons, that are easier to moderate), (ii) Li is a very chemically reactive element and harder to handle than Be, (iii) these reactions generate a high amount of heat and Li has a low melting point (180.4 °C) in comparison with Be, (iv) Be is toxic when becomes powder, (v) Li can be used in low energy proton accelerators, etc [115].

The current status of development of accelerator based source projects worldwide relevant by the end of 2022, [113, 115, 116] are summarized in Table 6.1.

Nowadays, BNCT continues to be a promising primary or adjuvant therapy with different fields on development, [112, 113, 117], such as third generation boron drugs, Monte Carlo patients dose planning and new neutron sources.

6.2.1 Optical Couplers in BNCT

We believe that optical couplers considered in previous Sections 6.1.1, 6.1.2 and 6.1.3, as well as other multi coupler geometries, may play a role in BNCT. Some conjectures on possible applications of Polycapillary Glass Fibers to BNCT of small tumours were presented in [109].

As we stated above, a thermal neutron beam exhibits low penetrability in tissues. Consequently, if one wants to reach a deep-seated brain tumour, one has to do it through a craniotomy (up to early 90s) or by using an epithermal neutron source.

Our proposal for the use of optical couplers, [62, 63], could incumvent this problem. We could employ small waveguides where thermal neutrons propagate as propagation modes, with a maximum diameter in the order of mm, directly inserted into the brain. A very important aspect is to control, as much as possible, the delivery of neutrons to malignant cells and, so, to avoid that normal tissue could receive the neutron radiation. This would allow us to make thermal neutrons reach directly deep tumours. In this way, absorption of neutron dose by surrounding healthy tissues is prevented (or greatly diminished).

On the other hand, since we deal directly with thermal neutrons, the requirements of IAEA TECDOC-1223, [114], for epithermal neutrons are no longer relevant. Consequently, it would enable an expansion of the possible BNCT sources.

Table 6.1: Accelerator-based BNCT projects

Location	Accelerator type	Purpose	Current status
Particle Radiation Oncology Research Center Kumatori, Japan	Cyclotron	BNCT research	experimental use
Southern Tohoku BNCT Research Center Fukushima, Japan	Cyclotron	Clinical BNCT	patient treatment
Kansai BNCT Medical Center Osaka, Japan	Cyclotron	Clinical BNCT	patient treatment
National Cancer Center Hospital Tokyo, Japan	RFQ	Clinical BNCT	phase I clinical trial
Edogawa Hospital BNCT Center Japan	RFQ	Clinical BNCT	under construction
Ibaraki Neutron Medical Reserch Center University of Tsukuba, Japan	RFQ+DTL	Clinical BNCT	experimental use
Helsinki University Hospital Finland	Electrostatic	Clinical BNCT	commissioning
Shonan Kamakura General Hospital Kanagawa Prefecture, Japan	Electrostatic	Clinical BNCT	installing
Granada University Hospital Spain	Electrostatic	Clinical BNCT	under development
Xiamen Humanity Hospital Xiamen City, China	Electrostatic Tandem	Clinical BNCT	preclinical trial
CNAO Pavia, Italy	Electrostatic Tandem	Clinical BNCT	under construction
Budker Institute of Nuclear Physics Novosibirsk, Russia	Electrostatic Tandem	BNCT research	experimental use
BNMRCO Moscow, Russia	Electrostatic Tandem	Clinical BNCT	under construction
Nagoya University Japan	Electrostatic	BNCT research	experimental use
Soreq Nuclear Research Center Israel	RFQ+HWR	Multi-purpose research	experimental use
CNEA Buenos Aires, Argentina	ESQ	BNCT research	under construction
Dongguan Neutron Science Center Dongguan campus of IHEP, China	RFQ	BNCT research	experimental use
Dongguan People's Hospital China	RFQ	Clinical BNCT	under construction
Gachon University Gil Medical Center Songdo, Incheon, South Korea	RFQ+DTL	Clinical BNCT	preclinical trial
KIRAMS Seoul, South Korea	Electrostatic	BNCT research	under construction
Birmingham University UK	Electrostatic	Multi-purpose research	under construction
INFN Legnaro (Padova), Italy	RFQ	BNCT research	under development
University of Torino Italy	Electron LINAC	Multi-purpose research	experimental use
CIAE Beijing, China	Cyclotron	BNCT research	commissioning
Mazu Hospital, Putian City Fugian Province, China	RFQ	Clinical BNCT	under construction
China Medical University Hsinchu Hospital Zhubei City, Taiwan	Cyclotron	Clinical BNCT	under construction

A minimum epithermal neutron flux is required in order to perform treatments in a reasonable time. Standard BNCT treatments for standard (normal size) tumours last for a time interval between 30 minutes and one hour. In fact, for one (standard) tumour having surface about 16 cm^2 (exposed to an incoming flux 10^9 neutrons/(cm^2·s) and a treatment lasting 40 minutes, one has roughly: 10^9 neutrons/(cm^2·s)$\times 2.4 \cdot 10^3$ s $\times 16$ cm^2 $= 4 \times 10^{13}$ neutrons.

Consequently, we will assume that, for a thermal neutron beam to be effective in standard BNCT, its flux should be not smaller than 5×10^8 neutrons/(cm^2·s) (say, about a few dozen grays) and that a typical full BNCT treatment requires a total of about 10^{14} neutrons.

One could argue, at least qualitatively (through a simple proportionality), that a small tumour with volume 1 mm^3 (requiring a smaller total number of neutrons) could possibly be treated, during approximately a similar time duration, by a flux about 10^4 neutrons/(cm^2·s).

Let us consider the accelerator-based neutron source, constructed by the private Japanese company Sumitomo [118, 119]. It employs a proton beam equivalent to 1 mA and produces a flux 10^9 neutrons/(cm^2·s) for 1 hour treatment, which is specifically designed for BNCT. Let the latter flux enter into the first waveguide in the above proposal in Section 6.1.1 (see Figure 6.1). Then, plausibly, the slow neutron flux at the exit of the first waveguide, just at the entrance of the second waveguide, could be about 10^5 neutrons/(cm^2·s). If losses upon entering into the second waveguides are moderately small the outgoing flux at the exit of the second waveguide, having air core, should not suffer further appreciable attenuation, say, could be about 10^4 neutrons/(cm^2·s); possibly enough for the treatment of small tumours.

Let us now turn very briefly to the proposal in Section 6.1.2 (with lateral confinement in both transverse directions x and y). A direct application of the θ_{cr}^2 reduction factor in the confined flux (see Eq.(2.3)) would suggest an outgoing flux at the exit of the second waveguide (having air core) comparable to the above proposal. One could also speculate that the coupling of the incoming neutrons to the propagation modes in the Ti core of the first waveguide could be enhanced adequately (perhaps, through lateral illumination).

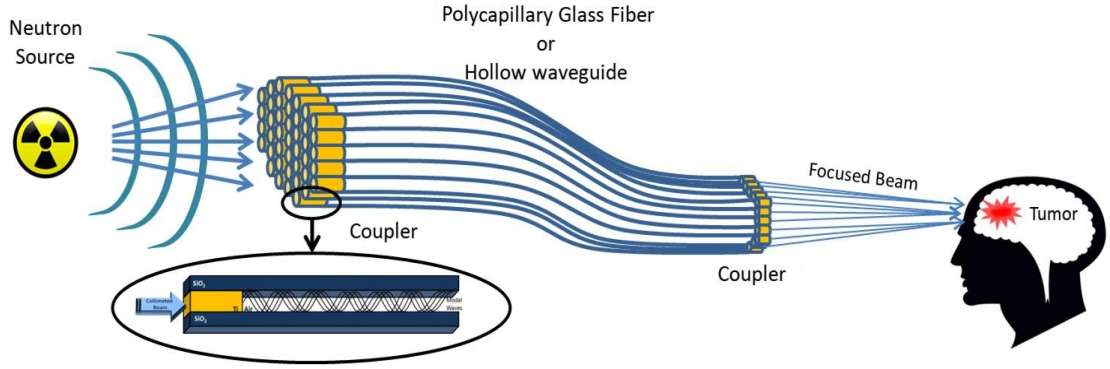

Figure 6.5: Possible use of optical couplers and PGFs in BNCT

One could also entertain other possibilities beyond our proposal in Section 6.1.3 (for example, multiple Ti coupling waveguides to collect, plus multiple polycapillary glass fibres to focus those neutrons and, finally, another Ti coupling waveguide to a hollow (single) waveguide directly inserted in the patient's brain) that would enable

additional improvements transporting neutrons. In any case, let's not forget the possibility of using these devices to focus neutrons on malignant tissues without the need to perform surgery on patients. This research line already holds promise of improving the efficiency of neutron sources for BNCT.

In conclusion, our a priori, general interest of pursuing the exploration of shorter scales by means of slow neutrons yields possible improvements (whatever the device employed) in focalizing neutrons that could enable to concentrate them onto malignant tissues and to reduce their delivery to normal tissues in BNCT.

- He hecho lo correcto, ¿verdad? Al final todo ha salido bien.
- "¿Al final?" Nada acaba, Adrian. Nada termina jamás.
- ¿Jon? ¡Espera! ¿Qué quieres decir con...?
- ...

Watchmen

7 Conclusions

This thesis was primarily devoted to the characterization of how an impinging thermal neutron beam is diffracted, propagates and gives rise to propagation modes in waveguides, in particular, hollow ones and those based on Titanium. This characterization is a necessary first step to identify critical design parameters and geometries for improving current devices. The problem is to compute the probability amplitude of the propagation modes generated in terms of the incoming neutron wave.

- In Chapter 2, we tried different approaches. The Schrödinger equation, provides rich information about the propagating wavefunction at the cost of (often) unaffordable numerical computation. The analysis of the energy level structure in the waveguide relates with propagation modes but the quantification of how much is excited each propagation mode is a major challenge. For last, we used refractive optics geometrical approximation (Section 2.5), which provides information of the excitation of a propagation mode for an incoming wavefunction by an incoming wave. In any case, that analysis neglects physical phenomena such as diffraction at the entrance and generation of evanescent waves. These three approaches provide complementary information and can be used to a proper characterization of waveguides. They fail to provide a complete picture and, thus, it makes difficult their use to design new waveguides.

- In Chapter 3 we made a rigorous development of a new formulation for describing the wavefunction in semi-infinite waveguides with infinitely repulsive potential (Dirichlet boundary conditions) in the clad. Our formulation shows both mathematical and physical consistency as it yields the conservation of the probability current (Section 3.3) and relates with the extinction theorem.

This formulation, being mathematically rigorous, can only yield analytical solutions in certain simple cases (Sections 3.2.1 and 3.2.2) and under certain approximations. In any case, we were able to extract valuable information about waveguides, such as critical angle, and geometry of the propagation modes, diffraction at the waveguide's entrance, extinction of the incoming wave, etc.

- In Chapter 4, we presented a new, efficient and robust method for computing confined neutron beam propagation for those cases in which Dirichlet boundary conditions play a key role. Our algorithm proved to be versatile and powerful to deal with a variety of physical situations: (i) reflection (Section 4.2.1) for arbitrary angles, (ii) single and multiple slit diffraction (Sections 4.2.2 and 4.2.3) for any angle of incidence, (iii) waveguiding regime (Section 4.2.4), (iv) free propagation and its relation with Fresnel regime (Section 4.2.6), (v) Fresnel lenses (including Arago-Poisson spot) (Sections 4.2.7 and 4.2.8). Thus, we have overcome the computational challenges we faced in the early stages of this thesis.

  Indeed, Dirichlet boundary conditions can be understood as a zero-th order approximation for guides where the neutron suffers total reflection (i.e. for all waves with angle of incidence smaller than the critical angle). In these cases, our formulation will enable to study the neutron propagation along the waveguide at large scales compared to its wavelength. Moreover, since the degree of confinement of the neutron beam increases as the neutron energy E decreases, our formulation may describe the propagation of ultracold neutrons in waveguides.

  Beyond this, we were able to modify our formulation, in Section 4.3, with the aim to interpret Dirichlet conditions as objects oriented in space. Our initial results showed that, with some modifications, our algorithm can be extended to digital holography. We claimed a patent for our method, [5].

- In Chapter 5, we performed a non-trivial extension of our approach to more realistic conditions, where finite potentials play a role. We introduced a quantum-mechanical formulation. Two new scattering integral equations ($LS_1 \rightarrow LS_2$ and $LS_2 \rightarrow LS_1$) were proposed and discussed for the two half-spaces using suitable Green functions. Those integral equations yield: (i) the reflection amplitude ($T_{ref}\left(\vec{l}\right)$), (ii) the amplitudes for the α-th propagation mode ($T_{pm,\alpha}$), (iii) the scattering amplitude (T_{scat}). This formulation constitutes an important improvement compared to the previous one. It accounts for neutron beam losses in the waveguide via tunnelling effect in certain quasi-discrete propagation modes with positive transverse energy. This would provide an upper bound for the probability for mode decay versus distance as in Section 5.5.3. This information is crucial for the adequate design of

a neutron waveguide since it deals with the neutron flux attenuation in the waveguide and accounts for the radiation field outside the waveguide, that would relate, eventually, with the personnel radiological protection.

- In Chapter 6 we use the acquired knowledge to the improvement of present neutron waveguides and the design of new ones. We propose the use of devices (based on hollow guides and Titanium guides) similar to optical couplers to improve the efficiency of neutron waveguides. These waveguides may be used in Boron Neutron Capture Therapy (BNCT) for tumours of small size.

To summarize, our work has generated a quite active research. During this thesis, we achieved the publication of a patent, six research papers and a book chapter, in which we focus in a variety of subjects; state of the art in neutron waveguiding, analytical formulation of neutron optics, quantum-mechanics problems and computational physics (for a list, see Appendix E). Our topic is widely transversal to many areas of research interest in physics.

Appendices

- ¡Eh! ¡Spambo! ¿Te dejan usar el enchufe de la maquinilla?
- Claro... Por cierto, ¿Sabes ese DAT donde estás almacenado? Perderá gradualmente su información. Yo tengo un cubo de un trillonbyte.

Top-10

A

Recorded Computing Requirements for Simulations

In Section 4.2, we carried out a series of simulations for different simple cases. The following tables summarize the computation requirements in terms of defined auxiliary functions, $\mu_i(\boldsymbol{x_i})$ (Table A.1), memory usage (Table A.2), and computation times (Table A.3).

Table A.1: Auxiliary functions defined for cases in Section 4.2

Case	**Computing Method**	**Auxiliary Functions $\mu_i(\boldsymbol{x_i})$**
***15°* Reflection**	Numerical Integration	$\mu_1(x, z=0)$
	Inverse FFT	$\mu_1(x, z=0)$
***30°* Reflection**	Numerical Integration	$\mu_1(x, z=0)$
	Inverse FFT	$\mu_1(x, z=0)$
***10°* Diffraction**	Numerical Integration	$\mu_1\left(x \geqslant +\frac{x_0}{2}, z=0\right)$
		$\mu_2\left(x \leqslant -\frac{x_0}{2}, z=0\right)$
	Inverse FFT	$\mu_1\left(x \geqslant +\frac{x_0}{2}, z=0\right)$
		$\mu_2\left(x \leqslant -\frac{x_0}{2}, z=0\right)$
***0°* Diffraction**	Numerical Integration	$\mu_1\left(x \geqslant +\frac{x_0}{2}, z=0\right)$
		$\mu_2\left(x \leqslant -\frac{x_0}{2}, z=0\right)$
	Inverse FFT	$\mu_1\left(x \geqslant +\frac{x_0}{2}, z=0\right)$
		$\mu_2\left(x \leqslant -\frac{x_0}{2}, z=0\right)$
***10°* Double Slit Diffraction (Near Field)**	Inverse FFT	$\mu_1\left(x \geqslant +\frac{x_1}{2}+x_0, z=0\right)$
		$\mu_2\left(-\frac{x_1}{2} \leqslant x \leqslant +\frac{x_1}{2}, z=0\right)$
		$\mu_3\left(x \leqslant -\frac{x_1}{2}-x_0, z=0\right)$
***10°* Double Slit Diffraction**	Inverse FFT	$\mu_1\left(x \geqslant +\frac{x_1}{2}+x_0, z=0\right)$

Case	Computing Method	Auxiliary Functions $\mu_i(\boldsymbol{x_i})$
(Far Field)		$\mu_2\left(-\frac{x_1}{2} \leqslant x \leqslant +\frac{x_1}{2}, z=0\right)$
		$\mu_3\left(x \leqslant -\frac{x_1}{2} - x_0, z=0\right)$
Waveguide	Numerical Integration	Sommerfeld-Rayleigh (see Section A.1)
		$\mu_3\left(x=+\frac{x_0}{2}, z \geqslant 0\right)$
		$\mu_4\left(x=-\frac{x_0}{2}, z \geqslant 0\right)$
	Inverse FFT	$\mu_1\left(x \geqslant +\frac{x_0}{2}, z=0\right)$
		$\mu_2\left(x \leqslant -\frac{x_0}{2}, z=0\right)$
		$\mu_3\left(x=+\frac{x_0}{2}, z \geqslant 0\right)$
		$\mu_4\left(x=-\frac{x_0}{2}, z \geqslant 0\right)$
3D Fresnel Regime	2D Inverse FFT*	$\mu_1(x, y, z=0)$
3D Poisson Spot	2D Inverse FFT*	$\mu_1(x, y, z=0)$
Fresnel Lens	2D Inverse FFT*	$\mu_1(x, y, z=0)$

* Note: These simulations were performed in 3D by simulating a circular aperture or plate.

A.1 Approximation of Auxiliary Functions

In Section 4.2.4, we approached the solution of Eq.(3.5) for a waveguide by using, in step 4, two computational methods; numerical integration and inverse FFT. This implied setting four auxiliary functions $\mu_i(x, z)$ (see Table A.1).

In order to lighten up computation, we approximated the diffraction effects of the aperture of the waveguide, as commented below,, for numerical integration, as a new incoming wave, $\varphi^*_{in}(x, z)$.

In Sections 3.2.4 and 3.2.3, we considered two main effects: (i) the waveguide's aperture diffraction effects, and (ii) the generation of propagation modes. Even if both effects cannot be strictly separated from each other, we can state approximately that (i) is related to the auxiliary functions $\mu_1(x)$ and $\mu_2(x)$ and that (ii) is related to $\mu_3(z)$ and $\mu_4(z)$, respectively. Thus, as a first approximation, one can separate these two effects in the simulations. So, one can replace the former incoming plane wave, $\varphi_{in}(x, z)$, and the auxiliary functions, $\mu_1(x)$ and $\mu_2(x)$ by a new incoming wave $\varphi^*_{in}(x, z)$ that takes into account the aperture diffraction. This enabled us afterwards to concentrate in updating $\mu_3(z)$ and $\mu_4(z)$.

We shall remind the Sommerfeld-Rayleigh integrals (see [85, 86, 87, 120]) for a screen with a limited aperture. In our case, the 2D Green's function considered in the Sommerfeld-Rayleigh integral is

$$G(\bar{r}) = \frac{i}{4} H_0^{(1)}\left(\bar{k_{in}} r\right) \tag{A.1}$$

where $H_0^{(1)}$ is the zero-th order Hankel function of first kind (or Bessel function of third kind) [7] and $r = \sqrt{x^2 + z^2}$ is the 2D distance from the origin to the point.

Substituting Eq.(A.1) into the standard Sommerfeld-Rayleigh integral for a limited aperture of size x_0 (in 2D space, see, for example [121]) and operating, one obtains the new $\varphi_{in}^{*}(x,z)$

$$\varphi_{in}^{*}(x,z)=\frac{1}{4\pi}\int_{-\frac{x_0}{2}}^{+\frac{x_0}{2}}U_0(x')\,\frac{ik_{in}}{2}\,\frac{z}{\sqrt{(x'-x)^2+z^2}}H_1^{(1)}\left[\sqrt{(x'-x)^2+z^2}\right]dx' \quad \text{(A.2)}$$

where $H_1^{(1)}$ is the first-order Hankel function of first kind [7] and $U_0(x')$ is an adequately chosen incident field. In our case we use $U_0(x')=e^{ik_{in,x}x}$ to simulate a limited aperture wave with arbitrary angle of incidence by setting adequately the value of $k_{in,x}$. Notice that $k_{in}^2=k_{in,x}^2+k_{in,z}^2$.

In Section 4.2.4, we implemented this result upon the following approximations: (i) in Eq.(3.5), we replace the incoming plane wave, $\varphi_{in}(x,z)$, and the two contributions due to $\mu_1(x)$ and $\mu_2(x)$ by the new $\varphi_{in}^{*}(x,z)$ in Eq.(A.2) (ii) in the right-hand-side of Eq.(3.16) for $i=3,4$, we replace the incoming plane wave $\varphi_{in}(x,z)$, and the two contributions due to $\mu_1(x)$ and $\mu_2(x)$ by the new $\varphi_{in}^{*}(x,z)$ in Eq.(A.2) and, thus, Eq.(3.16) for $i=1,2$ is no longer considered. Then, Eq.(3.5) becomes a representation for the slow neutron wavefunction in terms of the new $\varphi_{in}^{*}(x,z)$, $\mu_3(z)$ and $\mu_4(z)$. In turn, Eq.(3.16) for $i=3,4$ becomes a new system of two inhomogeneous integral equations for $\mu_3(z)$ and $\mu_4(z)$, with the new inhomogeneous term in Eq.(A.2).

In Table A.2, this method provided us a direct procedure to save computing memory (without significant gain in computation time). On the other hand, in Table A.3, we see that the computation of the $\varphi_{in}^{*}(x,z)$ through this method and the computation of $\mu_3(z)$ and $\mu_4(z)$ involve computation times of the same order of magnitude, so this method, although correct, does not seem to have had a significant positive impact.

Table A.2: Arrays and memory load for cases in Section 4.2

Case	**Computing Method**	**Array Size ($N \times M$) Complex Double Precission**	**Array Size (Megabytes)**
***15°* Reflection**	Numerical Integration	3 Arrays (501×5001)	40 MB
	Inverse FFT	3 Arrays (501×16384)	130 MB
***30°* Reflection**	Numerical Integration	3 Arrays (501×5001)	40 MB
	Inverse FFT	3 Arrays (501×16384)	130 MB
***10°* Diffraction**	Numerical Integration	1 Array (501×5001)	40 MB
	Inverse FFT	1 Array (501×16384)	130 MB
***0°* Diffraction**	Numerical Integration	1 Array (1001×5001)	80 MB
	Inverse FFT	1 Array (1001×16384)	262 MB
***10°* Double Slit (Near Field)**	Inverse FFT	1 Array (501×5001)	40 MB
***10°* Double Slit (Far Field)**	Inverse FFT	1 Array (501×5001)	40 MB

Case	Computing Method	Array Size ($N \times M$) Complex Double Precission	Array Size (Megabytes)
Waveguide	Numerical Integration	4 Arrays (500×1001)	8 MB
		6 Arrays (1×32768)	0.5 MB
	Inverse FFT	4 Arrays (16384×1592)	412 MB
		8 Arrays (1×32768)	0.5 MB
3D Fresnel Regime	2D Inverse FFT*	6 Arrays (4096×4096)	264 MB
3D Poisson Spot	2D Inverse FFT*	6 Arrays (4096×4096)	264 MB
Fresnel Lens	2D Inverse FFT*	6 Arrays (4096×4096)	264 MB

* Note: Simulations were performed in 3D by simulating a circular aperture or plate.
** Note: These arrays were reduced by deleting superfluous information to save memory. Otherwise their size would be 16384×32768 (about 8.6 GB each array).

Table A.3: Iterations and running times for cases in Section 4.2

Case	Computing Method	Step 1 $\varphi_{in}(\boldsymbol{x})$	Step 2 $\mu_i(\boldsymbol{x_i})$	Step 3-6 Iterations	Step 7 $\varphi_{total}(\boldsymbol{x})$	TOTAL
***15°* Reflection**	Numerical			1 iteration		
	Integration	5.87 s	0.07 s	0.22 s	1328.55 s	1334.71 s
				1 iteration		
	Inverse FFT	41.95 s	0.05 s	≈0 s	0.41 s	42.41 s
***30°* Reflection**	Numerical			1 iteration		
	Integration	4.32 s	0.05 s	0.04 s	1316.28 s	1320.69 s
				1 iteration		
	Inverse FFT	28.47 s	0.08 s	0.40 s	0.62 s	29.57 s
***10°* Diffraction**	Numerical			1 iteration		
	Integration	-	0.07 s	0.04 s	1403.29 s	1403.40 s
				1 iteration		
	Inverse FFT	-	1.26 s	4.38 s	1.10 s	6.74 s
***0°* Diffraction**	Numerical			1 iteration		
	Integration	-	0.14 s	0.07 s	2572.84 s	2573.04 s
				1 iteration		
	Inverse FFT	-	0.22 s	≈0 s	0.53 s	0.75 s
***10°* Double Slit (Near Field)**	Inverse FFT	-	1.01 s	1 iteration 0.34 s	3.29 s	4.64 s
***10°* Double Slit (Far Field)**	Inverse FFT	-	0.76 s	1 iteration 0.29 s	2.84 s	3.89 s
Waveguide	Numerical	2D S-R*	2D S-R*	5 iterations		
	Integration	1585.22 s	103.94 s	541.45 s	1030.29 s	3260.91 s
				5 iterations		
	Inverse FFT	10.27 s	0.01 s	0.07 s	4.03 s	14.39 s
3D Fresnel Regime	2D Inverse FFT**			1 iteration		
		-	0.84 s	0.91 s	1276.87 s	1278.72 s
3D Poisson Spot	2D Inverse FFT**			1 iteration		
		-	1.65 s	0.48 s	1335.96 s	1338.09 s
Fresnel Lens	2D Inverse FFT**			1 iteration		
		-	1.56 s	0.84 s	1298.35 s	1300.75 s

* Note: $\mu_1(x)$ and $\mu_2(x)$ are included in $\varphi^*_{in}(x,z)$ through the 2D-Sommerfeld-Rayleigh integral representation. See Section A.1).
**Note: These simulations were performed in 3D by simulating a circular aperture or plate.

- ¿Queréis daros prisa?
¡No tengo toda la noche!

Sin City

B

Demonstration of the Cancellation of Divergent Terms in Flux

A direct analysis of the term $F_{scat,fin}$ (see Section 5.4) will be outlined, aimed at verifying explicitly that the various divergent terms contained in it cancel out so that, after the cancellation, $F_{scat,fin}$ is finite.

We recall here the term $F_{scat,fin}$ to be

$$\begin{aligned} F_{scat,fin} =& \frac{\hbar k_z}{m} Re\left[T_{scat}\left(\bar{k}\right) + T_{scat}\left(\bar{k}\right)^*\right] + \\ &+ \frac{\hbar}{m}\int_{\left(2mE/\hbar^2-\bar{l}^2\right)^{1/2}\geq 0} \frac{d^2\bar{l}}{\left(2\pi\right)^2}\left(2mE/\hbar^2-\bar{l}^2\right)^{1/2} \mid T_{scat,1}\left(\vec{l}\right) + T_{scat,2}\left(\vec{l}\right) \mid^2 \end{aligned} \tag{B.1}$$

It is easy to see that the only divergent contributions in $F_{scat,fin}$ are contained separately in each of the two terms in

$$\begin{aligned} &\frac{\hbar}{m}\int_{\left(2mE/\hbar^2-\bar{l}^2\right)^{1/2}\geq 0} \frac{d^2\bar{l}}{\left(2\pi\right)^2}\left(2mE/\hbar^2-\bar{l}^2\right)^{1/2} \mid T_{scat,1}\left(\vec{l}\right) \mid^2 + \\ &\qquad + \frac{\hbar k_z}{m} Re\left[T_{scat,1}\left(\bar{k}\right) + T_{scat,1}\left(\bar{k}\right)^*\right] \end{aligned} \tag{B.2}$$

Moreover, the remaining contributions in $F_{scat,fin}$ (besides those in (B.2)) are two integrals, which turn out to be finite. In fact, the one in (ii) containing $\mid T_{scat,2}\left(\vec{l}\right) \mid^2$ is obviously finite. Besides, while $T_{scat,1}\left(\vec{l}\right)$ diverges, the integral containing the interference terms $T_{scat,1}\left(\vec{l}\right) T_{scat,2}\left(\bar{k}\right)^* + T_{scat,1}\left(\bar{k}\right)^* T_{scat,2}\left(\bar{k}\right)$ is finite, due to the integration over $\int_{\left(2mE/\hbar^2-\bar{l}^2\right)^{1/2}\geq 0} d^2\bar{l}$.

At this point (and in order to stablish the finiteness of Eq.(B.2)), we remind that the right-hand-side of the 2D Eq.(5.20) becomes, as $\mid \bar{x} \mid \rightarrow +\infty$ along a fixed direction $(\bar{x}/ \mid \bar{x} \mid)$ (with $\bar{q}_1 = \mid \bar{q} \mid \cdot (\bar{x}/ \mid \bar{x} \mid)$)

$$e^{i\bar{q}\bar{x}} + \mid \bar{x} \mid^{-1/2} e^{i\pi/4} e^{i|\bar{q}||\bar{x}|} f(\bar{q}_1, \bar{q}) \tag{B.3}$$

$$f(\bar{q}_1, \bar{q}) = -\left(2m/\hbar^2\right) (2/\pi \mid \bar{q} \mid)^{1/2} \int d^2\bar{x}_1 e^{-i\bar{q}_1\bar{x}_1} V(\bar{x}_1)\, \phi_{\bar{q}}(\bar{x}_1) \tag{B.4}$$

$f(\bar{q}_1, \bar{q})$ being the 2D scattering amplitude. The latter fulfils the *2D optical theorem*

$$\frac{1}{2} (\mid \bar{q} \mid /2\pi)^{1/2} \int_0^{2\pi} d\beta \mid f(\bar{q}_1, \bar{q}) \mid^2 - Im\left[f(\bar{q}_1 = \bar{q}, \bar{q})\right] = 0 \tag{B.5}$$

β and $f(\bar{q}_1 = \bar{q}, \bar{q})$ being the angle between $\bar{q}_1$ and $\bar{q}$ and the 2D scattering amplitude in the forward direction, respectively.

The important point here is that the two terms in the 3D expression Eq.(B.2) resemble, term by term, the two contributions in the left-hand-side of the 2D Eq.(B.5). This suggests that as the difference of the latter two vanishes, as Eq.(B.5) indicates, a cancellation could hold for the sum of the divergent terms in Eq.(B.2). In fact, a detailed computation shows that each of the two divergent terms in the 3D expression Eq.(B.2) equals a constant divergent factor (diverging as the infinite length of the semi-infinite waveguide) times its mate in the left-hand-side of Eq.(B.5) (up to subdominant finite corrections). Then, by factorizing out that constant divergent factor, the divergent part of Eq.(B.2) vanishes. This establishes the finiteness of $F_{scat,fin}$.

One can also show, through a detailed analysis, that the finite contribution $-\frac{\hbar k_z}{m} Re\left[T_{scat,2}\left(\bar{k}\right) + T_{scat,2}\left(\bar{k}\right)^*\right]$ is non-negative.

La clave no es lloriquear, ni perder, es intentarlo.
Tal vez nunca sea lo que debería ser, lo que quiero ser
pero, ¿Cómo lo sabré si no lo intento?

Lobezno: Honor

C
Future Work

The analysis of the mathematical system described by each of the formulations proposed in this thesis (i.e.: Dirichlet conditions in Chapter 3 and Lippmann-Schwinger equations in Chapter 5) provide useful information to estimate the guiding efficiency. There are important physical aspects that have been disregarded. As a general issue, the most ambitious simulation of neutron propagation should have into account the different nuclear reactions with the media, incoherent scattering, thermal and epithermal absorption, etc.

Some effects, accounting for neutron losses due to incoherent scattering or absorption may be described by virtue of certain (non trivial) modifications in our formulations considering absorbing (with imaginary part $\neq 0$) potentials.

In this appendix, we provide an overview of the formulation's potential future developments and applications currently in progress.

C.1 Extension of the Green's Functions Method

The use of the formulation in Section 3.1 and its implementation as an algorithm, can be considered one of the highlights of this thesis. The Green's functions used make Fourier transforms to arise naturally in this formulation for problems under study. It yields multiple advantages both for their analytical solution (through multiple tabulated properties) and for their implementation through efficient computational algorithms (FFT). One possible next step would be to expand the algorithm to solve more general boundary conditions problems, including those involving different propagation media. It is clear that the extension of the formulation to cases of finite potential can be of great interest in multiple areas of physics described by the wave equation, including the one that concerns us here.

We made several attempts and developments with partial results that will be briefly exposed here.

In Section 3.2.1 we stated the similarities of our formulation (that, in our case, comes from the so-called potential theory) with what arises from the use of Green's theorem for the case of the Kirchoff approximation; $\psi(\vec{r}) = \int_{\partial\Omega}\left[\mu\frac{\partial G}{\partial\vec{n}} - G\frac{\partial\mu}{\partial\vec{n}}\right]dS$. In fact, in that section we showed that one may obtain the same solution for total reflection by formulating Eq.(3.24) if one sets the auxiliary function to be $\mu(x,z) = -\mu e^{ik_{in,x}x}e^{ik_{in,z}z}$. In this simple physical case, Neumann and Dirichlet conditions would yield the same results. This encourages looking for a description of a more complex system through the use of Green's theorem.

Using this formulation, the neutron wavefunction for a certain medium is

$$\varphi(\boldsymbol{x}) = \varphi_{in}(\boldsymbol{x}) - \int_{\partial\Omega} d\bar{x}'\left[\mu(\bar{x}')\frac{\partial G(\boldsymbol{x}-\boldsymbol{x'})}{\partial\bar{n}} - G(\boldsymbol{x}-\boldsymbol{x'}))\frac{\partial\mu(\bar{x}')}{\partial\bar{n}}\right] \tag{C.1}$$

where $\partial\Omega$ is an arbitrary surface (where secondary waves emerge). Notice that, in this case, $\bar{x}'$ is the two-dimensional coordinate associated to $\partial\Omega$ and $\bar{n}$ is the two-dimensional unitary vector normal to $\partial\Omega$.

One may describe reflexion and refraction considering medium 1 and medium 2 as two disjoint regions, each one described by its own Green's function, $G_1(\bar{x}-\bar{x}', z-z')$ and $G_2(\bar{x}-\bar{x}', z-z')$ by setting the total neutron energy in each case (i.e.: neutron kinetic energy and potential). In this case, the problem is to characterize the auxiliary functions that would arise in each medium; $\mu_1(\bar{x}')$, $\mu_2(\bar{x}')$, $\frac{\partial\mu_1}{\partial\bar{n}}(\bar{x}')$ and $\frac{\partial\mu_2}{\partial\bar{n}}(\bar{x}')$ so that the boundary conditions (continuity of the wavefunction and its derivative at the point) are met so as to ensure the conservation of flux. Note that a priori we assume that the auxiliary functions that characterize each medium are different from each other.

We performed an attempt for a geometry similar to that of Section 3.2.1, considering that medium 2 has a finite potential. The resulting equations are cumbersome and we will omit details here. In any case, we showed that if we consider (neglecting the y coordinate for simplicity) an incoming plane wave $\varphi_{in}(x,z) = e^{iK_x x}e^{iK_z z}$, one obtains Fresnel's equations for neutron reflection and refraction (see, for example [122]) setting $\mu_1(x',z') = e^{iK_x x'}e^{i2\frac{K_{2z}K_{1z}}{K_{1z}+K_{2z}}z'}$ and $\mu_2(x',z') = e^{iK_x x'}e^{i\frac{K_{1z}-K_{2z}}{K_{1z}+K_{2}z}K_{2z}z'}$ as auxiliary functions.

Similar attempts were made, by Lalor and Wolf, for obtaining Fresnel's coefficients for semi-infinite dielectric domains, [123]. In that case, like in ours, they did not obtain a solution for any general geometry. Moreover, they used Green's functions in Weyl's representation, which do not yield directly Fourier transforms.

We made attempts for a more general geometry instead of an infinite wall, but we could not prove a general relationship between auxiliary functions and the incoming wave as in Eq.(3.16). It is clear that achieving this would be a milestone since wave simulations would benefit of reducing one dimension the problem and, moreover,

these Green's functions would lead naturally to Fourier transforms (using, thus, FFT algorithm). In any case, it is not clear whether imposing values both on the auxiliary functions and their derivative would not imply the wavefunction be overdetermined. Notice that this is a possible research line that lies outside the scope of this thesis.

A more practical attempt (under development) comes from the possibility of expanding one of the Green's function for the two media in a Taylor series. Indeed, the Green's function for a medium 1 where there is a constant potential, V_1, would be

$$G_1(x-x',z-z') = -\int \frac{dK'_x dK'_z}{(2\pi)^2} \frac{e^{i[K'_x(x-x')+K'_z(z-z')]}}{(E-V_1)+i\varepsilon-\frac{\hbar^2}{2m}(K'^2_x+K'^2_z)} \tag{C.2}$$

In the case of thermal neutrons, the neutron energy $E = 25\times10^{-3}$ eV exceeds by various orders of magnitude the potential value in the medium $V_1 \approx 10^{-7}$ eV. Consequently, one may expand Eq.(C.2) in a Taylor series

$$\begin{aligned} G_1(x-x',z-z') = &-\int \frac{dK'_x dK'_z}{(2\pi)^2} e^{i[K'_x(x-x')+K'_z(z-z')]}\times \\ &\times\left[\frac{1}{E+i\varepsilon-\frac{\hbar^2}{2m}(K'^2_x+K'^2_z)}+\frac{V_1}{\left(E+i\varepsilon-\frac{\hbar^2}{2m}(K'^2_x+K'^2_z)\right)^2}+...\right]= \\ &= G(x-x',z-z')+V_1G_V(x-x',z-z')+O(V_1^2) \end{aligned} \tag{C.3}$$

where $G(x-x',z-z')$ is the standard Green's function in vacuum and $G_V(x-x',z-z')$ is a first order correction due to the potential that is likely to be three to four orders of magnitude lower. $O(V_1^2)$ represents the terms of order 2 and higher. Notice that due to the presence of the standard Green's function, conservation of flux must be imposed by hand.

C.2 Extension of the Lipmann-Schwinger Equation

In the case of the $LS_1 \to LS_2$ and $LS_2 \to LS_1$ equations exposed in Chapter 5 the next obvious step is to add some terms quantifying for absorbing media. This may be accomplished by considering a complex potential (i.e.: $Im\,(V) \neq 0$). In this case, the imaginary part of the potential would turn the propagating waves into damped waves. This may have the advantage of assuring the convergence of the iterative integral series that emerged in Sections 5.2.4 and 5.2.5. In this way it will be possible to obtain a more precise picture of the behaviour of a hypothetical neutron guide.

Moreover, in Section 6.2.1 we stated the interest in the development of optical couplers based in Ti. In this way, the development of a quantum-mechanical description which would account for three regions (along the z axis): $LS_1 \to LS_2 \to LS_3$, where region 1 would be vacuum (or air), region 2, the Ti coupling waveguide

and region 3 the (hollow) waveguide, would allow to properly characterize the behaviour and efficiency of the device. This extension is far from trivial, since the previous basis for $LS_1 \rightarrow LS_2$ with the associated eigenfunctions in each media extending to infinity has to be generated. Thus, adding a finite media would imply to make some more general ansatz.

C.3 Holography Applications

In Section 4.3 we demonstrated that our algorithm may be used in digital holography, since one may simulate, also as a zeroth-order approximation, the interaction of a plane wave beam with a surface with arbitrary shape (through the Dirichlet condition): the reflection of the waves from the surface and their interference (under partial coherent conditions) with the incoming plane wave may be used to calculate the interference pattern that would appear in any arbitrary point in space. The algorithm itself can act as a convenient reading system of that pattern, leading to the reconstruction of the hologram. In this scenario, the main advantage of the present algorithm would be: a) a correct simulation of the interference pattern for objects with sizes much larger than the wavelength, at an affordable computational cost, and b) the possibility of focusing in obtaining only the interference pattern.

This research line could be very interesting, since it opens a new variety of possible physical applications. The latter exposed, is related with our claims in the patent Ref.P202230979, "Sistema para generación de hologramas digitales vía simulación" (System for generation of digital holograms via simulation), [5], presented by Universidad Complutense and still under review.

The assumption of Dirichlet conditions for simulating flat plane structures implies that they are perfectly reflective (i.e.: like performing an hologram of a perfect mirror). The algorithm itself would benefit of adding some condition to enhance the wave scattering in all directions that would improve the object visibility.

Moreover, as we set and control the (digital) reference beam, one deals with a simple numerical treatment enabling to study the effects in the algorithm efficiency of the implementation of each of the four terms arising in Eq.(4.7), making thus, a more efficient hologram.

The neutron holography technique has had a limited field of development due, among other things, to the difficulty of generating and interpreting interferograms: for them, the present algorithm could be used as a laboratory technique. One clear example would be that of calculating the diffraction pattern to obtain bottleneck and doughnuts-like structures that would allow a better control of them in the laboratory. This application lies beyond the scope of neutron holography, since no data on neutron beams with such structures are available.

Being based on scalar wave equations, this method was designed especially for neutron holography (assuming partially coherent neutron beams), but it is

directly applicable to any holographic system represented by a scalar wave and can be exported directly, almost trivially, to a generic vector wave method (to any holographic field).

No puedes culpar a un superordenador alienígena por almacenar información. Todo lo que hacía era de acuerdo a mi directriz principal.

Superman: Hijo Rojo

D

Neutron Scattering Lengths and Cross Sections

For easier reference, we will reproduce here the scattering lenghts and cross sections for a thermal neutron beam ($E = 0.025$ eV), extracted from [33]. Isotopes that are not present in natural concentrations are labelled as "unstable". Uncertainties are not stated in this table. They correspond to the last decimal unless stated otherwise.

Table D.1: Neutron scattering lengths and cross sections for different isotopes and natural elements.

Isotope	Natural Abundance (%)	b_{coh} (10^{-13}) cm	b_{inc} (10^{-13}) cm	σ_{coh} (10^{-24}) cm^2	σ_{inc} (10^{-24}) cm^2	σ_{scat} (10^{-24}) cm^2	σ_{abs} (10^{-24}) cm^2
Natural H	—	-3.739	—	1.7568	80.26	82.02	0.3326
^{1}H	99.985	-3.7406	25.274	1.7583	80.27	82.03	0.3326
^{2}H	0.015	6.671	4.04	5.592	2.05	7.64	0.000519
^{3}H	Unstable	4.792	-1.04	2.89	0.14	3.03	0
Natural He	—	3.26 ±3	—	1.34	0	1.34	0.00747
^{3}He	0.00014	5.74-1.483i	-2.5+2.568i	4.42	1.6	6	5333.0 ±7.0
^{4}He	99.99986	3.26	0	1.34	0	1.34	0
Natural Li	—	-1.9	—	0.454	0.92	1.37	70.5
^{6}Li	7.5	2.00-0.261i	-1.89+0.26i	0.51	0.46	0.97	940.0 ±4.0
^{7}Li	92.5	-2.22	-2.49	0.619	0.78	1.4	0.0454
Natural Be	100	7.79	0.12	7.63	0.0018	7.63	0.0076
Natural B	—	5.30-0.213i	—	3.54	1.7	5.24	767.0 ±8.0
^{10}B	20	-0.1-1.066i	-4.7+1.231i	0.144	3	3.1	3835.0 ±9.0
^{11}B	80	6.65	-1.3	5.56	0.21	5.77	0.0055
Natural C	—	6.646	—	5.551	0.001	5.551	0.0035
^{12}C	98.9	6.6511	0	5.559	0	5.559	0.00353
^{13}C	1.1	6.19	-0.52	4.81	0.034	4.84	0.00137
Natural N	—	9.36	—	11.01	0.5	11.51	1.9
^{14}N	99.63	9.37	2	11.03	0.5	11.53	1.91
^{15}N	0.37	6.44	-0.02	5.21	0.00005	5.21	0.000024
Natural O	—	5.803	—	4.232	0.0008	4.232	0.00019
^{16}O	99.762	5.803	0	4.232	0	4.232	0.0001
^{17}O	0.038	5.78	0.18	4.2	0.004	4.2	0.236
^{18}O	0.2	5.84	0	4.29	0	4.29	0.00016
Natural F	100	5.654	-0.082	4.017	0.0008	4.018	0.0096
Natural Ne	—	4.566	—	2.62	0.008	2.628	0.039
^{20}Ne	90.51	4.631	0	2.695	0	2.695	0.036
^{21}Ne	0.27	6.66	±0.6	5.6	0.05	5.7	0.67
^{22}Ne	9.22	3.87	0	1.88	0	1.88	0.046
Natural Na	100	3.63	3.59	1.66	1.62	3.28	0.53

Isotope	Natural Abundance (%)	b_{coh} (10^{-13}) cm	b_{inc} (10^{-13}) cm	σ_{coh} (10^{-24}) cm^2	σ_{inc} (10^{-24}) cm^2	σ_{scat} (10^{-24}) cm^2	σ_{abs} (10^{-24}) cm^2
Natural Mg	—	5.375	—	3.631	0.08	3.71	0.063
^{24}Mg	78.99	5.66	0	4.03	0	4.03	0.05
^{25}Mg	10	3.62	1.48	1.65	0.28	1.93	0.19
^{26}Mg	11.01	4.89	0	3	0	3	0.0382
Natural Al	100	3.449	0.256	1.495	0.0082	1.503	0.231
Natural Si	—	4.1491	—	2.163	0.004	2.167	0.171
^{28}Si	92.23	4.107	0	2.12	0	2.12	0.177
^{29}Si	4.67	4.7	0.09	2.78	0.001	2.78	0.101
^{30}Si	3.1	4.58	0	2.64	0	2.64	0.107
Natural P	100	5.13	0.2	3.307	0.005	3.312	0.172
Natural S	—	2.847	—	1.0186	0.007	1.026	0.53
^{32}S	95.02	2.804	0	0.988	0	0.988	0.54
^{33}S	0.75	4.74	1.5	2.8	0.3	3.1	0.54
^{34}S	4.21	3.48	0	1.52	0	1.52	0.227
^{36}S	0.02	3.0 ±1.0	0	1.1	0	1.1	0.15
Natural Cl	—	9.577	—	11.5257	5.3	16.8	33.5
^{35}Cl	75.77	11.65	6.1	17.06	4.7	21.8	44.1
^{37}Cl	24.23	3.08	0.1	1.19	0.001	1.19	0.433
Natural Ar	—	1.909	—	0.458	0.225	0.683	0.675
^{36}Ar	0.337	24.9	0	77.9	0	77.9	5.2
^{38}Ar	0.063	3.5	0	1.5 ±3.1	0	1.5 ±3.1	0.8
^{40}Ar	99.6	1.83	0	0.421	0	0.421	0.66
Natural K	—	3.67	—	1.69	0.27	1.96	2.1
^{39}K	93.258	3.74	1.4	1.76	0.25	2.01	2.1
^{40}K	0.012	3.0 ±1.0	—	1.1	0.5	1.6	35.0 ±8.0
^{41}K	6.73	2.69	1.5	0.91	0.3	1.2	1.46
Natural Ca	—	4.7	—	2.78	0.05	2.83	0.43
^{40}Ca	96.941	4.8	0	2.9	0	2.9	0.41
^{42}Ca	0.647	3.36	0	1.42	0	1.42	0.68
^{43}Ca	0.135	-1.56	—	0.31	0.5	0.8	6.2
^{44}Ca	2.086	1.42	0	0.25	0	0.25	0.88
^{46}Ca	0.004	3.6	0	1.6	0	1.6	0.74
^{48}Ca	0.187	0.39	0	0.019	0	0.019	1.09
Natural Sc	100	12.29	-6	19	4.5	23.5	27.5
Natural Ti	—	-3.438	—	1.485	2.87	4.35	6.09
^{46}Ti	8.2	4.93	0	3.05	0	3.05	0.59
^{47}Ti	7.4	3.63	-3.5	1.66	1.5	3.2	1.7
^{48}Ti	73.8	-6.08	0	4.65	0	4.65	7.84
^{49}Ti	5.4	1.04	5.1	0.14	3.3	3.4	2.2
^{50}Ti	5.2	6.18	0	4.8	0	4.8	0.179
Natural V	—	-0.3824	—	0.0184	5.08	5.1	5.08
^{50}V	0.25	7.6	—	7.3 ±1.1	0.5	7.8 ±1.0	60.0 ±40.0
^{51}V	99.75	-0.402	6.35	0.0203	5.07	5.09	4.9
Natural Cr	—	3.635	—	1.66	1.83	3.49	3.05
^{50}Cr	4.35	-4.5	0	2.54	0	2.54	15.8
^{52}Cr	83.79	4.92	0	3.042	0	3.042	0.76
^{53}Cr	9.5	-4.2	6.87	2.22	5.93	8.15	18.1 ±1.5
^{54}Cr	2.36	4.55	0	2.6	0	2.6	0.36
Natural Mn	100	-3.73	1.79	1.75	0.4	2.15	13.3
Natural Fe	—	9.45	—	11.22	0.4	11.62	2.56
^{54}Fe	5.8	4.2	0	2.2	0	2.2	2.25
^{56}Fe	91.7	9.94	0	12.42	0	12.42	2.59
^{57}Fe	2.2	2.3	—	0.66	0.3	1	2.48
^{58}Fe	0.3	15.0 ±7.0	0	28	0	28.0 ±26.0	1.28
Natural Co	100	2.49	-6.2	0.779	4.8	5.6	37.18
Natural Ni	—	10.3	—	13.3	5.2	18.5	4.49
^{58}Ni	68.27	14.4	0	26.1	0	26.1	4.6
^{60}Ni	26.1	2.8	0	0.99	0	0.99	2.9
^{61}Ni	1.13	7.6	±3.9	7.26	1.9	9.2	2.5
^{62}Ni	3.59	-8.7	0	9.5	0	9.5	14.5
^{64}Ni	0.91	-0.37	0	0.017	0	0.017	1.52
Natural Cu	—	7.718	—	7.485	0.55	8.03	3.78
^{63}Cu	69.17	6.43	0.22	5.2	0.006	5.2	4.5
^{65}Cu	30.83	10.61	1.79	14.1	0.4	14.5	2.17
Natural Zn	—	5.68	—	4.054	0.077	4.131	1.11
^{64}Zn	48.6	5.22	0	3.42	0	3.42	0.93
^{66}Zn	27.9	5.97	0	4.48	0	4.48	0.62
^{67}Zn	4.1	7.56	-1.5	7.18	0.28	7.46	6.8
^{68}Zn	18.8	6.03	0	4.57	0	4.57	1.1
^{70}Zn	0.6	6.0 ±1.0	0	4.5	0	4.5 ±1.5	0.092
Natural Ga	—	7.288	—	6.675	0.16	6.83	2.75
^{69}Ga	60.1	7.88	-0.85	7.8	0.091	7.89	2.18
^{71}Ga	39.9	6.4	-0.82	5.15	0.084	5.23	3.61
Natural Ge	—	8.185	—	8.42	0.18	8.6	2.2
^{70}Ge	20.5	10	0	12.6	0	12.6	3
^{72}Ge	27.4	8.51	0	9.1	0	9.1	0.8
^{73}Ge	7.8	5.02	3.4	3.17	1.5	4.7	15.1
^{74}Ge	36.5	7.58	0	7.2	0	7.2	0.4
^{76}Ge	7.8	8.2	0	8.0 ±3.0	0	8.0 ±3.0	0.16
Natural As	100	6.58	-0.69	5.44	0.06	5.5	4.5

Isotope	**Natural Abundance (%)**	b_{coh} (10^{-13}) **cm**	b_{inc} (10^{-13}) **cm**	σ_{coh} (10^{-24}) **cm²**	σ_{inc} (10^{-24}) **cm²**	σ_{scat} (10^{-24}) **cm²**	σ_{abs} (10^{-24}) **cm²**
Natural Se	—	7.97	—	7.98	0.32	8.3	11.7
^{74}Se	0.9	0.8	0	0.1	0	0.1	51.8 ±1.2
^{76}Se	9	12.2	0	18.7	0	18.7	85.0 ±7.0
^{77}Se	7.6	8.25	±0.6 ±1.6	8.6	0.05	8.65	42.0 ±4.0
^{78}Se	23.5	8.24	0	8.5	0	8.5	0.43
^{80}Se	49.6	7.48	0	7.03	0	7.03	0.61
^{82}Se	9.4	6.34	0	5.05	0	5.05	0.044
Natural Br	—	6.795	—	5.8	0.1	5.9	6.9
^{79}Br	50.69	6.8	-1.1	5.81	0.15	5.96	11
^{81}Br	49.31	6.79	0.6	5.79	0.05	5.84	2.7
Natural Kr	—	7.81	—	7.67	0.01	7.68	25.0 ±1.0
^{78}Kr	0.35	—	0	—	0	—	6.4
^{80}Kr	2.25	—	0	—	0	—	11.8
^{82}Kr	11.6	—	0	—	0	—	29.0 ±20.0
^{83}Kr	11.5	—	—	—	—	—	185.0 ±30.0
^{84}Kr	57	—	0	—	0	6.6	0.113
^{86}Kr	17.3	8.1	0	8.2	0	8.2	0.003
Natural Rb	—	7.09	—	6.32	0.5	6.8	0.38
^{85}Rb	72.17	7.03	—	6.2	0.5	6.7	0.48
^{87}Rb	27.83	7.23	—	6.6	0.5	7.1	0.12
Natural Sr	—	7.02	—	6.19	0.06	6.25	1.28
^{84}Sr	0.56	7.0 ±1.0	0	6.0 ±2.0	0	6.0 ±2.0	0.87
^{86}Sr	9.86	5.67	0	4.04	0	4.04	1.04
^{87}Sr	7	7.4	—	6.88	0.5	7.4	16.0 ±3.0
^{88}Sr	82.58	7.15	0	6.42	0	6.42	0.058
Natural Y	100	7.75	1.1	7.55	0.15	7.7	1.28
Natural Zr	—	7.16	—	6.44	0.02	6.46	0.185
^{90}Zr	51.45	6.4	0	5.1	0	5.1	0.011
^{91}Zr	11.32	8.7	-1.08	9.5	0.15	9.7	1.17
^{92}Zr	17.19	7.4	0	6.9	0	6.9	0.22
^{94}Zr	17.28	8.2	0	8.4	0	8.4	0.0499
^{96}Zr	2.76	5.5	0	3.8	0	3.8	0.0229
Natural Nb	100	7.054	-0.139	6.253	0.0024	6.255	1.15
Natural Mo	—	6.715	—	5.67	0.04	5.71	2.48
^{92}Mo	14.84	6.91	0	6	0	6	0.019
^{94}Mo	9.25	6.8	0	5.81	0	5.81	0.015
^{95}Mo	15.92	6.91	—	6	0.5	6.5	13.1
^{96}Mo	16.68	6.2	0	4.83	0	4.83	0.5
^{97}Mo	9.55	7.24	—	6.59	0.5	7.1	2.5
^{98}Mo	24.13	6.58	0	5.44	0	5.44	0.127
^{100}Mo	9.63	6.73	0	5.69	0	5.69	0.4
Natural Tc	Unstable	6.8	—	5.8	0.5	6.3	20.0 ±1.0
Natural Ru	—	7.03	—	6.21	0.4	6.6	2.56
^{96}Ru	5.5	—	0	—	0	—	0.28
^{98}Ru	1.9	—	0	—	0	—	<8.
^{99}Ru	12.7	—	—	—	—	—	6.9 ±1.0
^{100}Ru	12.6	—	0	—	0	—	4.8
^{101}Ru	17	—	—	—	—	—	3.3
^{102}Ru	31.6	—	0	—	0	144.8	1.17
^{104}Ru	18.7	—	0	—	0	4.483	0.31
Natural Rh	100	5.88	—	4.34	0.3	4.6	144.8
Natural Pd	—	5.91	—	4.39	0.093	4.48	6.9
^{102}Pd	1.02	7.7 ±7	0	7.5 ±1.4	0	7.5 ±1.4	3.4
^{104}Pd	11.14	7.7 ±7	0	7.5 ±1.4	0	7.5 ±1.4	0.6
^{105}Pd	22.33	5.5	-2.6 ±1.6	3.8	0.8	4.6 ±1.1	20.0 ±3.0
^{106}Pd	27.33	6.4	0	5.1	0	5.1	0.304
^{108}Pd	26.46	4.1	0	2.1	0	2.1	8.55
^{110}Pd	11.72	7.7 ±7	0	7.5 ±1.4	0	7.5 ±1.4	0.226
Natural Ag	—	5.922	—	4.407	0.58	4.99	63.3
^{107}Ag	51.83	7.555	1	7.17	0.13	7.3	37.6 ±1.2
^{109}Ag	48.17	4.165	-1.6	2.18	0.32	2.5	91.0 ±1.0
Natural Cd	—	4.87-0.70i	—	3.04	3.46	6.5	2520.0 ±50.0
^{106}Cd	1.25	5.0 ±2.0	0	3.1	0	3.1 ±2.5	1
^{108}Cd	0.89	5.4	0	3.7	0	3.7	1.1
^{110}Cd	12.51	5.9	0	4.4	0	4.4	11
^{111}Cd	12.81	6.5	—	5.3	0.3	5.6	24
^{112}Cd	24.13	6.4	0	5.1	0	5.1	2.2
^{113}Cd	12.22	-8.0-5.73i	—	12.1	0.3	12.4	20600.0 ±400.0
^{114}Cd	28.72	7.5	0	7.1	0	7.1	0.34
^{116}Cd	7.47	6.3	0	5	0	5	0.075
Natural In	—	4.065-0.0539i	—	2.08	0.54	2.62	193.8 ±1.5
^{113}In	4.3	5.39	±0.017	3.65	0.000037	3.65	12.0 ±1.1
^{115}In	95.7	4.01-0.0562i	-2.1	2.02	0.55	2.57	202.0 ±2.0
Natural Sn	—	6.225	—	4.871	0.022	4.892	0.626
^{112}Sn	1	6.0 ±1.0	0	4.5 ±1.5	0	4.5 ±1.5	1
^{114}Sn	0.7	6.2	0	4.8	0	4.8	0.114
^{115}Sn	0.4	6.0 ±1.0	—	4.5 ±1.5	0.3	4.8 ±1.5	30.0 ±7.0
^{116}Sn	14.7	5.93	0	4.42	0	4.42	0.14
^{117}Sn	7.7	6.48	—	5.28	0.3	5.6	2.3
^{118}Sn	24.3	6.07	0	4.63	0	4.63	0.22

Isotope	Natural Abundance (%)	b_{coh} (10^{-13}) cm	b_{inc} (10^{-13}) cm	σ_{coh} (10^{-24}) cm^2	σ_{inc} (10^{-24}) cm^2	σ_{scat} (10^{-24}) cm^2	σ_{abs} (10^{-24}) cm^2
^{119}Sn	8.6	6.12	—	4.71	0.3	5	2.2
^{120}Sn	32.4	6.49	0	5.29	0	5.29	0.14
^{122}Sn	4.6	5.74	0	4.14	0	4.14	0.18
^{124}Sn	5.6	5.97	0	4.48	0	4.48	0.133
Natural Sb	—	5.57	—	3.9	0.007	3.9	4.91
^{121}Sb	57.3	5.71	-0.05	4.1	0.0003	4.1	5.75
^{123}Sb	42.7	5.38	-0.1	3.64	0.001	3.64	3.8
Natural Te	—	5.8	—	4.23	0.09	4.32	4.7
^{120}Te	0.096	5.3	0	3.5	0	3.5	2.3
^{122}Te	2.6	3.8	0	1.8	0	1.8	3.4
^{123}Te	0.908	-0.05-0.116i	-2.04	0.002	0.52	0.52	418.0 ±30.0
^{124}Te	4.816	7.96	0	8	0	8	6.8 ±1.3
^{125}Te	7.14	5.02	-0.26	3.17	0.008	3.18	1.55
^{126}Te	18.95	5.56	0	3.88	0	3.88	1.04
^{128}Te	31.69	5.89	0	4.36	0	4.36	0.215
^{130}Te	33.8	6.02	0	4.55	0	4.55	0.29
Natural I	100	5.28	1.58	3.5	0.31	3.81	6.15
Natural Xe	—	4.92	3.04	2.96	0	—	23.9 ±1.2
^{124}Xe	0.1	—	0	—	0	—	165.0 ±20.0
^{126}Xe	0.09	—	0	—	0	—	3.5
^{128}Xe	1.91	—	0	—	0	—	<8
^{129}Xe	26.4	—	—	—	—	—	21.0 ±5.0
^{130}Xe	4.1	—	0	—	0	—	<26.
^{131}Xe	21.2	—	—	—	—	—	85.0 ±10.0
^{132}Xe	26.9	—	0	—	0	—	0.45
^{134}Xe	10.4	—	0	—	0	—	0.265
^{136}Xe	8.9	—	0	—	0	—	0.26
Natural Cs	100	5.42	1.29	3.69	0.21	3.9	29.0 ±1.5
Natural Ba	—	5.07	—	3.23	0.15	3.38	1.1
^{130}Ba	0.11	-3.6	0	1.6	0	1.6	30.0 ±5.0
^{132}Ba	0.1	7.8	0	7.6	0	7.6	7
^{134}Ba	2.42	5.7	0	4.08	0	4.08	2.0 ±1.6
^{135}Ba	6.59	4.67	—	2.74	0.5	3.2	5.8
^{136}Ba	7.85	4.91	0	3.03	0	3.03	0.68
^{137}Ba	11.23	6.83	—	5.86	0.5	6.4	3.6
^{138}Ba	71.7	4.84	0	2.94	0	2.94	0.27
Natural La	—	8.24	—	8.53	1.13	9.66	8.97
^{138}La	0.09	8.0 ±2.0	—	8.0 ±4.0	0.5	8.5 ±4.0	57.0 ±6.0
^{139}La	99.91	8.24	3	8.53	1.13	9.66	8.93
Natural Ce	—	4.84	—	2.94	0.001	2.94	0.63
^{136}Ce	0.19	5.8	0	4.23	0	4.23	7.3 ±1.5
^{138}Ce	0.25	6.7	0	5.64	0	5.64	1.1
^{140}Ce	88.48	4.84	0	2.94	0	2.94	0.57
^{142}Ce	11.08	4.75	0	2.84	0	2.84	0.95
Natural Pr	100	4.58	-0.35	2.64	0.015	2.66	11.5
Natural Nd	—	7.69	—	7.43	9.2	16.6	50.5 ±1.2
^{142}Nd	27.16	7.7	0	7.5	0	7.5	18.7
^{143}Nd	12.18	14.0 ±2.0	±21.0 ±1.0	25.0 ±7.0	55.0 ±7.0	80.0 ±2.0	337.0 ±10.0
^{144}Nd	23.8	2.8	0	1	0	1	3.6
^{145}Nd	8.29	14.0 ±2.0	—	25.0 ±7.0	5.0 ±5.0	30.0 ±9.0	42.0 ±2.0
^{146}Nd	17.19	8.7	0	9.5	0	9.5	1.4
^{148}Nd	5.75	5.7	0	4.1	0	4.1	2.5
^{150}Nd	5.63	5.3	0	3.5	0	3.5	1.2
Natural Pm	Unstable	12.6	±3.2 ±2.5	20.0 ±1.3	1.3 ±2.0	21.3 ±1.5	168.4 ±3.5
Natural Sm	—	0.80-1.65i	—	0.422	39.0 ±3.0	39.0 ±3.0	5922.0 ±56.0
^{144}Sm	3.1	-3.0 ±4.0	0	1.0 ±3.0	0	1.0 ±3.0	0.7
^{147}Sm	15.1	14.0 ±3.0	±11.0 ±7.0	25.0 ±11.0	143 ±19.0	39.0 ±16.0	57.0 ±3.0
^{148}Sm	11.3	-3.0 ±4.0	0	1.0 ±3.0	0	1.0 ±3.0	2.4
^{149}Sm	13.9	-19.2-11.7i	±31.4-10.3i	63.5	137.0 ±5.0	200.0 ±5.0	42080.0 ±400.0
^{150}Sm	7.4	14.0 ±3.0	0	25.0 ±11.0	0	25.0 ±11.0	104.0 ±4.0
^{152}Sm	26.6	-5	0	3.1	0	3.1	206.0 ±6.0
^{154}Sm	22.6	9.3	0	11.0 ±2.0	0	11.0 ±2.0	8.4
Natural Eu	—	7.22-1.26i	—	6.57	2.5	9.2	4530.0 ±40.0
^{151}Eu	47.8	6.13-2.53i	±4.5-2.14i	5.5	3.1	8.6	9100.0 ±100.0
^{153}Eu	52.2	8.22	±3.2	8.5	1.3	9.8	312.0 ±7.0
Natural Gd	—	6.5-13.82i	—	29.3	151.0 ±2.0	180.0 ±2.0	49700.0 ±125.0
^{152}Gd	0.2	10.0 ±3.0	0	13.0 ±8.0	0	13.0 ±8.0	735.0 ±20.0
^{154}Gd	2.1	10.0 ±3.0	0	13.0 ±8.0	0	13.0 ±8.0	85.0 ±12.0
^{155}Gd	14.8	6.0-17.0i	±5.0-13.16i	40.8	25.0 ±6.0	66.0 ±6.0	61100.0 ±400.0
^{156}Gd	20.6	6.3	0	5	0	5	1.5 ±1.2
^{157}Gd	15.7	-1.14-71.9i	±5.0-55.8i	650.0 ±4.0	394.0 ±7.0	1044.0 ±8.0	259000.0 ±700.0
^{158}Gd	24.8	9.0 ±2.0	0	10.0 ±5.0	0	10.0 ±5.0	2.2
^{160}Gd	21.8	9.15	0	10.52	0	10.52	0.77
Natural Tb	100	7.38	-0.17	6.84	0.004	6.84	23.4
Natural Dy	—	16.9-0.276i	—	35.9	54.4 ±1.2	90.3	994.0 ±13.0
^{156}Dy	0.06	6.1	0	4.7	0	4.7	33.0 ±3.0
^{158}Dy	0.1	6.0 ±4.0	0	5.0 ±6.0	0	5.0 ±6.0	43.0 ±6.0
^{160}Dy	2.34	6.7	0	5.6	0	5.6	56.0 ±5.0
^{161}Dy	19	10.3	±4.9	13.3	3.0 ±1.0	16.0 ±1.0	600.0 ±25.0

Isotope	Natural Abundance (%)	b_{coh} (10^{-13}) cm	b_{inc} (10^{-13}) cm	σ_{coh} (10^{-24}) cm²	σ_{inc} (10^{-24}) cm²	σ_{scat} (10^{-24}) cm²	σ_{abs} (10^{-24}) cm²
^{162}Dy	25.5	-1.4	0	0.25	0	0.25	194.0 ±10.0
^{163}Dy	24.9	5	1.3	3.1	0.21	3.3	124.0 ±7.0
^{164}Dy	28.1	49.4-0.79i	0	307.0 ±3.0	0	307.0 ±3.0	2840.0 ±40.0
Natural Ho	100	8.01	-1.7	8.06	0.36	8.42	64.7 ±1.2
Natural Er	—	7.79	—	7.63	1.1	8.7	159.0 ±4.0
^{162}Er	0.14	8.8	0	9.7	0	9.7	19.0 ±2.0
^{164}Er	1.56	8.2	0	8.4	0	8.4	13.0 ±2.0
^{166}Er	33.4	10.6	0	14.1	0	14.1	19.6 ±1.5
^{167}Er	22.9	3	1	1.1	0.13	1.2	659.0 ±16.0
^{168}Er	27.1	7.4	0	6.9	0	6.9	2.74
^{170}Er	14.9	9.6	0	11.6	0	11.6 ±1.2	5.8
Natural Tm	100	7.07	0.9	6.28	0.1	6.38	100.0 ±2.0
Natural Yb	—	12.43	—	19.42	4	23.4	34.8
^{168}Yb	0.14	-4.07-0.62i	0	2.13	0	2.13	2230.0 ±40.0
^{170}Yb	3.06	6.77	0	5.8	0	5.8	11.4 ±1.0
^{171}Yb	14.3	9.66	-5.59	11.7	3.9	15.6	48.6 ±2.5
^{172}Yb	21.9	9.43	0	11.2	0	11.2	0.8
^{173}Yb	16.1	9.56	-5.3	11.5	3.5	15	17.1 ±1.3
^{174}Yb	31.8	19.3	0	46.8	0	46.8	69.4 ±5.0
^{176}Yb	12.7	8.72	0	9.6	0	9.6	2.85
Natural Lu	—	7.21	—	6.53	0.7	7.2	74.0 ±2.0
^{175}Lu	97.39	7.24	±2.2	6.59	0.6	7.2	21.0 ±3.0
^{176}Lu	2.61	6.1-0.57i	±3.0+0.61i	4.7	1.2	5.9	2065.0 ±35.0
Natural Hf	—	7.7	—	7.6	2.6	10.2	104.1
^{174}Hf	0.2	10.9 ±1.1	0	15.0 ±3.0	0	15.0 ±3.0	561.0 ±35.0
^{176}Hf	5.2	6.61	0	5.5	0	5.5	23.5 ±3.1
^{177}Hf	18.6	0.8 ±1.0	±0.9 ±1.3	0.1	0.1	0.2	373.0 ±10.0
^{178}Hf	27.1	5.9	0	4.4	0	4.4	84.0 ±4.0
^{179}Hf	13.7	7.46	±1.06	7	0.14	7.1	41.0 ±3.0
^{180}Hf	35.2	13.2	0	21.9	0	21.9 ±1.0	13.04
Natural Ta	—	6.91	—	6	0.01	6.01	20.6
^{180}Ta	0.012	7.0 ±2.0	—	6.2	0.5	7.0 ±4.0	563.0 ±60.0
^{181}Ta	99.988	6.91	-0.29	6	0.011	6.01	20.5
Natural W	—	4.86	—	2.97	1.63	4.6	18.3
^{180}W	0.1	5.0 ±3.0	0	3.0 ±4.0	0	3.0 ±4.0	30.0 ±20.0
^{182}W	26.3	6.97	0	6.1	0	6.1	20.7
^{183}W	14.3	6.53	—	5.36	0.3	5.7	10.1
^{184}W	30.7	7.48	0	7.03	0	7.03	1.7
^{186}W	28.6	-0.72	0	0.065	0	0.065	37.9
Natural Re	—	9.2	—	10.6	0.9	11.5	89.7 ±1.0
^{185}Re	37.4	9	±2.0	10.2	0.5	10.7	112.0 ±2.0
^{187}Re	62.6	9.3	±2.8	10.9	1	11.9	76.4 ±1.0
Natural Os	—	10.7	—	14.4	0.3	14.7	16
^{184}Os	0.02	10.0 ±2.0	0	13.0 ±5.0	0	13.0 ±5.0	3000.0 ±150.0
^{186}Os	1.58	11.6 ±1.7	0	17.0 ±5.0	0	17.0 ±5.0	80.0 ±13.0
^{187}Os	1.6	10.0 ±2.0	—	13.0 ±5.0	0.3	13.0 ±5.0	320.0 ±10.0
^{188}Os	13.3	7.6	0	7.3	0	7.3	4.7
^{189}Os	16.1	10.7	—	14.4	0.5	14.9	25.0 ±4.0
^{190}Os	26.4	11	0	15.2	0	15.2	13.1
^{192}Os	41	11.5	0	16.6	0	16.6 ±1.2	2
Natural Ir	—	10.6	—	14.1	0.0 ±3.0	14.0 ±3.0	425.0 ±2.0
^{191}Ir	37.3	—	—	—	—	—	954.0 ±10.0
^{193}Ir	62.7	—	—	—	—	—	111.0 ±5.0
Natural Pt	—	9.6	—	11.58	0.13	11.71	10.3
^{190}Pt	0.01	9	0	10.0 ±2.0	0	10.0 ±2.0	152.0 ±4.0
^{192}Pt	0.79	9.9	0	12.3 ±1.2	0	12.3 ±1.2	10.0 ±2.5
^{194}Pt	32.9	10.55	0	14	0	14	1.44
^{195}Pt	33.8	8.83	-1	9.8	0.13	9.9	27.5 ±1.2
^{196}Pt	25.3	9.89	0	12.3	0	12.3	0.72
^{198}Pt	7.2	7.8	0	7.6	0	7.6	3.66
Natural Au	100	7.63	-1.84	7.32	0.43	7.75	98.65
Natural Hg	—	12.692	—	20.24	6.6	26.8	372.3 ±4.0
^{196}Hg	0.2	30.3 ±1.0	0	115.0 ±8.0	0	115.0 ±8.0	3080.0 ±180.0
^{198}Hg	10.1	—	0	—	0	—	2
^{199}Hg	17	16.9	±15.5	36.0 ±2.0	30.0 ±3.0	66.0 ±2.0	2150.0 ±48.0
^{200}Hg	23.1	—	0	—	0	—	<60.
^{201}Hg	13.2	—	—	—	—	—	7.8 ±2.0
^{202}Hg	29.6	—	0	—	0	9.828	4.89
^{204}Hg	6.8	—	0	—	0	—	0.43
Natural Tl	—	8.776	—	9.678	0.21	9.89	3.43
^{203}Tl	29.524	6.99	1.06	6.14	0.14	6.28	11.4
^{205}Tl	70.476	9.52	-0.242	11.39	0.007	11.4	0.104
Natural Pb	—	9.405	—	11.115	0.003	11.118	0.171
^{204}Pb	1.4	9.9	0	12.3	0	12.3	0.65
^{206}Pb	24.1	9.22	0	10.68	0	10.68	0.03
^{207}Pb	22.1	9.28	0.14	10.82	0.002	10.82	0.699
^{208}Pb	52.4	9.5	0	11.34	0	11.34	0.00048
Natural Bi	100	8.532	—	9.148	0.0084	9.156	0.0338
Natural Po	—	—	0.259	0	—	—	—
Natural At	—	—	—	0	—	—	—

Isotope	Natural Abundance (%)	b_{coh} (10^{-13}) cm	b_{inc} (10^{-13}) cm	σ_{coh} (10^{-24}) cm^2	σ_{inc} (10^{-24}) cm^2	σ_{scat} (10^{-24}) cm^2	σ_{abs} (10^{-24}) cm^2
Natural Rn	—	—	—	0	—	12.6	—
Natural Fr	—	—	—	0	—	—	—
Natural Ra	Unstable	10.0 ±1.0	0	13.0 ±3.0	0	13.0 ±3.0	12.8 ±1.5
Natural Ac	—	—	—	0	—	—	—
Natural Th	100	10.31	0	13.36	0	13.36	7.37
Natural Pa	Unstable	9.1	—	10.4	0.1 ±3.3	10.5 ±3.2	200.6 ±2.3
Natural U	—	8.417	—	8.903	0.005	8.908	7.57
^{233}U	Unstable	10.1	±1.0 ±3.0	12.8	0.1	12.9	574.7 ±1.0
^{234}U	0.005	12.4	0	19.3	0	19.3	100.1 ±1.3
^{235}U	0.72	10.47	±1.3	13.78	0.2	14	680.9 ±1.1
^{238}U	99.275	8.402	0	8.871	0	8.871	2.68
Natural Np	Unstable	10.55	—	14	0.5	14.5	175.9 ±2.9
Natural Pu	—	—	—	—	—	—	—
^{238}Pu	Unstable	14.1	0	25.0 ±1.8	0	25.0 ±1.8	558.0 ±7.0
^{239}Pu	Unstable	7.7	±1.3 ±1.9	7.5	0.2	7.7	1017.3 ±2.1
^{240}Pu	Unstable	3.5	0	1.54	0	1.54	289.6 ±1.4
^{242}Pu	Unstable	8.1	0	8.2	0	8.2	18.5
Natural Am	Unstable	8.3	±2.0 ±7.0	8.7	0.3	9.0 ±2.6	75.3 ±1.8
Natural Cm	—	—	—	0	—	—	—
^{244}Cm	Unstable	9.5	0	11.3	0	11.3	16.2 ±1.2
^{246}Cm	Unstable	9.3	0	10.9	0	10.9	1.36
^{248}Cm	Unstable	7.7	0	7.5	0	7.5	3

No TV and no beer make Homer go crazy
No TV and no beer make Homer go crazy
No TV and no beer make Homer go crazy
...

Homer Simpson

E

Thesis Activities and Publications

Patents

- **Sistema para la generación de hologramas digitales vía simulación.**
  I. Molina de la Peña, M.L. Calvo and R.F. Alvarez-Estrada
  Patent registered for evaluation, Ref. P202230979, 2022.

Publications

- **Focalizing slow neutron beams at and below micron scales: Discussion on BNCT.**
  R.F. Alvarez-Estrada, I. Molina de la Peña and M.L. Calvo
  Phosphorus, Sulfur and Silicon and the Related Elements, **193**(2): 64-73, 2018.
  DOI: 10.1080/10426507.2017.1417300

- **Focalizing slow neutron beams at and below micron scales and discussion on BNCT (II).**
  I. Molina de la Peña, M.L. Calvo and R.F. Alvarez-Estrada
  Phosphorus, Sulfur and Silicon and the Related Elements, **194**(10, SI): 956-966, 2019.
  DOI: 10.1080/10426507.2019.1631309

- **Chapter 3: Neutron confinement and waveguiding**
  I. Molina de la Peña, M.L. Calvo and R.F. Alvarez-Estrada
  Advances in Neutron Optics: Fundamentals and Applications in Materials Science and Biomedicine, edited by M.L. Calvo and R.F. Alvarez-Estrada, CRC Press: Boca Raton (FL), 2019.

- **Neutron waveguides in neutron optics: Green's functions formalism with Dirichlet boundary conditions.**
  I. Molina de la Peña, M.L. Calvo and R.F. Alvarez-Estrada
  Journal of Modern Optics, **67**(10): 899-913, 2020.
  DOI: 10.1080/09500340.2020.1786181

- **Neutron waveguides: a proposal for slow neutrons confinement and applications in neutron optics.**[1]
  I. Molina de la Peña, M.L. Calvo and R.F. Alvarez-Estrada
  Asian Journal of Physics, **30**(8-9): 1289-1294, 2021.

- **Neutron optics: New algorithm based on Green's functions for simulating waveguides with Dirichlet boundary conditions.**
  I. Molina de la Peña, M.L. Calvo and R.F. Alvarez-Estrada
  Applied Mathematical Modelling, **101**: 694-715, 2021.
  DOI: 10.1016/j.apm.2021.09.007

- **Neutron waveguides with finite repulsive potential in clad.**
  I. Molina de la Peña, R.F. Alvarez-Estrada and M.L. Calvo
  The European Physical Journal Plus, **137**(987), 2022.
  DOI: 10.1140/epjp/s13360-022-03182-9

Third Party Reviews

- **Advances in neutron optics.**
  F. Arqueros Martínez
  Review of our book in section *Reseñas de libros de interés.*
  Revista Española de Física, **34**(2): 57, 2020

- **Neutron waveguides with finite repulsive potential in clad.**
  A. Beléndez
  Review of our research in section *Puntos de interés.*
  Revista Española de Física, **35**(4): 46-47, 2021

Seminars and Congress[2]

- **Neutron optics: Application to modal waveguides**
  I. Molina de la Peña, M.L. Calvo and R.F. Alvarez-Estrada
  Poster contribution to the X Reunión Nacional de Optoelectrónica. OPTOEL 2017
  July 12th - 14th, 2017, Santiago de Compostela (Spain).

[1] Not indexed journal.
[2] Presenting author is underlined

- **Focalizing Thermal Neutron Beams at and Below Micron Scales: Discussion on BNCT**
  R.F. Alvarez-Estrada, I. Molina de la Peña and M.L. Calvo
  Oral contribution to the International Conference on Phosphorus, Boron and Silicon. PBSi 2017.
  July 3rd - 5th, 2017, Paris (France).

- **Neutron Waveguides: a proposal for slow neutrons confinement and applications in neutron optics**
  I. Molina de la Peña, M.L. Calvo and R.F. Alvarez-Estrada
  Oral contribution to the 24th Congress of the International Commission for Optics. ICO-24.
  August 21st - 25th, 2017, Tokio (Japan).

- **Study of the Potential Application of Low Energy Neutrons from Neutron Guides to BNCT Radiosurgery**
  P. Torres, I. Molina de la Peña, M.L. Calvo, J. Praena, R.F. Alvarez-Estrada and I. Porras
  Poster contribution to the 18th International Congress on Neutron Capture Therapy.
  October 28th - November 2nd, 2018, Taipei (Taiwan).

- **Focalizing Thermal Neutron Beams at and Below Micron Scales: Discussion on BNCT (II)**
  I. Molina de la Peña, M.L. Calvo and R.F. Alvarez-Estrada
  Oral contribution to the International Conference on Phosphorus, Boron and Silicon. PBSi 2018.
  December 12th - 14th, 2018, Barcelona (Spain).

- **Fundamentals of neutron waveguides: a proposal for slow neutron beams confinement and applications**
  M.L. Calvo, I. Molina de la Peña and R.F. Alvarez-Estrada
  Oral contribution to the 4th International Conference on Applications of Optics and Photonics. AOP 2019.
  May 31st - June 4th, 2019, Lisbon (Portugal).

- **Confined propagation of slow neutron beams in very thin waveguides with possible application to BNCT**
  I. Molina de la Peña, M.L. Calvo and R.F. Alvarez-Estrada
  Oral contribution to the 19th International Congress on Neutron Capture Therapy.
  October 27th - November 1st, 2021, Granada (Spain).

- **Neutron optics: Applications to neutron waveguides**
  I. Molina de la Peña, R.F. Alvarez-Estrada and M.L. Calvo
  Seminar organized by the department of Theoretical Physics. Universidad Complutense de Madrid (Spain).
  March 23rd, 2022.

- Quién sabe lo que diría mi señor si se enterase de que dejé que me robaran un libro de su biblioteca.
- ¿Sabes cuánto hace que no se me extravía un libro?

Sandman

Bibliography

[1] J. Chadwick. Possible Existence of a Neutron. *Nature*, **129**:312, 1932. DOI: 10.1038/129312a0

[2] E. Fermi and W.H. Zinn. Collimation of neutron beam from thermal column of CP-3 and the index of refraction for themal neutrons. Technical report, Argonne Laboratory, Chicago, IL, USA, 1944.

[3] R.F. Alvarez-Estrada and M.L. Calvo. Neutron fibers. A possible application of neutron optics. *Journal of Physics D-Applied Physics*, **17**(3):475–502, 1984. DOI: 10.1088/0022-3727/17/3/007

[4] M.L. Calvo and R.F. Alvarez-Estrada. Neutron fibers.II. Some improving alternatives and analysis of bending losses. *Journal of Physics D-Applied Physics*, **19**(6):957–973, 1986. DOI: 10.1088/0022-3727/19/6/012

[5] I. Molina de la Peña, M.L. Calvo and R.F. Alvarez-Estrada. Sistema para la generación de hologramas digitales vía simulación. Patent registered for evaluation, Ref. P202230979, 2022.

[6] A. W. Snyder and J. Love, Chapter 20: Illumination, tilts and offsets, in *Optical Waveguide Theory*, edited by A. W. Snyder and J. Love, Springer: Boston (MA), 1983.

[7] M. Abramowitz and I.A. Stegun. *Handbook of Mathematical Functions*. Martino Publishing: Mansfield Centre, CT, 2014.

[8] G.E. Bacon. *Neutron Diffraction (3rd Ed.)*. Clarendon Press: Oxford, 1975.

[9] J. Byrne. *Neutrons, Nuclei and Matter. An Exploration of the Physics of Slow Neutrons.* Institute of Physics Publishing: Bristol, Philadelphia, 1995.

[10] V.F. Sears. *Neutron Optics. An Introduction to the Theory of Neutron Optical Phenomena and their Applications*. Oxford University Press: New York, 1989.

[11] R.E. DeWames and S.K. Sinha. Possibility of guided-neutron-wave propagation in thin films. *Physical Review B*, **7**(3):917–921, 1973. DOI: 10.1103/PhysRevB.7.917

[12] M.A. Kumakhov and V.A. Sharov. A neutron lens. *Nature*, **357**(6377):390–391, 1992. DOI: 10.1038/357390a0

[13] Y.P. Feng, C.F. Majkrzak, S.K. Sinha, D.G. Wiesler, H. Zhang and H.W. Deckman. Direct observation of neutron-guided waves in a thin-film waveguide. *Physical Review B*, **49**(15):10814–10817, 1994. DOI: 10.1103/PhysRevB.49.10814

[14] R. Balian and C. Bloch. Distribution of eigenfrequencies for wave equation in a finite domain: I. Three-dimensional problem with smooth boundary surface. *Annals of Physics*, **60**(2):401–447, 1970.
DOI: 10.1016/0003-4916(70)90497-5

[15] J.W. Cooley and J.W. Turkey. An algorithm for the machine calculation of complex Fourier series. *Mathematics of Computation*, **19**(90):297–301, 1965.
DOI: 10.2307/2003354

[16] T.E. Mason, T.J. Gawne, S.E. Nagler, M.B. Nestor and J.M. Carpenter. The early development of neutron diffraction: science in the wings of the Manhattan Project. *Acta Crystallographica Section A*, **69**(1):37–44, 2013.
DOI: 10.1107/S0108767312036021

[17] J. Chadwick. The existence of a neutron. *Proceedings of the Royal Society of London A*, **136**:692–708, 1932.
DOI: 10.1098/rspa.1932.0112

[18] H. Halban and P. Preiswerk. Preuve expérimentale de la diffraction des neutrons. *Comptes Rendus de L'Académie des Sciences Paris*, **203**:73–75, 1936.

[19] D.P. Mitchell and P.N. Powers. Bragg reflection of slow neutrons. *Physical Review*, **50**(5):486, 1936.

[20] E. Fermi, E. Amaldi, O. D'Agostino, F. Rasetti and E. Segrè. Artificial radioactivity produced by neutron bombardment. *Proceedings of the Royal Society of London A*, **146**(857):483–500, 1934.
DOI: 10.1098/rspa.1934.0168

[21] E. Fermi. Artificial radioactivity produced by neutron bombardment (Nobel lecture). *Royal Swedish Academy of Sciences*, 1938.
https://www.nobelprize.org/uploads/2018/06/fermi-lecture.pdf .

[22] E. Fermi and W.H. Zinn. Reflection of neutrons on mirrors. *Physical Review*, **70**(1-2):103, 1946.

[23] H.D. Smyth. Atomic energy for military purposes (Smyth Report). Technical report, Princeton University Press, 1945.

[24] P.A. Zyla et al. (Particle Data Group). Review of particle physics. *Progress of Theoretical and Experimental Physics*, **Volume 2020**(8):083C01, 2020.
DOI: 10.1093/ptep/ptaa104

[25] S. Arzumanov, L. Bondarenko, S. Chernyavsky, P. Geltenbort, V. Morozov, V.V. Nesvizhevsky, Yu. Panin and A. Strepetov. A measurement of the neutron lifetime using the method of storage of ultracold neutrons and detection of inelastically up-scattered neutrons. *Physics Letters B*, **745**:79–89, 2015.
DOI: 10.1016/j.physletb.2015.04.021

[26] R.C. Martin, J.B. Knauer and P.A. Pablo. Production, distribution and applications of Californium-252 neutron sources. *Applied Radiation and Isotopes*, **53**(4-5):785–792, 2000.
DOI: 10.1016/S0969-8043(00)00214-1

[27] J.A. Grundl. Fission neutron spectra: Macroscopic and integral results. *National Bureau of Standards, Washington, D.C.*, (Technical Report: CONF-701002), 1971.
DOI: 10.2172/4754459

[28] R.F. Alvarez-Estrada and M.L. Calvo, Chapter 1: Neutron optics: Fundamentals, in *Advances in Neutron Optics: Fundamentals and Applications in Materials Science and Biomedicine*, edited by M.L. Calvo and R.F. Alvarez-Estrada, CRC Press: Boca Raton (FL), 2019.

[29] Y. Kasesaz, E. Bavarnegin, M. Golshanian, A. Khajeali, H. Jarahi, S.M. Mirvakili and H. Khalafi. BNCT project at Tehran Research Reactor: Current and prospective plans. *Progress in Nuclear Energy*, **91**:107–115, 2016.
DOI: 10.1016/j.pnucene.2016.04.010

[30] I. Molina de la Peña, M.L. Calvo and R.F. Alvarez-Estrada, Chapter 3: Neutron confinement and waveguiding, in *Advances in Neutron Optics: Fundamentals and Applications in Materials Science and Biomedicine*, edited by M.L. Calvo and R.F. Alvarez-Estrada, CRC Press: Boca Raton (FL), 2019.

[31] Technical characteristics: Description of the ILL high-flux reactor. https://www.ill.eu/reactor-and-safety/high-flux-reactor/technical-characteristics .

[32] ESS revises project plan and budget. https://europeanspallationsource.se/article/2021/12/10/ess-revises-project-plan-and-budget .

[33] V.F. Sears. Neutron scattering lengths and cross sections. *Neutron News*, **3**(3):26–37, 1992.
DOI: 10.1080/10448639208218770

[34] L.E. Ballentine. *Quantum Mechanics: A Modern Development.* World Scientific: Singapore, 1998.

[35] R.F. Alvarez-Estrada, Chapter 6: Ecuación de Schrödinger e introducción a la interpretación probabilística, in *Física Cuántica: I [Spanish] 7th Ed.*, edited by C. Sánchez del Río, Pirámide: Madrid, 2020.

[36] L.D. Landau and E.M. Lifshitz. *Quantum Mechanics: Non-relativistic Theory.* Pergamon: London, 1977.

[37] M.L. Calvo (Coord.). *Óptica Avanzada [Spanish].* Ariel Ciencias: Barcelona, 2002.

[38] D.M. Greenberger. The neutron interferometer as a device for illustrating the strange behavior of quantum systems. *Review of Modern Physics*, **55**(4):875–905, 1983.
DOI: 10.1103/RevModPhys.55.875

[39] D.F.R. Mildner, Chapter 63: Neutron Optics, in *Handbook of Optics (Vol V) 2nd Ed.*, edited by M. Bass, McGraw-Hill: New York (NY), 2001.

[40] A.G. Klein and S.A. Werner. Neutron optics. *Reports on Progress in Physics*, **46**(3):259–335, 1983.
DOI: 10.1088/0034-4885/46/3/001

[41] P.D. Kearney, A.G. Klein, G.I. Opat and R. Gähler. Imaging and focusing of neutrons by a zone plate. *Nature*, **287**:313–314, 1980.
DOI: 10.1038/287313a0

[42] F.J. Landkammer. Beugungsversuche mit langsamen Neutronen. *Zeitschrift für Physik*, **189**(2):113–137, 1969.
DOI: 10.1007/BF01327150

[43] C. G. Shull. Single-slit diffraction of neutrons. *Physical Review*, **179**(3):752–754, 1969.
DOI: 10.1103/PhysRev.179.752

[44] H. Kurz and H. Rauch. Beugung thermischer Neutronen an einem Strichgitter. *Zeitschrift für Physik*, **220**(5):419–426, 1969.
DOI: 10.1007/BF01394786

[45] V.I. Lushchikov, Y.N. Pokotilovsky, A.V. Strelkov and Shapiro F.L. Observation of ultracold neutrons. *Soviet Physics JETP Letters*, **9**(23):40–45, 1969.

[46] L.V. Groshev, V.N. Dvoretsky, A.M. Demidov, Y.N. Panin, V.I. Lushchikov, Y.N. Pokotilovsky, A.V. Strelkov and Shapiro F.L. Experiments with ultracold neutrons. *Physics Letters B*, **234**(4):293–295, 1971.
DOI: 10.1016/0370-2693(71)90608-3

[47] H. Maier-Leibnitz and T. Springer. The use of neutron optical devices on beam-hole experiments. *Journal of Nuclear Energy A/B*, **17**(4-5):217–225, 1963.
DOI: 10.1016/0368-3230(63)90022-3

[48] H. Rauch, W. Treimer and U. Bonse. Test of a single crystal neutron interferometer. *Physics Letters A*, **47**(5):369–371, 1974.
DOI: 10.1016/0375-9601(74)90132-7

[49] S. A. Werner, R. Colella, A. W. Overhauser and C. F. Eagen. Observation of the phase shift of a neutron due to precession in a magnetic field. *Physical Review Letters*, **35**(16):1053–1055, 1975.
DOI: 10.1103/PhysRevLett.35.1053

[50] R. Colella, A. W. Overhauser and S. A. Werner. Observation of gravitationally induced quantum interference. *Physical Review Letters*, **34**(23):1472–1474, 1975.
DOI: 10.1103/PhysRevLett.34.1472

[51] V.V. Nesvizhevsky, H.G. Börner, A.K. Petukhov, H. Abele, S. Baeßler, F.J. Rueß, T. Stöferle, A.M. Westphal, A. Gagarski, G.A. Petrov and A.V. Strelkov. Quantum states of neutrons in the earth's gravitational field. *Nature*, **415**:297–299, 2002.
DOI: 10.1038/415297a

[52] J.R. Dunning, P.N. Powers and H.G. Beyer. Experiments on the magnetic properties of the neutron. *Physical Review*, **51**(1):51–51, 1937.
DOI: 10.1103/PhysRev.51.51

[53] L. Cser, G.y. Török, G. Krexner, I. Sharkov and B. Faragó. Holographic imaging of atoms using thermal neutrons. *Physical Review Letters*, **89**(17):175504, 2002.
DOI: 10.1103/PhysRevLett.89.175504

[54] E. Fermi. Sul moto dei neutroni nelle sostanze idrogenate. *La Ricerta Scientifica*, **7**(2):13–52, 1936.

[55] L.L. Foldy. The multiple scattering of waves. I. General theory of isotropic scattering by randomly distributed scatterers. *Physical Review*, **67**(3-4):107–119, 1945.
DOI: 10.1103/PhysRev.67.107

[56] M. Utsuro and V.K. Ignatovich. *Handbook of Neutron Optics*. Wiley: New York (NY), 2010.

[57] G. Breit and E. Wigner. Capture of slow neutrons. *Physical Review*, **49**(7):519–531, 1936.
DOI: 10.1103/PhysRev.49.519

[58] J.M. Cassels, Chapter: The scattering of neutrons by crystals, in *Progress in Nuclear Physics: I*, edited by O.R. Frisch, Butterworth-Springer, London, 1950.

[59] R.F. Alvarez-Estrada and M.L. Calvo, Chapter 9: Óptica de neutrones, in *Óptica Avanzada [Spanish]*, edited by M.L. Calvo, Ariel Ciencias: Barcelona, 2002.

[60] F. Bloch. On the magnetic scattering of neutrons. *Physical Review*, **50**(3):259–260, 1936.
DOI: 10.1103/PhysRev.50.259

[61] N. Pleshanov, Chapter 5: Neutron spin optics: Concepts, verification and prospects, in *Advances in Neutron Optics: Fundamentals and Applications in Materials Science and Biomedicine*, edited by M.L. Calvo and R.F. Alvarez-Estrada, CRC Press: Boca Raton (FL), 2019.

[62] R.F. Alvarez-Estrada, I. Molina de la Peña and M.L. Calvo. Focalizing slow neutron beams at and below micron scales: Discussion on BNCT. *Phosphorus, Sulfur and Silicon and the Related Elements*, **193**(2):64–73, 2018.
DOI: 10.1080/10426507.2017.1417300

[63] I. Molina de la Peña, M.L. Calvo and R.F. Alvarez-Estrada. Focalizing slow neutron beams at and below micron scales and discussion on BNCT (II). *Phosphorus, Sulfur and Silicon and the Related Elements*, **194**(10, SI):956–966, 2019.
DOI: 10.1080/10426507.2019.1631309

[64] Research neutron source Heinz Maier-Leibnitz (FRM II): Guiding the beams. https://www.frm2.tum.de/en/frm2/the-neutron-source/reactor/guiding-the-beams .

[65] W. Sauerwein, R. Moss and A. Wittig. *Research and Development in NCT*. Monduzzi Editore: Bologna, 2002.

[66] D. Marx. Microguides for neutrons. *Nuclear Instruments and Methods*, **94**(3):533–536, 1971.
DOI: 10.1016/0029-554X(71)90017-6

[67] F. Ott, Chapter 7: Focusing Optics for Neutrons, in *Modern Developments in X-Ray and Neutron Optics*, edited by A. Erko, M. Idir, T. Krist and A. G. Michette, Springer: Berlin, Heidelberg, 2010.

[68] M. Rossbach, O. Schärpf, W. Kaiser, W. Graf, A. Schirmer, W. Faber, J. Duppich and R. Zeisler. The use of focusing supermirror neutron guides to enhance cold neutron fluence rates. *Nuclear Instruments and Methods in Physics Research Section B*, **35**(2):181–190, 1988.
DOI: 10.1016/0168-583X(88)90491-0

[69] A. Schebetov, A. Kovalev, B. Peskov, N. Pleshanov, V. Pusenkov, P. Schubert-Bischoff, G. Shmelev, Z. Soroko, V. Syromyatnikov, V. Ul'yanov and A. Zaitsev. Multi-channel neutron guides of PNPI: results of neutron and X-ray reflectometry tests. *Nuclear Instruments and Methods in Physics Research Section A*, **432**(2):214–226, 1999.
DOI: 10.1016/S0168-9002(99)00480-5

[70] H. Chen, R.G. Downing, D.F.R. Mildner, W.M. Gibson, M.A. Kumakhov, I.Y. Ponomarev and M.V. Gubarev. Guiding and focusing neutron beams using capillary optics. *Nature*, **357**(6377):391–393, 1992.
DOI: 10.1038/357391a0

[71] M.A. Kumakhov and F.F. Komarov. Multiple Reflection from surface X-ray optics. *Physics Reports - Review Section of Physics Letters*, **191**(5):289–350, 1990.
DOI: 10.1016/0370-1573(90)90135-O

[72] M. Kumakhov. Neutron capillary optics: status and perspectives. *Nuclear Instruments and Methods in Physics Research Section A*, **529**(1):69–72, 2004.
DOI: 10.1016/j.nima.2004.04.179

[73] S.P. Pogossian, A. Menelle, H. LeGall, J.M. Desvignes and M. Artinian. Experimental observation of guided polarized neutrons in magnetic-thin-film waveguides. *Physical Review B*, **53**(21):14359–14363, 1996.
DOI: 10.1103/PhysRevB.53.14359

[74] A. Menelle, S.P. Pogossian, H. LeGall, J.M. Desvignes and J. Ben Youssef. Observation of magnetic thin films neutron waveguides. *Physica B*, **234**:510–512, 1997.
DOI: 10.1016/S0921-4526(96)01028-9

[75] S.P. Pogossian, A. Menelle, H. LeGall, J. Ben Youssef and J.M. Desvignes. Observation of neutron guided waves from the open end of a thin film waveguide and a waveguide interferometry. *Journal of Applied Physics*, **83**(3):1159–1162, 1998.
DOI: 10.1063/1.366810

[76] S.P. Pogossian. Enhanced neutron concentration in Uranium thin film waveguides. *Journal of Applied Physics*, **102**(10):104501, 2007.
DOI: 10.1063/1.2811851

[77] S. V. Kozhenikov, Y. N. Khaydukov, T. Keller, F. Ott and F. Radu. Polarized neutron channeling as a tool for the investigations of weakly magnetic thin films. *JETP Letters*, **103**:36–40, 2016.
DOI: 10.1134/S0021364016010082

[78] A. Muñoz Sudupe, Chapter 8: Estados ligados en una dimensión, in *Física Cuántica: I [Spanish] 7th Ed.*, edited by C. Sánchez del Río, Pirámide: Madrid, 2020.

[79] K. Yee. Numerical solution of initial boundary value problems involving Maxwell's equations in isotropic media. *IEEE Transaction on Antennas and Propagation*, **14**(3):302–307, 1966.
DOI: 10.1109/TAP.1966.1138693

[80] J.R. Nagel. A review and application of the finite-difference time-domain algorithm applied to the Schrödinger equation. *Applied Computational Electromagnetics Society Journal*, **24**(1):1–8, 2009.

[81] FDTD Algorithm. The FDTD Method. Solver Numerics. https://support.lumerical.com/hc/en-us/articles/360044941854-FDTD-Algorithm-The-FDTD-Method-Solver-Numerics .

[82] M.L. Calvo. Neutron fibres: a three-dimensional analysis of bending losses. *Journal of Physics D: Applied Physics*, **33**(14):1666–1673, 2000.
DOI: 10.1088/0022-3727/33/14/306

[83] A. Messiah. *Quantum Mechanics (Vol. 1).* North-Holland Publishing: Amsterdam, 1960.

[84] I. Molina de la Peña, M.L. Calvo and R.F. Alvarez-Estrada. Neutron waveguides in neutron optics: Green's functions formalism with Dirichlet boundary conditions. *Journal of Modern Optics*, **67**(10):899–913, 2020.
DOI: 10.1080/09500340.2020.1786181

[85] M. Nieto-Vesperinas, Chapter 2: Propagación de luz y otras ondas electromagnéticas, in *Óptica Avanzada [Spanish]*, edited by M.L. Calvo, Ariel Ciencias: Barcelona, 2002.

[86] M. Nieto-Vesperinas. *Scattering and Diffraction in Physical Optics.* Wiley-Interscience: New York (NY), 1991.

[87] L. Mandel and E. Wolf. *Optical Coherence and Quantum Optics.* Cambrigde University Press: Cambridge, 1995.

[88] O.D. Kellogg. *Foundations of Potential Theory.* Springer-Verlag: Berlin-Heidelberg-New York, 1967.

[89] S. Bochner and K. Chandrasekharan. *Fourier Transforms.* Princeton University Press: Princeton (NJ), 1949.

[90] N.J. Pandey. *The Hilbert transform of Schwartz distributions and applications.* Wiley-Interscience: New York (NY), 1996.

[91] R. Bracewell. *The Fourier transform and its applications.* McGraw-Hill: New York (NY), 1996.

[92] E. Bedrosian. A product theorem for Hilbert transforms. Technical report, Santa Monica (CA): The Rand Corporation Memorandum, 1962.

[93] R.G. Newton. *Scattering theory of waves and particles*. Dover Books on Physics: New York, 2013.

[94] I. Molina de la Peña, M.L. Calvo and R.F. Alvarez-Estrada. Neutron optics: New algorithm based on Green's functions for simulating waveguides with Dirichlet boundary conditions. *Applied Mathematical Modelling*, **101**:694–715, 2021.
DOI: 10.1016/j.apm.2021.09.007

[95] M. Frigo and S.G. Johnson. The design and implementation of FFTW3. *Proceedings of the IEEE*, **93**(2):216–231, 2005.
DOI: 10.1109/JPROC.2004.840301

[96] A. Shojaei, U. Galvanetto, T. Rabczuk, A. Jenabi and M. Zaccariotto. A generalized finite difference method based on the peridynamic differential operator for the solution of problems in bounded and unbounded domains. *Computer Methods in Applied Mechanics and Engineering*, **343**:100–126, 2019.
DOI: 10.1016/j.cma.2018.08.033

[97] A. Shojaei, F. Mossaiby, M. Zaccariotto and U. Galvanetto. A local collocation method to construct Dirichlet-type absorbing boundary conditions for transient scalar wave propagation problems. *Computer Methods in Applied Mechanics and Engineering*, **356**:629–651, 2019.
DOI: 10.1016/j.cma.2019.07.033

[98] J. Ojeda-Castañeda and C. Gomez-Reino. Selected papers on zone plates. *SPIE Milestone Series*, **128**, 1996.

[99] M.L. Calvo. m-Learning and holography: Compatible techniques? In *Proceedings of SPIE*, volume 9289, pages 928903–1–8, 2014.

[100] D. Gabor. A new microscopic principle. *Nature*, **161**(4098):777–778, 1948.
DOI: 10.1038/161777a0

[101] B.A. Lippmann and J. Schwinger. Variational principles for scattering processes. I. *Physical Review*, **79**(3):469–480, 1950.
DOI: 10.1103/PhysRev.79.469

[102] I. Molina de la Peña, R.F. Alvarez-Estrada and M.L. Calvo. Neutron waveguides with finite repulsive potential in clad. *The European Physical Journal Plus*, **137**(987), 2022.
DOI: 10.1140/epjp/s13360-022-03182-9

[103] F. Scheck. *Quantum Physics (2-nd Ed.)*. Springer-Verlag: Berlin-Heidelberg, 2013.

[104] M. Gell-Mann and M.L. Goldberger. The formal theory of scattering. *Physical Review*, **91**(2):398–408, 1953.
DOI: 10.1103/PhysRev.91.398

[105] W. Brenig and R. Haag. The formal theory of scattering. *Fortschritte der Physik*, **7**:183–242, 1959.
DOI: 10.1002/prop.19590070402

[106] M.L. Goldberger and K.M. Watson. *Collision Theory (Structure of Matter Series)*. Wiley: New York (NY), 1964.

[107] M.L. Calvo and V. Lakshminarayanan. An analysis of the modal field in absorbing optical waveguides and some useful approximations. *Journal of Physics D: Applied Physics*, **22**(5):603–610, 1989.
DOI: 10.1088/0022-3727/22/5/006

[108] S.V. Kozhevnikov, V.D. Zhaketov and F. Radu. Neutron microbeam from a planar waveguide. *Journal of Experimental and Theoretical Physics*, **127**:593–607, 2018.
DOI: 10.1134/S1063776118100163

[109] R.F. Alvarez-Estrada and M.L. Calvo. Neutron fibres and possible applications to NCT. *Applied Radiation and Isotopes*, **61**(5):841–844, 2004.
DOI: 10.1016/j.apradiso.2004.05.039

[110] H. Hatanaka, Chapter 2: Clinical results of boron neutron capture therapy, in *Neutron Beam Design, Development, and Performance for Neutron Capture Therapy*, edited by Otto K. Harling, John A. Bernard and Robert G. Zamenhof, Springer: Boston (MA), 1990.

[111] Y. Mishima, M. Ichihashi, S. Hatta, C. Honda, K. Yamamura, T. Nakagawa, H. Obara, J. Shirakawa, J. Hiratsuka and K. Taniyama. First human clinical trial of melanoma neutron capture. Diagnosis and therapy. *Strahlentherapie und Onkologie*, **165**(2-3):251–254, 1989.

[112] M.A. Dymova, S.Y. Taskaev, V.A. Richter and E.V. Kuligina. Boron neutron capture therapy: Current status and future perspectives. *Cancer Communications*, **40**(9):406–421, 2020.
DOI: 10.1002/cac2.12089

[113] I. Porras, Chapter 6: Applications of Neutron Optics to Biomedicine: BNCT, in *Advances in Neutron Optics: Fundamentals and Applications in Materials Science and Biomedicine*, edited by M.L. Calvo and R.F. Alvarez-Estrada, CRC Press: Boca Raton (FL), 2019.

[114] International Atomic Energy Agency. *Current status of neutron capture therapy*. IAEA, Vienna, 2001.

[115] I. Kiyanagi, Y. Sakurai, H. Kumada and H. Tanaka. Status of accelerator-based BNCT projects worldwide. *AIP Conference Proceedings*, **2160**(1):050012, 2019.
DOI: 10.1063/1.5127704

[116] Accelerator-based BNCT projects. https://isnct.net/bnct-boron-neutron-capture-therapy/accelerator-based-bnct-projects-2021/ .

[117] R.L. Moss. Critical review, with an optimistic outlook, on Boron Neutron Capture Therapy (BNCT). *Applied Radiation and Isotopes*, **88**:2–11, 2014.
DOI: 10.1016/j.apradiso.2013.11.109

[118] SHIN-1: First commercialization of cyclotron-based BNCT system “NeuCure”. https://nucleus.iaea.org/sites/accelerators/TMBNCT/Document.

[119] T. Mitsumoto, K. Fujita, T. Ogasawara, H. Tsutsui, S. Yajima, Y. Maruhashi Sakurai and H. Tanaka. BNCT system using 30 mev H-cyclotron. In *CYCLOTRONS'2010: The 19-th International Conference on Cyclotrons and Their Applications*, 2010.

[120] J. Schwinger, L. Deraad Jr., K. Milton and W.Y. Tsai. *Classical Electrodynamics*. CRC Press: Boca Raton (FL), 1998.

[121] M.L. Calvo. Linear behaviour in the aperture pupil of single photoreceptors: Consequences related to the degree of inhomogeneity. *Biological Cybernetics*, **54**(3):201–210, 1986.
DOI: 10.1007/BF00356859

[122] R.F. Alvarez-Estrada and M.L. Calvo, Chapter 9: Neutron Waveguides and Applications, in *Optical Waveguides. From Theory to Applied Technologies*, edited by M.L. Calvo and V. Lakshminarayanan, CRC Press: Boca Raton (FL), 2007.

[123] E. Lalor and E. Wolf. Exact solution of the equations of molecular optics for refraction and reflection of an electromagnetic wave on a semi-infinite dielectric. *Journal of the Optical Society of America*, **62**(10):1165–1174, 1972.
DOI: 10.1364/JOSA.62.001165